

**A STUDY OF SOME OF THE FOUNDRY
PROCESSING
FACTORS INFLUENCING THE QUALITY
OF TITANIUM ALLOY INVESTMENT
CASTINGS**

By
IMAN EFFAT A. KHALED

A thesis submitted to

The School of Metallurgy and Materials

The University of Birmingham

For the degree of

DOCTOR OF PHILOSOPHY

The University of Birmingham

Birmingham B15 2TT

United Kingdom

May 2015

UNIVERSITY OF
BIRMINGHAM

University of Birmingham Research Archive

e-theses repository

This unpublished thesis/dissertation is copyright of the author and/or third parties. The intellectual property rights of the author or third parties in respect of this work are as defined by The Copyright Designs and Patents Act 1988 or as modified by any successor legislation.

Any use made of information contained in this thesis/dissertation must be in accordance with that legislation and must be properly acknowledged. Further distribution or reproduction in any format is prohibited without the permission of the copyright holder.

Acknowledgment

I would like to express my gratitude and thanks to my supervisor Dr. Richard Harding, for his guidance, valuable advice and continuous support during carrying out my experimental research. I would also like to thank Professor Nick Green for encouraging my modelling work.

My special appreciation and thanks is extended to Dr. William Griffiths, who did not spare his time and his valuable comments which have enriched my thesis by brilliant suggestions.

A special thanks to the staff and colleagues in the School of Metallurgy and Materials for their sincere support. I especially acknowledge Mr. Mick Wickins for his help during experimental castings.

Lastly, my appreciation and gratitude is directed to my homeland Egypt for funding my research.

Dedication

To my beloved husband Reda Farouk Elsaid, your love, encouragement and support have been always the fuel of my achievements and success.

To my precious mother and beloved sisters Hoda, Shima and Soheir and my big brother Mohammed, and to my mother in law, all your love and prayers were what I depended on to strive towards my goal.

Finally, I dedicate all my success and achievement to my precious children Ahmed, Aly and to my expected baby, I hope this will always be a light on your road to your brilliant future. You will look back to see how much I worked hard to achieve my goal, and you will never give up your dreams and will never underestimate your capabilities.

ABSTRACT

Titanium aluminide alloys, specifically Ti-46Al-8Nb alloy, are characterized by a high strength to density ratio at high temperatures combined with high corrosion and oxidation resistance, which make them very important in high temperature applications. Increasing demand for more complex net-shape components signifies an opportunity for investment casting, and accordingly increases the pressure to improve the reliability of cast Ti-46Al-8Nb components.

Titanium aluminide alloys are prone to extensive shrinkage porosity, particularly interdendritic layer porosity, which threaten its outstanding mechanical properties. This research aims to develop a better understanding of shrinkage porosity in Ti-46Al-8Nb alloy and how to minimize it, and to investigate the correlation between shrinkage defects, casting parameters and solidification conditions.

Practical measurements in conjunction with computer simulations were carried out in order to study the effects of cooling rate and temperature gradient on shrinkage porosity in Ti-46Al-8Nb investment castings, through investigating the influence of casting geometry, specifically mould taper on cylindrical bars, and preheating mould temperature on the macrostructure and the formation of shrinkage porosity.

Experimental measurements of thermal boundary conditions of the investment shell mould were conducted in order to build a reliable model of the casting process. The heat-transfer coefficient of the ceramic shells was determined using measured cooling curves obtained in 200 mbar of Argon and in vacuum. Furthermore, the interfacial heat transfer coefficient between the investigated alloy and the mould material was estimated by trial-and-error modelling and was verified by comparing measured and predicted cooling curves of Ti-46Al-8Nb to give a temperature-dependant interfacial heat transfer coefficient curve with a maximum value of $1000 \text{ W/m}^2 \cdot \text{K}$ followed by a decrease to $300 \text{ W/m}^2 \cdot \text{K}$, which was found to achieve the closest fit.

Thermal-only and tilt-filling models were developed by using a commercial FE casting simulation software package, and used to predict thermal parameters and criterion functions in different test bars with different taper angles, with $500 \text{ }^\circ\text{C}$ and $1000 \text{ }^\circ\text{C}$ mould temperatures.

By analysing the model results and matching them with experimentally measured area percentages of porosity, it was revealed that enhancing directional solidification by increasing the taper coefficient from 0 to 0.1 mm/mm in 100 mm length, significantly reduced the amount of porosity. This was attributed to the fact that promoting directional solidification delayed the columnar-to-equiaxed transition, which in turn could enhance interdendritic feeding.

The Niyama criterion function was validated to predict shrinkage-related porosity in Ti-46Al-8Nb castings, through either thermal or tilt-filling ProCastTM simulation models. Positions in a casting with Niyama values above $4 \text{ (}^\circ\text{C} \cdot \text{min)}^{0.5} \text{cm}^{-1}$; $(3 \text{ (K} \cdot \text{s)}^{0.5} \text{mm}^{-1})$; could be considered completely sound. The critical value of the Niyama function was $2 \text{ (}^\circ\text{C} \cdot \text{min)}^{0.5} \text{cm}^{-1}$; $(1.5 \text{ (K} \cdot \text{s)}^{0.5} \text{mm}^{-1})$; below which the position tested was susceptible to macroshrinkage porosity.

CONTENTS

LIST OF SYMBOLS AND ABBREVIATIONS

CHAPTER 1

INTRODUCTION

1.1 Introduction	1
1.2 Aims and Objectives	4

CHAPTER 2

LITERATURE REVIEW

2.1 Structure and Classification of Titanium and its Alloys	6
2.2 Solidification of TiAl Intermetallics	8
2.2.1 The Phase Diagrams of TiAl and TiAlNb Systems	8
2.2.2 The Phase Transformations and As-Cast Microstructure of Nb Containing TiAl-Based Alloys	13
2.3 The Columnar to Equiaxed Grain Transition (CET)	20
2.3.1 Mechanisms of Columnar to Equiaxed Grain Transition	20
2.3.1.1 The Constitutional Supercooling Theory	21
2.3.1.2 The “Big Bang hypothesis”	22
2.3.1.3 Fragmentation of Dendrite Arms.....	22
2.3.2 Solidification Parameters Influencing the CET	23
2.4 Melting and Casting of Titanium Alloys: Induction Skull Melting (ISM)	28
2.5 Feeding Mechanisms during Solidification	33
2.6 Classification of Shrinkage-Related Casting Defects	35
2.6.1 Pipe (open) Shrinkage Defect	36
2.6.2 Macroshrinkage Cavities	36
2.6.3 Microshrinkage Porosity	37
2.6.4 Layer Porosity	41
2.7 Gas Porosity	42
2.7.1 The nucleation process of gas bubbles	42
2.7.2 Heterogeneous nucleation	43
2.8 Prediction of Shrinkage Porosity during the Solidification of Metal Castings	45
2.8.1 Thermal Models	45
2.8.2 Thermal/Volume Models	48
2.8.3 Gas Segregation Models	50
2.8.4 Stress Analysis and Plastic Deformation Models	52
2.9 Prediction of Shrinkage Porosity by Niyama and other Criteria Functions	53
2.10 Prediction of Shrinkage Porosity in Ti-Based Alloys	59

2.11 Determination of the Interfacial Heat Transfer Coefficient	60
2.12 Heat Transfer Coefficient at the Metal/Mould Interface during Investment Casting Process	64
2.13 Thermophysical Properties of γ -TiAl Intermetallics	66
2.14 Effect of Porosity on Mechanical Properties of Titanium-Alloy Castings	70
2.15 Summary of Literature	72

CHAPTER 3

EXPERIMENTAL METHODS

3.1 Gravity Casting of Commercial Purity Ti, Ti-6Al-4V and Ti-46Al-8Nb	74
3.1.1 Mould Design	74
3.1.2 Mould Preparation	75
3.1.3 Melting and Gravity Casting of (CP) Ti and Ti-6Al-4V alloys	77
3.2 Tilt Casting of Titanium Aluminide	78
3.2.1 Mould Design and Preparation	78
3.2.2 Melting and Tilt Casting	79
3.3 Casting Assessment	80
3.3.1 X-ray Radiography	80
3.3.2 Sectioning and Metallographic Preparation	81
3.3.3 Stereological Measurements of Microstructure Features and Porosity	81
a) Image Processing	81
a.1) Noise Reduction	81
a.2) Brightness and Contrast Manipulation	82
a.3) Segmentation and Thresholding	82
b) Image Analysis for Metallurgical Applications	82
C) Sources of Errors in Digital Measurements and Remedies Actions	83
3.3.4 Quantitative Assessment of Porosity	84
3.3.5 Quantitative Assessment of Macrostructure	86
3.4 Temperature Measurements during Gravity Casting and Solidification of Ti-46Al-8Nb Alloy	88
3.5 Temperature Measurements during Tilt Casting	89
3.5.1 Mould Preparation and Thermocouples Setup	89
3.5.2 Tilt Pouring Cycle	92
3.6 Measurement of Mould/Surroundings Interface Heat Transfer Coefficient	93
3.6.1 Design of the Test Piece and the Experiment Description	93
3.6.2 Temperature Measurements in Vacuum	95
3.6.3 Temperature Measurements in Argon	96
3.6.4 Temperature Measurements in Air	96
3.7 Thermal Analysis of Cooling Curves	96
3.7.1 Smoothing of a Cooling Curve Data	98

3.7.2 Source of Thermocouple Errors	99
---	----

CHAPTER 4

MODELLING OF TITANIUM ALUMINIDE INVESTMENT CASTING

4.1 Computational Modelling by FDA and FEA Methods	100
4.2 Thermophysical Properties of the Investment Mould Material	103
4.2.1 Comparison between values of Thermophysical properties in different research works	103
a) Specific Heat Capacity C_p	103
b) Thermal Conductivity k	104
4.2.2 Data used in ProCast Modelling of Ti-46Al-8Nb Investment Casting in this Research	105
4.3 Thermophysical and Physical Properties of Ti-46Al-8Nb alloy	107
4.3.1 Density	107
4.3.2 Specific heat capacity C_p	108
4.3.3 Thermal Conductivity	109
4.3.4 Latent Heat	110
4.3.5 Determination of Fraction of Solid	110
4.4 Sensitivity Analysis Tests	112
4.4.1 Solid Modelling and Meshing	113
4.4.2 Test 1: Thermal Conductivity of the Mould Material	113
4.4.3 Test 2: Heat boundary conditions (Interface heat transfer coefficient between the mould and its surroundings, hb)	115
4.4.4 Test 3: Interfacial Metal/Mould Heat Transfer Coefficient (h)	117
4.4.5 Estimation of the Metal/Mould Interfacial Heat Transfer Coefficient	119
4.5 Modelling of the Ceramic Test	122
4.5.1 Solid Modelling and Meshing	122
4.5.2 Model parameters and boundary conditions	122
4.5.3 Verification of Mould/Surroundings Heat Transfer Coefficient	122
4.6 Modelling of Solidification of Gravity Casting of Ti-46Al-8Nb	123
4.6.1 Geometry and Meshing	123
4.6.2 Initial temperatures and boundary conditions	123
4.7 Thermal Model of Ti-46Al-8Nb Test Casting.....	124
4.7.1 Geometry and Meshing	124
4.7.2 Boundary Conditions	125
4.7.3 Analysis of the Model Results	126
4.8 Tilt-filling Model of Ti-46Al-8Nb Test Casting	128
4.8.1 Geometry and Meshing	128
4.8.2 Boundary Conditions and Process Assignment	129

CHAPTER 5: RESULTS

PREDICTION OF SHRINKAGE POROSITY IN Ti-46Al-8Nb AND DETERMINATION OF THERMAL BOUNDARY CONDITIONS	130
<i>5.1 Effect of Casting Parameters on the Formation of Casting Defects in Commercial Purity Titanium, Ti-6Al-4V and Ti-46Al-8Nb Investment Casting Alloys</i>	131
5.1.1 Effect of Mould Temperature	131
5.1.2 Effect of Castings' Size and Geometry	131
5.1.3 Effect of Alloy Composition	132
<i>5.2 Microstructure and Macrostructure of the Investigated Alloys</i>	136
5.2.1 Microstructure and Macrostructure of Commercial Purity Titanium	136
5.2.2 Microstructure and Macrostructure of Ti-6Al-4V	136
5.2.3 As-Cast Structure of Ti-46Al-8Nb Gravity Casting	138
5.2.4 Microstructure and EDS Analysis of the Ti-46Al-8Nb Gravity Casting	141
<i>5.3 Shrinkage Porosity in Ti-46Al-8Nb Gravity Casting</i>	143
5.3.1 Visual Inspection and Qualitative Comparisons	
5.3.2 Quantitative Distribution of Porosity	148
<i>5.4 Shrinkage Porosity and Macrostructure in Ti-46Al-8Nb Tilt Casting</i>	150
5.4.1 Visual Inspection and Qualitative Comparisons	150
5.4.2 Macrostructure of Tilt Cast Cylindrical and Tapered Bars	151
5.4.3 Effect of Bar Geometry on Shrinkage Porosity	157
<i>5.5 Determination of the Heat Transfer Coefficient for Mould/Surrounding Interface</i>	160
5.5.1 Calculation of the Surface Temperature of the Ceramic Test Bar	160
5.5.2 Calculation of the Heat Transfer Coefficient at the Ceramic Mould/Surrounding Interface	163
5.5.3 Verification of the ProCast™ Model of the Ceramic Test with the Measured Data	168
<i>5.6 Analysis of the Cooling Curve of Ti-46Al-8Nb Alloy</i>	171
5.6.1 Sources of Errors and Uncertainty of Measurements	178
<i>5.7 Using Criteria Functions for Predicting Shrinkage Porosity in Ti-46Al-8Nb Alloy</i>	180
5.7.1 Analysis of Results	
5.7.2 Predicted Solidification Time	181
5.7.3 Thermal Gradient	182
5.7.4 Feeding Efficiency Parameter	185
<i>5.8 Correlation between Niyama Criterion and Porosity Distribution</i>	189
5.8.1 Distribution of Porosity along the Central Line of the Test Bars	189
5.8.2 Distribution of Porosity in the Longitudinal Section of the Test Bars	192
5.8.3 Porosity Distribution as Predicted by Niyama Criterion using the Tilt-Filling Model	199
CHAPTER 6	
DISCUSSION	207

6.1 <i>Boundary Conditions for Ti-46Al-8Nb Investment Casting</i>	207
6.1.1 The Heat Transfer Coefficient at the Ceramic Mould/Surroundings Interface	207
6.1.2 Interfacial Metal/Mould Heat Transfer Coefficient	208
a) Pure-Iron Test Model	208
b) Estimation of h for Ti-46Al-8Nb Investment Casting Model	212
6.2 <i>The Features of the As-Cast Macrostructure of Ti-46Al-8Nb Casting</i>	215
6.2.1 The Macrostructure of the Ti-46Al-8Nb Gravity-Castings	215
6.2.2 The Macrostructure of the Ti-46Al-8Nb Tilt-Castings	216
6.3 <i>The Columnar-To-Equiaxed Transition in Ti-46Al-8Nb</i>	216
6.3.1 The Effect of Superheat on Columnar-To-Equiaxed Transition	217
6.3.2 The Effect of Taper Geometry on the Columnar-To-Equiaxed Transition	217
6.3.3 The Effect of Preheat Mould Temperature on the Columnar-To-Equiaxed Transition	219
6.4 <i>Effect of Thermal Parameters on Feeding Mechanisms</i>	220
6.4.1 Feeding-related Shrinkage Porosity in Gravity-Casting Ti-46Al-8Nb alloy	221
6.4.2 Feeding-related Shrinkage Porosity in Tilt-Casting Ti-46Al-8Nb alloy	223
6.5 <i>Prediction of Factors affecting Shrinkage Porosity in Ti-46Al-8Nb using a ProCast™ Modelling</i>	225
6.5.1 The Local Solidification Time	225
6.5.2 The Cooling Rate	227
6.5.3 The Temperature Gradient	228
6.6 <i>Prediction of Shrinkage Porosity Using the Niyama Criterion Function</i>	230
6.6.1 Factors Influencing the Niyama Function	230
6.6.2 <i>Critical Values of the Niyama Criterion to Predict Shrinkage Porosity in Ti-46Al-8Nb Investment Castings</i>	233
6.7 <i>A Comparison between Casting Defects in CP Ti, Ti-6Al-4V and Ti-46Al-8Nb Investment Casting Alloys</i>	237
6.7.1 Misrun and Cold Laps in CP Ti and Ti-6Al-4V	237
6.7.2 Gas Bubbles	238
6.7.3 Layer Porosity	239

CHAPTER 7 **240**

CONCLUSIONS

CHAPTER 8

FUTURE WORK **244**

REFERENCES **245**

APPENDIX A: **261**

I. A. KHALED, "Prediction of Shrinkage Porosity in Ti-46Al-8Nb Tilt-Casting Using the Niyama Criterion Function", International Journal of Metal casting, (IJMC) AFS, Fall 2013.

LIST OF SYMBOLS AND ABBREVIATIONS

G	Gibbs Free Energy, (defined locally)
V	Velocity of solidification front
β	Solidification shrinkage
d	Dendrite arm spacing
P_i	Partial pressure
P_o	Initial pressure
ΔP	Pressure drop in the mushy zone
γ	Surface tension
r^*	Critical radius of a pore
t	Solidification time
G	Temperature gradient, (defined locally)
ΔH_f	Heat of fusion
K	Permeability
k	Thermal conductivity
α	Thermal diffusivity
μ	Dynamic viscosity
ρ	Density
H	Enthalpy
C_p	Specific heat
f_s	Fraction solid
f_l	Fraction liquid

N_c	Niyama criterion function
L	Cooling rate
T	Temperature
T_s	Surface temperature
T_∞	Ambient temperature
h	Interfacial heat transfer coefficient, (at metal/mould interface).
q	Heat flux
ε	Emissivity
h_b	Heat transfer coefficient, at mould/surroundings interface
A_p	Total area of porosity
A_s	Area of longitudinal section
L_c	Columnar length
TC	Thermocouple
D	Diffusion coefficient
C_s	Composition of solid phase
C_L	Composition of liquid phase

CHAPTER 1

INTRODUCTION

1.1 Introduction

Titanium alloys generally, and titanium aluminide specifically, are characterized by a combination of good mechanical and physical properties, high biocompatibility, good corrosion resistance and high specific strength, particularly at high temperatures.

For instance, Titanium-based-alloys are characterized by low density, almost half that of Ni alloys, high strength-to-density ratio, compared to Al alloys and structural steels, (especially in high temperature services at up to 600 °C), as shown in Figure 1.1. Titanium aluminide alloys compete with Ni-based super alloys in elevated temperature applications of up to 800 °C. Ti alloys also exhibit excellent corrosion resistance in different chemical environments due to the formation of a thin layer of adhesive protective oxide surface layer, (TiO₂). This suggests that Ti alloys can be exploited in a vast range of applications such as in the aerospace sector, chemical industry, leisure sector and for high-temperature applications [1-4].

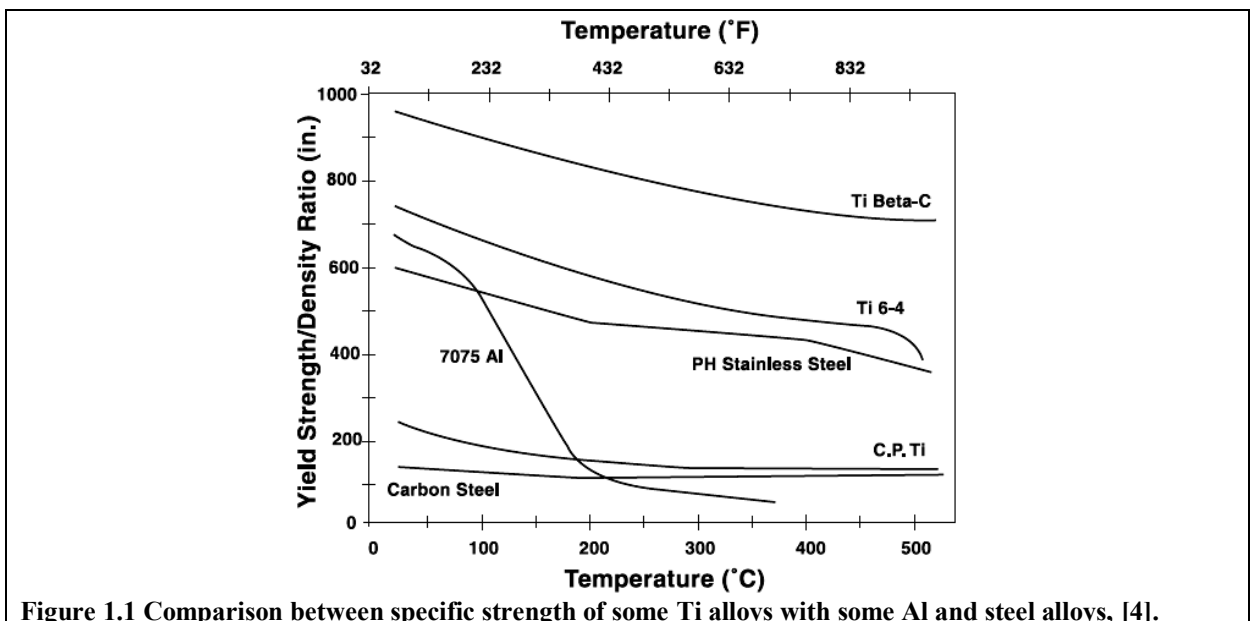


Figure 1.1 Comparison between specific strength of some Ti alloys with some Al and steel alloys, [4].

Investment casting can fulfil the increasing demand for more complex near net-shape components, as a cost-effective processing route which provides a high quality surface finish and minimizes the need for difficult and costly machining.

However, the high reactivity of the molten alloy with the crucible and mould materials is a significant challenge in casting titanium alloys.

Nevertheless, Induction Skull Melting (ISM), under vacuum, suggests itself as a clean and rapid technique for melting Ti alloys, in which the melt is contained in a solid skin of itself, which prevents any interaction between the molten metal and the crucible material. In addition, no oxygen pick-up is to be expected, non-metallic inclusions cannot be formed and there should be no contamination due to melt/crucible reactions.

However, the low achievable superheat is the main disadvantage of the process, [40]. Attempts to overcome this disadvantage by rapid pouring and high mould temperatures can lead to severe casting defects like entrapped gas bubbles and shrinkage porosity. HIPping (Hot Isostatic Pressing) is used to eliminate closed porosity in castings, but it is an expensive procedure and can cause a deformed surface, in the form of sinks, and hence require machining which adds to the cost, [80].

In view of the above, extensive research has been conducted to reveal the influence of important melting and casting variables on the quality of titanium alloy castings. The present research aims to achieve a better understanding of the casting variables that can control the soundness of titanium aluminide castings, in particular the formation of shrinkage porosity in titanium aluminide. This can be related to many factors, such as the filling technique, the casting geometry and its direct influence on temperature gradient, the mould temperature and the way this can affect cooling rate.

These factors are investigated by producing and assessing cylindrical and tapered bars of different sizes and with different mould temperatures, by both gravity and tilt casting.

Subsequently, the effects of temperature gradient and cooling rate on the macrostructure are studied and correlated to the formation of shrinkage porosity.

Currently, computer modelling is a powerful tool to study casting parameters and aspects of solidification. Nevertheless, the reliability of computer simulation of the investment casting process depends strongly on the inputs of thermophysical properties of the casting and mould materials, and also on the boundary conditions assigned to the process.

However, the available thermophysical data of titanium aluminide are rather limited and the boundary conditions of the investment casting process have not been precisely determined. Therefore, the determination of these data is an essential objective of this project in order to set up a simulation model that can predict casting parameters which affect the formation of shrinkage porosity in titanium aluminide.

Using criterion functions to predict porosity in Ti-46Al-8Nb is generally investigated, in terms of the consistency of the calculated functions with the experimentally measured data. However, the principal aim of this research focuses on the validity of the Niyama criterion to predict shrinkage in Ti-46Al-8Nb.

1.2 Aims and Objectives

The main aim of this research is to achieve a better understanding of shrinkage porosity in Ti-46Al-8Nb alloy and how to minimize it. This is achieved by coupling experimental and computer modelling investigations. The project objectives are set out below:

1. The relationship between the formation of shrinkage porosity and casting parameters by studying the following:
 - The filling process, specifically to produce gravity- and tilt-cast test bars and to assess the presence of porosity in both cases.
 - Thermal parameters, to analyse the effects of cooling rate and temperature gradient on the formation of shrinkage porosity in different casting geometries with different mould temperatures.
 - Alloy composition, specifically to carry out a limited comparison between the susceptibility of three Ti alloys, (commercially pure Ti, Ti-6Al-4V and Ti-46Al-8Nb), to layer porosity.
2. To set up a simulation model of a Ti-46Al-8Nb investment casting, based on a database of the thermophysical properties and measured values of the thermal boundary conditions. To achieve this, the following procedures were performed:
 - Cooling curve measurements of the ceramic shell during cooling from 1000 °C were carried out to determine the temperature dependent heat transfer coefficients of the ceramic shell surface in 200 mbar of Argon, and in vacuum.
 - Cooling curve measurements for gravity and tilt casting of the Ti-46Al-8Nb alloy were carried out to validate the interfacial heat transfer coefficient between a Ti-46Al-8Nb casting and a ceramic mould surface, using a trial and error methodology.

- To study the availability and reliability of the thermophysical properties of Ti-46Al-8Nb alloy and the ceramic mould material, in order to create a reliable input database of properties.
- 3. To use the ProCastTM [94] software to predict temperature gradients and cooling rates in different test bar geometries, with different mould temperatures in order to correlate these conditions with shrinkage porosity formation in the Ti-46Al-8Nb alloy.
- 4. To study the effects of cooling rate and temperature gradient on the macrostructure of Ti-46Al-8Nb alloy and how would this affect the formation of shrinkage porosity.
- 5. To assess the validity of thermally-based criterion functions applied to predict shrinkage porosity in Ti-46Al-8Nb investment castings, by analyzing and matching the model results with an experimentally measured percentage area of porosity in test bars of different size and taper angle, with two different mould temperatures.

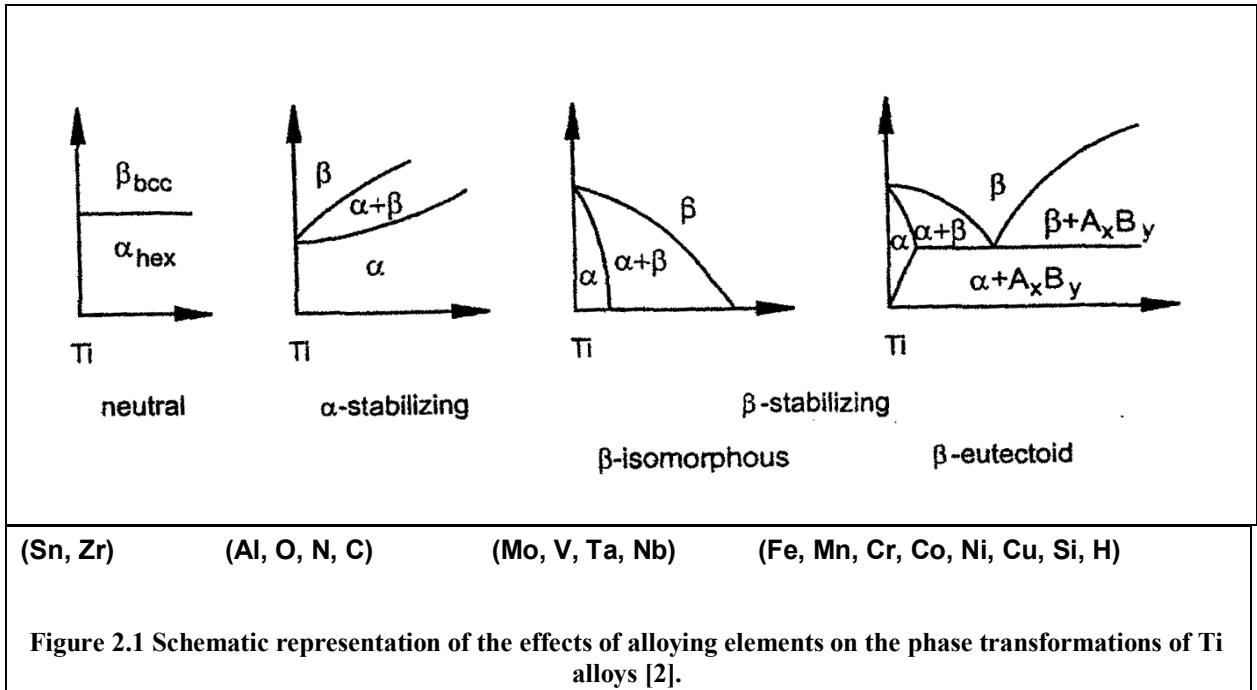
CHAPTER 2

LITERATURE REVIEW

2.1 Structure and Classification of Titanium and its Alloys

Titanium undergoes allotropic phase transformations. Pure Ti solidifies at 1670 ± 5 °C in a bcc (β) structure [1]. Upon cooling, just below the β -transus temperature (882 ± 2 °C) β -grains transform into the close packed (hcp) α -Ti. The α planes can form with twelve possible orientations, inherited from six planes and two directions of the β unit cell. This large number of possible orientations results in a very characteristic microstructure, upon slow cooling, similar in appearance to the weave pattern of a basket and is therefore referred to as a basket-weave structure. Upon fast cooling, i.e., quenching, martensitic transformation of β results in a very fine needle-like (α') microstructure [2].

The alloying elements in Ti alloys are classified according to their role in stabilizing the two allotropic phases, α and β , depending on their effect on the β -transus temperature. The α -stabilizing elements (Al, O, N and C) extend the α -phase field to higher temperatures and develop a two-phase field of ($\alpha+\beta$). While β -stabilizing elements are subdivided into β -isomorphous (Mo, V, Ta and Nb) which have a higher solubility in Ti, and β -eutectoid (Fe, Mn, Cr, Co, Ni, Cu, Si, and H) which form intermetallic compounds with Ti [2, 3]. These effects of the alloying elements on the phase transformations of Ti alloys are summarised schematically in Figure 2.1.



Titanium alloys are classified according to chemical composition into α –alloys, near α – alloys, β alloys, and titanium aluminide alloys.

The α – alloys include different grades of commercial purity Ti, such as high purity 99.98%Ti, and grades 1 to 4 such as, Grade 1 (commercial purity Ti: Ti-0.2Fe-0.18O) and Grade 4 (commercial purity Ti: Ti-0.5Fe-0.4O). This group also includes alloys that are alloyed with neutral elements (such as Sn and Zr), and/or α -stabilizers, (Al), like Grade 6 (Ti-5Al-2.5Sn).

The near α -alloys contain minor fractions of β -stabilizers, while the β group includes the alloys containing an ($\alpha+\beta$) microstructure and the metastable β alloys. Generally, the β alloys are characterized by having the highest tensile strength and fatigue properties among all of the Ti alloys, in addition to high corrosion resistance [5].

The titanium aluminide alloys are composed of 46-52 at. %Al, and 1-10 at.% of one or more of the elements (V, Cr, Mn, W, Mo, Nb and Ta). Ti-Al intermetallic alloys are characterized by low density with high strength, together with high melting point, and most importantly, excellent creep strength and high oxidation resistance [6].

2.2 Solidification of TiAl Intermetallics

2.2.1 The Phase Diagrams of TiAl and TiAlNb Systems

Aluminium is the most commonly used alloying element in Ti-based alloys due to its high solubility in both α and β titanium phases, and thus it can provide high solution strengthening in Ti-based alloys [7].

As shown in the Ti-Al phase diagram, Figure 2.2, several intermetallic phases are formed at equilibrium for different Al contents in the Ti-Al system, such as α_2 -Ti₃Al, γ TiAl, TiAl₂ and TiAl₃. All these intermetallic compounds are extremely brittle, except the α_2 -Ti₃Al and γ TiAl which are of technical importance.

The engineering alloys based on (γ TiAl) usually have Al concentrations of between 45-48 at. %. According to the shown phase diagram, binary alloys in this composition range start solidification by the formation of primary phase β , and then the peritectic reaction takes place at 1503 °C. Upon further cooling, the alloys undergo several solid state phase transformations, where α phase of (hcp) structure transforms to γ phase of (fcc) crystal structure and the ordered (Ti₃Al) α_2 phase. Because it is an α stabilizer, any slight increase in the Al content, (1-2 at. %) can shift the solidification path of the alloy to the (L+ α) zone where α is the primary phase of solidification.

Alloying elements such as (Nb, Cr, V, Mn, Fe, or B), are used in titanium aluminide group to form ternary intermetallic phases, like Ti₂AlNb, aiming mainly to improve their mechanical properties.

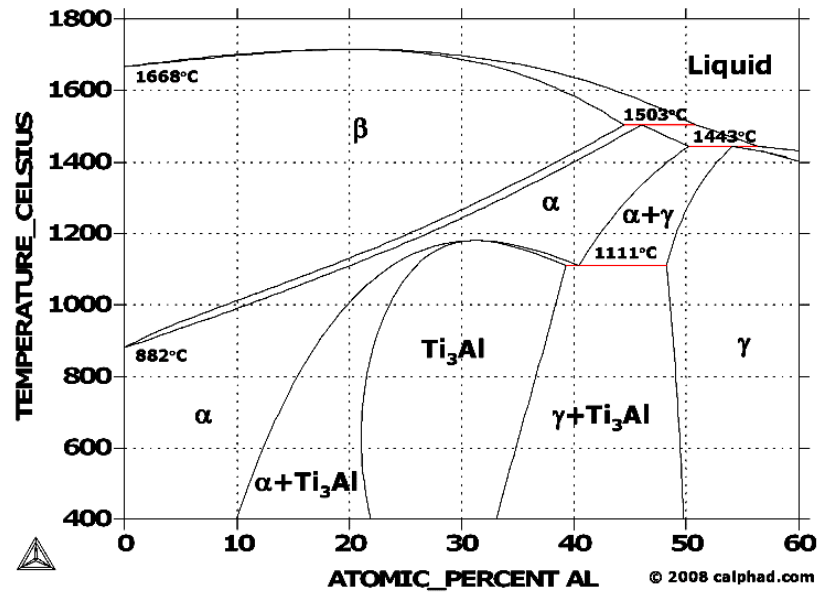


Figure 2-2 Ti-Al phase diagram, (expressed in at. % Al and temperature in °C) [7].

The multi-component TiAl phase diagram was created by using experimental data in conjunction with computer calculations of thermodynamics of its different components. CALPHAD is a modelling approach that was used to calculate the Gibbs Free Energy of the individual phases according to the general Gibbs Free Energy equation:

$$\Delta G = \Delta G^O + \Delta G_{mix}^{ideal} + \Delta G_{mix}^{X_s} \quad \text{Eq. 2.1}$$

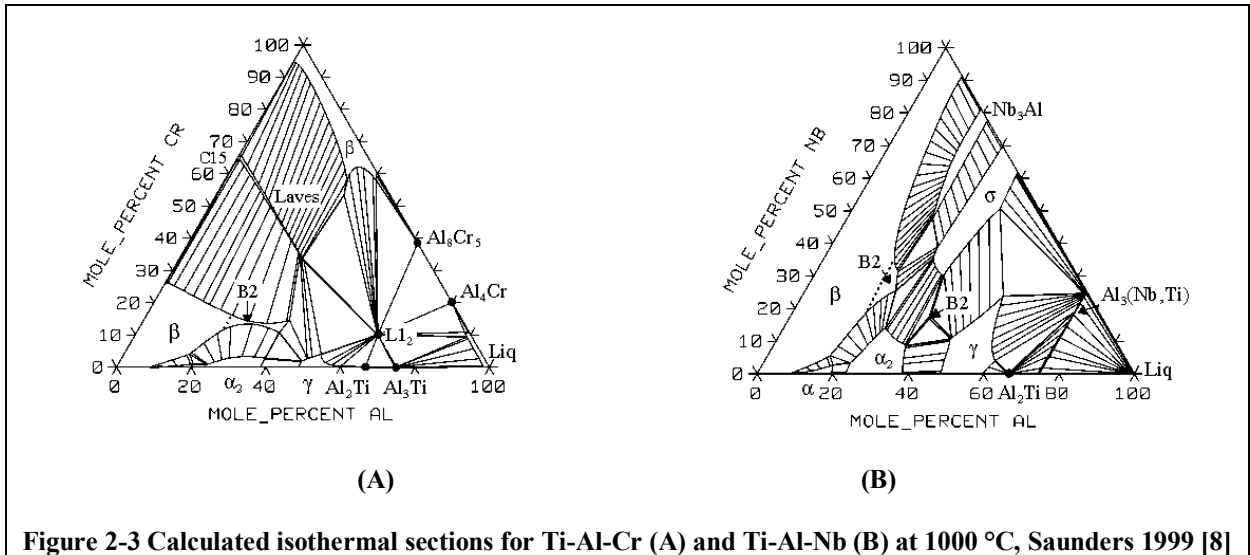
Where; ΔG^O is the Gibbs energy of the pure phase

ΔG_{mix}^{ideal} is the ideal Gibbs energy of the mixed components

$\Delta G_{mix}^{X_s}$ is the excess Gibbs energy of the mixed components

Subsequently, Saunders 1999 [8], calculated the phase equilibria for the binary system Ti-Al and the ternary system Ti-Al-X phase diagrams by using the Thermo-Calc software package. The isothermal sections for Ti-Al-Cr and Ti-Al-Nb, alloys are shown in Figure 2.3, in which the systems were calculated at 1000 °C. The formation of the ordered-cubic-centred B2 phase, (the ordered form of the bcc structure (β) phase), was attributed to the stabilizing effect of Nb and Cr on the β phase.

However, the calculated phase diagram of the Ti-Al-Nb system neglected the formation of the intermetallic orthorhombic Ti_2AlNb phase, (the O phase), and the metastable disordered A2 form of the β phase.



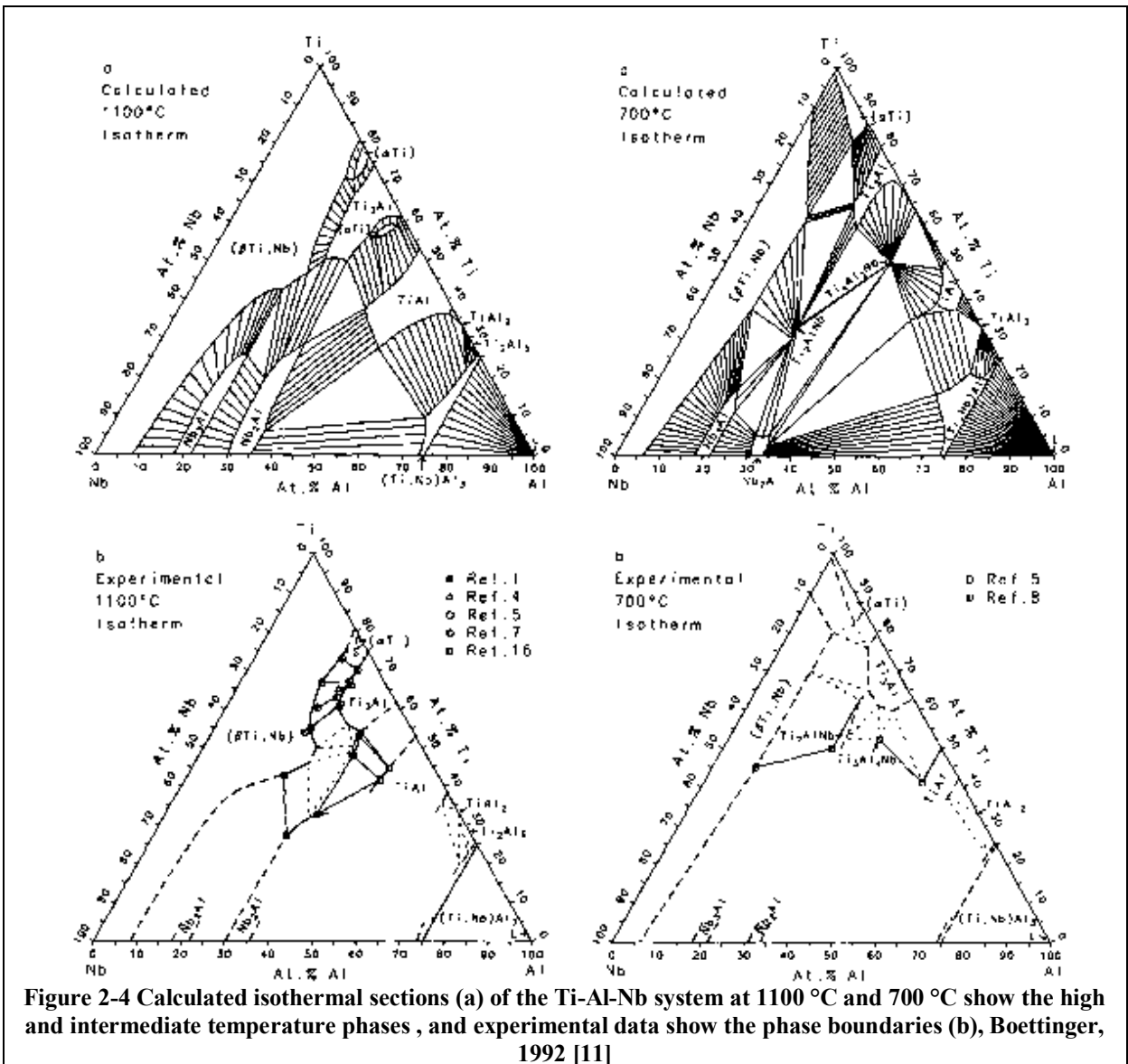
The introduction of Nb into TiAl-based alloys significantly improved mechanical and physical properties of the Ti-Al system alloys. Nb increases the oxidation resistance due to its high solubility in titanium, which suggests that Nb can obstruct the solubility of oxygen in the alloy and induce the formation of the protective oxides, TiO_2 and Al_2O_3 , on the surface, it was also found to encourage the formation of titanium nitride beneath the scale layer, which hinder further penetration of oxygen into the alloy [9].

In addition, the influence of Nb on the microstructure of these alloys can affect tensile strength and high temperature strength, as a result of inducing a fully or near fully laminar (α_2/γ) structure and solid solution strengthening of the γ phase [10].

Nb is known to be a β -isomorphous forming element, the high temperature bcc phases can take the form of the ordered B2 or the disordered A2 structures, while the hcp α structure is the stable low temperature phase with low Nb content and the orthorhombic O phase,

(Ti₂AlNb), of Nb content higher than 30 at. %, as appear in the isothermal sections of the Ti-Al-Nb phase diagram at 1100 °C and 700 °C in Figure 2.4 [11, 12].

Upon quenching from a temperature in the B2 phase field the metastable beta phase, orthorhombic B19 phase, forms which has Bragg reflections that coincide or superimpose with the reflections of the equilibrium O phase in the XRD pattern [13].



Calculated phase diagrams of the Ti-Al-Nb system are shown in Figure 2.5. XRD analysis of the as-cast alloys revealed that β is the primary phase upon solidification of the ternary

alloys, with Al in the range (45 to 48 at. %) and Nb of 8 at. % and up to 12 at.%, giving an equilibrium microstructure of $(\alpha_2+\gamma)$. Table 2-1 shows the expected primary phases and the as-cast microstructure of some of the ternary alloys in the Ti-Al-Nb system [14].

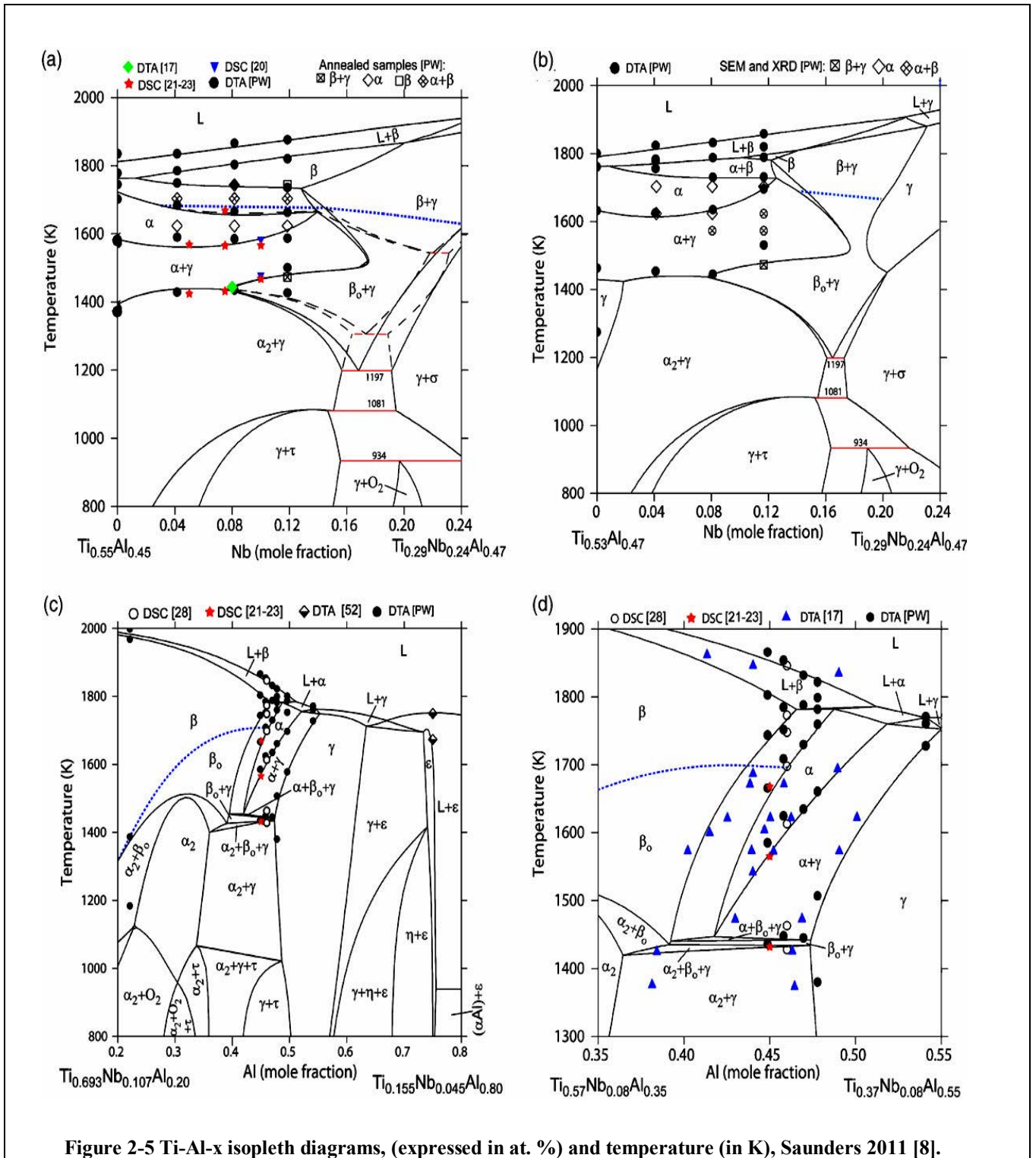


Figure 2-5 Ti-Al-x isopleth diagrams, (expressed in at. %) and temperature (in K), Saunders 2011 [8].

Table 2-1 Phase transformation reactions upon solidification, as-cast and annealed structure of Ti-Al-Nb system alloys [6].

No.	Composition (at.%)						XRD and metallographic phase identification			
	Nominal			EDX analysis			As-cast alloy		Annealed alloy	
	Ti	Nb	Al	Ti	Nb	Al	Primary phase	Phase constituents	Annealing conditions, T (K)/t (h)/quench	Phase constituents
1	0	5.0	95.0	0	5.1	94.9	ϵ	$\epsilon + (\alpha\text{Al})$	–	–
2	0	24.5	75.5	0	24.9	75.1	ϵ	$\epsilon + (\alpha\text{Al})$	Ar, 1823/5/fc ^a	$\epsilon + (\alpha\text{Al})$
3	0	24.7	75.3	0	25.1	74.9	ϵ	ϵ	Ar, 1823/5/fc	ϵ
4	0	24.9	75.1	0	25.3	74.5	ϵ	ϵ	Ar, 1823/5/fc	ϵ
5	0	25.2	74.8	0	25.5	74.5	ϵ	ϵ	Ar, 1823/5/fc	ϵ
6	0	25.6	74.4	0	25.9	74.1	ϵ	$\epsilon + \sigma$	Ar, 1823/5/fc	$\epsilon + \sigma$
7	0	45.0	55.0	0	45.6	54.4	σ	$\epsilon + \sigma$	–	–
8	0	70.0	30.0	0	70.9	29.1	δ	$\sigma + \delta$	–	–
9	0	77.0	23.0	0	77.8	22.2	β	$\beta + \delta$	–	–
10	0	79.0	21.0	0	81.2	18.8	β	$\beta + \delta$	–	–
11	46	8	46	46.1	8.1	45.8	β	$\alpha_2 + \gamma$	Ar, 1703/10/fc Ar, 1633/2/H ₂ O Ar, 1633/2 + 1200/15/H ₂ O	α_2 α $\alpha + \gamma$
12	45	8	48	44.5	7.7	47.8	β	$\alpha_2 + \gamma$	Ar, 1673/10/fc	$\alpha_2 + \gamma$
13	44	8	50	43.1	7.3	49.6	β	$\alpha_2 + \gamma$	Ar, 1673/10/fc	$\alpha_2 + \gamma$
14	38	8	55	38.3	7.6	54.1	α	$\alpha_2 + \gamma$	Ar, 1673/10/fc	γ
15	65	11	24	67.3	10.6	22.1	β	$\alpha + \alpha_2 + \beta$	Vac., 1673/4.5/fc Vac., 1673/4.5 + Ar, 973/625/fc	$\alpha + \alpha_2 + \beta$ $\alpha + \alpha_2$
16	58	17	25	57.7	17.1	25.2	β	$\alpha_2 + \beta + \text{O}$	Vac., 1673/4.5/fc Vac., 1673/4.5 + Ar, 973/625/fc	$\alpha + \alpha_2 + \beta$ $\alpha_2 + \text{O}$
17	50.0	12.5	37.5	50.4	12.6	37.0	β	$\alpha_2 + \beta$	Vac., 1673/4.5/fc Vac., 1673/4.5 + Ar, 973/625/fc	$\alpha_2 + \gamma$ $\alpha_2 + \gamma + \text{T}$
18	25	19	56	25.3	19.0	55.7	γ	γ	Ar, 1673/8/H ₂ O	γ
19	55	0	45	55.8	0	44.2	β	$\alpha_2 + \gamma$	Ar, 1703/10/fc	$\alpha_2 + \gamma$
20	51	4	45	51.0	4.2	44.8	β	$\alpha_2 + \gamma$	Ar, 1703/10/fc	$\alpha_2 + \gamma$
21	47	8	45	47.0	8.2	44.9	β	$\alpha_2 + \gamma$	Ar, 1703/10/fc	$\alpha_2 + \gamma$
22	43	12	45	43.8	11.9	44.3	β	$\beta + \gamma$	Ar, 1703/10/fc Ar, 1473/3/H ₂ O	$\beta + \alpha_2 + \gamma$ $\beta + \alpha + \gamma$
23	53	0	47	53.2	0	46.8	β	$\alpha_2 + \gamma$	Ar, 1703/10/fc	$\alpha_2 + \gamma$
24	49	4	47	48.8	4.1	47.1	β	$\alpha_2 + \gamma$	Ar, 1703/10/fc	$(\alpha_2?) + \gamma$
25	45	8	47	45.0	8.1	46.9	β	$\alpha_2 + \gamma$	Ar, 1703/10/fc	$\alpha_2 + \gamma$
26	41	12	47	41.5	11.7	46.8	β	$\beta + \gamma$	Ar, 1473/3/H ₂ O	$\beta + \alpha + \gamma$

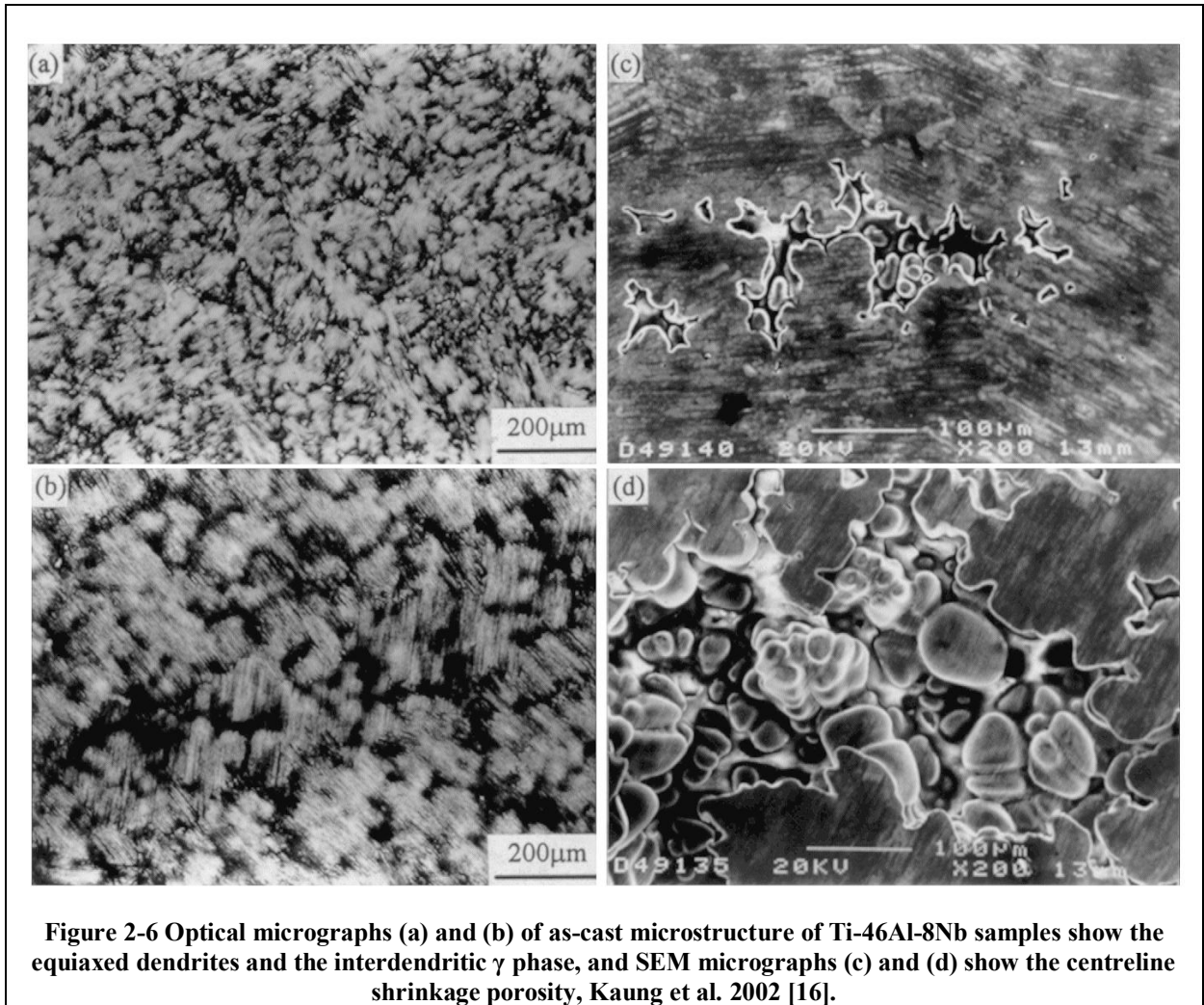
^a fc denotes cooling in a furnace with rate of 180 K min⁻¹.

2.2.2 The Phase Transformations and As-Cast Microstructure of Nb Containing TiAl-Based Alloys

The as-cast structure of γ TiAl alloy of composition 48 %Al, 2 %Nb and 2 % Mo (atomic %) was investigated by Kaung et al. [16]. They described the as-cast macrostructure as an equiaxed zone located at the centre of the structure, composed of lamellae of α_2/γ with a small amount of fine γ -grains which were segregated at the grain-boundaries or in the interdendritic area. The γ -grains can be seen clearly as the dark areas in the micrographs in Figure 2.6 (a) and (b). Their description of the as-cast microstructure agreed well with an earlier investigation of a similar alloy carried out by Rishel et al. [17]. The cast structure which contained the lamellar (α_2/γ) phases was explained in terms of a long solidification time, followed by a low cooling rate in the two phase field.

When the cooling time is long enough, the casting undergoes an eutectoid reaction as the temperature decreases from the single phase field to the two phase field, where the high

temperature α phase decomposes to a (α_2/γ) lamellar eutectoid structure. As can be seen in the phase diagrams, (see Figure 2.5), the titanium aluminide based alloys with a composition of up to 8 at. % Nb undergo this eutectoid reaction at around 1125 °C.

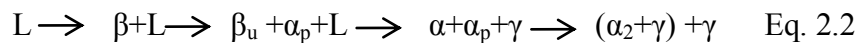


The formation of the lamellar (α_2/γ) structure was proposed by Ramanujan [18], with two possible mechanisms, the α phase decomposes into ($\alpha+\gamma$) then the α phase undergoes an ordering transformation to α_2 , or the ordering transformation of α into α_2 takes place before the decomposition into the two phases $\alpha_2+\gamma$.

The nucleation and growth of the γ , (fcc, TiAl L1₀), lamellae from the α , (hcp) phase involves changes in the crystallographic structure of the lattice. In addition to changes in the chemical composition which are determined by diffusion of Al atoms into the α Ti lattice.

Despite being a slow process in the hcp structure of the α phase, diffusion is expected to be even slower and requires more energy in the case of the α_2 phase with the ordered hexagonal Ti₃Al (DO19) lattice. Thus, it seems logical to believe that the γ lamellae nucleate first from the α phase, and then the two phase field ($\alpha+\gamma$) is created and subsequently, the residual α phase undergoes an ordering transformation to α_2 .

Sujata et al. [19] studied the solidification path of a Ti-48%Al-2V alloy. The primary phase (β) reacts with the remaining liquid according to the peritectic reaction, (Eq. 2.2), and resulted in peritectic α and untransformed β , with further cooling through the ($\alpha+\beta$) region resulting in the formation of a lamellar (α_2/γ) structure;



The α grains formed as a result of the peritectic reaction, and formed as envelopes surrounding the primary β dendrites, the nucleation process of the α phase takes place at the liquid/ β interface [20]. And hence, a solid phase transformation takes place through which γ is formed.

Zollinger et al. [21] showed that oxygen, which is an α stabilizing element, in the range of 0.8 to 1.5 at. % interstitially dissolves in the α phase and shifts the peritectic transformation to Al content lower than the peritectic composition of 45 at. % Al. And hence, oxygen broadens the field of the single phase (α). In addition, microsegregation is expected to be found in the as-cast structure of these TiAl intermetallics, due to the rejection of Al into the liquid phase while oxygen segregates to the α phase with partitioning coefficients of 0.90 and 1.29

respectively. Upon cooling, the α -dendrites transform to lamellar ($\alpha_2+\gamma$), and the interdendritic region contains the remaining γ phase, where oxygen dissolves into the lamellar structure with a maximum solubility of 230 ppm in the γ phase [22].

The as-cast microstructure of the titanium aluminide alloys, (Ti47Al-Ti50Al), is expected to contain microsegregation, (partitioning), due to the difference of solubility of Al in the liquid and the primary solidifying phase. This phenomenon has been investigated in several studies using EDS [23-25].

The α -stabilizer, Al, is expected to segregate to the liquid phase during the formation of the β dendrites in the liquid, and hence the interdendritic γ has higher Al content than the mean alloy composition. In addition, coring takes place during the formation of the α phase, where β stabilizer elements, such as Nb, which were dissolved in the pre-peritectic phase segregate into the core of the newly nucleated α grains, thus the centre of the dendrite arms are enriched with Nb and appear as the bright regions in Figures 2-7 and 2-8.

As can be seen in the micrographs, α and β primary phases form according to the alloy composition, specifically the Al content. And, as can be predicted from the Ti-Al-x phase diagram, (shown in Figure 2-5 (d)), the alloy starts solidification in the (L+ α) zone if the Al content is higher than 50 at. %, and the primary α phase is formed. While the primary β phase is formed upon solidification of alloys with Al content lower than 50 at. %, where solidification starts in the (L+ β) zone.

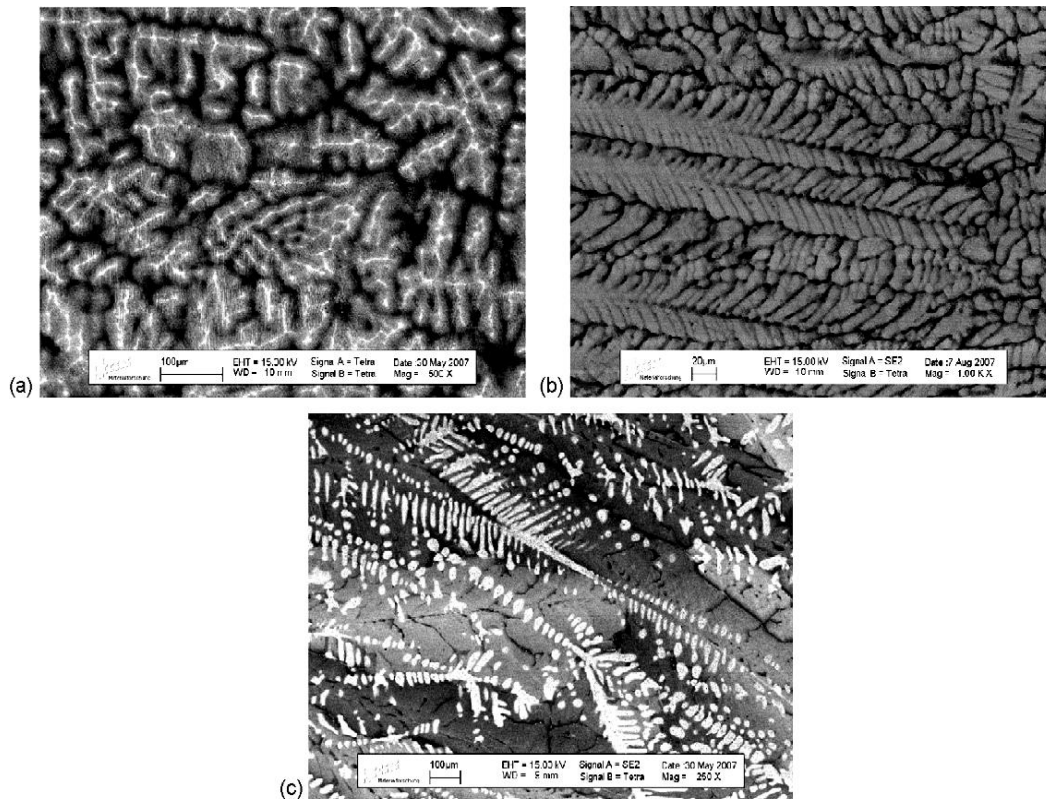


Figure 2-7 As-cast microstructure shows the primary phase upon solidification in sample (a) β -primary phase in sample Ti44.5Nb7.7Al47.8, (b) α -primary phase in sample Ti38.3Al54.1Nb7 and (c) α dendrites surrounded by γ phase in sample Ti38Al54Nb7.6, Witusiewicz et al. 2009 [14].

Kartavykh [15] carried out isothermal solidification experiments on Ti-46Al-8Nb samples, aiming to investigate the solidification path of the alloy. The samples were held at 1670 °C, 100 °C above the liquidus temperature, for 5 minutes, and then different quenching cycles were applied, (with cooling rates of 20, 10, and 5 Ks⁻¹) down to 1470 °C, just below the solidus temperature, followed by quenching to 400 °C, aiming at retaining the equilibrium phases.

The β dendrites were the primary phase solidifying with a slower cooling rate, (5 Ks⁻¹), where the solidification time was long enough to develop secondary and third order dendritic arms, as shown in the micrographs (b) and (c) in Figure 2.8. The fastest cooling rate, (20 Ks⁻¹), resulted in an equiaxed grain structure as shown in the micrograph of sample 1 (Figure 2.8 (a)).

The researcher claimed that the solidification path of the Ti-46Al-8Nb contradicted the expected solidification path in the calculated phase diagram by Saunders [8], in which the solidification path goes from the mushy zone (L+ β) through a single phase field of (β) directly without going through the peritectic reaction in Eq.2.2. However, it was reported that a slight increase in the Al content of the melt can therefore shift the solidification path to the peritectic composition.

However, according to the preceding discussion about the rejection of Al into the liquid phase during the formation of the primary β phase, this can explain the discrepancy with the calculated phase diagram. The investigated alloy is expected to go through the peritectic reaction, the residual liquid in the (L+ β) region is enriched with Al, and subsequently the high temperature α phase forms, and solid state phase decomposition of the α finally resulting in the equilibrium room temperature phases $\alpha_2+\gamma$, as discussed before, and as given in the CALPHAD phase diagram, (see Figure 2.5).

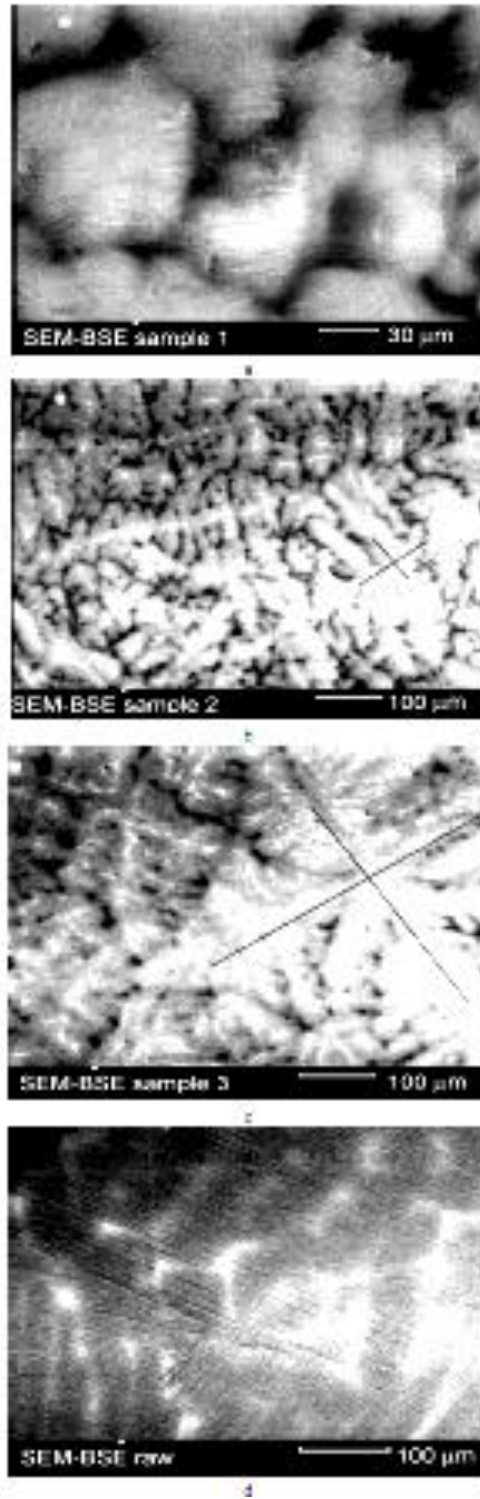


Figure 2-8 SEM-BSE micrographs of rapid-solidification Ti-46Al-8Nb samples with cooling rate (a) 20, (b) 10 and (c) 5 K/s, (d) shows the micrograph of a sample of slow cooling solidification, Kartavykh 2012 [15].

2.3 The Columnar to Equiaxed Grain Transition (CET)

2.3.1 Mechanisms of Columnar to Equiaxed Grain Transition

Columnar grains generally grow and elongate in one dimension normal to the solidifying front, which is the direction of the steepest temperature gradient and antiparallel to the direction of heat flow. On the other hand, equiaxed grains grow equally in all directions in the central supercooled liquid, where the temperature gradient is shallow enough to be equal in all directions, which encourages growth in multiple favourable crystallographic orientations.

The columnar-to-equiaxed grain transition, (denoted as the CET hereafter), occurs if a band of equiaxed grains appears at the head of the columnar tips and terminates further growth of the columnar grains. Figure 2.9 shows the CET in an Al-base alloy, where the red-dotted line indicates where the equiaxed grains have blocked the columnar grains from further progression [26].

Several hypotheses; [27-32]; were proposed to explain the mechanism of the CET in the case of no added nucleants:

- Constitutional supercooling
- The “Big Bang hypothesis”
- Fragmentation of Dendrite Arms
- Solute elements accumulation at the columnar front



Figure 2-9 Macrograph of Al-4%Cu (wt. %) shows columnar to equiaxed transition, J. A. Spittle et al. 2006 [26].

2.3.1.1 The Constitutional Supercooling Theory

The constitutional supercooling hypothesis was proposed by Tiller et al. [27]. Based on the role of constitutional supercooling in the formation of equiaxed grains, where the liquid at the head of the columnar tips is constitutionally undercooled and hence allows the heterogeneous nucleation of equiaxed grains which subsequently arrest any further growth of the columnar grains. The constitutional undercooling mechanism is expected to occur upon solidification when the following condition was fulfilled:

$$G/R < -mc_o(1-k)/kD \quad \text{Eq. 2.3}$$

Where G is the temperature gradient in the liquid, R is the velocity of the solidification front, m is the slope of the liquidus line at the original composition of the alloy in the phase diagram,

k is the partitioning coefficient, C_o is the original alloy composition and D is the diffusion coefficient of the solute element.

Under a critical value of temperature gradient to solidification rate, which satisfies the above equation, the CET prevails upon the solidification structure.

2.3.1.2 The “Big Bang hypothesis”

Another hypothesis was proposed by Chalmers [28], the "Big Bang hypothesis", which assumed that the grains in the equiaxed zone nucleate simultaneously with pouring as the molten metal cools in contact with the cold mould walls, and hence, grains that survive remelting will be transported into the bulk liquid by convection, (due to pouring turbulence or convection due to temperature and composition variations), and will grow in the constitutionally supercooled liquid ahead of the interface advancing from the mould walls.

The difference between this theory and the mechanism proposed by the constitutional supercooling theory is that the nucleation process occurs on the mould walls upon pouring, and then the nuclei can be mechanically transported to the bulk liquid where the growth of the grains takes place, while the constitutional super cooling suggested that both heterogeneous nucleation and subsequent growth happen in the bulk supercooled liquid.

2.3.1.3 Fragmentation of Dendrite Arms

On the other hand, the separation of dendrite arms, which swept to the liquid bulk and act as nuclei for new grains was also suggested as a mechanism of the CET, and this fragmentation is encouraged by low thermal gradient and expected in non-refined alloys [29, 31].

It can be assumed that the roots of dendrite branches, (the neck), which connect the primary and the secondary dendrite arms to the dendrite stem, have the smallest section size in the dendrite. Thus, remelting starts at the dendrite roots with a size smaller than the critical size

that can survive the remelting due to solute accumulation in the adjacent liquid, and hence the branches break and are carried away by the metal flow.

2.3.2 Solidification Parameters Influencing the CET

Various parameters influence the CET during solidification, such as cooling rate and temperature gradient ahead of the columnar front, and constitutional supercooling which in turn is governed by the alloy system and composition. A critical value of the cooling rate determines when the columnar growth is impeded, and also both the temperature gradient and the growth rate affect the CET in any alloy system [32].

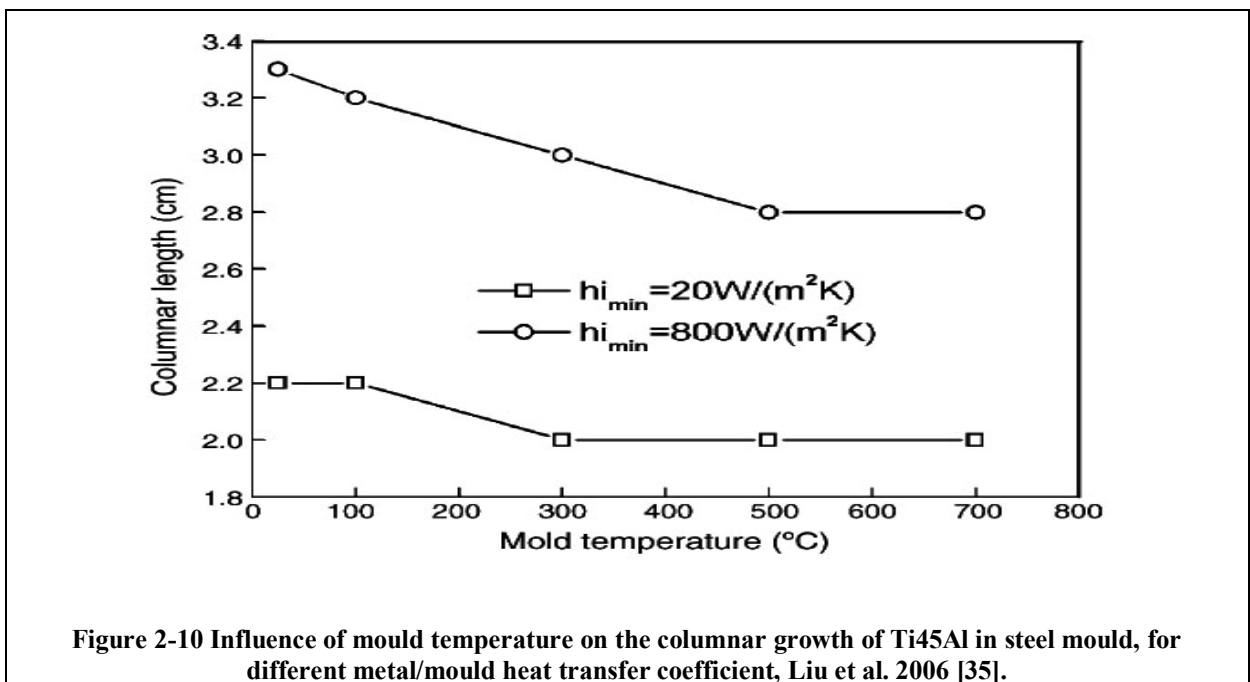
It was also stated by Shi-ping et al. [33] that the high pouring temperature of the molten metal raises the temperature gradient of the liquid zone and hence depresses the constitutional undercooling which in turn delays the CET.

Witzke et al. [34] developed a mathematical model to correlate the conditions in the liquid layer ahead of the columnar front which promote the growth of the equiaxed grains. The model proposed that constitutional undercooling depends on the superheat of the liquid, its thermal diffusivity and chemical diffusivity. The critical value of superheat to undercooling ratio is the condition under which the liquid region is constitutionally undercooled. However, the model represented only the case of the CET in binary alloy systems.

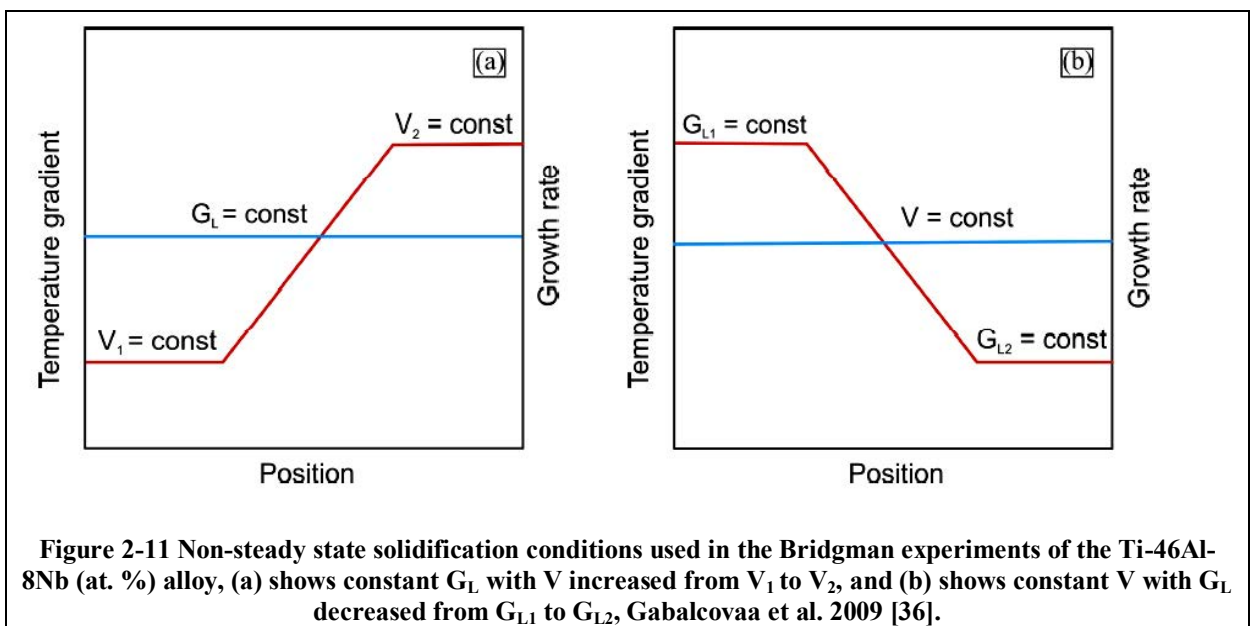
A stochastic model was developed by Liu et al. [35] for the CET in Ti-45Al alloy. This involved two models, based on the FDM (finite difference method) coupled with a CA (cellular automation) approach to simulate the solidification process and the grain growth of the alloy in an ingot in a cylindrical metal mould. The effect of the interfacial heat transfer coefficient on the CET was investigated by using two different values $h_{min} = 20$ and $800 \text{ W/m}^2\cdot\text{K}$; with the model results being in agreement with the experimental measurements.

It was pointed out that thermal conductivity of the mould could have an influence on the columnar growth and subsequently on the CET under the condition of high heat transfer coefficient at the casting/mould interface. The lower the mould preheating temperature the higher the cooling rate, and as a result the velocity of the columnar front increases and the temperature gradient of the liquid bulk increases too, all of which enhance the columnar growth and delay the columnar-to-equiaxed transition.

The model results also showed that the influence of the mould preheating temperature was dependant on the rate of heat transfer at the metal/mould interface, as with a low heat transfer coefficient the columnar length was almost constant with the mould preheating temperatures as shown in Figure 2.10. This can be attributed to the shallow temperature gradient produced by the low rate of heat extraction at the metal/mould interface, and the cooling efficiency of the mould, (which was expected to be higher with a low mould temperature, as mentioned above), had no influence on the temperature distribution within the solidifying metal, and subsequently the CET obstructed the growth of the columnar grains even with low mould temperature.



Likewise, the effect of temperature gradient and growth rate on the CET in Ti-46Al-8Nb was investigated by Gabalcovaa et al. [36]. They carried out a series of directional solidification experiments consisted of steady state solidification at constant temperature gradient G_L , (in the liquid at the solidification front), and constant growth rate V , (thermal velocity usually denoted R), and non-steady state solidification in case of constant G_L and increased V and in case of constant V and decreased G_L , as shown in Figure 2.11.



It was suggested that “a solidification parameter” G_L/V determines the tendency to the CET in the alloy investigated, with a critical value ($G_L/V < 6.92 \pm 0.31 * 10^6$ K. s. m^{-2}) is reached in the case of steady state growth conditions. Consequently, a CET diagram was developed using experimentally measured values of the growth rate and temperature gradient during solidification of Ti-46Al-8Nb alloy, and was compared to diagrams of other alloys, as shown in Figure 2.12.

The diagram shows that a high growth rate and low temperature gradient of the liquid at the advancing solidification front promote the CET. The CET in Ni-base super alloys can occur at a lower grain growth compared to the grain growth at which the CET in Ti-46Al-8Nb takes place at the same temperature gradient, this can be probably due to the high nucleation rate in Ni-base super alloy due to high microsegregation. Also, the slope of the CET lines can suggest that the solidification conditions, (growth rate and temperature gradient), which promote the CET in the Ti-46Al-8Nb alloy can be comparable to those in the Ni-base super alloys, this can be understandable due to the resemblance of the solidification range in both systems, (the solidification range of the Ni-base super alloy CMSX-4 is 52 degrees [37], while it is 60 degrees in the Ti-46Al-8Nb).

On the other hand, the CET in Al-Cu alloy requires lower temperature gradient than that in the Ti-46Al-8Nb alloy and the Ni-base super alloy, at the same growth rate, this can draw the attention again to the solidification range of the three systems where it is higher in the Al-Cu alloy (almost 100 degrees), in which latent heat of solidification is released gradually over a wider range of temperature which raise up the temperature of the bulk liquid and hence induce the remelting of the freshly nucleated nucleus, this can retard the nucleation and subsequent growth of the equiaxed zone, and hence delay the CET.

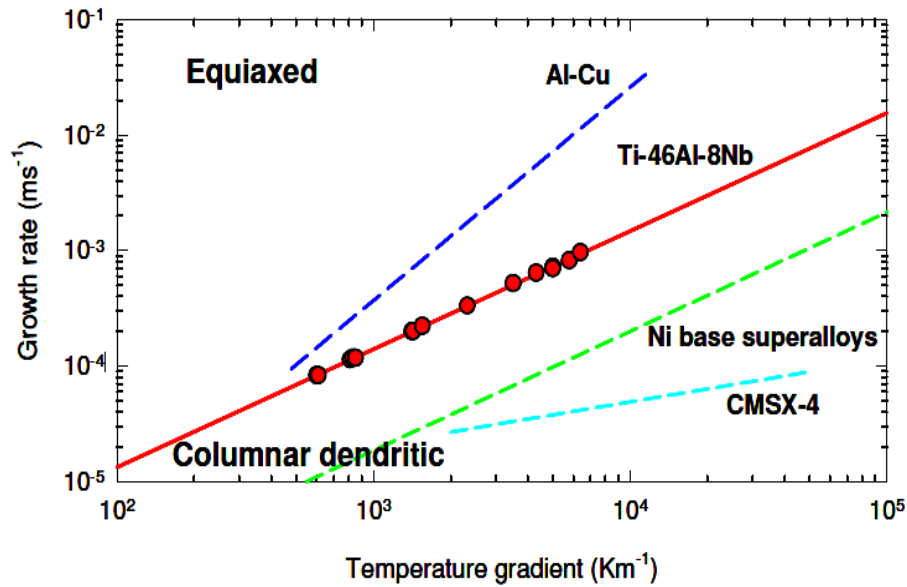


Figure 2-12 CET diagram of Ti-46Al-8Nb (at. %) alloy showing the growth rate as a function of the temperature gradient, Gabalcoava et al. 2009 [36].

Flood and Hunt [38, 39] developed a finite difference model to study the growth kinetics of the equiaxed grains ahead of the columnar front, and showed that the growth rate of the equiaxed grains was higher ahead of the columnar front. This was attributed to convection in the bulk liquid which dissipated the superheat, combined with a low cooling rate and low temperature gradient, all of which encouraged the equiaxed growth at the expense of progression of the columnar tips.

2.4 Melting and Casting of Titanium Alloys: Induction Skull Melting (ISM)

Titanium alloys are generally characterized by high reactivity in the molten state due to their great affinity for oxygen, hence they are prone to react with the crucible and the mould material [40]. For this reason, certain procedures must be followed during melting and casting, such as shielding the whole process by using a vacuum or inert gas, and using a suitable type of crucible and mould material. Some refractory crucibles, (typically $\text{CaAl}_2\text{Si}_2\text{O}_{10}$; CaO), were used for melting TiAl alloys [41].

Induction Skull Melting (ISM) provides an uncontaminated and rapid technique for melting Ti alloys, where melting is carried out in a water-cooled copper crucible which is heated by a high power induction coil, with a typical power of 300-350 kW. Consequently, the first metal to melt instantly solidifies against the cooled wall where it forms a skull which contains the remainder of the melt [42].

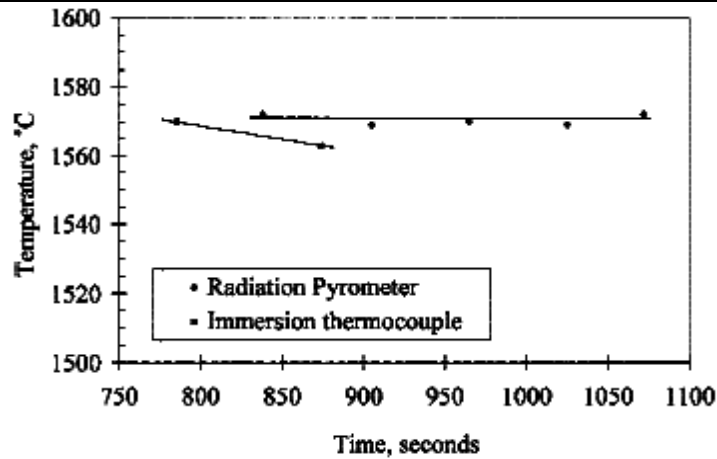
After achieving complete melting, the Cu-crucible is being continuously cooled, and the molten metal is contained in a skull of itself. This means the rate of heat extraction from the molten metal before and during pouring is high and it is difficult to maintain a superheat. Thus, the main disadvantage of the ISM technique is that mostly a low superheat, which can be as little as 10-20 °C is achieved, so the melt should be rapidly poured into the mould aiming to minimise temperature losses in order to avoid a mis-run casting. Therefore, severe surface turbulence is expected to arise due to rapid pouring.

The effect of increasing the induction power and the applied shielding gas pressure on the resultant superheat were investigated in several studies carried out in the IRC at the University of Birmingham, some of which are discussed in the following paragraphs.

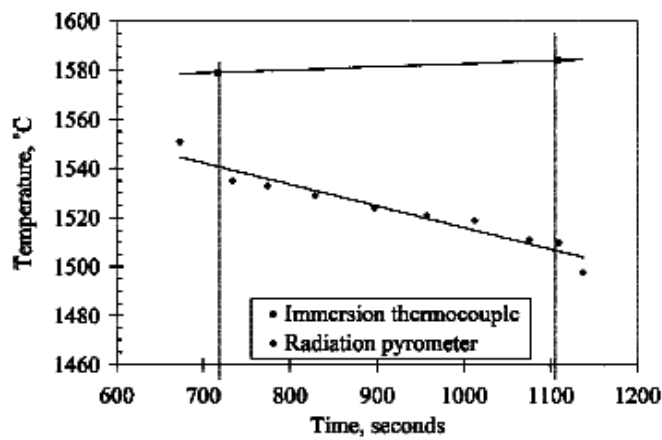
Harding et al. [43] carried out melting trials in a high power ISM furnace, using 200 kW and 350 kW power to melt a 5 kg charge of TiAl alloy. Temperature measurements were carried out by using an optical pyrometer and a dip thermocouple, and both techniques gave, more or less, comparable temperatures, (see Figure 2.13).

The superheats obtained in the case of melting in vacuum, in 200 mbar and in 800 mbar of Argon, were compared. Increasing the melting power from 200 kW to 350 kW did not significantly increase the superheat gained, and a possible reason for this was hypothesised, that at a higher melting power the mushy zone would be reduced in size and as a result the skull thickness decreased, and hence the heat extraction from the molten metal to the crucible increased.

On the other hand, it was concluded that a higher superheat was obtained when the melting process was carried out under a pressure of argon gas than when the superheat was obtained in a vacuum, (the obtained superheat increased from 30 K in a vacuum to 50 K in 200 mbar Ar and to 60 K in 800 mbar Ar). However, the role of the applied argon gas pressure in increasing the melt superheat was not clearly investigated in their study, and it was also implied that Al evaporation during vacuum melting of the TiAl alloy could be one of the explanations for this trend.



(a)



(b)

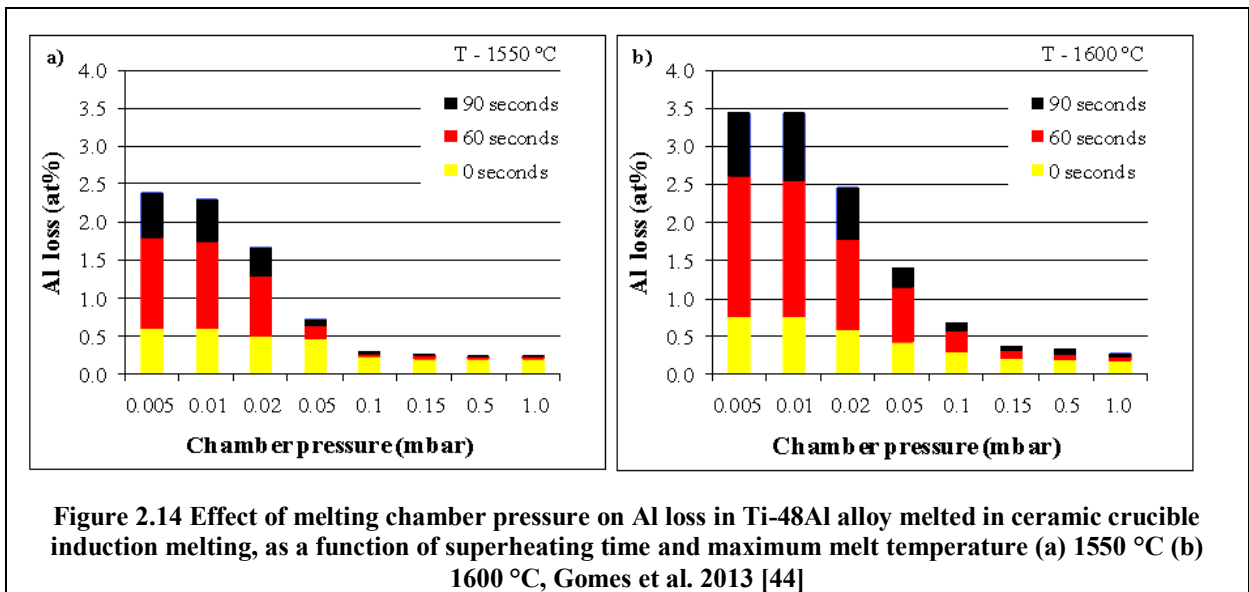
Figure 2.13 Temperature measurements, using dip thermocouple and optical pyrometer, of Ti45Al5Nb1W1B (a) in vacuum and (b) in 200 mbar Ar. Temperatures measured in vacuum showed much similarity in both measurement techniques, Harding et al. 2003[43]

It is well-known that the element with the higher vapour pressure evaporates in a vacuum, and in the case of a TiAl melt, the Al element has the lower melting point and is volatile at the melting temperature of the alloy which exceeds 1500 °C, thus Al was expected to evaporate in either a vacuum or a low pressure atmosphere.

This was confirmed in the study carried out by Gomes et al. [44], who showed that the evaporation of Al from the TiAl melt increased as the pressure of the melting chamber decreased, as shown in Figure 2.14. A maximum Al loss of 3.45 at.% was found at a vacuum pressure at 0.01 mbar, while it was under 0.5 at. % at a pressure higher than 0.1 mbar.

It was acknowledged that, as the surrounding pressure increases, the partial pressure of the volatile element decreases, and hence when the melting chamber is back-filled with argon, at a pressure of 200 mbar or higher the evaporation of Al was prevented and the Al loss was minimized [45].

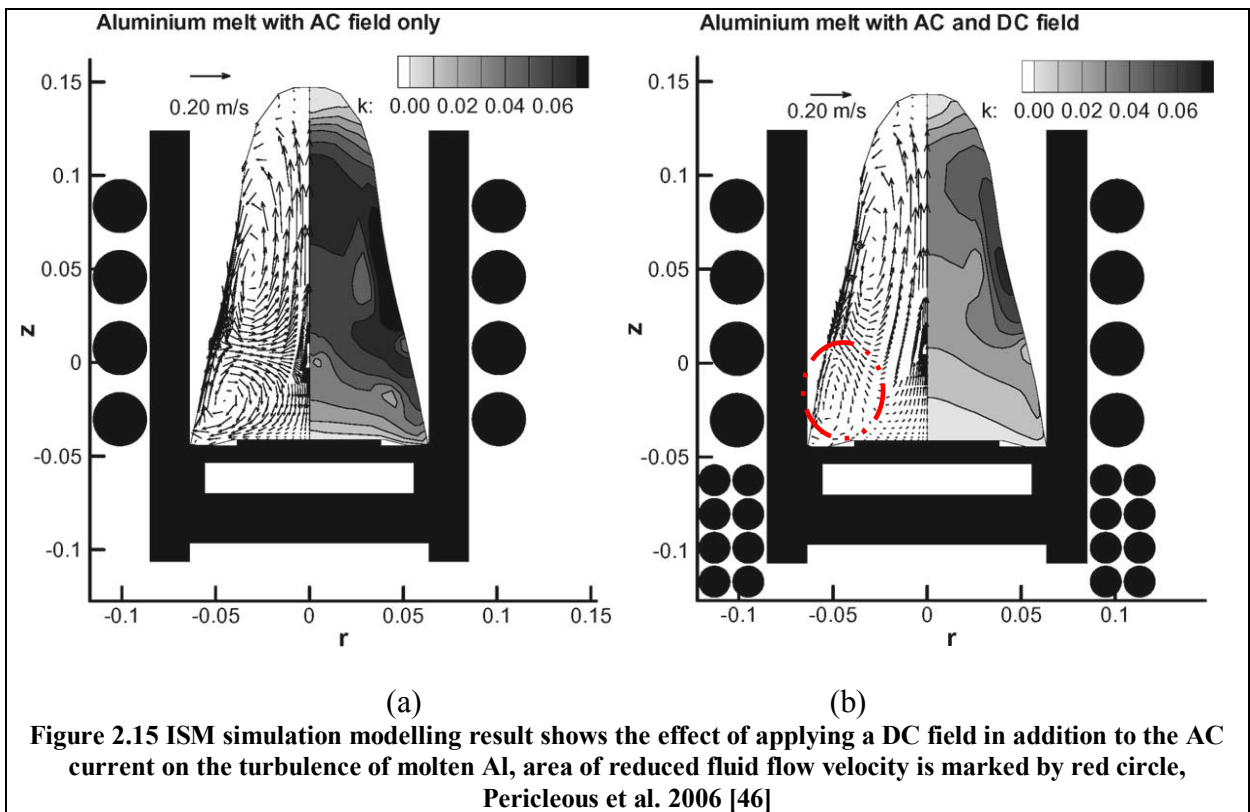
In the light of the preceding, the influence of the applied argon gas pressure in increasing the melt superheat during the melting process of TiAl can be explained in terms of the following: the Al loss in the TiAl alloy causes the liquidus temperature to increase, and hence the superheat that can be gained at a given melting temperature and holding time is decreased, while Al loss decreases with increasing the applied gas pressure and hence the obtained superheat increases at a given melting temperature.



In contrast to the results shown in reference [43] in the case of increasing the melting power, Pericleous et al. [46] showed that applying an additional direct current (DC) to the induction coil could reduce the heat lost from the crucible outer surface and hence maximize the superheat. By a coupled experimental and modelling study, it was declared that introducing a DC field into the molten metal just after the completion of melting suppressed the metal

turbulence, (see Figure 2.15), and hence the rate of heat transfer into the crucible was significantly reduced which in turn increased the superheat of Al by 60 K.

The direct current, DC, is expected to introduce an additional constant power to the electric power from the AC coil, and the electric power converts to thermal energy when passing through the conductive metal. This is known as Joule heating, and as the DC is increased the heat released in the molten metal is increased. More detail about this point can be found in reference [46].



2.5 Feeding Mechanisms during Solidification

Solidification shrinkage occurs as the metal is transformed from a liquid state to a solid state, due to structural changes from the liquid state in which there is no long range order to a densely packed crystallographic structure of atoms with long range order. The difference in the densities results in reduction in volume. [47].

According to Campbell [48, 49], feeding of a casting during solidification is a complicated procedure that can occur through one or more of five different mechanisms, as illustrated in Fig. 2-16. Four of these mechanisms are listed below, the burst feeding mechanism is more related to the formation mechanism of layer porosity, which is discussed in Section 2.6.4.

- ***Liquid feeding***

Liquid feeding plays an important role in feeding at the beginning of solidification, while the liquid still has a high fluidity to flow easily through the open feed path. The volume of the feeder must be suitable to provide the required liquid feeding, otherwise air suction, instead of liquid flow, takes place and causes the formation of shrinkage pipe in short freezing range alloys and interconnected cavities linked to the outer atmosphere through the feeder in long freezing alloys as will be discussed in Section 2.6.

- ***Mass feeding***

As solidification progresses the solid phase is present in the liquid as free dendrites and forms a slurry-like medium. The slurry flows in the direction of low pressure until this movement is arrested by the formation of a coherent dendrite network, Campbell suggested that the movement of the (solid + liquid) slurry slows down as the size of the grains increases and the grains become strongly attached to each other and to the wall of the casting, and will stop completely after the solid fraction reaches 0.68.

- ***Interdendritic feeding***

Interdendritic feeding starts when the slurry flow is arrested by a coherent dendritic network. It plays an important role in feeding during the latest stages of solidification, the residual liquid flows through the interdendritic gaps in a manner resembling the flow of a liquid in a capillary system. The Poiseuille equation expresses the pressure gradient along a capillary with radius R in the x direction as follows;

$$\frac{dp}{dx} = \frac{8v}{\delta R^4} \pi R^4 \quad \text{Eq. 2.4}$$

dp/dx is the temperature gradient which is required to cause a volume of fluid v to flow per second, μ is the dynamic viscosity. For the analysis of the pressure gradient in the mushy zone, a capillary system with N capillaries, equation 2.4 becomes:

$$\frac{dp}{dx} = \frac{8v}{\delta R^4} \mu / \pi R^4 N \quad \text{Eq. 2.5}$$

Campbell provided a final solution for the pressure drop equation by using the conservation of volume in unit time and then taking into account the rate of freezing as $\frac{dR}{dt} = \frac{-4\lambda^2}{R}$:

$$\Delta P = 32\eta \left(\frac{\beta}{1-\beta} \right) \left(\frac{\lambda L d}{R^2 D} \right)^2 \quad \text{Eq. 2.6}$$

Where λ is the heat flow constant, d is the dendrite arm spacing, β is the solidification shrinkage, and D is the area of the mushy zone.

- ***Solid feeding***

As the radius of the interdendritic flow path decreases with continuing solidification the pressure drop increases significantly to the limit that the solid layers could plastically deform inwards. In a comparison between the volume of the surface sinks in long, medium and short freezing range Al-Si alloys, Li et al. [50] pointed out that a thin solid layer formed in long

freezing range alloys at earlier stages of solidification and could easily collapse inwards, making solid feeding higher than in short freezing range alloys.

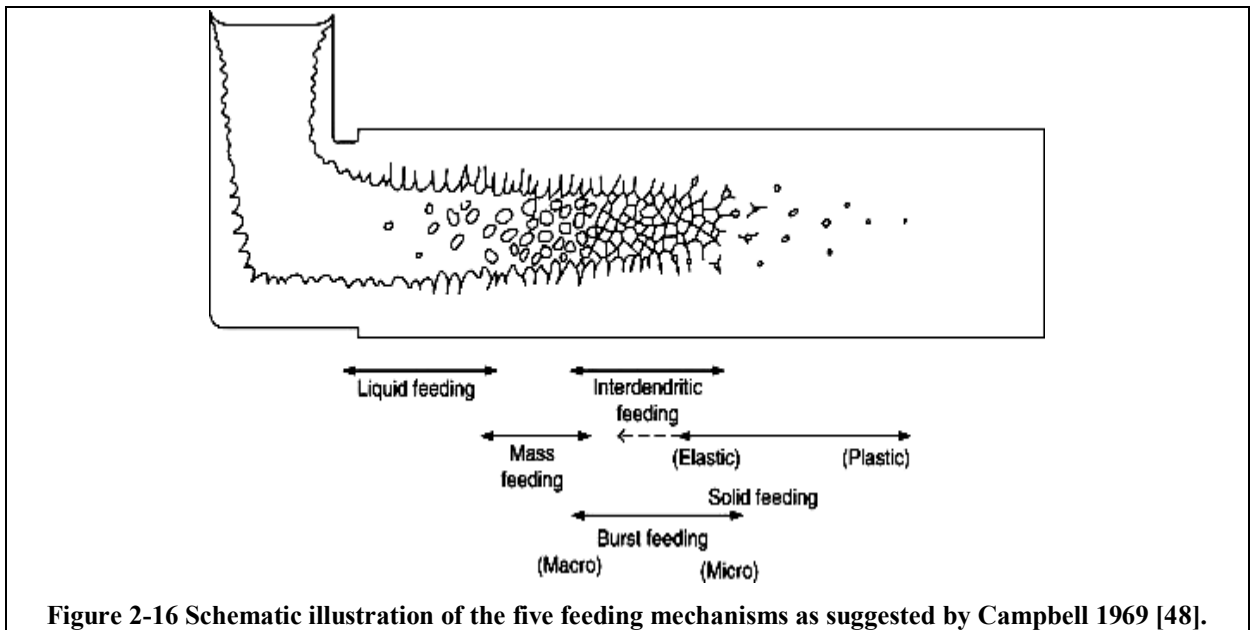


Figure 2-16 Schematic illustration of the five feeding mechanisms as suggested by Campbell 1969 [48].

2.6 Classification of Shrinkage-Related Casting Defects

Shrinkage-related defects, including pipe shrinkage, macroporosity (cavities) and microporosity can be a key cause of casting rejection [51], Figure 2.17 shows schematically different types of shrinkage defects.

It is acknowledged that shrinkage defects are linked to the solidification process of the casting, specifically to the liquid feeding mechanism which should compensate for solidification contraction. A classification of different types of shrinkage defects, based on the defect shape and the formation mechanism, is given in the following sections.

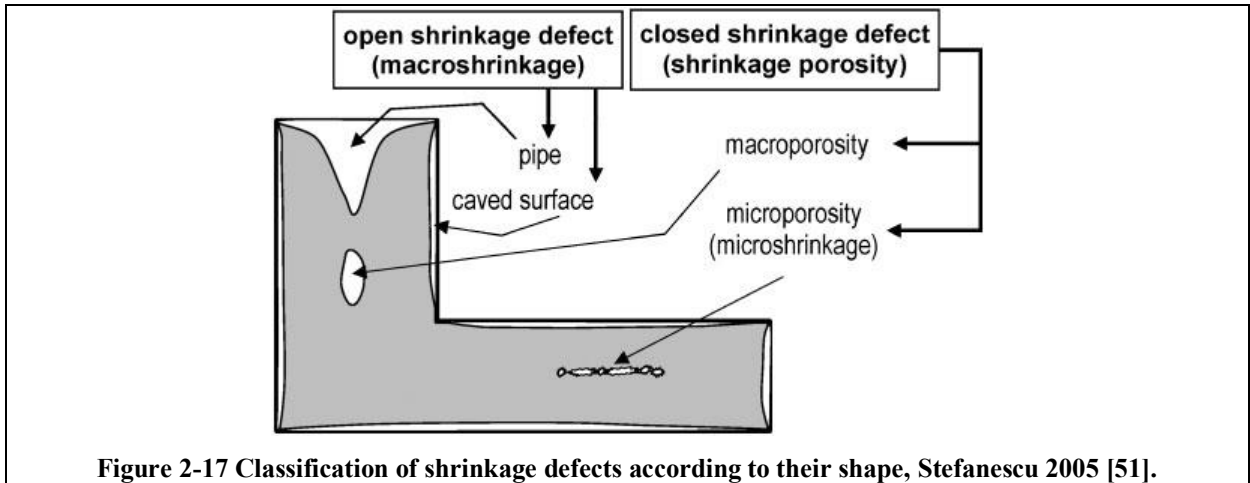


Figure 2-17 Classification of shrinkage defects according to their shape, Stefanescu 2005 [51].

2.6.1 Pipe (open) Shrinkage Defect

A pipe with a smooth internal surface is formed as a result of a continuous decrease in liquid height in the feeder. The contraction of the mushy zone in long-freezing range alloys and plastic deformation of the solid skin in short-freezing range alloys can both result in the formation of a shrinkage pipe which is connected to a free surface through the feeder, as shown in Figure 2.17. Pipe shrinkage is also known as primary shrinkage and it is normally located in a feeder. Under poor liquid feeding conditions the primary shrinkage can extend into the casting, forming a secondary-shrinkage pore. The secondary-shrinkage appears as disconnected pores, starts below the primary shrinkage pipe and can then be found scattered in other locations other than the thermal centre of the casting [52].

2.6.2 Macroshrinkage Cavities

Macroshrinkage cavities, also known as voids, (with a linear dimension of at less 5 mm), have more or less a rounded shape and can be detected by non-destructive tests [47].

Radiographic testing is widely used to detect internal casting defects by locating any changes in thickness and density as low as 1% of the tested material. Ultrasonic testing, UT, can detect porosity as small as 0.4 mm in diameter.

Macroshrinkage is a result of insufficient feeding or the presence of isolated liquid pockets (hot spots) after the formation of a coherent dendritic network of solid in the mushy zone. Thus, this type of casting defect is promoted by a long freezing range and by the geometry of the casting [53]. For instance, liquid metal paths can be interrupted (mechanically) at a junction of different thickness sections, or at a sharp corner, which leads to premature solidification of the metal combined with inadequate feeding which results in a cavity defect.

2.6.3 Microshrinkage Porosity

Microshrinkage porosity usually takes the shape of liquid entrapped in the interdendritic gaps during the last stages of solidification, the linear dimension of the pores ranges from micrometres up to millimetres [47].

Many theories have been proposed in order to explain the mechanism of formation of shrinkage porosity in different alloy systems, however, it seems that the formation mechanism of shrinkage-related porosity is a complicated process and may involve many factors contributing simultaneously. Some examples of these theories are briefly discussed below.

Walther et al. in 1956 [54], suggested that as solidification proceeds the dimensions of the feeding channels decrease, and as a result the pressure of the liquid trapped in the narrow feeding channels decreases, causing the liquid to rupture, and pores are formed.

However, the theory ignored the influence of the liquid tensile stress, which resists the rupture of the liquid due to the pressure drop. The pore volume depends not only on the width of the interdendritic channels, but also on the solid fraction and hydrogen content [55].

The mechanism of pore formation depends on the combined effects of shrinkage and gas. The internal pressure in a pore involves the internal gas pressure and the shrinkage resistance pressure, which together must exceed the external pressure, (as will be discussed in Section 2.7).

Couturier and Rappaz [56] studied the role of the partial pressure of volatile elements in porosity formation in multi-component alloy systems; such as zinc in Al alloys. The internal pressure of the pore can be represented as a function of the activity coefficients of the elements that compose the gas (A and B) inside the pore as follows:

$$\frac{P_i}{P_o} = K_i(T) (f_A^1 X_A^{1*})^{n_{A^i}} (f_B^1 X_B^{1*})^{n_{B^i}} \quad \text{Eq. 2.7}$$

Where P_i is the partial pressure of the internal gas, P_o is a reference pressure, $K_i(T)$ represents thermodynamic constants such as the entropy and enthalpy of formation, and f_A^1 and f_B^1 are the activity coefficients of the elements A and B in the liquid. X_A & X_B are the mole fractions of the elements present.

The coefficient of element A (gas) is calculated by the summation of the first- and second-order interaction coefficients, (e_A^s and r_A^s respectively), of each solute element in the liquid on the gaseous element A multiplied by its concentration C_s , (where C_s is in wt.%);

$$f_A^1 = 10^{\sum_s e_A^s C_s + r_A^s C_s^2} \quad \text{Eq. 2.8}$$

The solute elements in the liquid phase contribute indirectly to the formation of a pore through their effect on the partial pressure of the gases which form the internal pressure of the pore. As an example, some elements like copper and silicon reduce the solubility of hydrogen in liquid aluminium while other elements, such as magnesium, enhance it.

Therefore, the content of gas porosity is expected to be higher in the presence of solute elements which can reduce the solubility of the gaseous element in the molten alloy, however, this effect is dependent on the concentration of the solute elements, and it can be expected to be more influential if microsegregation is taken into account.

Mi et al. [57] discussed another mechanism of porosity formation in TiAl castings, based on the role of entrained oxide films. They revealed that a considerable amount (10-20%) of

dendrites inside the porosity were covered with thin oxide films, Figure 2.18 shows parts of oxide films that cover the dendrites at the edge of a pore. EDX analysis of two areas on the surface of the investigated defect was carried out. However, the information obtained from the microanalysis of the fracture surfaces and internal surfaces of the bubbles was not sufficient to determine their precise composition.

Moreover, although the melting and casting of the TiAl alloy was carried out under inert gas, (200 mbar of argon), the authors suggested that oxygen contamination took place due to outgasing from the mould during casting, despite being fired at 1000 °C.

Campbell [49] described the bifilms as parallel layers of thin oxide film separated by a thin layer of the ambient gas, which could undergo a mechanical tear during turbulent pouring and consequently parts of these oxides would be dispersed throughout the casting, and consequently would act as heterogeneous positions for pore initiation.

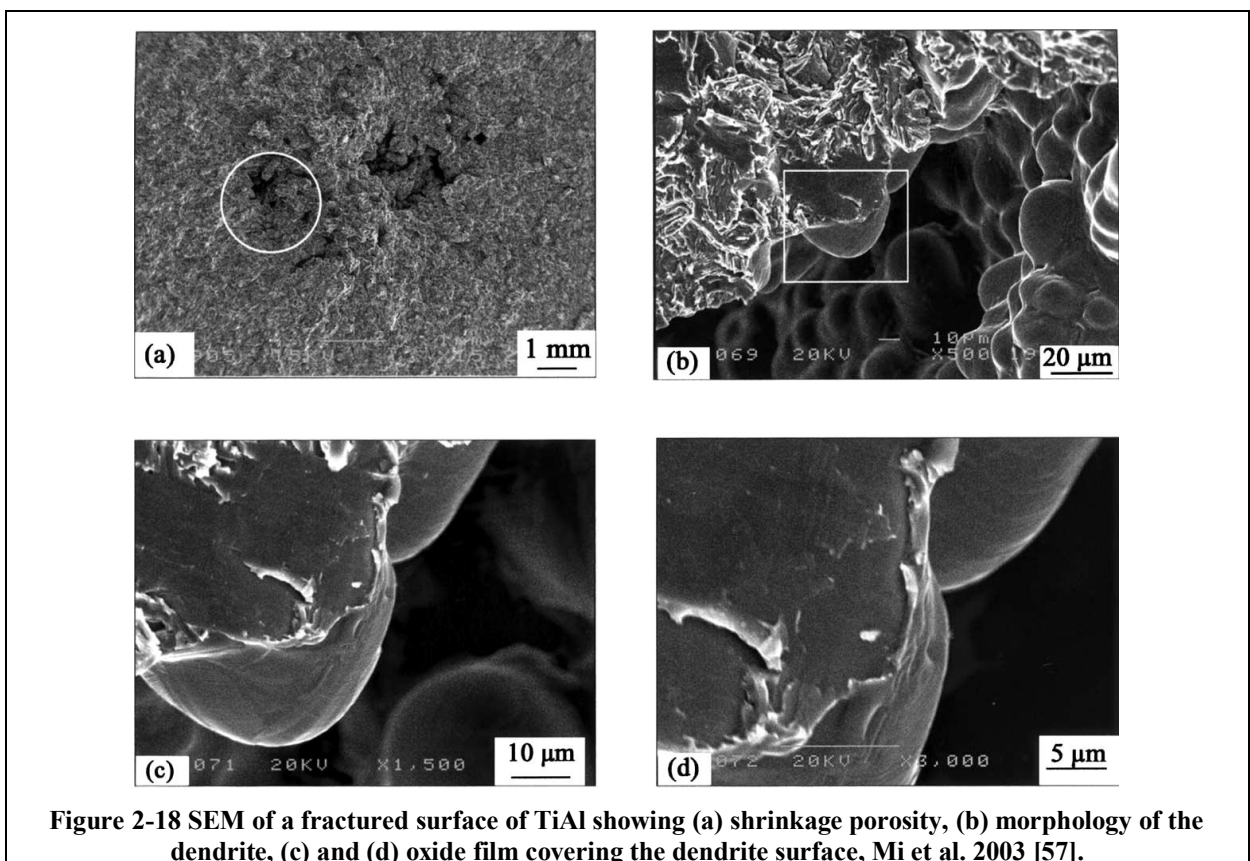


Figure 2-18 SEM of a fractured surface of TiAl showing (a) shrinkage porosity, (b) morphology of the dendrite, (c) and (d) oxide film covering the dendrite surface, Mi et al. 2003 [57].

Reilly et al. [58] carried out a critical review of the current computational simulation techniques utilized to model the entrainment oxide defect. For a typical filling related defect, the essential modelling procedure is to define the free surface and to track it as the mould fills in a turbulent flow, their review critically summarized the main approaches used for that purpose. The first approach is to track the development of the free surface during mould filling using FD or FE methods.

The complexity associated with modelling based on this approach was briefly discussed, like the limitations of using the Arbitrary Lagrangian-Eulerian (ALE)^{*1} techniques to create large fluid free surface when strong free surface turbulence like splashing and waves are expected. In such case a rebuild of the mesh for the free surface domain is required at every timestep which reduces the accuracy and computational efficiency of the model.

The more common approach is to define the mould and casting domains by a fixed grid for each, and then the free surface of the fluid flow is tracked by the volume of fluid and its interface can be located.

Although the computational modelling of the entrainment oxide film defect is beyond the scope of this study, the role that the entrapped oxide film can play in the formation of porosity in most conventional alloys, like steel and Al alloys, cannot be overlooked, and the different approaches and the techniques available for modelling this defect can be a prospective benefit in the accurate modelling of porosity.

For modelling research of porosity-oxide film linked defects, the reader is strongly advised to refer to the review by Reilly et al. [58] which compares between modelling techniques and commonly used simulation software packages, to give further insight into the topic.

^{*1} (A combination of algorithms used in structural mechanics, (Lagrangian), and algorithms used in fluid dynamics, (Eulerian), in which a node in a computational mesh can track the motion and the fixed position of a material particle [59])

2.6.4 Layer Porosity

Layer porosity is a type of shrinkage that tends to form in regularly arranged layers parallel to the advancing solidifying front. Although, this type of shrinkage is expected to form in long freezing range alloys it can also form in short freezing range alloys due to low temperature gradient conditions. Figure 2.19 shows extensive layer porosity formed in a carbon steel alloy. Campbell [60] proposed a mechanism for layer porosity formation in long freezing range alloys based on the accumulation of pressure in the mushy zone during interdendritic feeding.

Figure 2.20 illustrates the stages of the layer porosity formation as explained by Campbell. He assumed that hydrostatic tension is built up in the mushy zone to a point where it exceeds the required pressure for pore formation, and the pore can then form by any of the mechanisms described above. It slowly grows in the interdendritic channels, and thus the pore takes on the layer shape. This stage of pore formation and growth releases the tension in the mushy zone, however the radius of the interdendritic channels decreases with continuous solidification and consequently the hydrostatic tension increases again and as a result a new pore is formed.

As solidification proceeds, further pores are nucleated and grown to produce the following layers.

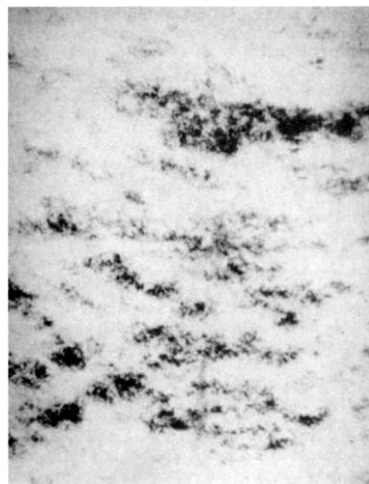
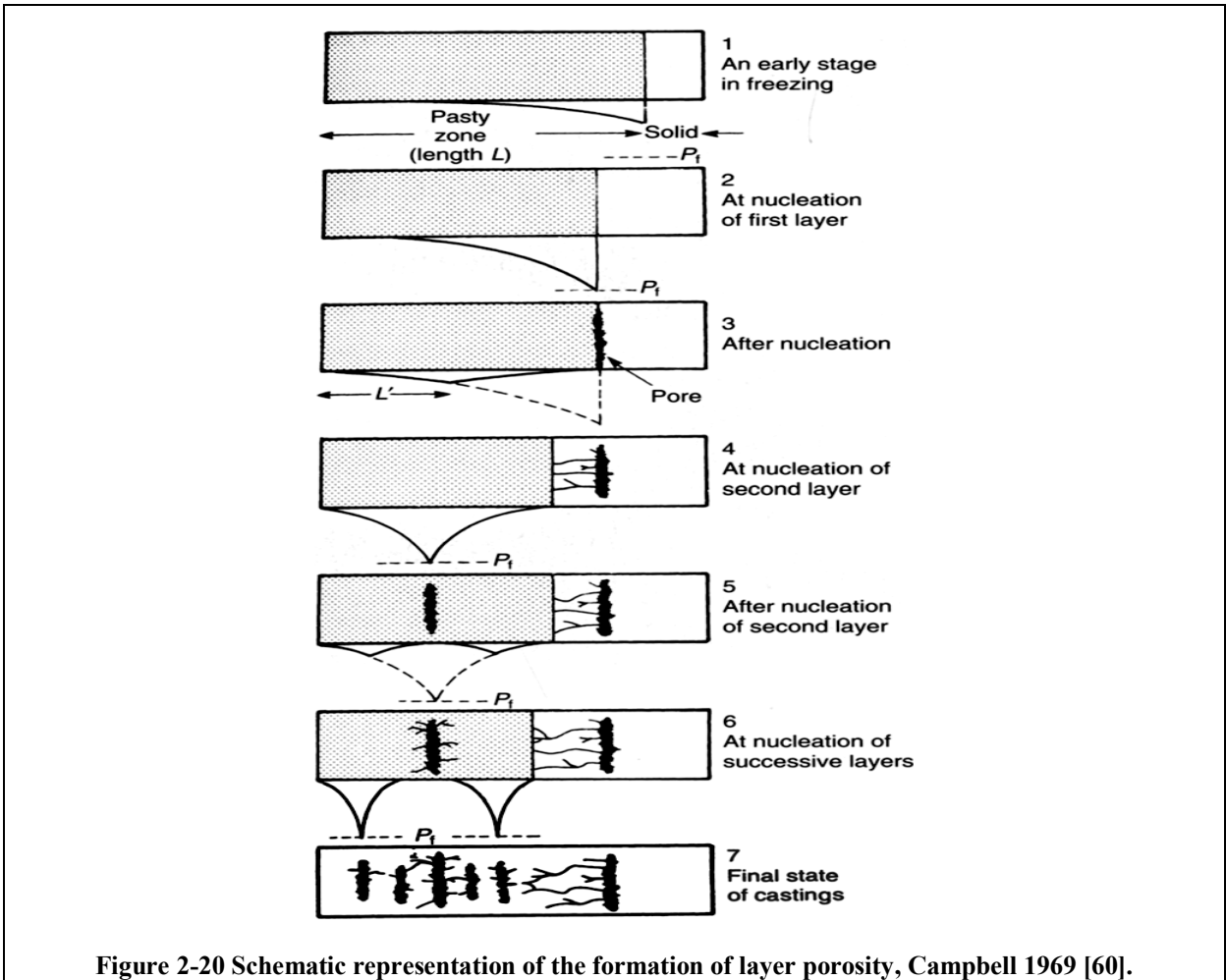


Figure 2-19 Layer porosity in carbon-steel alloy, Campbell 1969 [60].



2.7 Gas Porosity

Upon solidification, the solid phase rejects dissolved gas into the liquid phase, and a gas bubble can form if its internal pressure exceeds the surrounding pressure. If a gas bubble is formed in the mushy zone it will be entrapped in the interdendritic gaps, while gas bubbles in the liquid phase tend to float to the free surface. In both cases, the gas bubbles form as a spherical or ellipsoidal shape [51].

2.7.1 The nucleation process of gas bubbles

The nucleation process of gas bubbles can be discussed theoretically as homogeneous and heterogeneous nucleation actions. In order to survive, the gas bubble must have an internal gas pressure P_G that exceeds the external pressure, which includes the surface tension

component P_γ in addition to the local pressure of the mushy zone P_{mush} which in turn consists of the applied pressure on the mould P_{appl} , the metallostatic pressure P_{st} , the expansion pressure due to phase transformation P_{exp} , and finally the resistance to shrinkage contraction P_{sh} , which is a negative pressure, all influencing the overall pressure in the mushy zone.

$$P_G > (P_{mush}) + P_\gamma \quad \text{Eq. 2.9}$$

$$P_G > (P_{appl} + P_{st} + P_{exp} + P_{sh}) + P_\gamma \quad \text{Eq. 2.10}$$

The negative pressure P_{sh} contributes to the driving force for the pore formation and hence equation 2.10 can be rewritten as follows:

$$P_G + P_{sh} > (P_{appl} + P_{st} + P_{exp}) + P_\gamma \quad \text{Eq. 2.11}$$

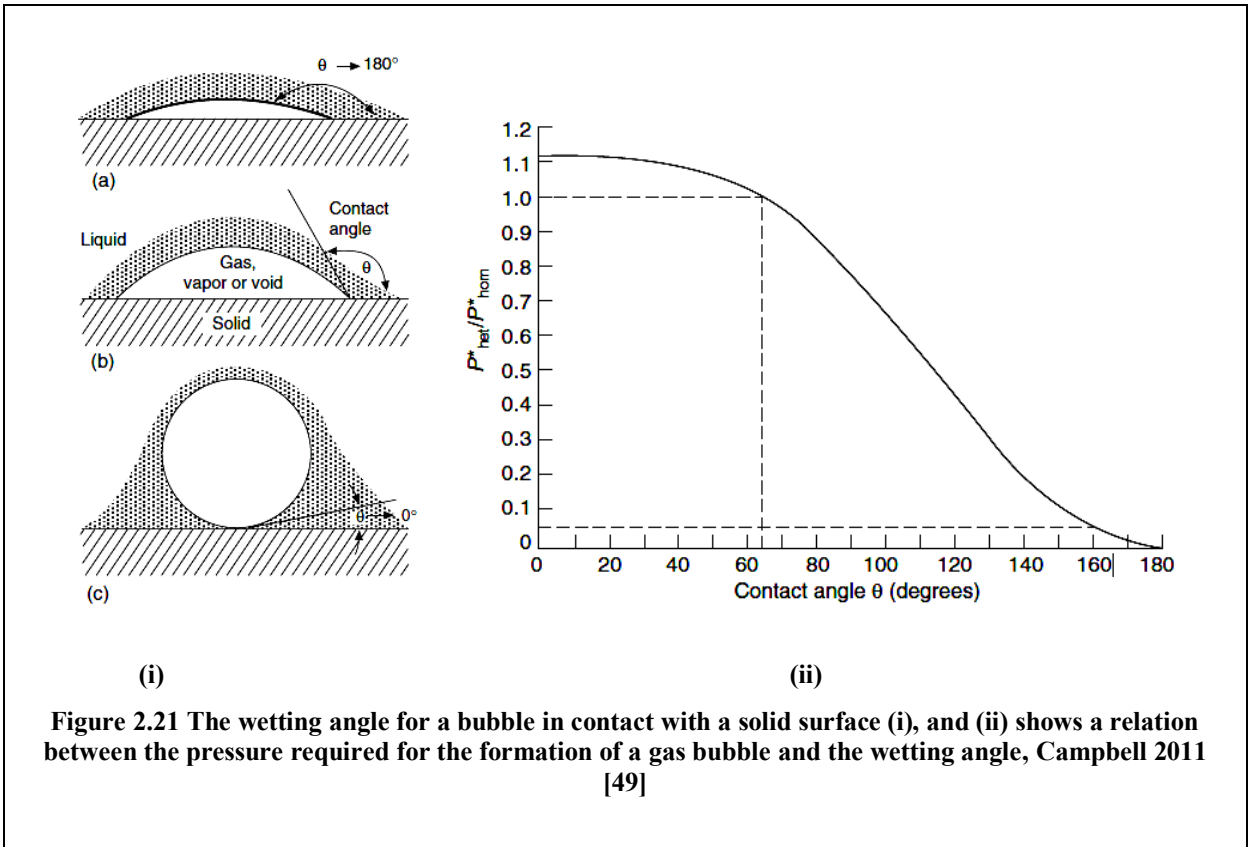
The surface tension γ_{LG} at the interface between the gas and the liquid determines the critical radius below which the pore will not survive the external pressure.

$$r^* = 2 \gamma_{LG} / P_\gamma \quad \text{Eq. 2.12}$$

Campbell argued that, since the pressure required for nucleation of a gas bubble with a radius as small as several atoms is extremely high, for example, 7.7 GPa for liquid iron, as calculated by equation 2.12, consequently the homogeneous nucleation of gas pores in the liquid metals is not possible.

2.7.2 Heterogeneous nucleation

Heterogeneous nucleation of a gas bubble takes place on a foreign substrate such as the solid surface of an impurity particle. According to Fisher [49] the nucleation of a bubble on a solid surface depends on the contact angle between the liquid and the solid surfaces, known as the wetting angle θ . A relationship between the ratio of the required pressure for heterogeneous nucleation to the required pressure for homogeneous nucleation and the wetting angle between the liquid and the solid phases is shown in Figure 2.21.



$\theta = 0$ represents a complete wetting, while $\theta = 180^\circ$ represents a complete non-wetting between the two phases, Figure 2-21 (i). As the wetting angle increases above 65° the pressure of the heterogeneous nucleation decreases, as shown in Figure 2-21 (ii), and hence the nucleation of a gas bubble is enhanced by the presence of poorly wetted inclusions such as non-metallic inclusions.

2.8 Prediction of Shrinkage Porosity during the Solidification of Metal Castings

Several attempts have been made to predict the location and size of shrinkage porosity in castings by creating complex thermal and thermal/fluid flow numerical models. Thermal models were designed to solve the energy transport equation and hence predict the last region to solidify and its feeding requirements. Other models combined the energy and mass flow equations to predict the free surface, along with the last region to solidify.

Other models have been used to predict the complicated pore nucleation and growth processes based on the role of gas. Equation 2.11 shows the driving force for the formation of a stable pore in the mushy zone of a solidifying metal, in terms of a pressure balance, between the internal pressure and external pressure of a pore. This includes the pressure of a segregated gas, where its solubility exceeds the solubility limit in the liquid phase, (P_G).

Finally there are stress analysis models, which have been used to predict casting defects, particularly hot tears, which form due to the coupled effect of a feeding deficiency and mechanical restraints arising from thermal contraction upon solidification.

On the other hand, criterion functions represent a simpler approach to predict the possibility of porosity formation as a result of local thermal and solidification conditions.

2.8.1 Thermal Models

The Chvorinov rule [61] is the most widely used shrinkage prediction model due to its simplicity, based on estimating the feeding requirements by calculating the solidification time t of the casting:

$$t = \text{const} \left(\frac{v}{A} \right)^2 \quad \text{Eq. 2.13}$$

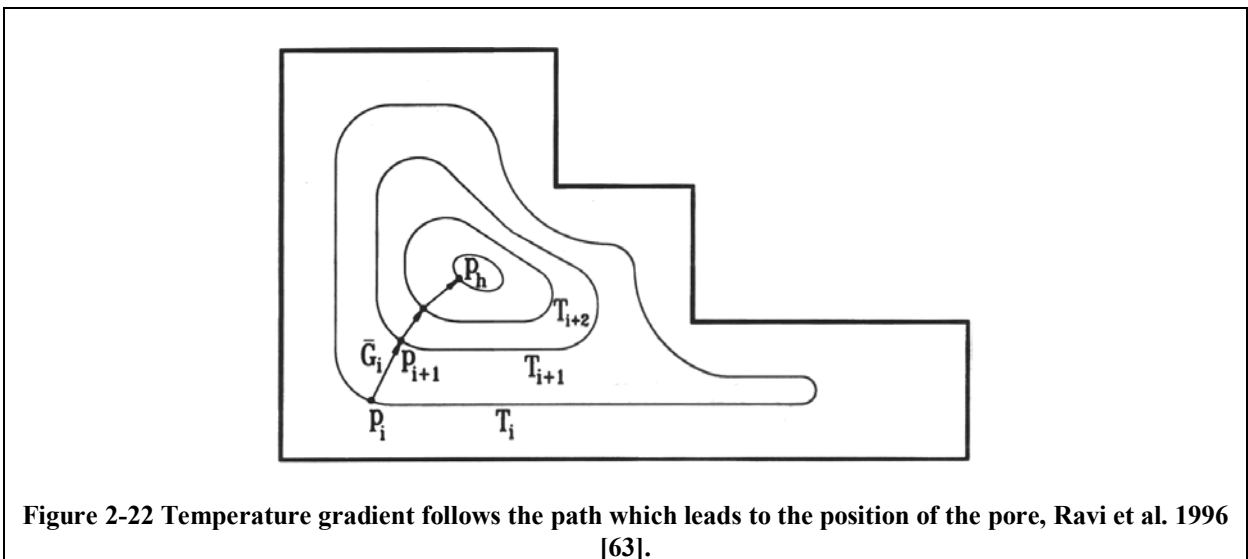
Where v is the casting volume and A is its cooling surface area.

A more intricate model was developed by Sigworth and Wang [62], to calculate the critical temperature gradient G_T^{cr} as a function of the angle of the feeding channel θ . Microshrinkage was expected when the temperature gradient was lower than a critical value:

$$G_T^{cr} \geq \left(1 + \frac{2\Delta T_{SL} k t}{\rho_S \Delta H_f l^2} \right) \frac{\rho_S \Delta H_f l}{4k t_c} \tan \theta \quad \text{Eq. 2.14}$$

Where ΔH_f is the heat of fusion, ΔT_{SL} is the solidification interval. The model combined the effect of solidification time t at the centre of the casting (a plate in the original experiments) with the physical properties of the cast alloy (the density of the solid phase ρ_S and the thermal conductivity k) along with the geometry of the casting (the thickness l).

Models that are mainly dependant on geometry provide easy and fast analysis for predicting shrinkage defects, especially in foundries (where numerical models which are strongly dependant on material properties are less commonly used). One geometry-dependant model for predicting porosity was proposed by Ravi et al. in 1996 [63]. Their main assumption was that the temperature gradient inside the casting part followed a path from points at the highest gradients to points at the lowest gradient, as illustrated in Figure 2.22.



Tracing the temperature gradient contour, the points of the highest temperatures and lowest values of temperature gradient determine the positions of hot spots, (see Figure 2.22).

The modulus of the regions surrounding these points is:

$$M_i = \frac{\sum_j V_{ij}}{\sum_j A_{ij}} \quad \text{Eq. 2.15}$$

The modulus vector for a two-dimensional section of the casting, g_{ij} , with area A_{ij} , is calculated using the following formula:

$$\vec{g}_{ij} = f_i \frac{3\beta}{2\pi} \frac{V_{ij}}{A_{ij}} (\vec{C}_{ijk} - \vec{p}_i) \quad \text{Eq. 2.16}$$

Where \vec{g}_{ij} is the modulus vector, f_i is the volume fraction of the region, \vec{C}_{ijk} and \vec{p}_i are position vectors of a point p_i , and β is a factor that represents the influence of casting parameters including the effects of cores and re-entrant corners and gating system design.

As an example of the commercial casting simulation software packages, FEEDERCALCTM is a 2-D modelling program that was originally developed by Foseco International plc. group [64] to provide a fast casting design tool for iron and steel castings. Calculations of the dimensions of the required feeder and the feeder neck along with the feeding distance were carried out by the program without the need for knowledge of the thermophysical properties of the alloy and the mould material or the heat transfer phenomena involved in the solidification process.

The SOLSTARTM solidification program was also developed by the same group, and was widely used in steel foundries during the 90's. The program predicted thermal history for each element based on heat exchange calculations for the nearest elements in 26 directions. Once the element reached a pre-set temperature value it transformed from liquid to solid, taking into

account density increase and volume loss due to liquid shrinkage. Metal flow in the liquid paths continually compensated for the volume loss until the last remaining liquid transformed into a solid and a shrinkage cavity was created.

Despite the simplicity of using an empirical rule based simulation, such as the SOLSTAR™ program, tracking the liquid element paths gives only a limited prediction of shrinkage porosity, compared to more sophisticated numerical-based software.

Mathematical equations for physical phenomena accompanied the casting and solidification process, heat transfer, fluid flow and stress analysis, are solved numerically to predict thermal history and shrinkage porosity, some examples of which are given in the following sections.

2.8.2 Thermal/Volume Models

Advanced models were proposed to predict the shape of the shrinkage porosity by solving the heat transfer equation along with the mass conservation to calculate the change in volume due to solidification contraction.

$$\Delta v = \beta v \Delta f_L \quad \text{Eq. 2.17}$$

Where v is the initial volume of the element, Δf_L is the fluid fraction, and β is the shrinkage ratio;

$$\beta = \frac{\rho_s - \rho_L}{\rho_L} \quad \text{Eq. 2.18}$$

Moreover, Beech et al. [65] improved the thermal/volume model by considering the solidification contraction of the isolated liquid for each region and the change of volume, Δv , due to this contraction was calculated as:

$$\Delta v = \beta v_o f_s F \quad \text{Eq. 2.19}$$

Where the volume element contains a volume of solid fraction (f_s) and a volume of liquid (F).

A more recent model was developed in 2005 by Battaglia et al. [66], where both heat and mass transfer equations were coupled in a FEM model to predict the microporosity in an Al-Si alloy. The energy balance equation represented the change of enthalpy with distance and time in both casting and mould material domains:

$$x \in V_1 \quad \frac{\partial H_1(x,t)}{\partial t} = \nabla \cdot (D_1(H_1) \nabla (H_1(x,t))) \quad \text{Eq. 2.20}$$

$$x \in V_2 \quad \frac{\partial H_2(x,t)}{\partial t} = \nabla \cdot (D_2(H_2) \nabla (H_2(x,t))) \quad \text{Eq. 2.21}$$

Where H_1 = the enthalpy of the casting (of volume V_1), and H_2 = the enthalpy of the mould, (of volume V_2).

They suggested that liquid movement, in the direction of the liquid pressure drop, caused volumetric changes due to contraction, and consequently the pressure drop due to movement of the liquid mass could be described by the following equation:

$$\Delta P = -B \frac{\Delta v}{v} \quad \text{Eq. 2. 22-a}$$

Where B is the Bulk modulus of the alloy.

In addition, the velocity of the liquid phase was deduced from the relationship between the semi-solid permeability K and the liquid dynamic viscosity μ according to the Darcy's law:

$$Q = \frac{-KA}{\mu} \frac{\Delta P}{L} \quad \text{Eq. 2. 22-b}$$

From Equation 2.22 (a) and (b) the velocity of the liquid phase was written as follows:

$$U_1 = \frac{-K}{g_l \mu_l} (\nabla P - \rho_l g) \quad \text{Eq. 2. 22-c}$$

From these relationships a formula that expressed the volume fraction of the shrinkage defects was produced in terms of the volume fractions of the liquid and solid phases plus the physical properties of the alloy:

$$\frac{\partial g_p}{\partial t} = -\beta \frac{\partial g_l}{\partial t} + \frac{\rho_l}{\rho_s} \nabla \cdot (g_l U_1) \quad \text{Eq. 2.23}$$

Another energy-flow coupled model was developed by Zhian Xu et al. [67] to predict internal shrinkage porosity as well as surface connected defects, such as depressed and caved surfaces. The solution of the conservation mass, momentum and energy equations is dependant on both the critical pressure and the solid fraction, where the enthalpy H is written in terms of solid fraction as follows:

$$H = \int_{T_o}^T C_p dT + (1 - f_s)L \quad \text{Eq. 2.24}$$

Where L is the latent heat.

In addition, the model determines the free surface between air and metal by tracking the fluid function element F , where $F=0$ when the element is empty, $F = 1$ when the element is completely filled and a partially filled element ($0 < F < 1$) represents the free surface element.

2.8.3 Gas Segregation Models

In alternative approaches, microporosity prediction models are based on solving heat and mass transport equations coupled with the role of gas segregation in the nucleation and growth of microporosity. Mainly, the pressure balance equation 2.11 is used to calculate the pressure required to create the pore, as discussed in section 2.7.3.

The pressure (P_g) is accumulated in the mushy zone by gas segregation, P_g (of a diatomic gas) is given in terms of an initial concentration of dissolved gas in the liquid phase V_i and the distribution coefficient of gas between solid and liquid phases K ($K=K_s/K_l$) by the following equation [68]:

$$P_g = \left[\frac{V_i}{K_L [f_L (1 - K) + K]} \right]^2 \quad \text{Eq. 2.25}$$

The change of the Free Energy of the pore formation was given by Kubo and Pehlke [62], where they suggested the formation of pores at the root of the secondary dendrite arm. They claimed that the effect of surface energy, γ , of the interfaces between the solid/gas and gas/liquid phases is reduced by the solid/ liquid interface which adds a negative value to the surface energy of the pore formation, making the homogeneous nucleation of pores possible:

$$\Delta G = v(P_G - P_{mush}) + A_{SG}\gamma_{SG} + A_{LG}\gamma_{LG} - A_{SG}\gamma_{SL} \quad \text{Eq. 2.26}$$

Where v is the volume of a pore, A_{SG} , A_{LG} are the area of the solid/gas and liquid/gas interfaces, respectively.

In the case of homogeneous nucleation of a gas bubble in a pure solidifying molten metal, three phases, (liquid, solid and gas), are in contact with each other, this can be described by the Young's equation [69], which described the angle of the three-phase contact point, (θ) as follows;

$$\gamma_{SG} = \gamma_{SL} + \gamma_{LG}\text{Cos}\theta \quad \text{Eq. 2.27}$$

By substituting for γ_{SL} in Equation 2.28, then the free energy required for pore formation ΔG becomes:

$$\Delta G = v\Delta P + A_{LG}\gamma_{LG} + A_{SG}[\gamma_{LG}\text{Cos}\theta] \quad \text{Eq.2.28}$$

A strong cohesion between liquid and solid phase of the same metal is expected, (i.e. dendrites in contact with liquid metal), which means complete wetting and a contact angle $\theta = 0$, and hence $\text{Cos}\theta = 1$, and in the case of a partially wetted interface, with a wetting angle $0 < \theta < 90$, the last term in the right hand side of Equation 2.28 is always positive. Therefore, the surface tension γ_{SL} at a solid/liquid interface is expected to increase the free energy of the bubble formation.

Accordingly, and in contrast to the assumption made by Kubo and Pehlke, the addition of surface tension due to the formation of a solid/liquid interface increases the value of the

negative pressure required to form a gas bubble homogeneously, which agrees with Campbell's argument about the difficulty of homogeneous nucleation of gas porosity.

Sung et al. [70] developed a model to predict microshrinkage porosity in steel castings by solving the conservation equations of mass, energy and momentum for all of the alloy components and the dissolved gases. Firstly, the continuity equation is given in terms of solidification shrinkage β :

$$\nabla \cdot u = \beta \frac{\partial \phi}{\partial t} \quad \text{Eq. 2.29}$$

Where u is the pore velocity and $\frac{\partial \phi}{\partial t}$ is the change in liquid volume fraction with time.

By considering the mushy zone as a porous medium, a momentum model was developed based on the assumptions that solid state diffusion takes place only for interstitially dissolved elements, namely C, H and N, and the local liquidus temperature was a function of the concentration, and any undercooling was ignored.

2.8.4 Stress Analysis and Plastic Deformation Models

The effect of casting deformation upon solidification on the size and distribution of porosity is considered in stress analysis porosity prediction models. In volume-averaged models three phases in a porous medium were considered in the analysis (solid, liquid and porosity), while in stress-analysis models the porosity phase (g_p) was split into shrinkage and deformation, and was written as:

$$g_p = g_{p.sh} + g_{p.d} \quad \text{Eq. 2.30}$$

Where $g_{p.sh}$ and $g_{p.d}$ represent the shrinkage porosity and deformation respectively [71].

The deformation porosity term can be obtained by integrating the plastic strain of a viscous medium over a range of time (t) which starts when the feeding flow stops at the end of the solidification time t_f , as follows;

$$g_{p,d} = \int_{t_f}^t g_s \varepsilon_s^{vp} dt \quad \text{Eq. 2.31}$$

Where ε_s^{vp} is the visco-plastic strain.

The model predicted centreline porosity as well as hot spot porosity and its results were in good agreement with the results obtained experimentally in steel sand casting experiments. However, the researchers drew attention to the importance of investigating the expected mechanical strains of the mould which can affect the plastic deformation of the casting. In addition, the high temperature mechanical properties of the casting alloy are crucial to obtain reliable model results.

2.9 Prediction of Shrinkage Porosity by Niyama and other Criteria Functions

The Niyama criterion is a well known criterion used in several casting simulation software for prediction of shrinkage. The Niyama criterion (N) was developed by Niyama et al. in 1981 [72], when they carried out several casting trials and defect inspections of different sized plates of carbon steel castings. The principles of their criterion were discussed in terms of shrinkage porosity formation as a result of both temperature and pressure drop in the mushy zone at late stages of solidification, and the governing equation was given as follows:

$$\int_{P_{cr}}^{P_{liq}} dP = \Delta P_{cr} = \int_{x_{cr}}^0 \frac{\mu_l \beta L g_l}{KG} dx = \int_{T_{cr}}^{T_{liq}} \frac{\mu_l \beta L g_l}{KG} \frac{dx}{dT} dT = \frac{\mu_l \beta L}{G^2} \int_{g_{l,cr}}^1 \frac{g_l dL}{K d g_l} \quad \text{Eq. 2.32}$$

Where P_{cr} is the critical pressure at the critical temperature T_{cr} and the position x_{cr} at which pores start to form, G is the temperature gradient and L is the cooling rate:

The criterion, N_c , was then defined by local thermal parameters:

$$Nc = \frac{G}{\sqrt{L}} \quad \text{Eq. 2.33}$$

The critical value of Nc gives an indication of local thermal gradient and cooling rate below which shrinkage porosity or centreline shrinkage is to be expected.

Carlson and Beckermann [73] developed a dimensionless form of the Niyama criterion, by introducing into the pressure drop equation a dimensionless temperature factor (θ), which represented the temperature drop at the end of solidification (9):

$$\theta = \frac{T - T_{sol}}{T_{liq} - T_{sol}} \quad \text{Eq. 2.34}$$

Where T_{sol} is the solidus temperature and T_{liq} is the liquidus temperature. The dimensionless Niyama criterion was given by the following equation:

$$N_Y^* = \frac{N_Y}{\sqrt{\mu_l \beta \Delta T_f / \Delta P_{cr} / \lambda_2}} = \sqrt{I(g_{l,cr})} \quad \text{Eq. 2.35}$$

Where $\lambda_2 = C L^{-1/3}$, which is the secondary dendrite arm spacing, calculated in terms of the cooling rate L and a material constant C . And, g_l is the fraction of solid, β is the solidification shrinkage, and ΔP_{cr} is the critical pressure drop at which porosity begins to form.

Equation 2.35 indicates that the dimensionless Niyama criterion takes into account the solidification characteristics and properties of the casting alloy in addition to thermal parameters.

However, in a critical discussion of the dimensionless Niyama criterion, Sigworth [74] raised some important points. Firstly, the Niyama criterion was developed based on a pressure drop model and ignored the contribution of other shrinkage mechanisms, particularly the role of dissolved gases. Sigworth suggested that a geometric model could be more suitable to describe the results obtained by the Niyama criterion and the dimensionless Niyama criterion.

The geometric model suggested that liquid feeding stops when the tapered angle, (θ), of a liquid stream is smaller than a critical value, as illustrated in Figure 2.23.

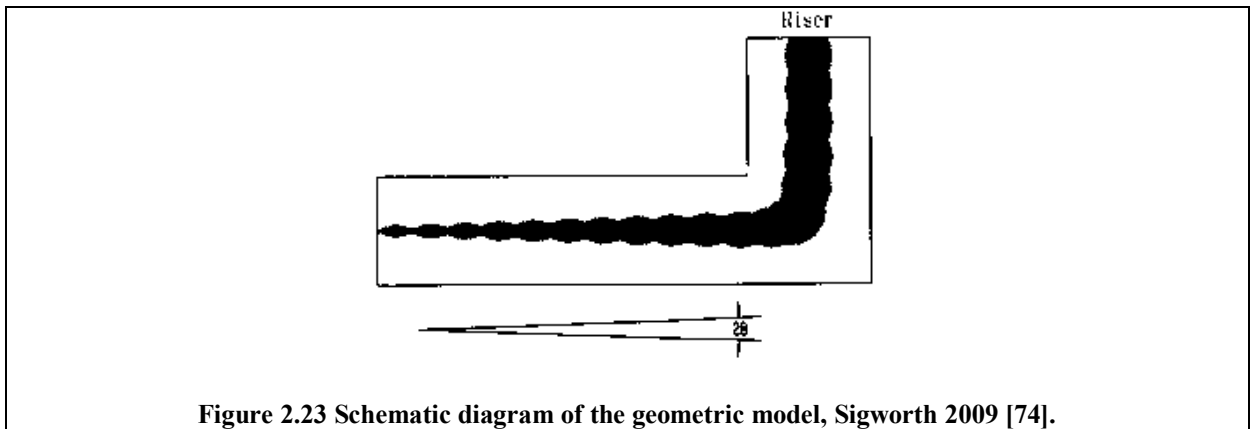


Figure 2.23 Schematic diagram of the geometric model, Sigworth 2009 [74].

Nonetheless, the proposed geometric model ignored the effect of the pressure drop in the mushy zone and the effect of solidification features on porosity formation mechanism, (such as the effect of temperature dependent solid fraction), while the modified dimensionless Niyama criterion takes into account the dendrite arm spacing and the amount of eutectic [75].

Several studies have been conducted to investigate the validity of the Niyama criterion to predict shrinkage in different alloys and different casting geometries.

Hardin et al. [76, 77] investigated the critical value of the Niyama criterion in a steel plate casting, and concluded, from several casting trials and x-ray inspection, that N was lower than the proposed value by Niyama, ($N_c = 0.775 \text{ K}^{1/2}\text{s}^{1/2}\text{mm}^{-1}$ in horizontal plates), and it could be as low as $0.1 (\text{K}^{1/2}\text{s}^{1/2}\text{mm}^{-1})$. They suggested two reasons for this shift of values, the accuracy of the data being used in the model, such as the value of the superheat, and secondly, physical phenomena during solidification that were not considered in the Niyama criterion, such as the role of dissolved gases and non-metallic inclusions in the formation of porosity.

On the other hand, Carlson and Beckermann [78] carried out casting experiments and investment casting simulation modelling, combined with metallographic analysis, of high Ni-

steel and Ni-based alloys. Their results showed that macroshrinkage pores were detected at positions with the lowest Niyama function (N_{Ymacro}) while microshrinkage porosity was predicted by higher values of the Niyama function (N_{Ymicro}). Above $N_{Ymicro} = 2 \text{ K}^{1/2}\text{s}^{1/2}\text{mm}^{-1}$, a sound position of the casting was expected.

Moreover, the validity of the Niyama criterion to predict shrinkage in Al alloys was also investigated. Liotti et al. [79] studied the prediction of porosity in plates and cylindrical shapes of Al-Si7-Mg alloy, and claimed that, although there was a general agreement between the measured porosity and the porosity predicted by Niyama, in the centre of the test bars, the values of porosity were underestimated, by using a limiting value of $N = 0.25-0.30$. However, this underestimation of porosity content was not evaluated, and hence the limiting value used in the Niyama criterion in Al alloy was not validated. Also, the model could not predict differences in porosity content due to different feeding systems.

The important restriction of applying Niyama criterion in Al alloys is the gas content, as the quantity of porosity was found to increase as the amount of gas in the melt increases, without influencing thermal variables [80].

In agreement with this, Spittle et al. [81] showed that thermal variables and solidification parameters are interrelated and their influences on porosity formation cannot be separated in numerical functions for predicting porosity. Thus, they suggested that numerical functions that predict porosity by thermal variables, like the Niyama criterion, should be used only in limited conditions of directional solidification.

While the Niyama criterion was originally developed for porosity prediction in short freezing alloys like steel, the Feeding Resistance Number (FRN), developed by Suri et al. [82], was developed as a general criterion that accounts for the solidification characteristics which affect porosity in long freezing range alloys based on the fact that the resistance to feeding exerted

in the mushy zone depends on macrostructural characteristics. The FRN (denoted as C_o in the original research paper) was given in terms of solidification characteristics in addition to thermal parameters, namely, the freezing range of the alloy ΔT , the liquid density ρ_l , the liquid viscosity μ , the solidification shrinkage β , the velocity of the solidification front V_s , the temperature gradient G and a characteristic length of the grains D :

$$FRN = \frac{N\mu\Delta T}{\rho_l G V_s \beta D^2} \quad \text{Eq. 2.36}$$

Where the characteristic length D is the primary arm spacing in the case of a columnar structure or the equiaxed grain size. The FRN signifies the resistance to feeding in the mushy zone, which indirectly represents the pressure drop and consequently the formation of porosity.

However, the solidification fraction in the feeding path was not considered in the FRN criterion, and hence the feeding path was assumed to be open throughout the solidification process, which is obviously not true.

On the contrary, the Fraction Solid in the Feeder (FSF) [83], is another criterion that represented a correlation between the quantity of porosity and the fraction solid in the feeder at the last stages of solidification.

Lee et al. [83] developed another thermal-based criterion, the feeding efficiency parameter, denoted LCC, $(G.t^{2/3})/V_s$, which included the effect of solidification time along with solidus velocity in addition to the temperature gradient. It was based on interdendritic feeding as analysed by Darcy's Law, and showed that porosity increases with increasing solidus velocity, and reaches a finite high value at which high pressure drop can cause the solid surface to deform plastically, as shown in Figure 2.24.

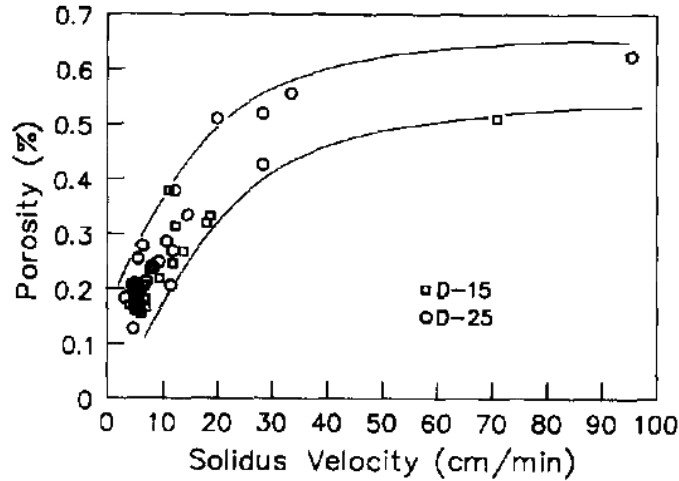


Figure 2-24 Relation between solidus velocity and local porosity in Al-7Si-0.3Mg alloy Lee et al. 1990 [83].

A criterion was recently proposed in 2011, and denoted, after its developers' initials (BLJ); (Böttger, Laqua, Jakumeit); [84].

A geometrical factor (f_{geo}) was introduced into the pressure drop equation, representing the ratio between the volume of the region in need of feeding ($V_{consuming}$) to the volume of the liquid available for feeding ($V_{feeding}$), Figure 2.25 shows a schematic representation of the f_{geo} factor.

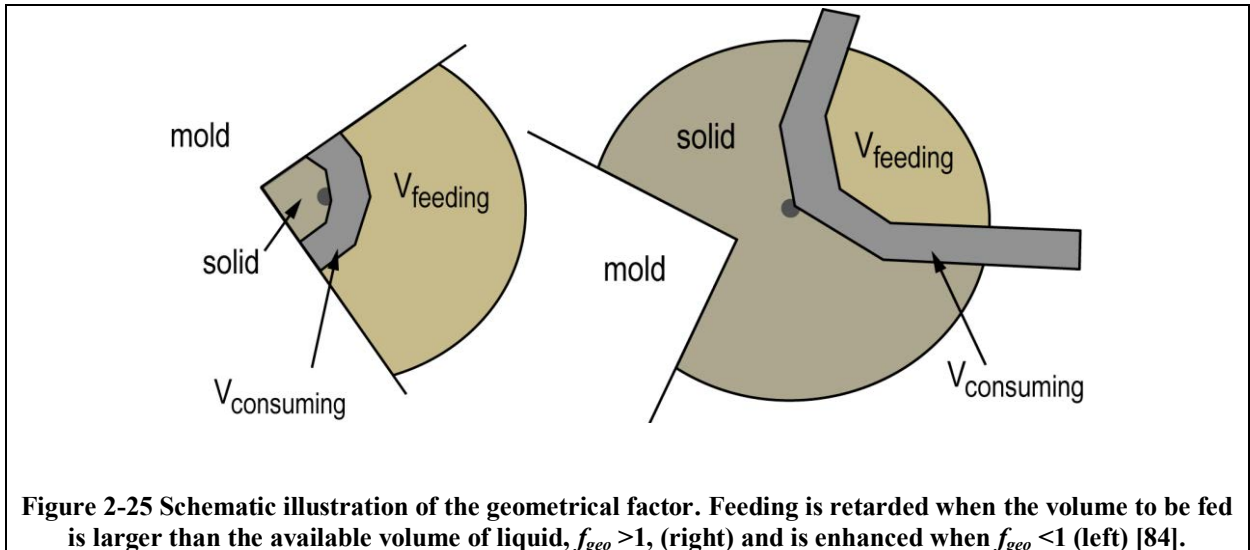
$$f_{geo} = F_{norm} \left(\frac{V_{consuming}}{V_{feeding}} \right) \quad \text{Eq. 2.37}$$

The pressure drop in the mushy zone was expressed by the following equation:

$$\Delta P_{mushy} = f_{geo} \cdot 180 \frac{\mu_l \beta \dot{T}}{\lambda_2^2 G^2} \int_{T_{crit}}^{T_{liq}} \frac{(1 - g_l)^2}{g_l^2} dT \quad \text{Eq. 2.38}$$

Where T_{crit} is the temperature at the critical solidification stage, \dot{T} is the cooling rate, and F_{norm} is a normalizing factor to account for a planer solidification front when $f_{geo} = 1$.

Hence the pressure drop can predict hot spots as well as shrinkage porosity depending on the geometrical factor at the position of the solidification front.



2.10 Prediction of Shrinkage Porosity in Ti-Based Alloys

Shrinkage porosity, particularly interdendritic layer porosity, is a serious problem in titanium aluminide castings [85-87]. Aiming to avoid these defects, numerical modelling is used to simulate solidification and cooling processes, and hence thermal and solidification factors are computed, and the output can be in the form of criteria functions that relate these parameters to shrinkage and porosity [88].

Although a useful tool to predict shrinkage, criterion functions neglect important factors involved in the formation of porosity, like gas content and alloy type [89, 90]. However, most of the casting-simulation software compute Niyama criterion functions to predict shrinkage defects in both ferrous and non-ferrous alloys.

Although, the validity of Niyama criterion applied to titanium aluminide investment castings has not been investigated thoroughly. Nevertheless, limited studies [91, 92] have been conducted in this area. It was claimed that shrinkage porosity in Ti-47Al-2Cr-2Nb can be predicted by the Niyama criterion with a threshold value in the range of 2.4 to $3.67 (\text{°C} \cdot \text{min})^{0.5} \text{cm}^{-1}$.

2.11 Determination of the Interfacial Heat Transfer Coefficient

A successful numerical model depends on the accuracy of the boundary conditions assigned to simulate the conditions of the casting process, in conjunction with the reliability of thermophysical properties of the metal and the mould material [93].

The inverse method depends mainly on using a set of precisely measured thermal data, initial conditions, a geometry of the casting and a measured thermal history during an experimental casting process, all of which are used as inputs in a modelling program, to calculate an unknown boundary condition, such as a temperature, heat flux, interface heat transfer coefficient or thermophysical properties of the casting alloy or mould materials [94].

This is based on the conservation of energy, written in the following form:

$$\rho \frac{\partial H}{\partial T} \frac{\partial T}{\partial t} - \nabla[k\nabla T] - S(r) = 0.0 \quad \text{Eq. 2.39}$$

Where k is thermal conductivity and $S(r)$ is a source of energy (the latent heat of fusion) and H is the enthalpy of solidification. The unknown temperature at the interface is calculated by solving the heat flow equation. The one dimensional heat flow equation, is written as follows:

$$C(T) \frac{\partial T}{\partial t} = \frac{\partial}{\partial x} \left(k(T) \frac{\partial T}{\partial x} \right) \quad \text{Eq. 2.40}$$

Where $C(T)$ consists of temperature dependant properties of the material, such as density, specific heat capacity, and thermal conductivity. By substituting known boundary conditions at $x=0$ and $x=L$ and representing the Equation 2.40 in the form of a matrix as:

$$[A]\{T^{n+1}\} = \{R_1(q_o^{n+1})\} + \{R_2(q_o^n)\} + \{R_3(T^n)\} \quad \text{Eq. 2.41}$$

The measured values T^n , q_o^n are known at the current time step t , and the relation between these values and T^{n+1} , q_o^{n+1} at the next time step is calculated. Subsequently, the heat flux at the interface can be deduced as $q(t)$ and used to calculate the interface heat transfer coefficient, h .

$$h = \frac{q(t)}{T_{metal} - T_{mould}} \quad \text{Eq. 2.42}$$

Where T_{metal} is the temperature of the casting surface at the interface and T_{mould} is the temperature of the mould surface at the interface.

In another approach, known as Beck's non-linear solution of the inverse heat conduction problem, [95], an unknown initial value of q is assumed, and hence the temperature distribution T_{est} according to this q is calculated and the difference between the estimated temperature and the measured temperature at the end of the time interval t is calculated for a certain number of iterations by a Finite Element Method (FEM) solver until a minimum difference between T_{est} and T_{mea} is reached. This determines the objective function $F(q)$ in the equation :

$$F(q) = \sum_{l=1}^I (T_{est} - T_{mea})^2 \quad \text{Eq. 2.43}$$

The sensitivity coefficient ϕ is a function of the increments of the assumed q in each iteration, and the new q is calculated as:

$$\nabla q = \frac{\sum_{i=1}^I (T_{mea} - T_{est}) \phi_i}{\sum_{i=1}^I (\phi_i)^2} \quad \text{Eq. 2.44}$$

$$q(\text{corrected}) = q(\text{old}) + \nabla q \quad \text{Eq. 2.45}$$

The corrected q replaces the initial (assumed) q and the process repeated until the ratio between them reaches a preset value. Subsequently, the temperature distribution of both the casting and the mould at the interface can be calculated using the calculated heat flux q at the interface. Finally, the interfacial heat transfer coefficient, h , is calculated using equation 2.42 divided by the area of the heat flow.

O'Mahoney et al. [96] calculated the interfacial heat transfer coefficient in investment casting for pure Al and for different freezing range Al alloys, by calculating the temperature drop at the casting/mould interface through an inverse process by combining integral and derivative methods. They showed that the influence of the metallostatic head on the interfacial heat transfer coefficient is dependent on the freezing range of the casting alloy, where higher metallostatic pressure head improves the contact between the metal and mould surfaces and in turn results in an increment in the rate of heat transferred into the mould during solidification of long freezing range alloys which is not significant in the case of short freezing range alloys.

On the other hand, Woodbury et al. [97] calculated the interfacial heat transfer coefficient of Al-based alloys in sand casting, as a function of time, and the results demonstrated that h depends on the size of the solidifying casting.

In a more recent study of the interfacial heat transfer coefficient between an Al alloy and a sand mould [98], the Beck's inverse method to calculate h was compared with a "lump capacitance" method, which assumes that both the solidifying metal and the mould material are treated as one system, and hence the heat released from the solidifying metal equals the heat received by the mould material under assumed steady state conditions.

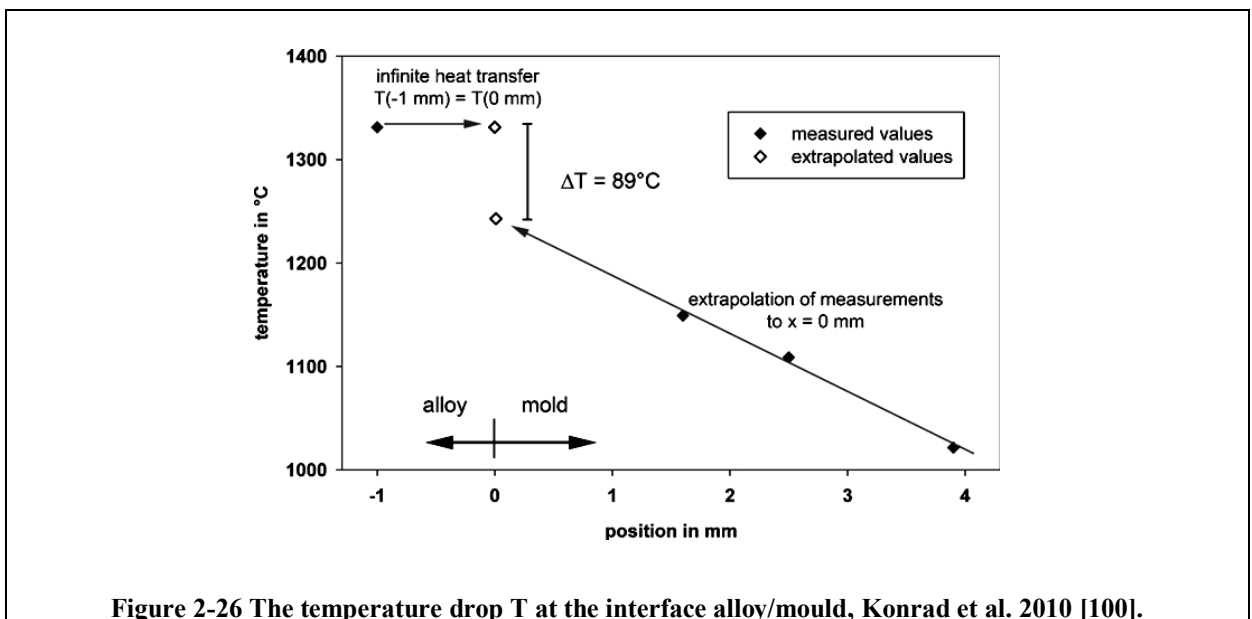
$$q_{metal} = \rho \frac{V}{A} \left[-C_p \frac{dT}{dt} + L_f \frac{df_s}{dt} \right] \quad \text{Eq. 2.46}$$

Where L_f is the latent heat, f_s is the fraction of solid, and V and A are the volume and surface area of the casting. The authors proposed a modification of the lump capacitance method by which the latent heat released during solidification was determined as a function of time by calculating the fraction of solid, which in turn is determined by the location of the liquid/solid interface with variation of time. Hence the interfacial heat transfer coefficient was calculated as a function of time and their results showed a good agreement between the two approaches.

Jin et al. [99] used the inverse method to compute the interfacial heat transfer coefficient during the investment casting of Ni-base single crystal. They reported that h as a function of temperature was $1000 \text{ W/m}^2\cdot\text{K}$, above the liquidus, and decreased to $500 \text{ W/m}^2\cdot\text{K}$ just below the solidus, then decreased further to approach $0 \text{ W/m}^2\cdot\text{K}$ at room temperature.

In another approach, using the assumption that the thermal conductivity of the ceramic mould is constant, Konrad et al. [100] determined the temperature at the mould side of the interface by extrapolating measured temperatures inside the mould, in order to calculate the temperature drop at the interface. They claimed that the temperature of the alloy was constant in the radial direction at any position in the casting, as shown in Figure 2.26. Hence they determined the heat flux at the interface and subsequently the interfacial heat transfer coefficient for Ni-base superalloy IN738LC that was investment cast. The maximum value found was $560 \text{ W/m}^2\cdot\text{K}$ for a cylindrical geometry.

Nonetheless, the assumption of constant temperature in the radial direction reflects a serious shortcoming as it contradicted the law of heat conduction (Fourier's Law) and consequently ignored the temperature gradient in the direction of heat flow from the solidifying casting and the mould material.



2.12 Heat Transfer Coefficient at the Metal/Mould Interface during Investment Casting Process

The process of heat transfer from a solidifying casting into its mould through the metal/ mould interface simultaneously coincides with heat transfer from the outer surface of the mould to the ambient atmosphere. This heat transfer involves one or more of the three heat transfer mechanisms, namely conduction, convection and radiation.

As mentioned earlier, investment casting of Ti alloys normally takes place in vacuum or under a pressure of an inert gas, typically Argon. The thermal conductivity of Argon is 0.0615 W/m. K at 1700 K [101]. Hence, conduction in an atmosphere of Argon can be ignored. Also, conduction will not occur in the case of casting in a vacuum.

Heat transfer by radiation is dependent on the shell temperature, which in turn is a function of time, and is determined by the following equation:

$$q_r = \varepsilon \sigma F (T_s^4 - T_r^4) \quad \text{Eq. 2.47}$$

where q_r is the radiation heat flux, ε is the emissivity of the mould material, σ is the Stefan-Boltzmann constant ($5.67 \times 10^{-8} \text{ W/m}^2 \cdot \text{K}^{-4}$), and T_s and T_r are the shell surface temperature and the ambient temperature, respectively. The effect of radiation on the rate of heat transfer from a ceramic mould surface is therefore expected to decrease with time as cooling continues.

Heat transfer by convection is expected to contribute more effectively than the radiation and conduction mechanisms, in the case of investment casting of Ti alloys, as a ceramic mould is being cooled in an atmosphere of argon. This is discussed in detail in Chapter 5.

O' Mahoney et al. [102, 103] measured cooling curves at two interior points of a ceramic test piece and used an inverse solution to determine the surface thermal profile and the surface heat flux using Fourier's law:

$$q_s = -k \frac{\partial T}{\partial r} \Big|_s \quad \text{Eq. 2.48}$$

Then the heat transfer coefficient between the mould surface and the ambient, $h_{ext}(T_s)$, was calculated using the following equation:

$$h_{ext}(T_s) = \frac{q_s}{T_s - T_{amb}} \quad \text{Eq. 2.49}$$

By using another approach, Hendricks et al. [104] assumed that heat is transferred through the shell depending on a “thermal transfer property” of that shell. Likewise gas can flow through the shell depending on the shell permeability, so the permeability equation was applied to determine the thermal transfer coefficient.

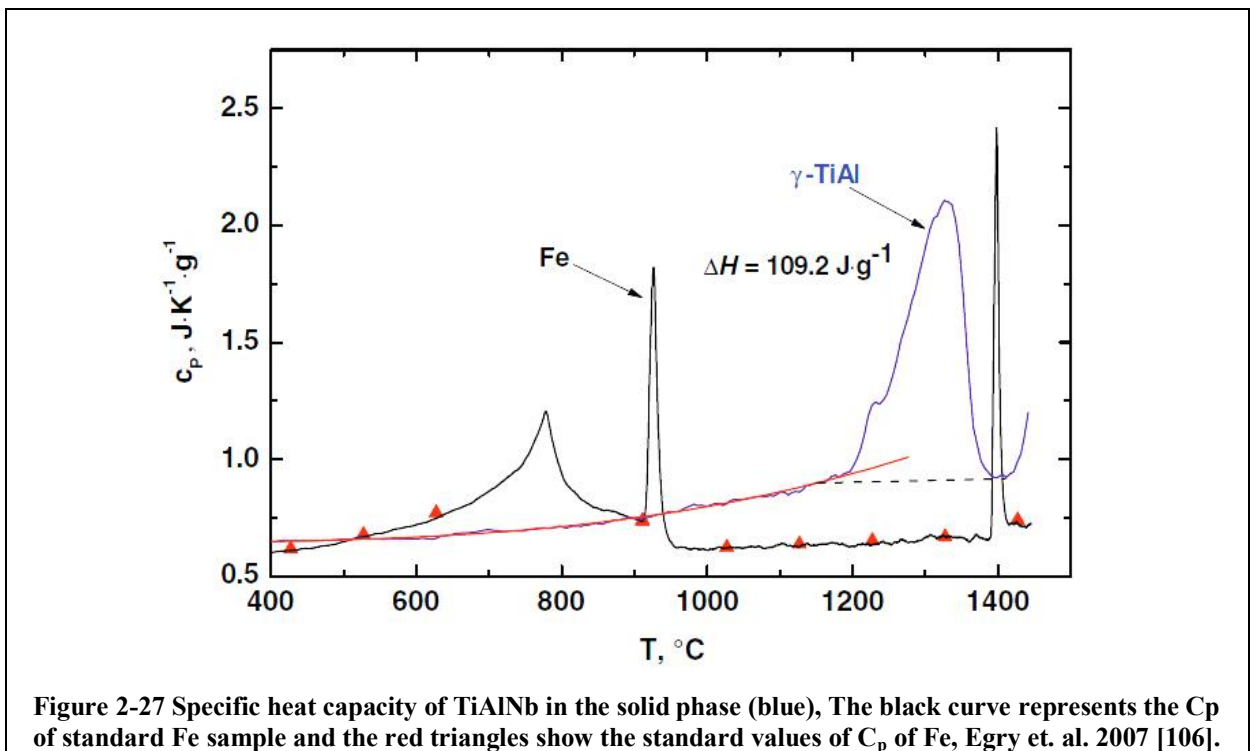
$$h_{ext} = \frac{D(dT/dt)}{(T_j - T_e)A} \quad \text{Eq. 2.50}$$

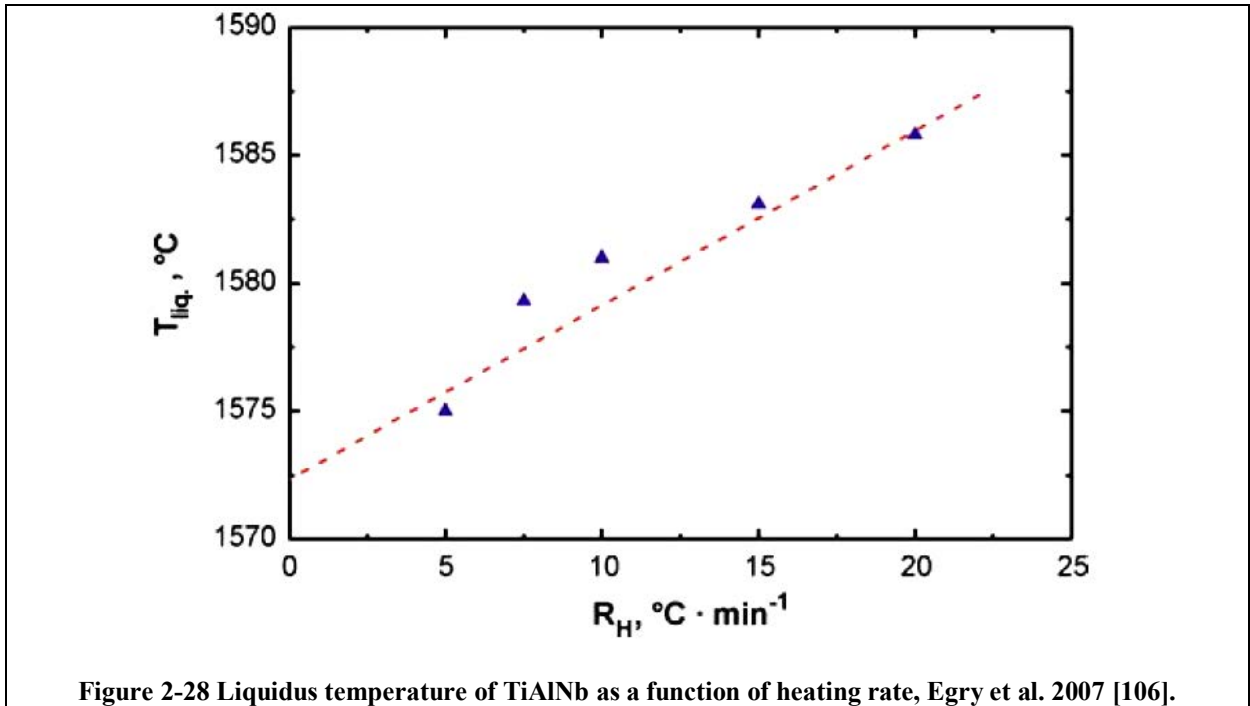
Where h_{ext} is the thermal transfer coefficient, i.e. the external heat transfer coefficient, D is the shell thickness, T_j is the shell temperature, T_e is the external temperature and A is the surface area.

2.13 Thermophysical Properties of γ -TiAl Intermetallics

In 2004, the European Commission started the IMPRESS project “Intermetallic Materials Processing in Relation to Earth and Space Solidification” to study the solidification and properties of intermetallics [105, 106]. The project included directional solidification experiments and casting trials on earth and in space in order to study the effect of gravity conditions on microstructure, and to measure thermophysical properties of the intermetallics. As a part of the IMPRESS project, high temperature differential scanning calorimetry was used to measure the specific heat capacity (C_p) of TiAlNb. The C_p against temperature curve in the solid state was compared with the resultant curve of a standard Fe sample, as shown in Figure 2.27.

The enthalpy of fusion was also measured, and found to be 340.2 ± 3 J/g, and the solidus and liquidus temperatures were also reported to be, $T_s = 1500 \pm 5$ °C and $T_l = 1572.8 \pm 5$ °C. The liquidus temperature was a dependant on the rate of heating, as shown in Figure 2.28.



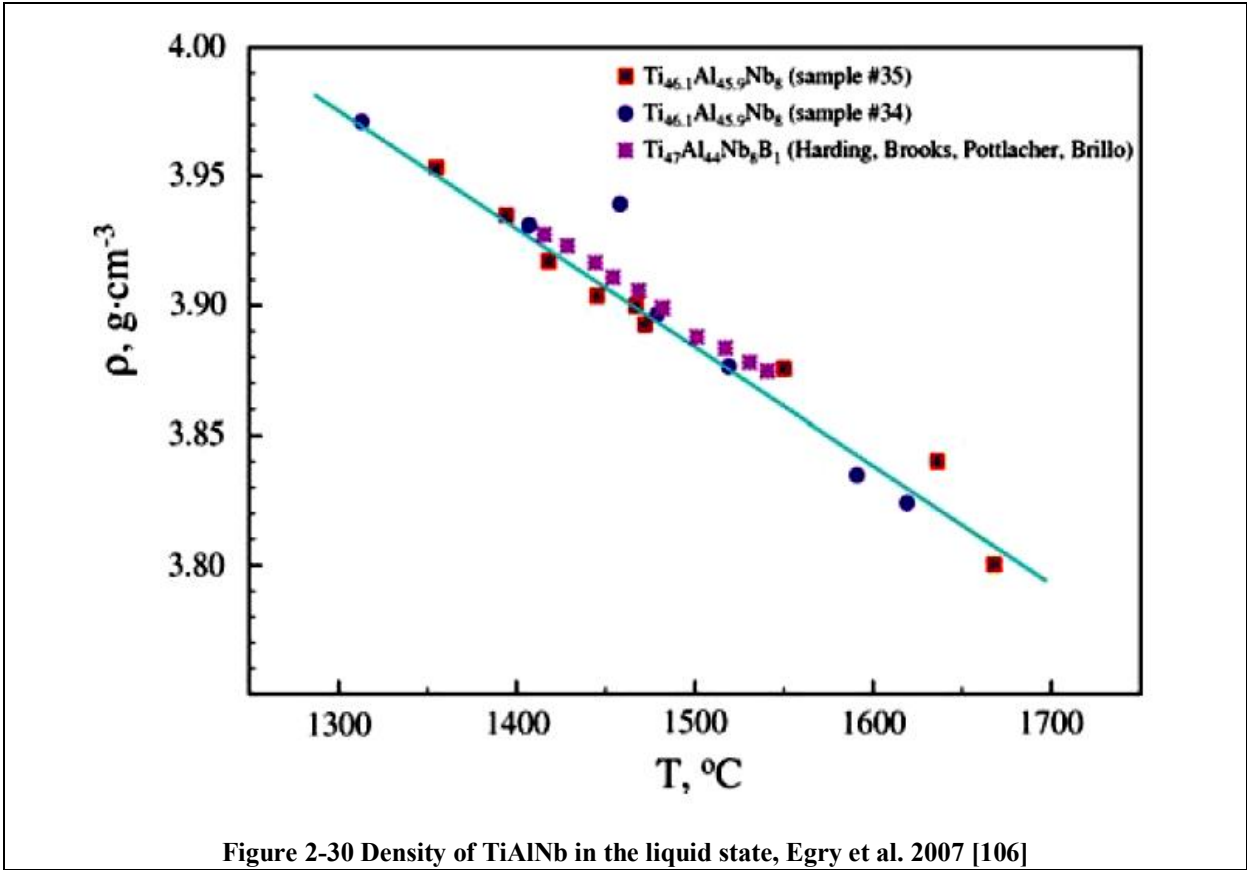
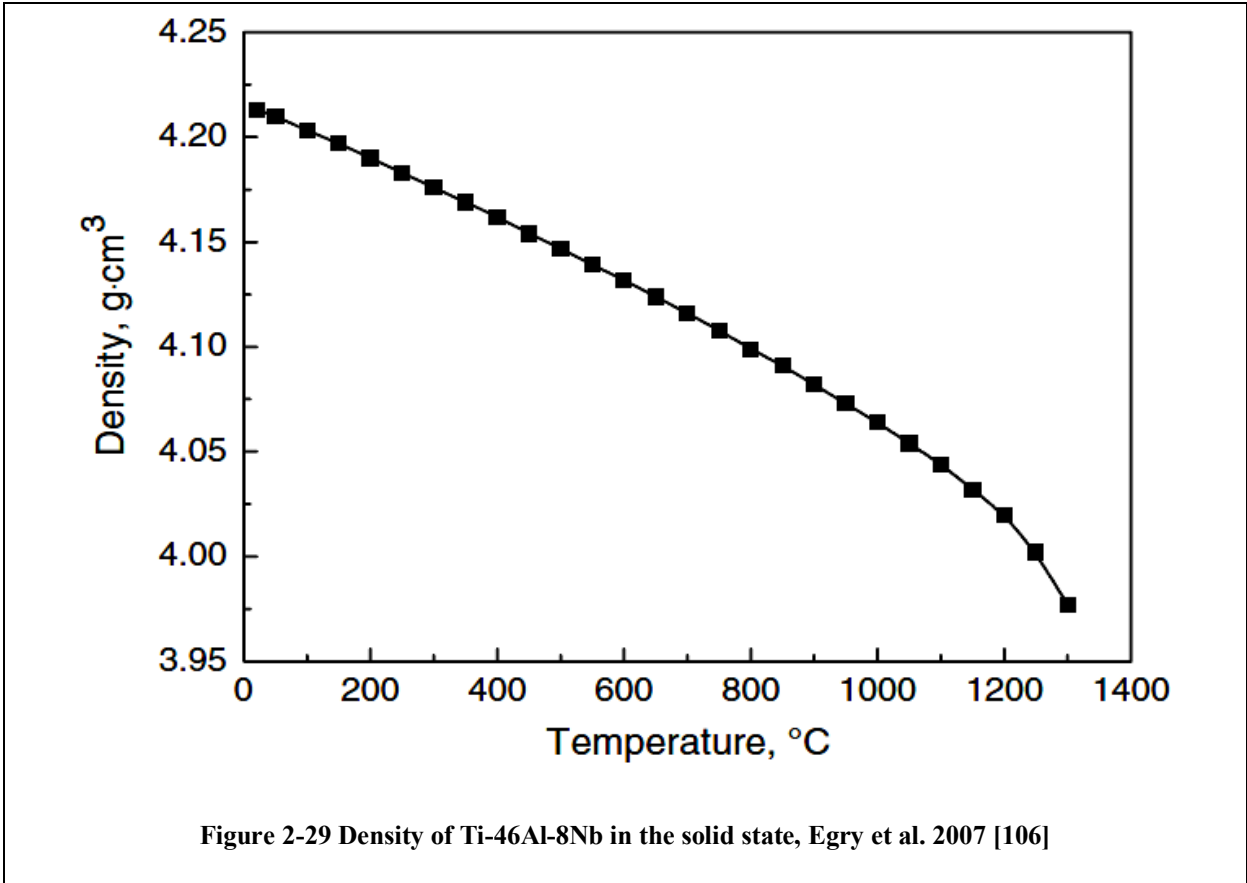


The Laser-Flash Diffusion method is used to measure thermal diffusivity of materials. One side of a plane-parallel sample is subjected to thermal energy from a laser source and the temperature rise on the other side of the sample is detected as a function of time. The faster the thermal energy is transmitted through the sample the higher its thermal diffusivity.

Thermal diffusivity, (α), of TiAlNb was measured by the Laser-Flash Diffusion method, and the results were fitted to a three order polynomial as:

$$\alpha = -3.01 \times 10^{-9} T^3 - 4.3 \times 10^{-7} T^2 + 5.18 \times 10^{-3} T + 5.36 \quad (20 \text{ }^\circ\text{C} < T < 1300 \text{ }^\circ\text{C}) \quad \text{Eq. 2.51}$$

The density of the intermetallic Ti-46Al-8Nb was determined by measuring its thermal expansion, (see Figure 2.29), while the Levitation Drop method was used to measure the density in the liquid state, (see Figure 2.30).



Cagran et al. [107], used a pulse-heating technique to measure specific enthalpy of the Ti-44Al-8Nb-1B alloy, where the liquid phase was obtained by passing a large current I through the samples. The voltage drop (U) was measured by two knife-edge probes and the radiation temperature was measured by a pyrometer. The specific enthalpy was then calculated by the following equation:

$$H - H_{(293)} = \frac{1}{m} \cdot \int I \cdot U \cdot dt \quad \text{Eq. 2.52}$$

where m is the mass of the sample

The differential scanning calorimeter (DSC) technique was also used to measure the specific heat, specific enthalpy, and the liquidus temperature, in which the amount of heat required when the test sample goes through a phase transformation process is compared with that amount of heat required to maintain the temperature of a reference sample, of a known heat capacity, at the same temperature of the test sample.

The measured values of enthalpy obtained by both techniques agreed well in the temperature range of 177 °C to 1227 °C, as shown in Figure 2.31

The enthalpy of fusion was determined as the difference between the enthalpy at the solidus and at the liquidus (as measured by the pulse-heating technique): $\Delta H = 411.5$ kJ/kg.

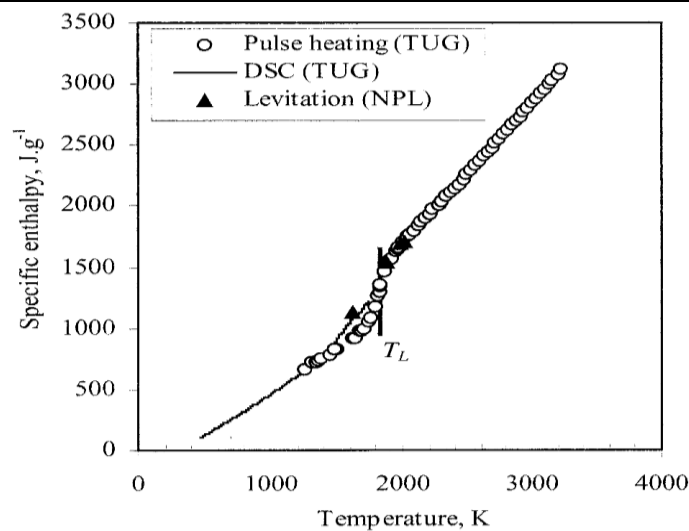


Figure 2-31 Specific enthalpy of Ti-44Al-8Nb-1B as a function of temperature, Cagran et al. 2003 [107]

2.14 Effect of Porosity on Mechanical Properties of Titanium-Alloy Castings

The unique combination of mechanical and corrosion properties of Ti-alloys make them attractive for a wide range of applications of different designs and sizes, for example, aerospace applications, medical and surgical applications, military and high temperature applications. Famous examples in high temperature applications of titanium aluminide investment castings are turbocharger rotors and turbine blades [108].

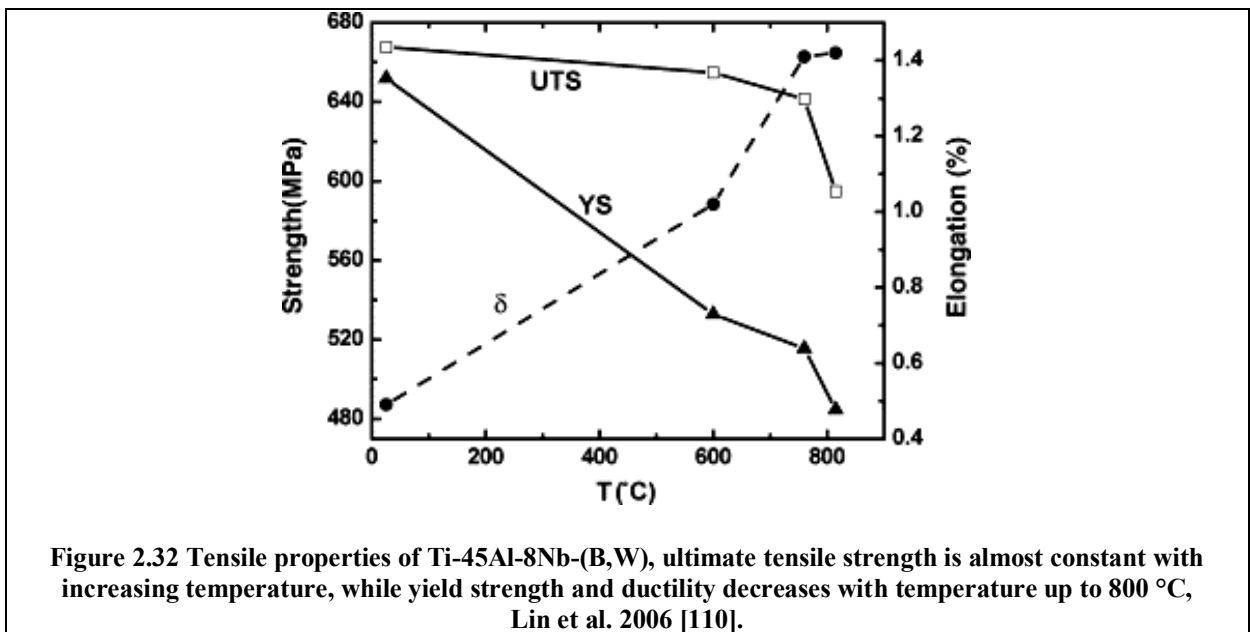
However, engineering applications require a good balance of various mechanical properties such as tensile strength, high temperature tensile strength, fatigue properties, high creep resistance for high temperature applications and high fracture toughness [109].

The as-cast tensile properties of TiAl alloys are generally low due to limited ductility at both room temperature and high temperature and the brittle-to-ductile transition temperature is higher than 815 °C [110]. However, it was found that the ultimate tensile strength of Ti-45Al-8Nb-(B,W) increases with temperature up to 800 °C, (see Figure 2.32), This was attributed to the fine lamellar as-cast structure and the strengthening effect of Nb on the interdendritic γ phase.

The effect of porosity on the tensile properties of castings has been studied in several research projects, and it has been reported that the yield stress can tolerate porosity of a certain level, which means that the ultimate tensile strength is not notably affected by the presence of porosity, while the ductility decreases significantly with the same level of porosity [111].

Not only the volume fraction of porosity, but also the distribution and geometry of the defect contribute to reducing the tensile strength and ductility of the casting; this is because the

region that contains porosity is assumed to yield first under an applied load and the strains are concentrated in this region having many defects [109].



A comparison made between different Ti alloys showed that fatigue cracks are more likely to initiate at the surface or subsurface casting-related pores [112].

Hot Isostatic Pressing “HIPping”, involves applying a high hydrostatic pressure of an inert gas, typically Argon, at an elevated temperature. For castings of Ti and its alloys, a Hipping pressure may be about 100 MPa, and the temperature in the range of 900 °C to 1150 °C [113]. The driving force for closing a spherical pore with a radius r , is determined by the applied pressure P and the surface energy of the pore γ , given by the following equation:

$$P = \frac{2\gamma}{r} \quad \text{Eq. 2.53}$$

HIPping is widely used in order to improve as-cast mechanical properties, especially tensile strength, by eliminating porosity, but it has also shown a limited effect on improving ductility [114, 115]. Moreover, HIPping may result in recrystallization of the interdendritic γ phase and a reduction in the volume fraction of the lamellar phases, which reduces the creep resistance of the γ -TiAl alloy [116].

2.15 Summary of Literature

Titanium alloys are classified according to their chemical composition into α , near α , β alloys and the titanium aluminide alloys. The phase diagram of the TiAl system shows several intermetallics for different Al content. The titanium aluminide alloys based on (γ TiAl and α_2 -Ti₃Al) structure, have a significant importance in several engineering applications, due to a combination of good mechanical and physical properties at elevated temperatures.

The as-cast microstructure of the titanium aluminide alloys is expected to contain a lamellar structure of ($\alpha_2+\gamma$), and a γ phase in the interdendritic regions, in which normal segregation is also found. The as-cast macrostructure also shows a Columnar-to-Equiaxed Transition feature.

Mechanisms of the CET have been explained by several theories, based on the role of constitutional undercooling and fragmentation of dendrite arms in the nucleation of equiaxed grains ahead of the columnar tips, and subsequently the equiaxed zone impedes further growth of the columnar grains. Several studies have shown that a shallow temperature gradient and low cooling rates encourage the CET to occur.

Due to the high reactivity of Ti alloys in the molten state they are melted by ISM and investment cast in a vacuum or under a pressure of argon gas. The low achievable superheat obtained can cause casting defects. Therefore, the effect of increasing the induction power and the effect of the pressure of the applied shielding gas on the resultant superheat have been investigated in several studies.

Feeding mechanisms during solidification are closely related to the formation of shrinkage porosity in castings. Microshrinkage porosity forms in the interdendritic gaps during the last stages of solidification, as a result of shrinkage and/or gas evolution in the remaining liquid.

The literature review highlighted the following gaps which required a further investigation and thus they are addressed in the current study:

- Titanium aluminide castings are prone to microshrinkage porosity. However, casting and solidification factors which contribute to the formation of shrinkage porosity in titanium aluminide castings have not yet been fully understood.
- Numerical models have been used to predict the location and size of shrinkage porosity in castings by creating complex thermal and thermal/fluid flow codes. Criterion functions, such as the Niyama criterion, represent a simpler approach to predict porosity as a result of local thermal and solidification conditions. However, the validity of applying the Niyama criterion to titanium aluminide investment castings has not been investigated thoroughly.
- Numerical modelling of the investment casting and solidification processes depends on the accuracy of the boundary conditions and the thermophysical properties of the metal and the mould material. However, the boundary conditions of investment casting of Ti alloys in argon gas and in vacuum have not yet been precisely determined.
- The work presented in this thesis investigates casting and solidification parameters of titanium aluminide alloy, which influence the formation of shrinkage defects. In addition to studying the relationship between the features of the as-cast macrostructure and the formation of shrinkage porosity in the investigated alloy.
- In addition to further investigation of thermal boundary conditions and the interfacial heat transfer coefficient in investment casting of titanium aluminide.
- Moreover, prediction of shrinkage defects in titanium aluminide alloys by using thermal-based criterion function, such as the Niyama criterion, is to be validated.

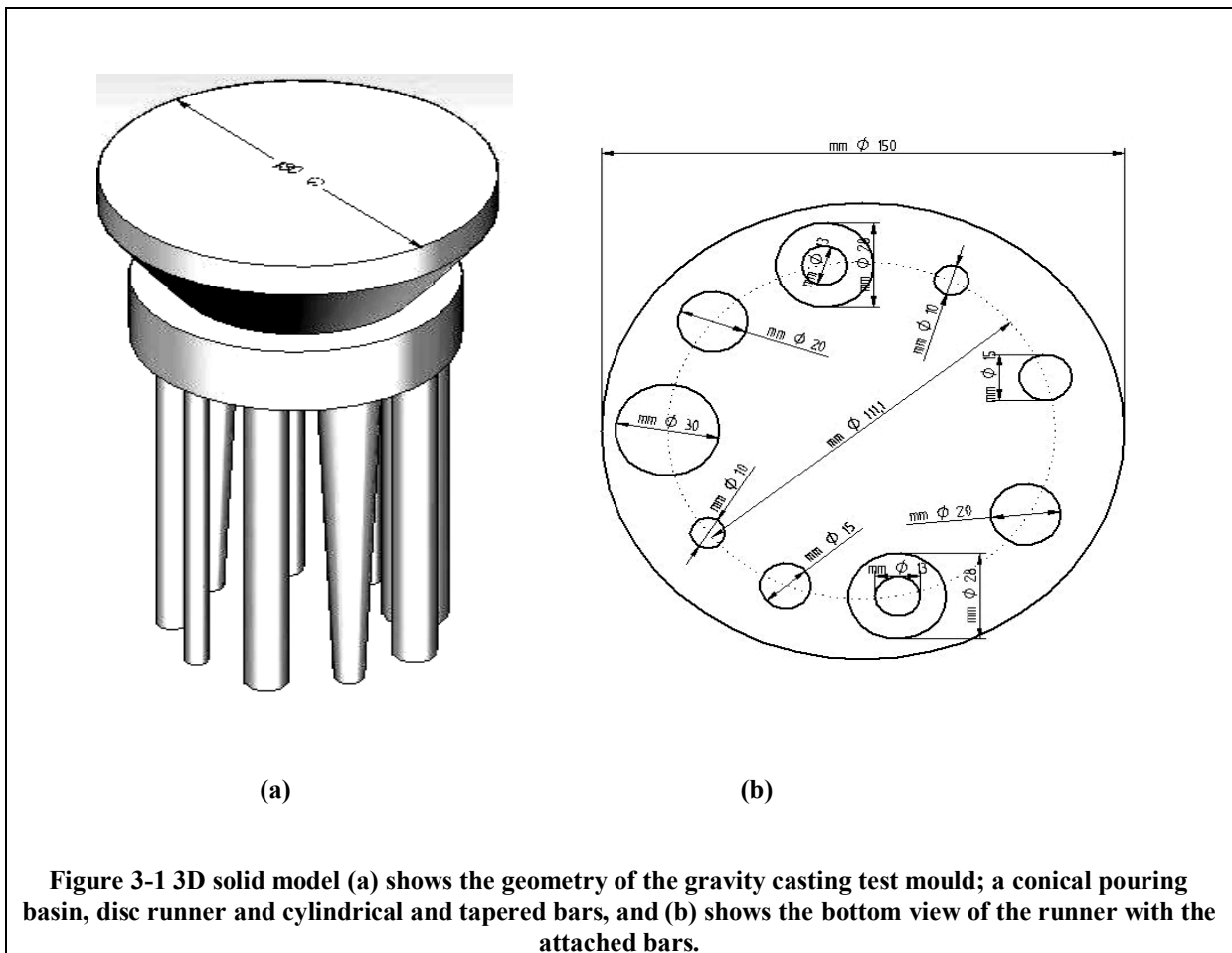
CHAPTER 3

EXPERIMENTAL METHODS

3.1 Gravity Casting of Commercial Purity Ti, Ti-6Al-4V and Ti-46Al-8Nb

3.1.1 Mould Design

Figure 3.1 shows the design of the gravity-cast mould which consisted of a conical pouring basin and a disc-shaped runner with an inner diameter of 150 mm. The following test bars were attached to the runner: seven cylindrical bars of 200 mm length with diameter of 10 mm (two bars), 15 mm (two bars), 20 mm (two bars) and 30 mm (one bar), in addition to two tapered bars with upper diameter of 28 mm and lower diameter of 13 mm.



3.1.2 Mould Preparation

The moulds were produced using the shell manufacture technique usually used in the investment casting process, as schematically illustrated in Figure 3.2. The wax patterns were made by injecting wax into metal dies which had the dimensions of the test bars. The wax bars were then assembled onto the wax pattern of the runner and the pouring basin.

The wax patterns of the moulds were then painted with a primary coat composed of non-reactive Yttria (99.9 % Y_2O_3 with a binder of hydroxypropyl methyl cellulose), then left to dry for 15 hours in moving air with a velocity of 0.1 m. s^{-1} . Consecutive coats were then applied by dipping into the slurry tank then rotating the mould under falling stucco. The slurry consisted of 200 mesh fused silica and 200 mesh Molochite filler in a Remet LP-BV binder. The stucco used for the second and third coats was fine Molochite of 30/80 mesh size, then coarse, 16/30 (mesh size) Molochite was used for the succeeding five coats. The moulds were left to dry after each coat for two hours in air with a velocity of 3 m. s^{-1} . The last coat (the seal coat) was applied by dipping the shells in the slurry tank and hanging them to dry for 16 hours in air with a velocity of 3 m. s^{-1} .

The ceramic shells were then dewaxed in a LBBC Boilerclave with a $200 \text{ }^\circ\text{C}$ steam at 8 bar pressure for 15 minutes. Then, a firing process was carried out in an electrical furnace at $1000 \text{ }^\circ\text{C}$ for two hours in order to remove any moisture or residual wax and to sinter the shell material. Table 3.1 shows the consecutive coats of the ceramic shell.

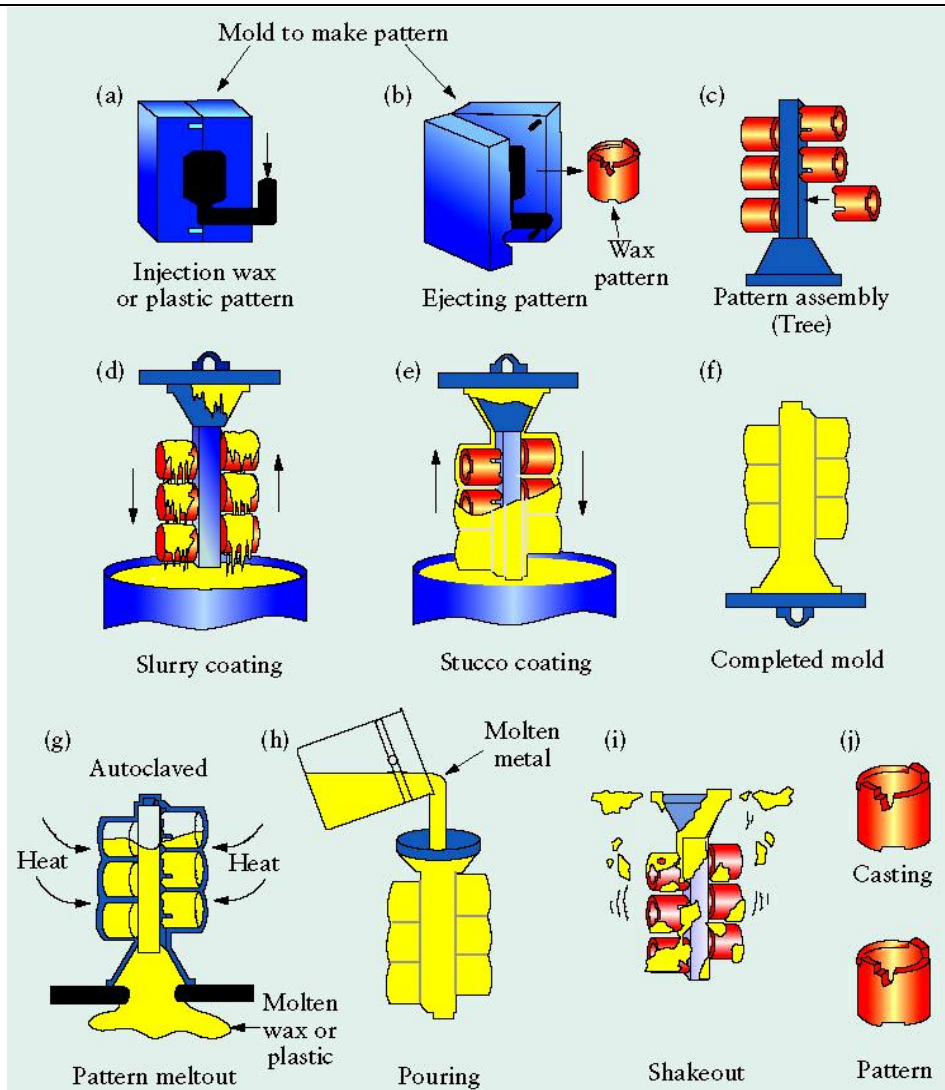


Figure 3.2 Schematic diagram shows the stages of the investment casting process; Source: Steel Founders' Society of America, [117].

Table 3.1 Yttria primary investment casting mould for Ti alloys

Coat No.	Type	Method	Slurry Code	Stucco	Air Speed ms^{-1}	Dry Time
1	Primary	Painted	Yttria	Yttria stucco	0.1	15 hours
2	Secondary	Dipped	IMP/2006/135	Molochite 30/80	3	2 hours
3	Secondary	Dipped	IMP/2006/135	Molochite 30/80	3	2 hours
4	Secondary	Dipped	IMP/2006/135	Molochite 16/30	3	2 hours
5	Secondary	Dipped	IMP/2006/135	Molochite 16/30	3	2 hours
6	Secondary	Dipped	IMP/2006/135	Molochite 16/30	3	2 hours
7	Secondary	Dipped	IMP/2006/135	Molochite 16/30	3	2 hours
8	Secondary	Dipped	IMP/2006/135	Molochite 16/30	3	2 hours
9	Seal	Dipped	IMP/2006/135	N/A	3	16 hours

3.1.3 Melting and Gravity Casting of (CP) Ti and Ti-6Al-4V alloys

The mould was placed inside a graphite mould-preheating furnace which was positioned inside the vacuum chamber of an Induction Skull Melting furnace. The charge for each melt weighed 4.5 kg of CP Ti or Ti-6Al-4V alloy, and was placed in the ISM water-cooled copper crucible.

The chamber was then evacuated to 5×10^{-2} mbar and vacuum leak checked. The test mould was heated to either 500 or 1000 °C and held for 1hr. The melts were carried out under a partial pressure of 200 mbar argon. The power supplied to the induction coil was increased gradually to reach a maximum of 350 kW in 8 minutes at which time melting started.

A thermocouple was dipped into each melt to measure the maximum temperature of the molten alloy. Table 3.2 shows the thermocouple recorded temperatures and the pyrometer reading of each melt. The molten metal was then gravity poured into the mould at a preset rate of 2 kg. s^{-1} .

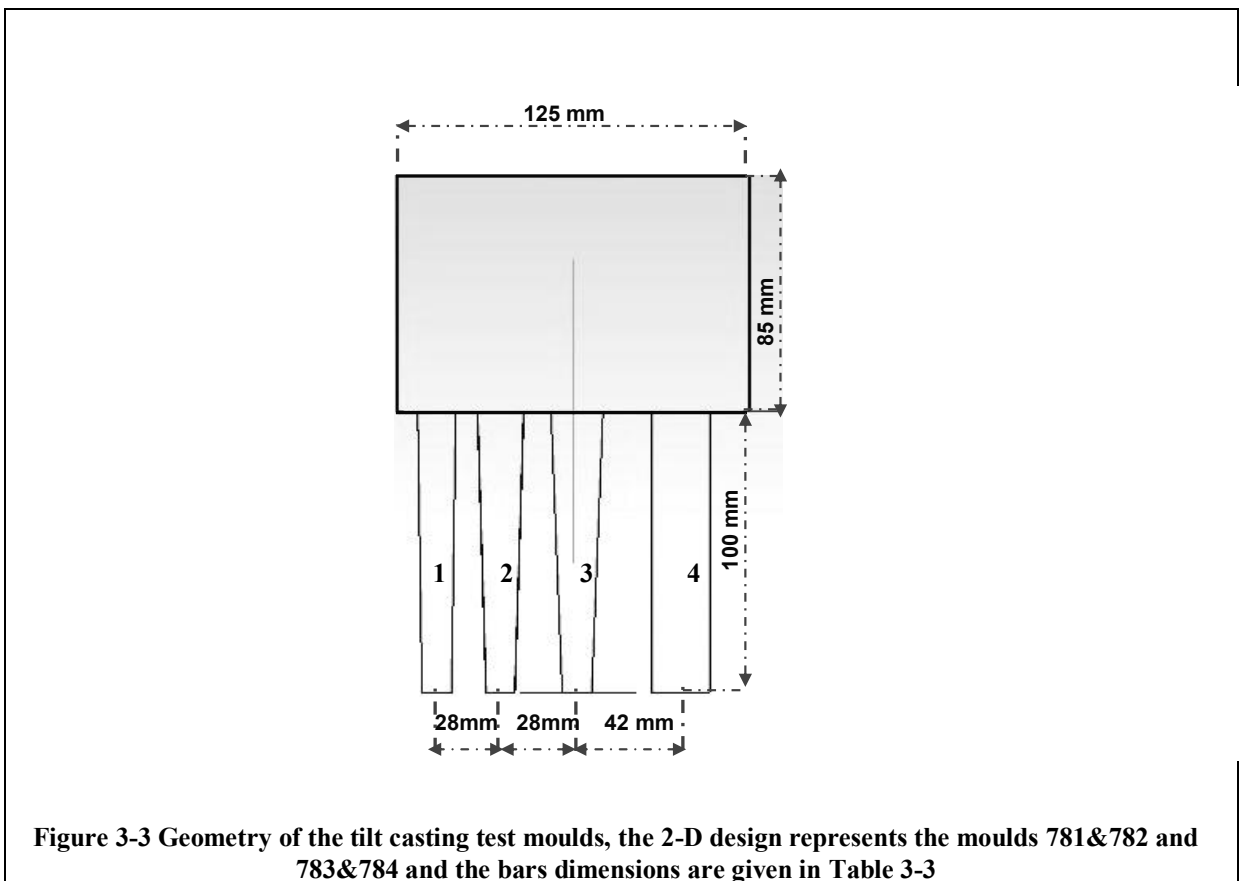
Table 3.2 Temperature measurements in CP Ti and Ti6Al4V investment gravity castings

Melt no.	Alloy composition	Mould temperature	Thermocouple reading	Pyrometer	Emissivity ϵ
719	CP Ti	1111 °C	Failed	1721 °C	1.97
711	CP Ti	500 °C	1715 °C	1722 °C	1.97
711	Ti6Al4V	500 °C	1713 °C	1714 °C	1.96
712	Ti6Al4V	1111 °C	1711 °C	1716 °C	1.97

3.2 Tilt Casting of Titanium Aluminide

3.2.1 Mould Design and Preparation

Figure 3.3 shows the geometry of the mould used for tilt casting trials of titanium aluminide, which consisted of a half-cylindrical shaped pouring basin, to which four 100 mm long bars were attached. The geometry of the test bars and their positions in the moulds are given in Table 3.3. The ceramic shells were made using the investment shell moulding techniques using the same materials and procedures as described in section 3.1.2.



Measurements of diameters and heights of the test bars were repeated three times and average values are given in Table 3.3

Table 3.3 Geometry and dimensions of tilt-casting test Bars

Mould No.	Bar number	Geometry	Nominal Dimensions			Measured Dimensions			Taper angle
			D1	D2	H	D1	D2	H	
781	1	Cylindrical	10	10	100	10.0	10.0	96.0	0.0°
	2	Tapered	10	12	100	10.0	11.3	95.0	0.5°
	3	Tapered	10	16	100	10.0	14.5	98.0	1.5°
	4	Tapered	10	18	100	10.0	17.5	94.0	2.5°
782	1	Cylindrical	10	10	100	10.0	10.0	90.0	0.0°
	2	Tapered	10	12	100	9.6	11.0	91.0	0.5°
	3	Tapered	10	16	100	9.8	14.8	90.0	1.5°
	4	Tapered	10	18	100	10.0	17.5	90.0	2.5°
783	1	Tapered	10	14	100	9.8	12.6	97.4	1.0°
	2	Tapered	10	16	100	9.8	15.8	96.0	2.0°
	3	Tapered	10	18	100	10.0	18.0	96.0	2.5°
	4	Cylindrical	20	20	100	20.0	20.0	98.0	0.0°
784	1	Tapered	10	14	100	9.7	12.7	98.0	1.0°
	2	Tapered	10	16	100	9.8	15.4	98.0	2.0°
	3	Tapered	10	18	100	10.0	17.8	93.0	2.5°
	4	Cylindrical	20	20	100	20.0	20.0	99.0	0.0°

3.2.2 Melting and Tilt Casting

Chemical analysis of the titanium aluminide alloy used was carried out by “London and Scandinavian Metallurgical Company, Limited” using the XRF (X-Ray Florescence) technique. Three samples were taken from the top, middle and bottom of the plasma melted billet and analyzed. The average of the three compositions was used as the average chemical composition of the alloy. The chemical analysis of the three samples in atomic percentage and the average chemical composition are given in Table 3.4.

A charge of 4.5 kg of titanium aluminide was loaded into the ISM copper crucible, and then the mould was inverted and sealed on the top. The chamber was evacuated to 5×10^{-2} mbar and vacuum leak checked. The preheating graphite furnace was closed around the mould, and the mould was preheated to either 1000 °C or 500 °C, and soaked for one hour.

Due to the complexity of the mould-crucible arrangement it was not possible to immerse a thermocouple to measure the melt temperature before pouring. The tilt pouring started by rotating the mould-crucible assembly in a clockwise direction according to a preset programme. The tilt cycle is described in more detail in Section 3.5.2.

Table 3.4 Chemical analysis of plasma melted ingot 417

	Top		Middle		Bottom	
Element	Wt.%	At.%	Wt.%	At.%	Wt.%	At.%
Ti	52.52	46.27	52.53	45.92	51.20	44.63
Al	28.98	45.31	29.35	45.53	30.10	46.57
Nb	17.35	07.88	17.80	08.02	18.30	08.22
V	00.09	00.08	00.13	00.11	00.11	00.09
O	00.15	00.15	00.15	00.15	00.15	00.15
C	00.02	00.08	00.02	00.07	00.02	00.08
Total	99.11	99.76	99.98	99.80	99.86	99.74
	Top	Middle	Bottom			
Element	At.%	At.%	At.%	Average		
Ti	46.27	45.92	44.63	45.61		
Al	45.31	45.53	46.57	45.80		
Nb	07.88	08.02	08.22	08.04		

3.3 Casting Assessment

3.3.1 X-ray Radiography

All cast bars were cut from the castings, cleaned and coded, and then sent to Bodycote Radiography and NDT, (Material Testing Laboratory, Cleveland, UK), for X-ray examination. The X-ray films were scanned on a Canon Scanner with 1200 dpi resolution and recorded as digital files. The brightness and contrast were adjusted to increase the visibility of the internal defects.

3.3.2 Sectioning and Metallographic Preparation

Samples for microstructure and macrostructure examination were cut transversely from the top, middle and bottom of the 200 mm long gravity-cast test bars. The tilt-casting test bars were sectioned along the mould parting line by using Electrical Discharge Machining (EDM) and divided into 23 mm long specimens.

Specimens were mounted in bakelite and marked in order of the direction of pouring. Metallographic preparation was carried out using the Struers machine and involved grinding on a Piano-grade disk for 30 seconds, then polishing using 9 µm diamond suspension on an MD-Largo disc for 5 to 20 minutes, (depending on the area of the prepared specimen), followed by a final step of polishing on an MD-Chem disc for 15 minutes.

3.3.3 Stereological Measurements of Microstructure Features and Porosity

a) Image Processing

The image analysis inspection in metallographic applications has been proven to be accurate and time saving procedure which also provides an extensive statistical representation of the measurements [118]. In order to use image analysis in metallographic applications the as-acquired image must undergo an enhancement process to correct any flaws in the image, this involves several consecutive steps, and some of them are summarized in the following points:

a.1) Noise Reduction

The source of noise in a digital image can be the variation in brightness level in any region of the image, which happens due to unsteadiness in the light source during the acquiring and digitizing time [119], or due to long exposure time, and it can be reduced by using a median filter which is available to apply on selected pixels in most image analysis software [120].

a.2) Brightness and Contrast Manipulation

Histogram equalization is a mean to adjust the brightness values or the contrast of the image in order to improve the visibility of details, this can be achieved by expanding or “compressing” the histogram which consists the intensity function of the grey levels, corresponding to all pixels so that the same number of pixels show every intensity of the possible brightness.

a.3) Segmentation and Thresholding

Segmentation is an important procedure of image processing that can be used to divide the image into foreground and background regions, by defining a threshold value in order to distinguish between different phases or objects [121]. Thresholding is done by selecting the features with the pixels that belong to the foreground (all pixels below the threshold value) and these pixels define the object or the phase, and all other features with pixels above the threshold value are belonging to the background.

Automatic thresholding is based on the analysis of the gray scale histograms, where the different objects like the polished surface (the background) and the porosity (the foreground) are expected to have distinguished peaks in the histogram. The resultant binary image consists of regions of two colours only (usually black and white) is used to carry out measurements of two distinguished features [122].

b) Image Analysis for Metallurgical Applications

Quantitative characterization of microstructure and other metallographic features requires several digital measurements to be carried out on the binary image. For example, surface area of the feature by counting the pixels that forming it, the Feret diameter which represents the outer dimension of the feature, the maximum Feret diameter which is described by length

and orientation angle, and the coordinates of the first point which is important to determine spatial distribution of the inspected features, Figure 3.4 shows these measures and some others.

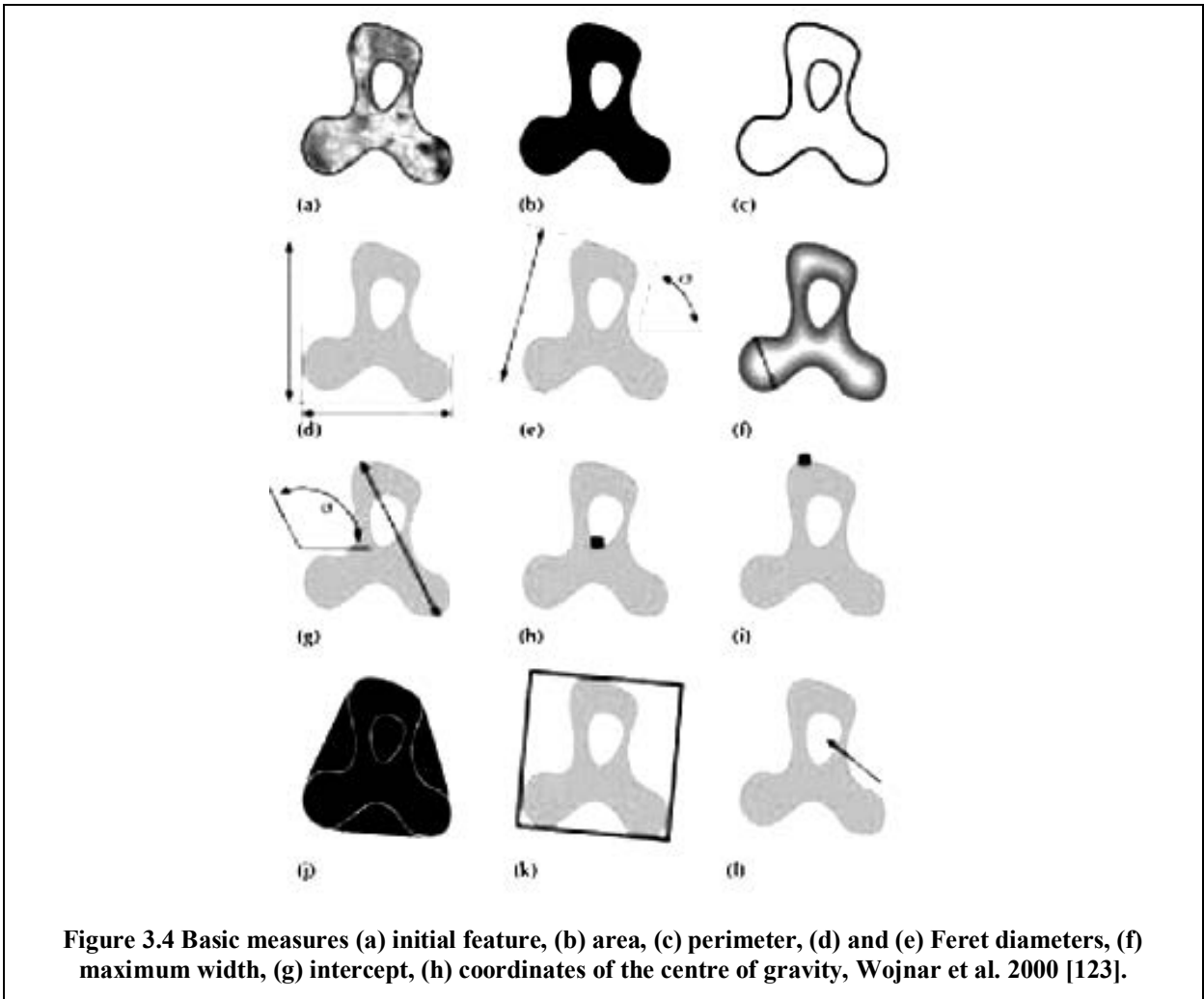
C) Sources of Errors in Digital Measurements and Remedies Actions

Most of the errors involved in image analysis and digital measurements can be related directly to the pre-processing procedures and can be avoided by simple additional steps. Basically, reducing the number of pre-processing steps would be desirable in order to keep the initial image information as much as possible.

However, carrying out measurements on raw images is almost impossible; therefore, restricting the number and sequence of the procedures applied on all images involved in the same experiment will be helpful to maintain the accuracy of the measurements. Incorrect segmentation or thresholding errors can be minimized by using automatic algorithms and histograms; as discussed previously.

In addition, bias can be introduced due to incorrect counting of the phases or objects whether by overestimating the quantity (counting the objects that are crossed by the edge of the image twice in two successive frames), or by underestimating the number by excluding those objects. This problem is solved by using “guard frame” technique, by which a selective frame is applied on the investigated field away from the edges of the image and any particles/objects inside or crossed by selected sides of the guard frame are counted.

It is important to notice that the exactly true values are not obligatory in many cases if the analysis is used for comparative purposes, as long as the same procedures and conditions of the analysis are used for the entire series of the investigated images in the experiment [123].



3.3.4 Quantitative Assessment of Porosity

A detailed quantitative assessment of shrinkage porosity was carried out on all test bars of the tilt casting experiments and on some selected samples from the gravity casting tests. Longitudinal sections in the as-polished condition were scanned on a Canon Scanner with 1200 dpi resolution.

The digital images at one-to-one scale were saved as 8-bit grey scale images in a Jpeg format. Digital image analysis software, AxioVision (V 4.8.2.0, 2006-2010) and, (Digimizer version 3.4.1, 2008), were used to carry out the porosity measurements. The brightness and contrast were manually adjusted in order to get the best clarification of the porosity.

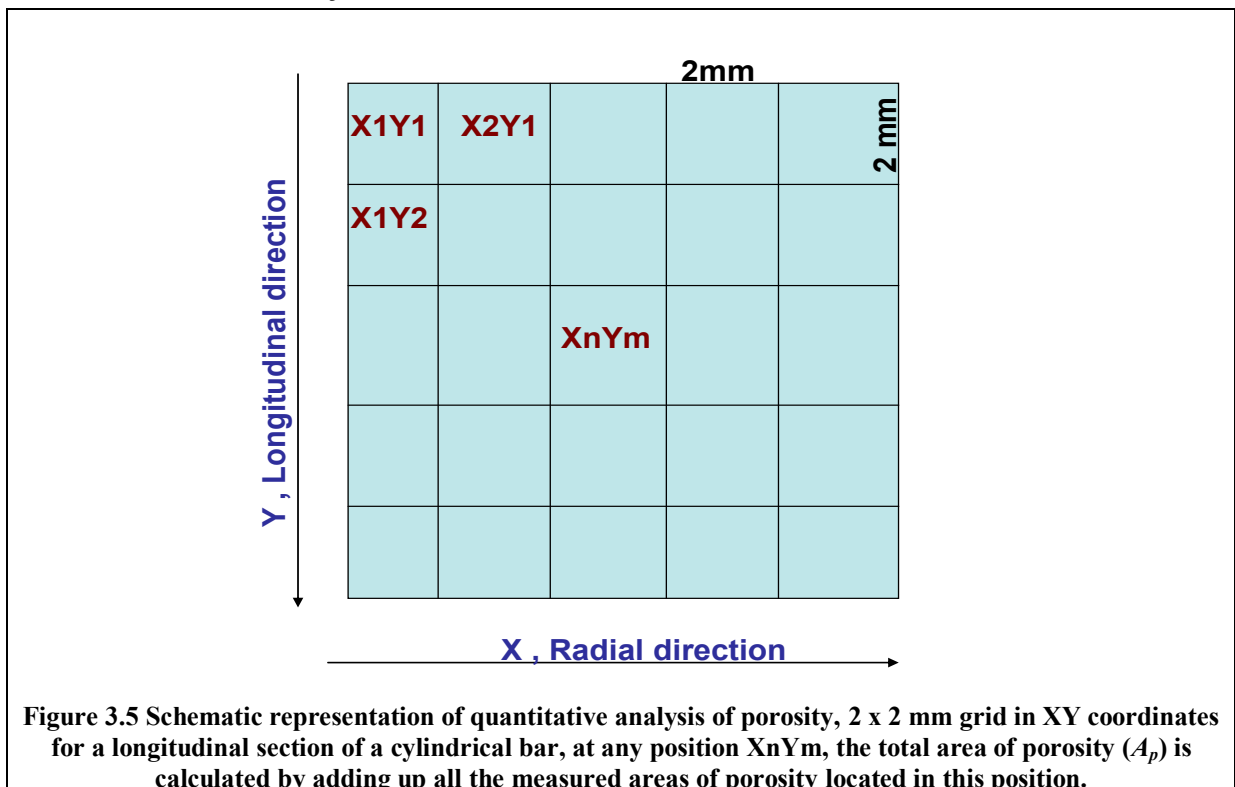
For the purpose of getting the most accurate measurements, the image processing and binarization (see Section 3.3.3) of the images were carried out manually so that the threshold limits coincided with the boundaries of the porosity.

The calibration of the measurements was carried out by drawing a line of a known length to represent the unit length. The area of porosity was measured automatically and the position of each pore was determined by its x-y coordinates.

An imaginary grid with a cell size of 2 x 2 mm was created on the longitudinal sections of the test bars to measure the average content of porosity in both radial and longitudinal directions. Figure 3.5 shows this grid in XY coordinates for a longitudinal section of a cylindrical bar. At any position X_nY_m , the total area of porosity (A_p) was calculated by adding up all the measured areas of porosity that were located in this position.

$$\%A_p = A_p \times 100 / A_c \quad \text{Eq. 3.1}$$

Porosity measurements and distribution



3.3.5 Quantitative Assessment of Macrostructure

The objective of the quantitative assessment of the macrostructure was to determine the relative amount of columnar to equiaxed grains at any position along the longitudinal section of the test bars. The etched sections were scanned on a Canon Scanner with 1200 dpi resolution.

The digital images with one-to-one scale were saved in a 8-bit RGB colour, Jpeg format. The image analysis software (Digimizer version 3.4.1, 2008) was used to carry out the macrostructure assessment. The brightness and contrast were manually adjusted so that optimum contrast between grains could be selected in order to get the best clarification of the micrographs.

Non-standard measures were made on the images of the macrographs as follows:

- A set of transverse lines were drawn on the image with 2 mm separation distance, this was sufficient to guarantee that adjacent lines cannot cross the same grains.
- The intersections between the columnar grains and the transverse lines were measured from both sides of the image.
- The percentage of columnar (% L_c) and equiaxed grains (% E) was calculated by the following equation:

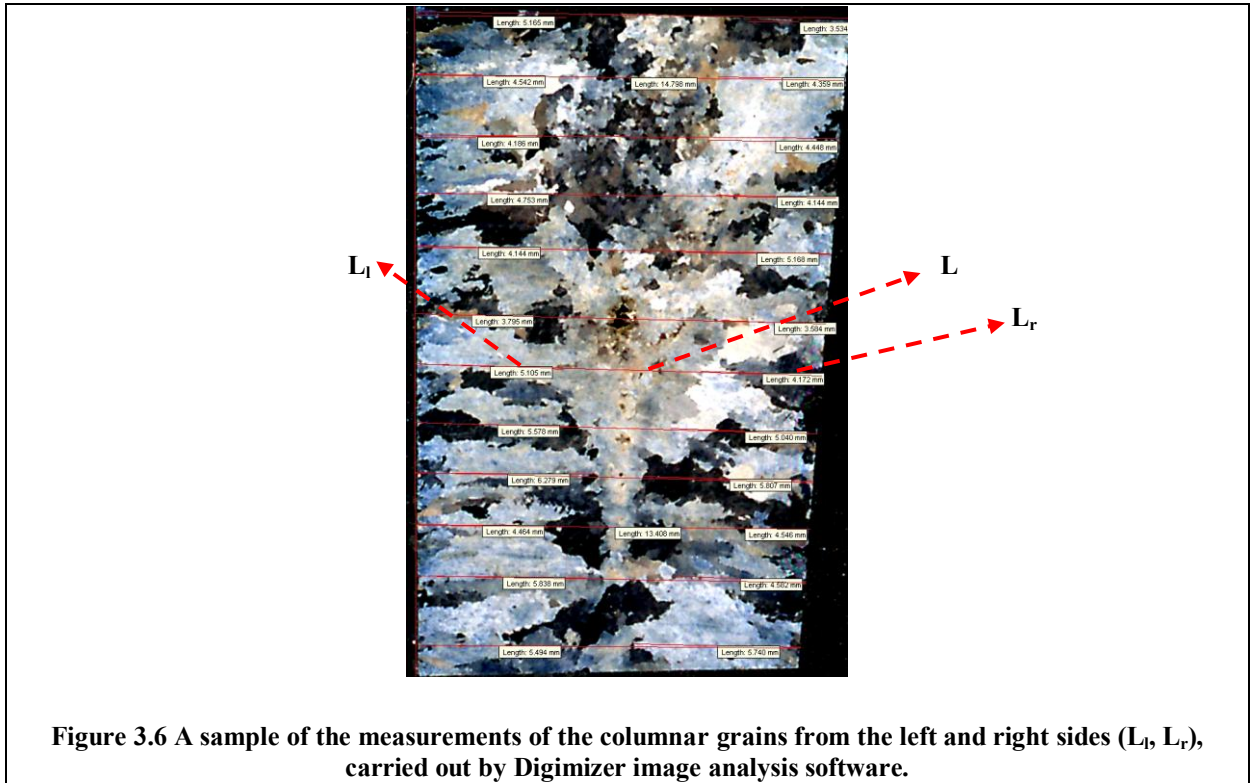
$$\%L_c = 100 \times (L_l + L_r) / L \quad \text{Eq. 3.2.a}$$

$$\%E = 100 - \%L_c \quad \text{Eq. 3.2.b}$$

Where: L is the length of the transverse line, L_l and L_r are the lengths of the intercepts of columnar grains on the left and right side of the image, respectively.

Five macrographs were chosen randomly to repeat the measuring process five times using the same image processing and measuring steps in order to determine the standard error of the

measurements. Figure 3.6 shows the measurements carried out on a macrograph of section 3 in bar 4 mould 782.



3.4 Temperature Measurements during Gravity Casting and Solidification of Ti-46Al-8Nb Alloy

Four investment moulds consisted of 100 mm diameter (nominal) x 300 mm long cylinder with a conical pouring basin were manufactured as described in section 3.1.2. Two more coarse stucco coats were added before sealing to the ones described in Table 3.1. The average thickness of the ceramic shell was measured after the end of the experiments and was found to be 10 mm.

Two holes were drilled into the moulds at the middle of the casting height (75 mm from the cylinder bottom) and a 5 mm outer diameter Alumina thermocouple sheath with closed ends was fixed in the holes. As illustrated in Figure 3.7, two R-type thermocouples made from 0.2 mm diameter wires of Pt-Pt/13%Rh were inserted in the Alumina sheaths such that; for the position TC1; the hot junction was very close to the geometric centre of the casting, and for the position TC2 the hot junction was almost at the casting/mould interface from the casting side.

Two dents of 2 mm and 5 mm deep were drilled into the outer surface of the mould and two K-type thermocouples made from 0.45 mm diameter wires of (Chromel 90%Ni+10%Cr and Alumel 90%Ni+2%Mn+2%Al+1%Si) were introduced at positions 3 and 4 so that their hot junctions were carefully attached with the concave surface and fixed into positions by a coat of slurry and Stucco, which resembled the mould material.

The mould was placed on a bed of insulating refractory (Mullite chips) in the vacuum chamber, and the thermocouples were connected by compensating cables to a National Instrument NI SCX 1-1000 temperature datalogger.

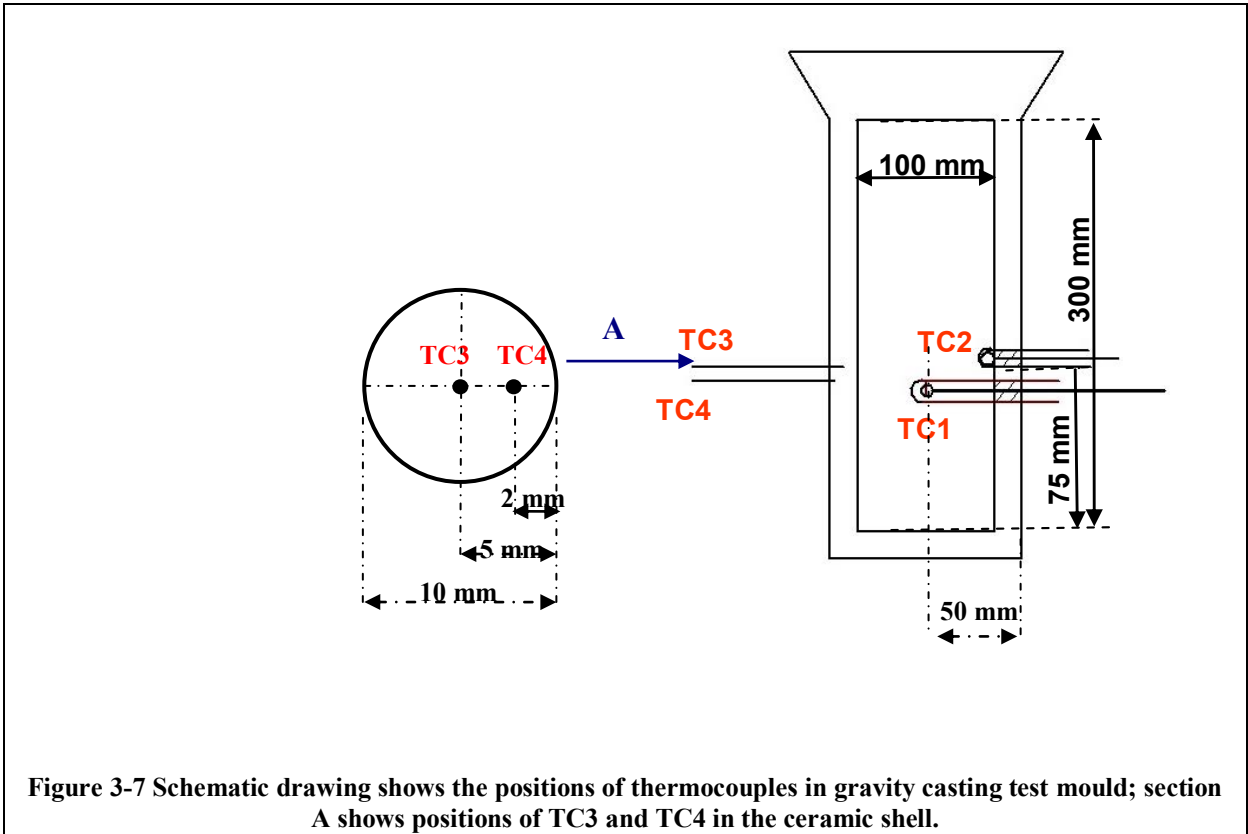


Figure 3-7 Schematic drawing shows the positions of thermocouples in gravity casting test mould; section A shows positions of TC3 and TC4 in the ceramic shell.

3.5 Temperature Measurements during Tilt Casting

3.5.1 Mould Preparation and Thermocouples Setup

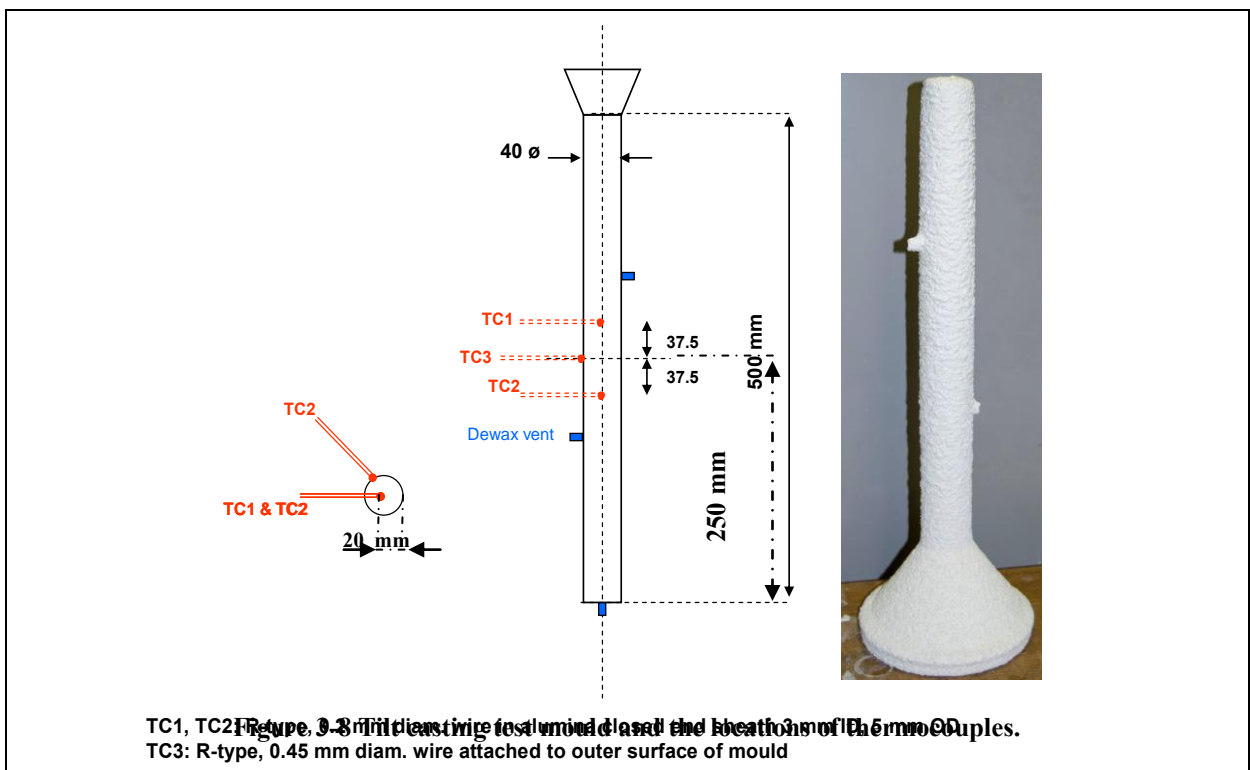
A test mould consisting of a 40 mm diameter, 500 mm long cylinder with a conical pouring basin was manufactured by the investment casting technique as explained in Section 3.1.2. Vents to assist dewaxing were located at 165 and 335 mm from the bottom of the cylinder and were plugged by fireclay before firing. Two thermocouples of B-type were calibrated by Rolls-Royce (Precision Casing Facility, Derby UK), by comparing them against a standard reference thermocouple of type R and the estimated total error was less than 2 °C.

The B-type thermocouples were implanted in the shell during manufacturing. Thermocouple 1 (TC1) was implanted after the primary coat of Ytria at the middle height of the cylinder. Alternate layers of fine Molochite 30/80 mesh size then course 16/30 Molochite were then applied.

The outer diameter of the mould was measured after the sixth coat and the shell thickness was found to be 6.45 mm, at which point the second thermocouple TC2 was introduced into the shell at the middle height before applying the last layer and the sealing dip.

Two 5 mm diameter holes were drilled at 37.5 mm above and 37.5 mm below the mid-height of the cylinder and two 5 mm outer diameter closed end Alumina sheaths were inserted into the holes and fixed in their positions by fireclay. Figure 3.8 shows the mould design and posit

Test mould for ISM 842



Two R-type thermocouples were inserted in the sheaths, and the remaining length of the thermocouple wire was housed inside ceramic insulator tubes that were connected to the datalogger by the compensation cables. Figure 3.9 shows the set-up of the mould inside the mould heater.

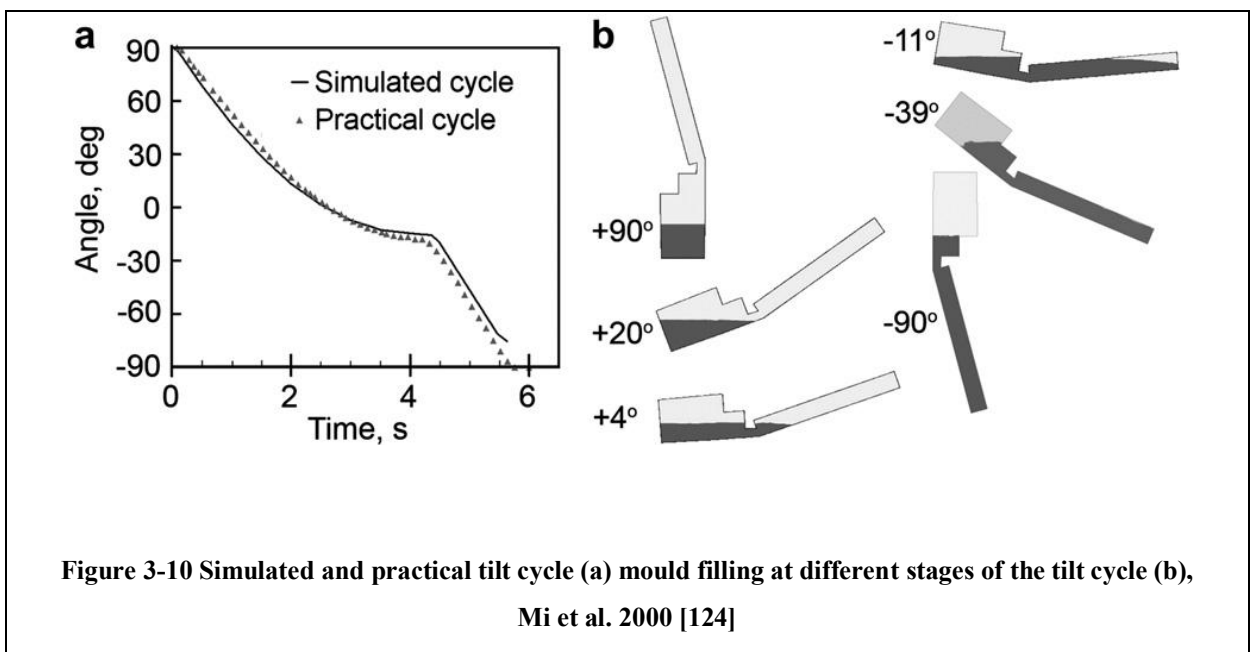


Figure 3-9 Setup of the mould for temperature measurements of tilt casting.

A 4.9 kg charge of the alloy was placed in the copper crucible of the ISM furnace, and the mould was mounted and sealed on the top of the crucible. The mould was heated to 1000 °C and soaked for one hour. Melting was carried out under 200 mbar of Argon, and the power of the induction coil was increased gradually to reach 350 kW in 7 minutes.

3.5.2 Tilt Pouring Cycle

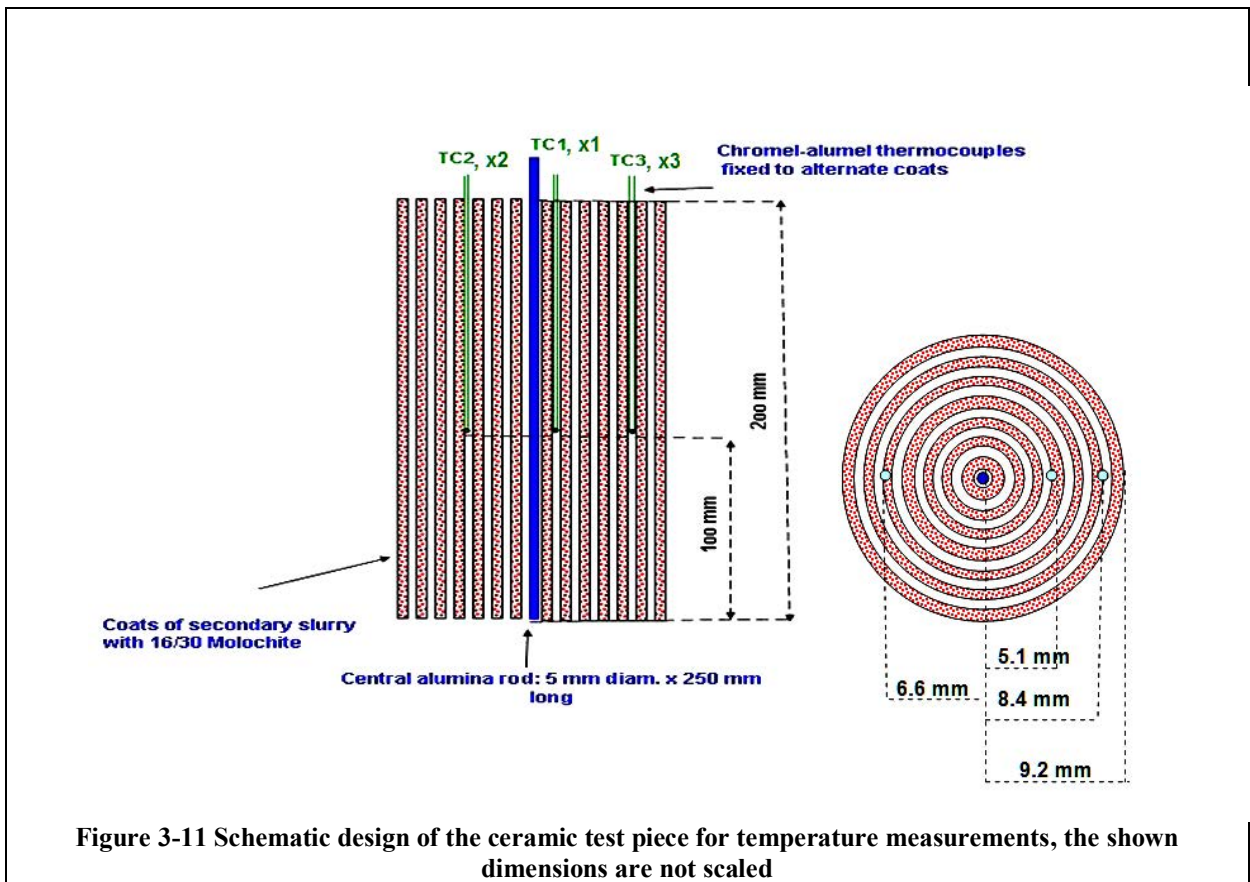
A preset rotation cycle, shown in Figure 3.10 was used for tilt pouring. The mould-crucible assembly rotates from its vertical position in a clockwise direction to reach its final position, as shown in Figure 3.10 (b), in a total rotation time of 6 seconds. The initial stage of the rotation cycle begins at 4.9 degrees per second, which allows a fast transfer of the molten metal from the crucible into the basin. Then the rotation speed decreases to reach zero velocity during horizontal filling of the mould, with the aim of minimizing the turbulence and maintain homogeneity of the molten metal temperature. The rotation velocity then accelerates again to reach 14 degrees per second during the final stage of rotation with the intention of minimizing heat loss [124].



3.6 Measurement of Mould/Surroundings Interface Heat Transfer Coefficient

3.6.1 Design of the Test Piece and the Experiment Description

Figure 3.11 shows a schematic design of the test piece used for measurements of the heat transfer coefficient between the investment mould outer surface and the ambient environment.



A ceramic shell was built up around a cylindrical alumina rod of 5 mm diameter and 250 mm length. Three K-type thermocouples were simultaneously implanted in the shell at positions determined by measuring the average shell thickness at different points after certain number of consecutive coats. The manufacturing process of the test piece and positioning of the thermocouples are illustrated in the diagram shown in Figure 3.12.

The final outer diameter of the shell was measured at three positions and the average thickness was calculated and recorded. The radii of the test rod at the position of the thermocouples are given in Table 3.5

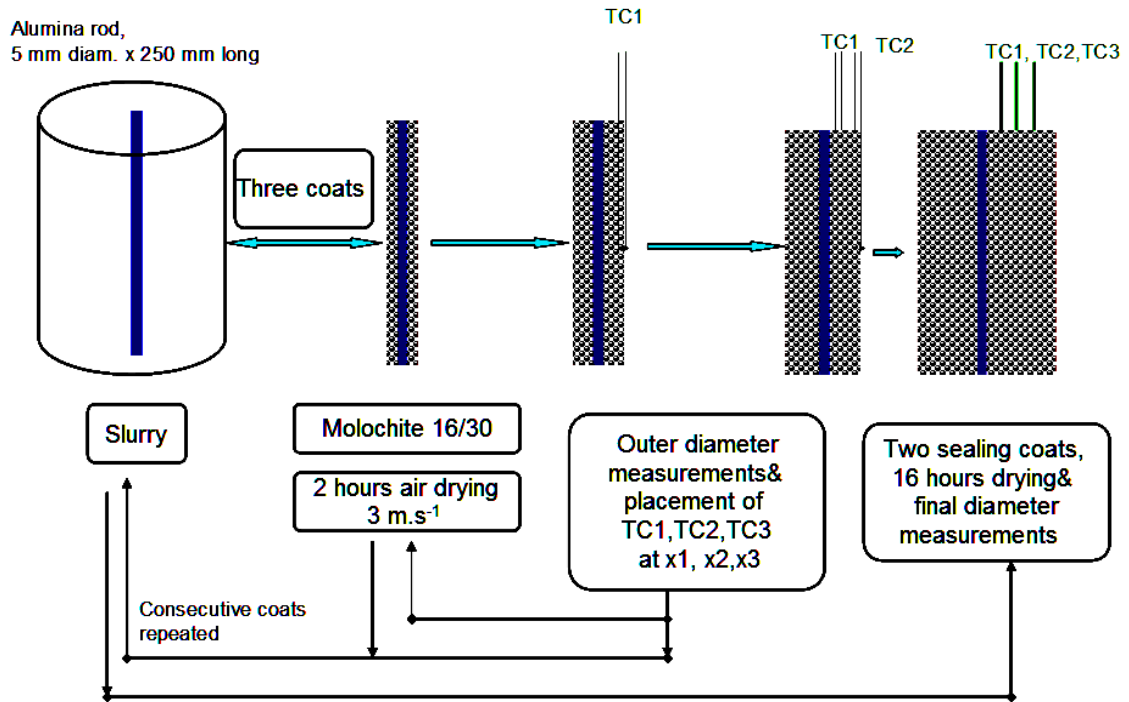


Figure 3.12 Flow diagram summarizes the production sequences of the ceramic test piece for heat transfer measurements

Table 3.5 Radius of the ceramic bar at positions of the thermocouples

Thermocouple and position	Average radius, mm
TC 1, x1	5.1
TC 2, x2	6.6
TC 3, x3	8.4
Final radius	9.2

The accuracy of the thermocouples' positions was checked by X-ray imaging, as shown in Figure 3.13.

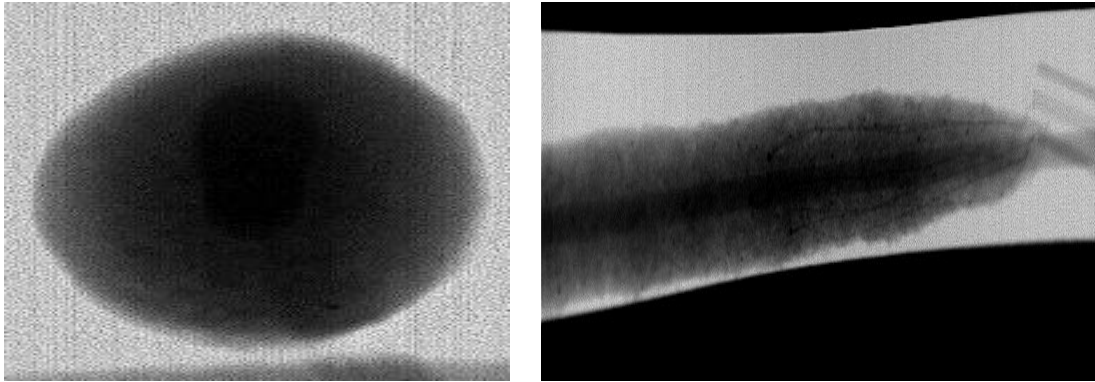


Figure 3.13 X-ray image of ceramic test bar shows the position of one of the thermocouples

The temperature measurement experiments were carried out in vacuum, Argon and in air in order to acquire the heat transfer coefficient between the investment mould surface and its surrounding atmosphere. The experimental arrangement was such that the test piece was mounted vertically on an upside down ceramic mould and clamped into position by means of a ceramic disk and a non-magnetic stainless steel ring.

The upside down mould was then placed on the top of the empty copper crucible and clamped into position by means of a non-magnetic stainless steel ring. The thermocouple insulated wires were held on a ceramic bar which in turn was fixed in a wooden arm outside the graphite mould heater furnace. The two-part door of the graphite furnace was closed and the thermocouples were connected to the data logger by extension cables.

3.6.2 Temperature Measurements in Vacuum

The vacuum chamber was evacuated to 5×10^{-2} mbar. The ceramic rod was then heated to $1000\text{ }^{\circ}\text{C}$ and soaked for one hour. The two-part door of the graphite furnace was opened and the assembly of the ceramic test piece with the thermocouples was rotated according to the preset tilting cycle which is shown in Figure 3.10.

The outputs of the thermocouples were recorded during heating up, soaking and cooling at a recording rate of 1 reading per second, a relatively low scanning rate chosen on the

assumption that no phase transformation was expected during heating up or cooling down of the ceramic material. The recorded data were then converted into Excel spreadsheets. The experiment was carried out in duplicate in order to guarantee the accuracy of the measurements.

3.6.3 Temperature Measurements in Argon

The vacuum chamber was evacuated to 5×10^{-2} mbar then backfilled with 200 mbar Argon. All the previously explained procedures were performed and the experiment was carried out in duplicate as well.

3.6.4 Temperature Measurements in Air

The furnace chamber was not evacuated before carrying out the heating process. The ceramic test piece was heated up to 1000 °C, soaked for one hour in the atmospheric pressure of the furnace. Then the power of the mould heater was turned off and the door was opened. The cooling cycle started with the rotation process aiming to resemble the tilt casting cooling conditions.

3.7 Thermal Analysis of Cooling Curves

Thermodynamic data and thermophysical properties can be determined by observing and interpreting temperature changes during constant cooling or heating of a sample [125].

Several techniques for thermal analysis have been used for decades. Differential thermal analysis (DTA) is one of the earliest techniques in the thermal analysis field. The method can detect phase transformations of a sample by measuring the difference between the sample temperature and the temperature of a reference material. Differential Scanning Calorimetry (DSC) is used to detect thermodynamic reactions. This can be used to determine the latent heat of fusion and specific heat by measuring the difference in the quantity of heat required to raise the temperature of the test sample and a reference material [126].

Saari et al. [127] used the DSC technique to study the thermophysical properties of γ -titanium aluminide alloy. They reported 1453 °C and 1522 °C for the solidus and the liquidus temperatures upon heating, respectively, and 1510 °C and 1420 °C for liquidus and solidus upon cooling, respectively. This difference between solidus and liquidus temperatures upon heating and cooling is expected due to the effect of undercooling which takes place during cooling, the shift in the alloy composition decreases the liquidus and the solidus temperatures.

Thermal analysis of an experimentally measured cooling curve is another thermal analysis technique, which aims to identify the inflection points which represent thermodynamic reactions and phase transformations that the metal undergoes during solidification and in the solid state.

Computer-aided cooling curve analysis is based on a computerized determination of the inflection points on the cooling curve, by calculating its first and second derivatives and its zero-curve, which is the first derivative curve calculated by assuming that the cooling curve does not show any phase transformations.

The computation process starts with smoothing the raw data of the cooling curve in order to eliminate any noise before calculating the derivatives. The resulted curves are analyzed in terms of points of inflections, and then the zero-curve is calculated by fitting the data just before and after the inflection points, as illustrated in Figure 3.14, in which an example of using the first derivative of a cooling curve to determine the characteristic temperatures of A356 aluminium alloy is shown. In computer-aided cooling curve analysis the area under the zero-curve is used to calculate the latent heat of solidification, and the peak points on the first and second derivatives are used to determine the liquidus and solidus temperatures, as well as the temperatures of phase transformations in the solid state [128].

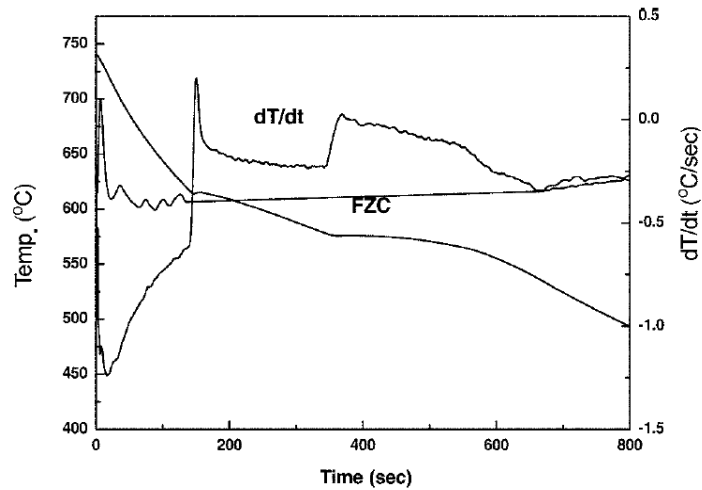


Figure 3-14 Cooling curve, first derivative and Fourier zero-curve for A356 alloy, I Ulhaq et al. 2004 [128].

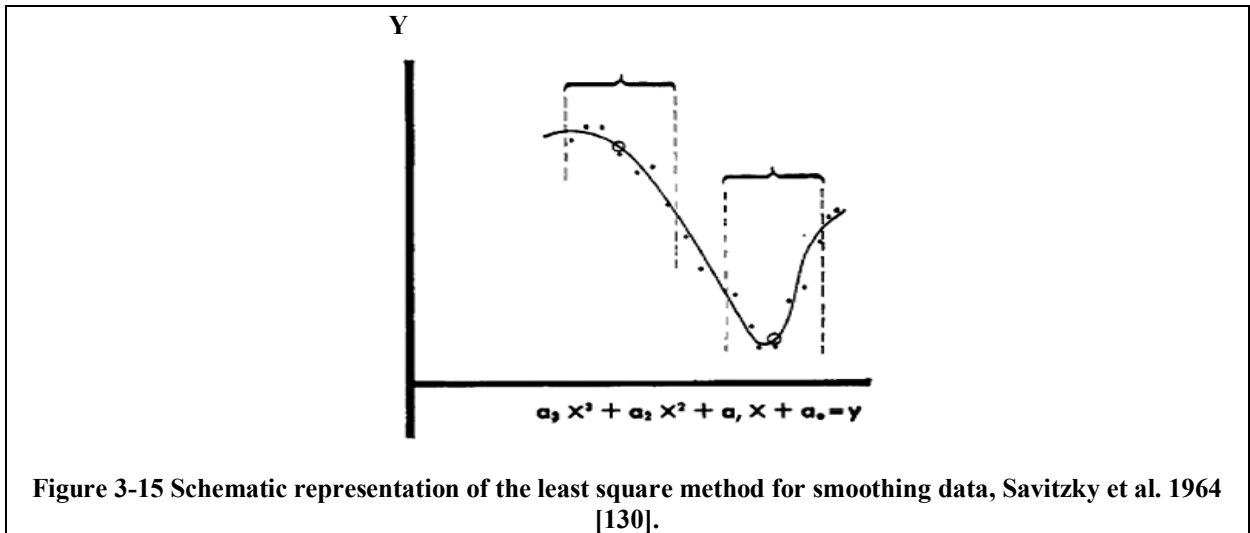
3.7.1 Smoothing of a Cooling Curve Data

In attempting to analyse an experimentally measured cooling curve, the raw data of the thermocouples must be refined by eliminating the noise as much as possible, without affecting the good data.

Several numerical methods can be employed to remove the noise from the measured curve, such as the moving average and the least square algorithms. In the moving average procedure, the average of a specific number of points is calculated at the centre point of the data set, and then the process is repeated by excluding the point from the top of the data set and including the next point from the end of it [129].

On the other hand, the least square algorithm is based on the concept of minimizing the difference between the computed and measured value of (Y) at the centre of a chosen set of data, the coefficients of the (X) points are selected so that the measured points can fit a polynomial equation. The process is repeated for a consecutive set of data by excluding one point from the top and including a new point at the bottom, Figure 3.15 shows a schematic representation of the least square procedures to fit a data set composed of seven points into a curve of the third degree polynomial function. The coefficients and the derivatives (up to the

fifth derivative) were predetermined and tabulated for polynomials up to the fifth degree, along with the normalizing factors for each set of data depending on the chosen number of points to be curve-fitted, the tabulated values were given in the Reference [130].



3.7.2 Source of Thermocouple Errors

The output signals of a thermocouple are prone to many sources of errors, which affect the accuracy of measurements by causing the noise or the bias in the measured cooling curve [131]. The most important sources of thermocouple errors are: the cold junction compensation CJC errors which resulted from the compensation for the difference between the measured temperature and the temperature of the connection point of the thermocouple and the measuring device, the offset error which can be avoided by using the auto-zero function in the measurement device, and the noise errors. The noise signals can be initiated either by the interference between the measured temperature and the surrounding environment or the measuring device, this type of noise can be minimised by using lowpass filters, or an isolation sheath in case of immersing the thermocouple in highly conductive material [132].

CHAPTER 4

MODELLING OF TITANIUM ALUMINIDE INVESTMENT CASTING

4.1 Computational Modelling by FDA and FEA Methods

Computational modelling of a casting process involves building up a mathematical model to represent the physical phenomena, which are determined by the governing equations in a set of partial differential equations, (PDEs), of the process. The Navier-Stokes equations represent fluid flow of an incompressible fluid [133];

$$\rho \left(\frac{\partial v}{\partial t} + v \cdot \nabla v \right) = -\nabla P + \sigma + f \quad \text{Eq. 4.1}$$

Where ρ is the density, v is the flow velocity, t is the time, P is pressure, σ is the total stress, and f is the total forces per unit volume acting on the fluid.

Finite Element Analysis (FEA) and Finite difference analysis (FDA) are both used to solve partial differential equations of physical phenomena through computer software.

FDA is used to solve the PDEs in a grid of elements, in which an element of a cubic shape is typically used, which limits the applicability of the FDA to simple geometries.

FEA has been used for several decades in fluid dynamics analysis, stress analysis, and in numerical simulation of metal casting, which involves heat transfer and solidification phenomena, and unlike FDA, FEA can be used to analyse complex geometries.

In FEA a geometric model is divided into domains consisting of elements of certain geometry, triangular or rectangular in 2-D models and tetrahedral, hexahedra or bricks in 3-D models. Each element is defined by a set of points known as nodes. The node is defined by an integer number and by its position in the 2-D or the 3-D coordinate system.

A set of properties and boundary conditions are assigned to each node in order to determine the change in temperature distribution, stresses distribution or any other unknown parameters [134]. Unlike FDA, the variable properties assigned at each node can be changed across the element.

ProCastTM is a casting simulation software that uses the finite element method to solve the heat flow and fluid flow equations [94]. It is widely used in casting simulation, because ProCast can provide an efficient, fast, and easy to use tool for foundry engineers, and can fulfil industrial requirements at the same time.

More importantly, ProCastTM can be used effectively in simulating the investment casting process. The software allows to account for the effect of radiation between adjacent sections of the casting on the overall heat transfer process during cooling by using the “view factor” technique [91, 92, 94]. Therefore, the ProCastTM package was employed in this research to create a simulation model of heat transfer and solidification of Ti-46Al-8Nb alloy, cast by gravity casting and tilt casting processes.

The **ProCastTM** package includes the following modules:

- MeshCast: is used to generate the mesh of the casting parts, the mould, and the virtual enclosure.
- PreCast: the pre-processing module, includes all the required database files, which contain the materials properties, the boundary conditions, the process variables and the run parameters.
- DataCast: transforms the data files “d.dat” which were created in the PreCast module into binary files “*.unf” which are used in the calculation process. Aiming to reduce the computation time of the calculations, a parallel solver using a distributed memory

processing (DMP) technique was used in this research to run the models on a Linux cluster domain.

- ViewCast: the post-processor module; is used to calculate the criterion functions and export the model results.

The following diagram briefly describes the modelling sequences by using ProCastTM.

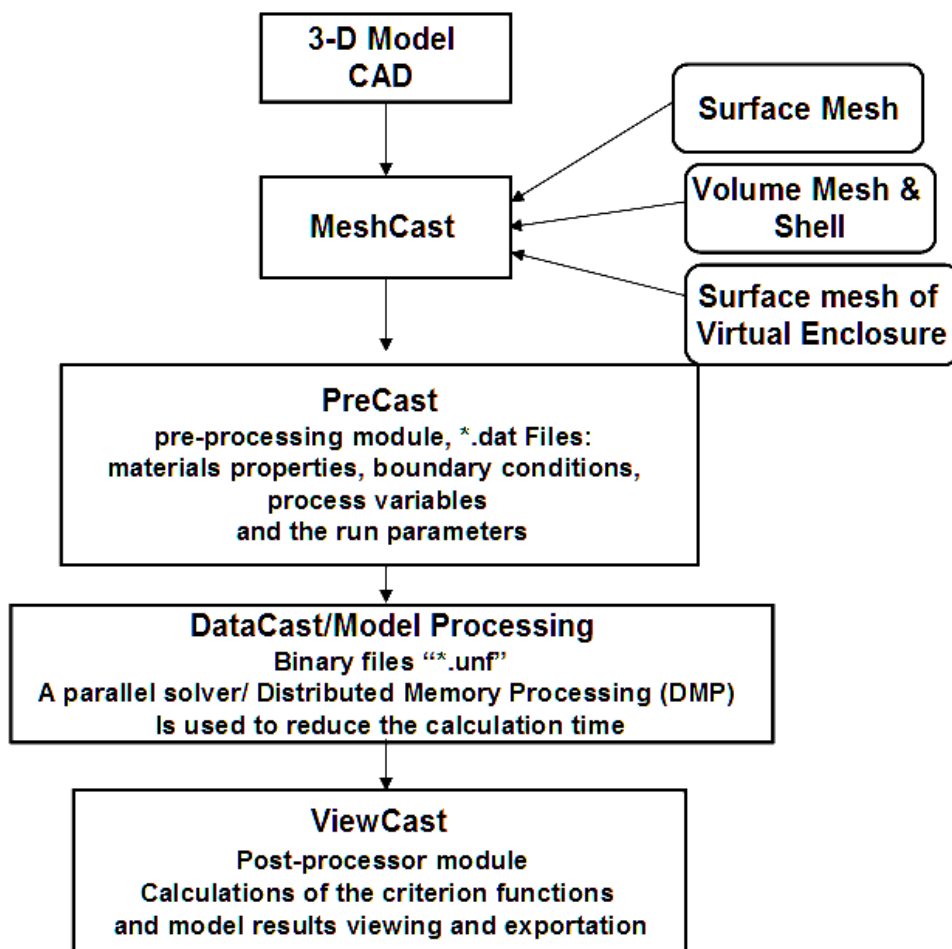


Figure 4-1 A flowchart describes the simulation modelling of investment casting process by using ProCastTM modules.

4.2 Thermophysical Properties of the Investment Mould Material

Thermophysical data for the mould material are essential for modelling of investment casting since they determine the boundary conditions of the model and hence the reliability of the simulation results. However, the availability of these data is very limited in the literature, and values are scattered. A considerable number of researchers neglect to report values of thermophysical properties of the mould material in their publications, and some other researchers state the values of these properties but without mentioning their origin.

The main properties of the mould material which should be used in any model of investment casting are density, specific heat, thermal conductivity and/or thermal diffusivity.

Section 4.2.1 summarizes some of the available data found in the literature for specific heat and thermal conductivity of the most frequently used constituents of ceramic moulds, typically molochite, bonded by zircon slurry.

4.2.1 Comparison between values of Thermophysical properties in different research works

a) Specific Heat Capacity C_p

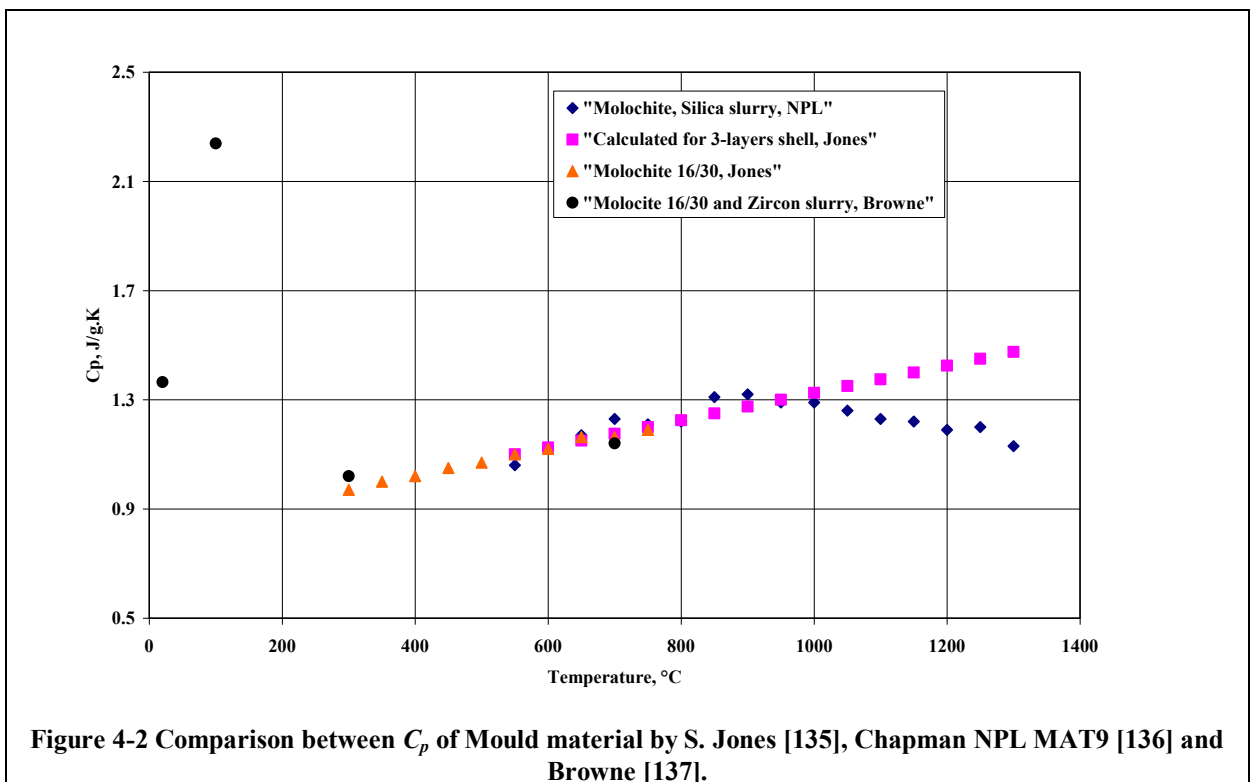
Jones et al. [135] measured the specific heat capacity of investment shell constituents by using DSC (Differential Scanning Calorimetry) and calculated the C_p of the overall shell by using the Rule of Mixtures. The shell was built up of three layers, the slurry composed of zircon and silica filler in colloidal silica suspension and the stucco, which was Molochite 16/30, 30/80 or 50/80.

Values of C_p of 16/30 Molochite were extracted from their results and fitted against temperature; the following equation was obtained:

$$C_p = 0.0005(T) + 0.8252 \quad \text{Eq. 4.1}$$

Where T in $^{\circ}\text{C}$ and C_p in $\text{J g}^{-1} \text{K}^{-1}$.

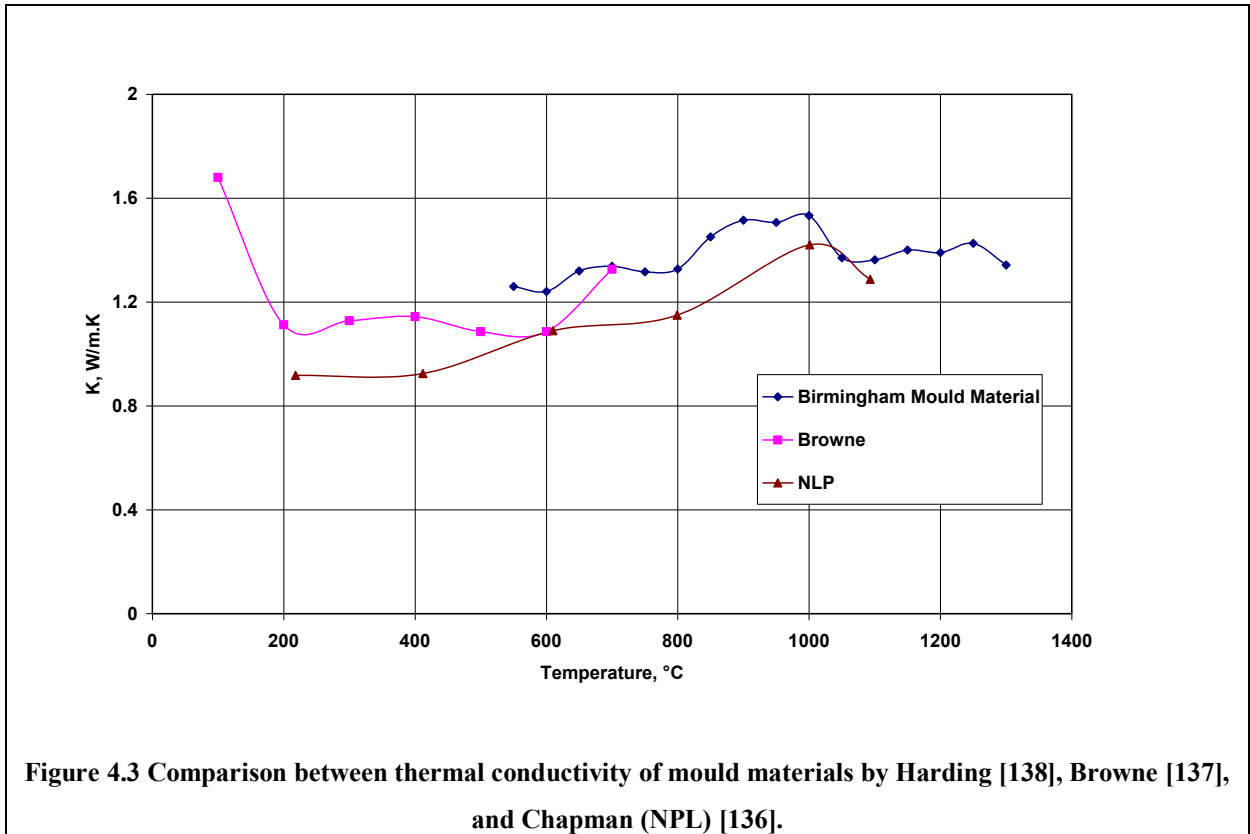
Figure 4.2 shows a comparison between the values of C_p (of molochite 16/30 and shell layers contained molochite 16/30 and zircon or silica slurry) obtained from the existing literature [135, 136, 137]. The values are so much comparable in the temperature range of $300\text{ }^{\circ}\text{C}$ to $1300\text{ }^{\circ}\text{C}$.



b) Thermal Conductivity k

The values of thermal conductivity k were obtained from different sources and showed a relatively close match; as can be seen in Figure 4.3. The main difference between the shell system PGN (zircon and silica slurry with Molochite stucco, provided by the NPL report MAT9 [136]), and the mould system used in the foundry of Birmingham University for investment casting of TiAl [138], is the primary coat of Yttria.

The average difference was 0.25 W/m. K), differences in relative mass and mesh size of each layer could be the reason for this slight disagreement, however the margin of error was not stated in both references.



4.2.2 Data used in ProCast Modelling of Ti-46Al-8Nb Investment Casting in this Research

The shell system used for investment casting of Ti-46Al-8Nb is given in Table 4-1. The bulk density (in the sintered condition) is 2014 kg/m³ [138].

Table 4-1. Consecutive coats of the investment shell

Primary Coat			Intermediate Coats				Back-up coats				Seal coat
Slurry binder	Slurry filler	Stucco	No. of Coats	Slurry binder	Slurry filler	Stucco	No. of Coats	Slurry binder	Slurry filler	Stucco	
Yttria sol	Yttria	Yttria	2	Silica sol	Blend of fused silica and Molochite	30/80 Molochite	5	Silica sol	Blend of fused silica and Molochite	16/30 Molochite	Yes

Two database files contain thermophysical properties of the mould material were created in the pre-processing module of the simulation software ProCast. One of them (Ceramic_2) contained the C_p values of the PGN material as a function of temperature, and the other one (CeramicBirmingham_constant k) contained a constant value of C_p which was the average of the values given in Figure 4.2. The effect of using the variable or the constant value of C_p on the model results was tested and was found to have no influence on the model predictions.

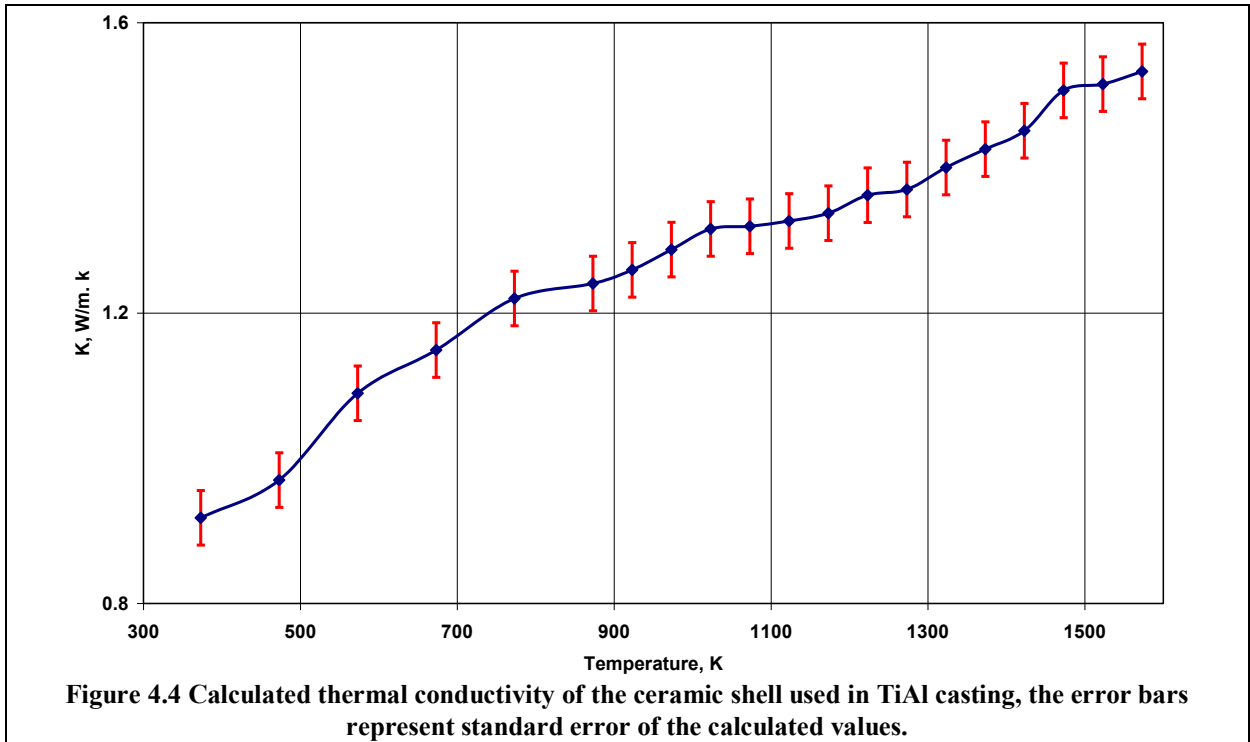
The thermal conductivity (k) was calculated as follows:

$$k = \alpha * C_p * \rho \quad \text{Eq. 4.2}$$

Where: α is the thermal diffusivity of the investment shell used for TiAl at Birmingham University as measured by NPL, ρ is the bulk density in the sintered condition and C_p is the specific heat capacity of the PGN shell [136].

The results of the calculations in the temperature range 100 °C to 1350 °C are given in Figure 4.4. The temperature-dependant k values were stored in the Ceramic_2 database file, and the average value of k (=1.4 W/m. K) was stored in the (Ceramic Birmingham_constant k) database file.

As k of the mould material had a significant role on the solidification time of the casting, the influence of changing the value of k was tested in the sensitivity analysis study.



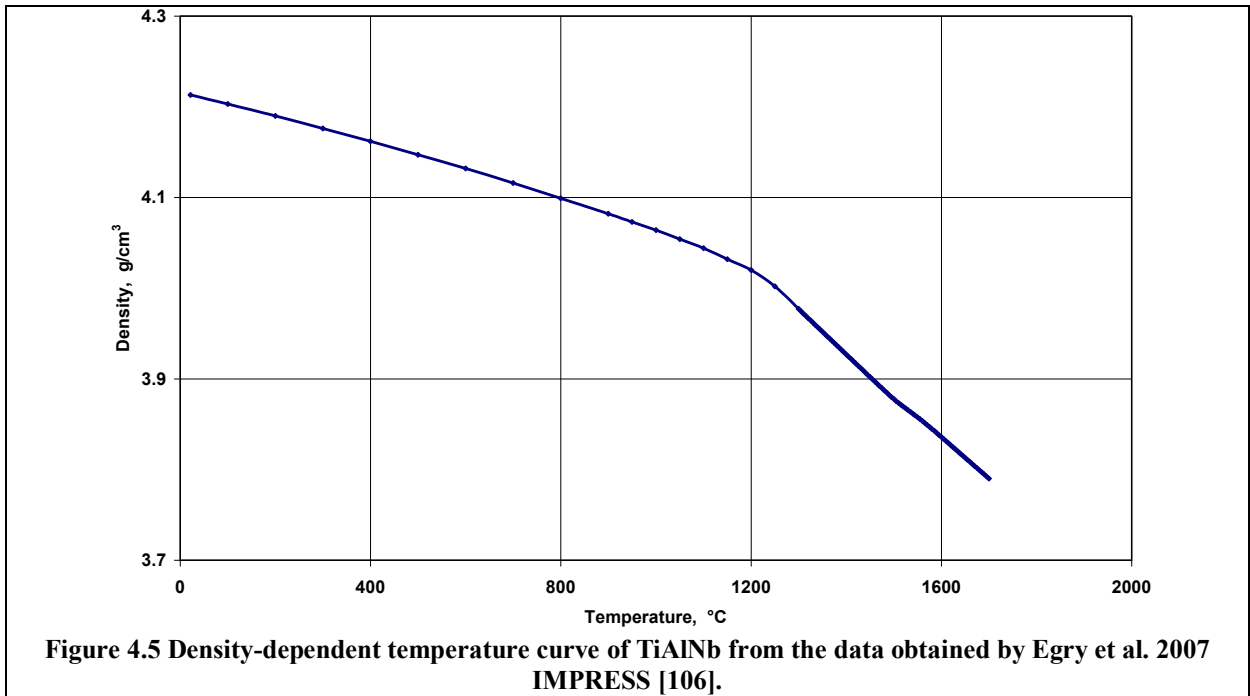
4.3 Thermophysical and Physical Properties of Ti-46Al-8Nb alloy

Thermophysical properties of the casting alloy were considered to be an influencing factor in the casting simulation process, although thermophysical properties of titanium aluminide are very scarce in the literature, and more importantly there was no database of γ -TiAl alloys in the simulation software at the commencement of this research. However, extensive experimental work was carried out as a part of the IMPRESS [106] (Intermetallic Materials in Relation to Earth and Space Solidification) project to measure some of these properties for γ -TiAl alloys.

4.3.1 Density

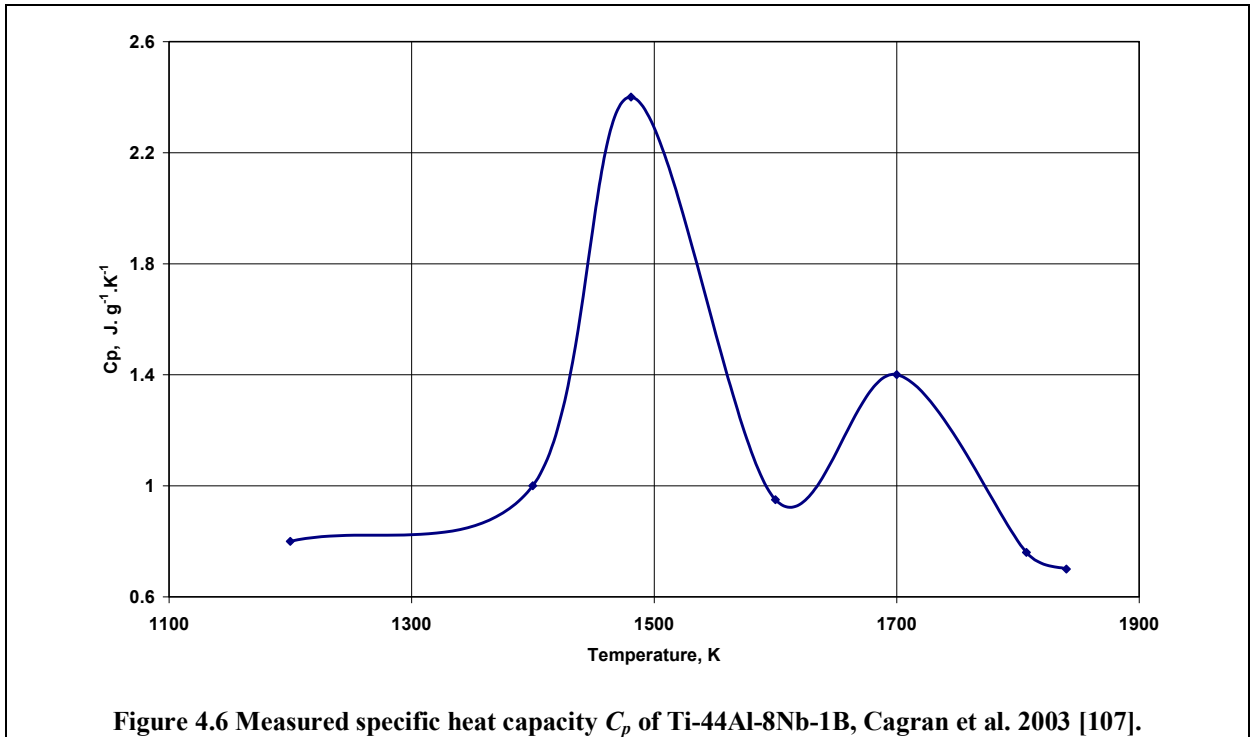
The density of Ti-46Al-8Nb alloy was investigated by the IMPRESS project, and the experimental methods and results are described in Chapter 2. The density of the investigated alloy was obtained as two sets of data in the solid and in the liquid states and combined together to form a continuous curve of density as a function of the temperature.

Figure 4.5 shows the density-dependent temperature curve which was created and stored in the database of the PreCast module for the casting material.



4.3.2 Specific heat capacity C_p

The C_p of Ti-44Al-8Nb-1B alloy was measured by the Differential Scanning Calorimeter (DSC) technique [107], the experimental methods and the obtained results in both solid and molten conditions are described in Chapter 2. Figure 4.6 shows the specific heat capacity C_p versus temperature which was stored as a database file in the PreCast module.



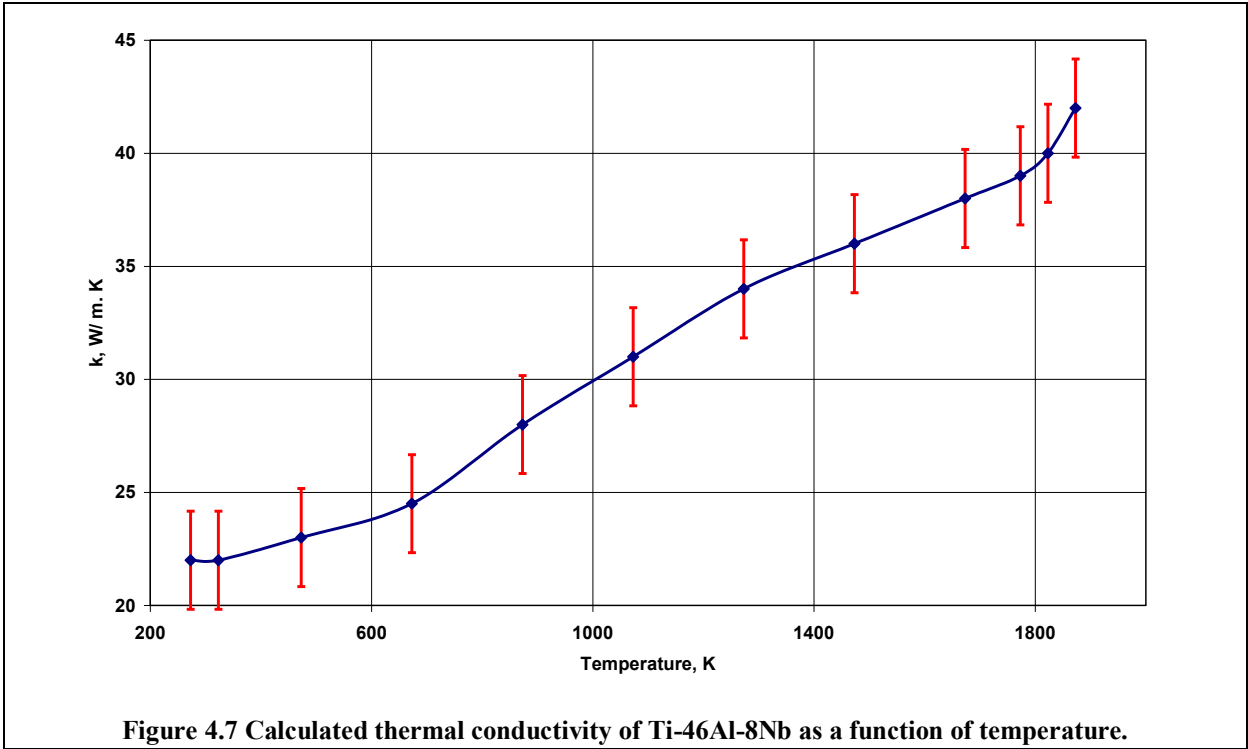
4.3.3 Thermal Conductivity

Thermal conductivity k was calculated by the following equation:

$$k = \alpha(T) \times \rho \times C_p(T) \quad \text{Eq. 4-3}$$

Where $\alpha(T)$ is the thermal diffusivity as a function of temperature, and was measured using the laser flash method [107], $C_p(T)$ is the specific heat capacity as a function of temperature, shown in Figure 4.6, and ρ is the density.

Figure 4.7 shows thermal conductivity k versus temperature, also stored in the database file in the PreCast module. The thermal conductivity of the metal was increased by a factor of 10% of its value, as recommended in Griffiths' study [139] to take into account the influence of fluid flow during pouring.



4.3.4 Latent Heat

The latent heat of fusion of Ti-44Al-8Nb-1B was calculated as the difference between the measured values of the enthalpy, using the pulse heating technique, at the solidus temperature and at the liquidus temperature ($\Delta H_f = 411.5 J.g^{-1}$) [107].

4.3.5 Determination of Fraction of Solid

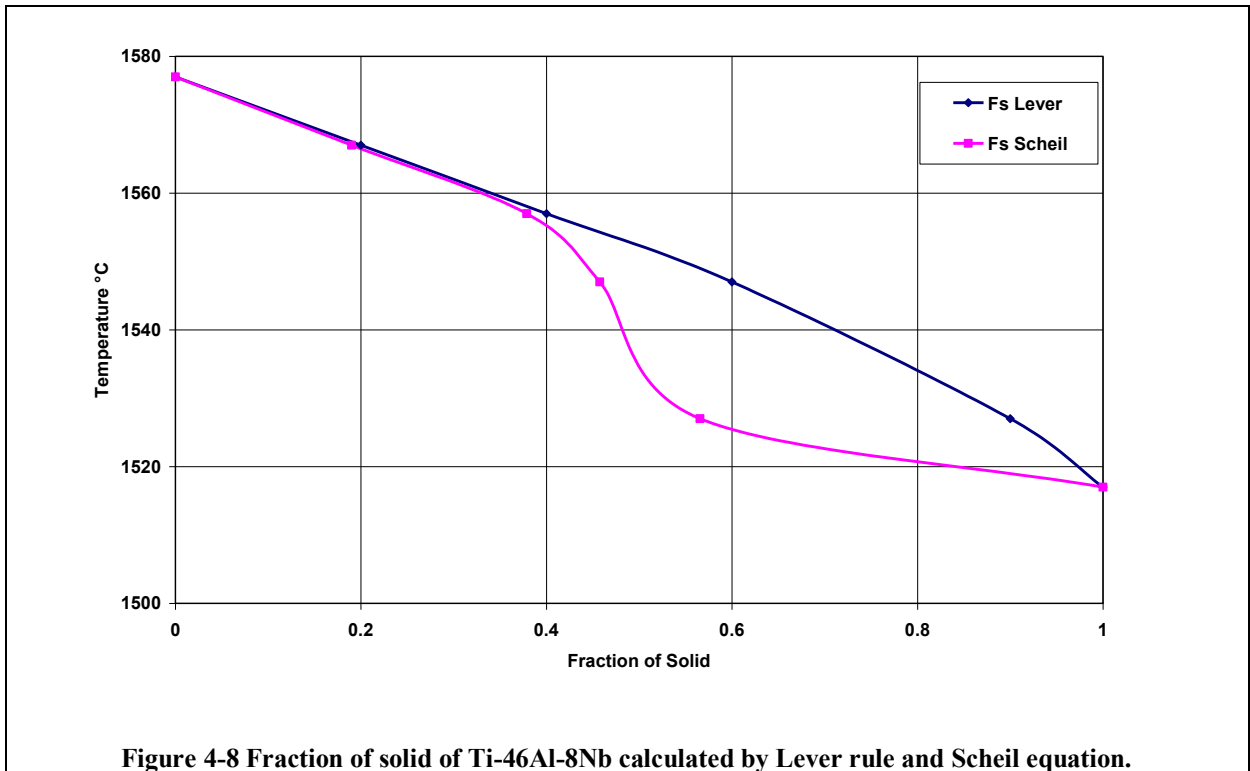
The fraction of solid in the mushy zone determines the release of latent heat of fusion. Fraction solid was calculated by using the liquid and solid compositions and temperatures in the phase diagram shown in Figure 2.5. The Scheil equation for non-equilibrium solidification was used to calculate the fraction of solid as follows:

$$D = \frac{C_s}{C_L} \quad \text{Eq. 4-4}$$

$$f_s + f_L = 1 \quad \text{Eq. 4-5}$$

$$f_s = 1 + \left(\frac{C_s}{C_o * D} \right)^{\frac{1}{D-1}} \quad \text{Eq. 4-6}$$

The Lever rule was also used to calculate the fraction solid and the results were compared with the Scheil equation in Figure 4.8.



Two database files containing both results were created and stored in the PreCast module and the fraction solid calculated by the Scheil equation was used in the Ti-46Al-8Nb casting-simulation models.

4.4 Sensitivity Analysis Tests

The main goal in carrying out these sensitivity analysis tests was to assess the influence of materials properties and boundary conditions on the validity of the model. Since the properties of the investment mould material as well as the casting alloy were from limited literature and had a range of uncertainty, it was essential to investigate how changing these properties would affect the simulation results negatively or positively in comparison with experimentally measured data.

In addition, various options are available in the simulation software regarding how to set the boundary conditions and which thermodynamic/ thermophysical properties should be used according to the restrictions which the software operates under.

The sensitivity analysis tests included the following:

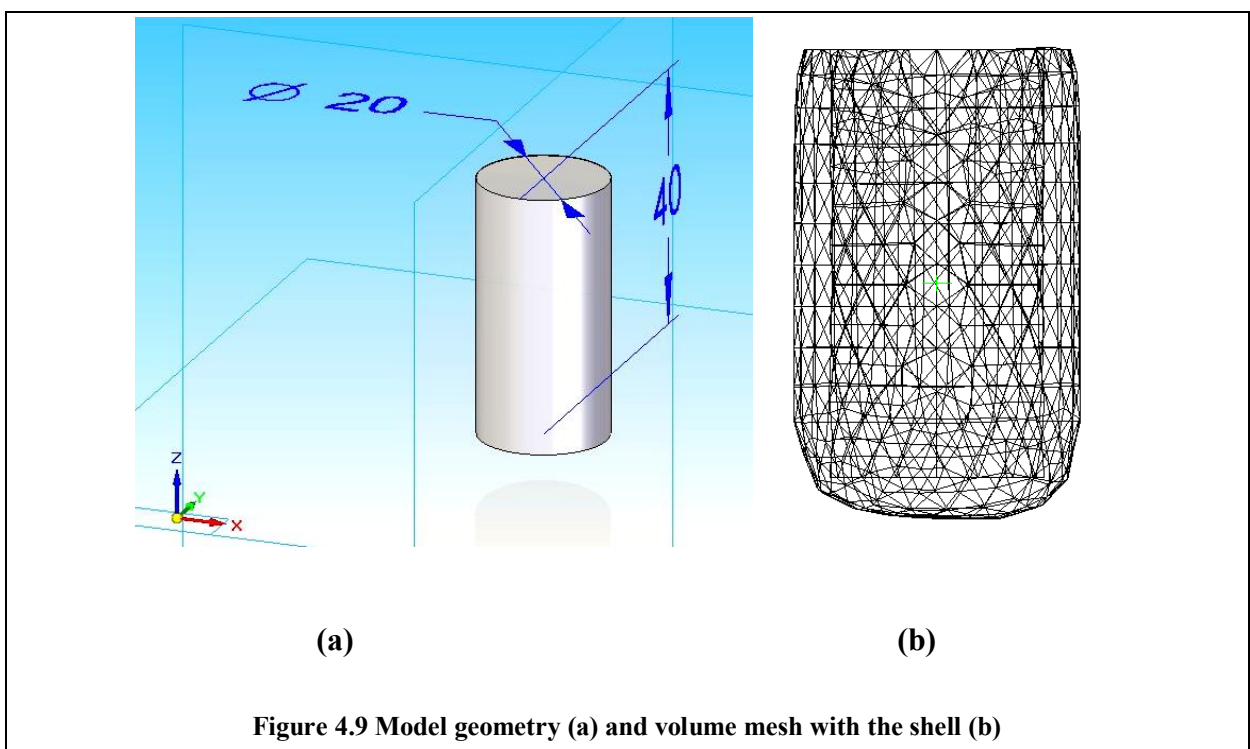
- 1- Thermal conductivity of the mould material
- 2- Heat boundary conditions at the external surface of the mould
- 3- Interfacial heat transfer coefficient

To save computation time, a model with small dimensions and relatively large mesh size was used in some of the tests. Moreover, in order to study the effect of each parameter individually and eliminate the influence of other variables, pure iron was used as the cast alloy in the tests of the effect of mould material, boundary conditions, and interfacial heat transfer coefficient.

The models used in these tests were thermal-only models where the filling process was excluded from the simulation, and the computation process started while the mould was filled with 100% liquid metal.

4.4.1 Solid Modelling and Meshing

A 20 mm diameter, 40 mm long cylindrical shape was created using the commercial software Solid Edge. Figure 4.9 shows the geometry and the mesh of the test model. The surface mesh was generated with a cell size = 1 mm and a 3 mm thickness shell was added, then the tetrahedral volume mesh was produced with the following characteristics: total number of nodes = 2241; total number of elements = 10063.



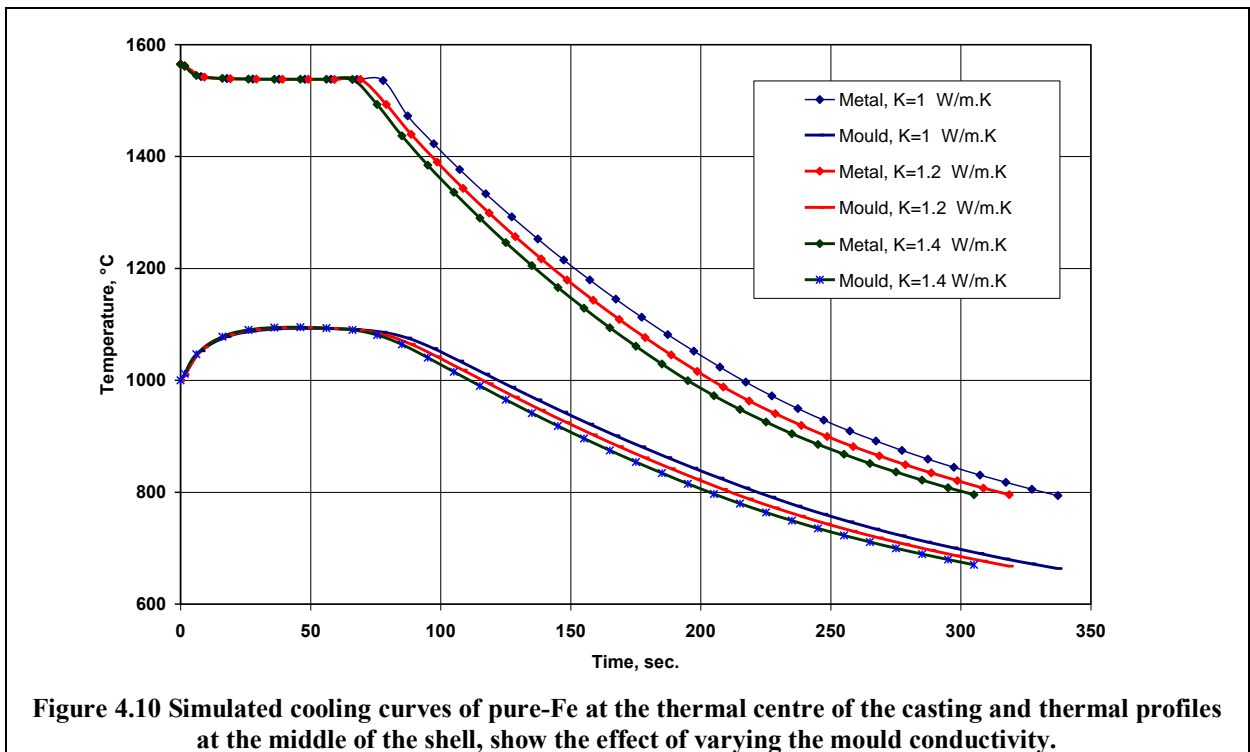
4.4.2 Test 1: Thermal Conductivity of the Mould Material

As discussed in Section 4.2.1, thermal conductivity of the mould material was not documented precisely in the literature. Thus, the influence of varying k of the mould material from a base value of 1 W/m. K to 1.4 W/m. K was studied in a sensitivity analysis test. Three database files of mould materials were created in PreCast with constant k values of 1, 1.2 or 1.4 W/m. K, (all other parameters were fixed), and were assigned as the shell in three different runs.

The same nodes were selected from each run, and the cooling curves were plotted for the nodes at the middle (thickness and height) of the shell and at the thermal centre of the casting.

The test results are shown in Figure 4.10. The model results obtained from the three runs showed that the thermal profiles of the mould were so much comparable. However, increasing the thermal conductivity from 1 W/m. K to 1.2 W/m. K decreased the solidification time by 11%, while the results converged when k changed from 1.2 W/m. K to 1.4 W/m. K and the solidification time decreased by 4% only. This implies that thermal conductivity of the ceramic mould could have a significant effect on the solidification time of the casting.

Based on this test and the calculations of thermal conductivity of the mould, given in Section 4.2.2, the database file of “CeramicBirmingham_constant k ” with $k=1.4$ W/m. K was used in the rest of the following models.



4.4.3 Test 2: Heat boundary conditions (Interface heat transfer coefficient between the mould and its surroundings, h_b)

A boundary condition was assigned to the outer surface of the mould as a heat transfer coefficient between the mould and its surroundings. Four simulation runs were carried out in order to study the effect of this parameter on the results of the Pure-Fe casting-simulation model.

Constant values of the boundary heat transfer coefficient were used in three of the test models: 10, 100 and 1000 W/m². K, while the heat transfer coefficient was made a function of time, in the range of 20 to 200 W/m². K for 300 seconds for the fourth run.

The results of the runs are shown in Figures 4.11 and 4.12. The cooling curves at the centre of the Fe-casting showed that the solidification time decreased by 15%, 30%, and 45% as the mould/surroundings heat transfer coefficient increased from (a base value) 10 W/m². K to 100 W/m². K, 200 W/m². K and 1000 W/m². K, respectively. This variation in time of the steady state interval could imply that the rate of heat extraction from the mould surface had an influence on the metal temperature during the exothermic reaction of losing the latent heat of fusion.

On the other hand, the model with the lower heat transfer coefficient (10 W/m².K) showed the slower cooling rate in the solid state part of the metal cooling curve. The metal cooling curve with a heat transfer coefficient of 100 W/m². K was the closest to that obtained when the heat transfer coefficient was made time-dependent.

The effect of the interfacial heat transfer coefficient between the mould and its surroundings on the thermal profile of the shell was much more obvious. As can be seen in Figure 4.12, the higher the heat transfer coefficient the faster the cooling rate and the lower the maximum temperature that the mould can reach.

Again, the curve with $100 \text{ W/m}^2\text{K}$ was close to the curve with the variable heat transfer coefficient, except that the maximum temperature was decreased by 14 % in case of the variable heat transfer coefficient.

This test showed that the boundary condition at the mould/surroundings interface has a significant role on the predicted cooling curves of both the metal and the mould, and hence this parameter was then experimentally measured.

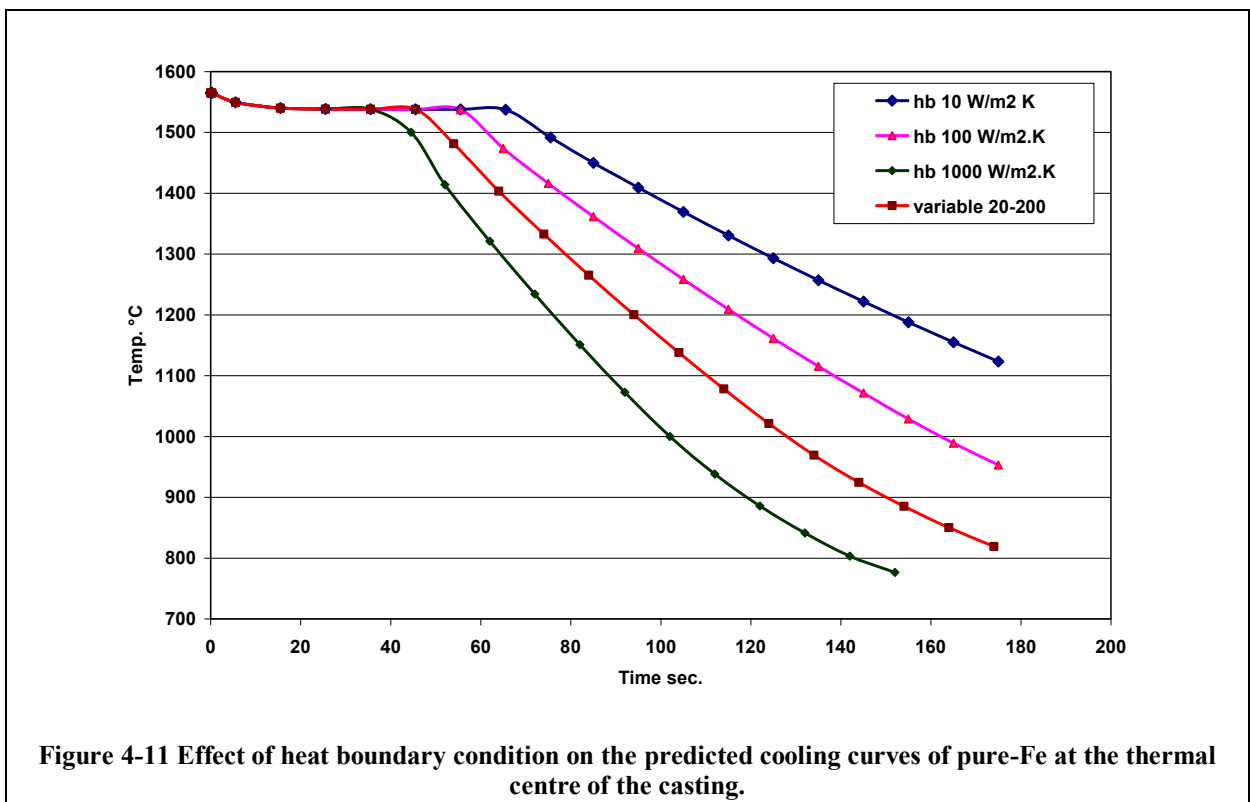


Figure 4-11 Effect of heat boundary condition on the predicted cooling curves of pure-Fe at the thermal centre of the casting.

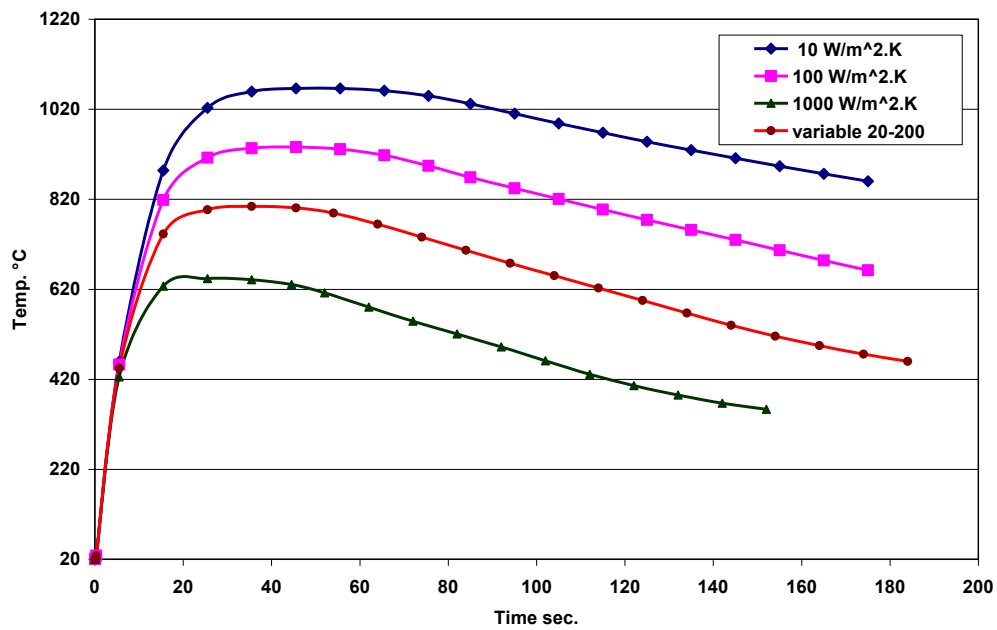


Figure 4-12 Effect of heat boundary condition on the results of the test model of pure-Fe casting at the middle of the shell.

4.4.4 Test 3: Interfacial Metal/Mould Heat Transfer Coefficient (h)

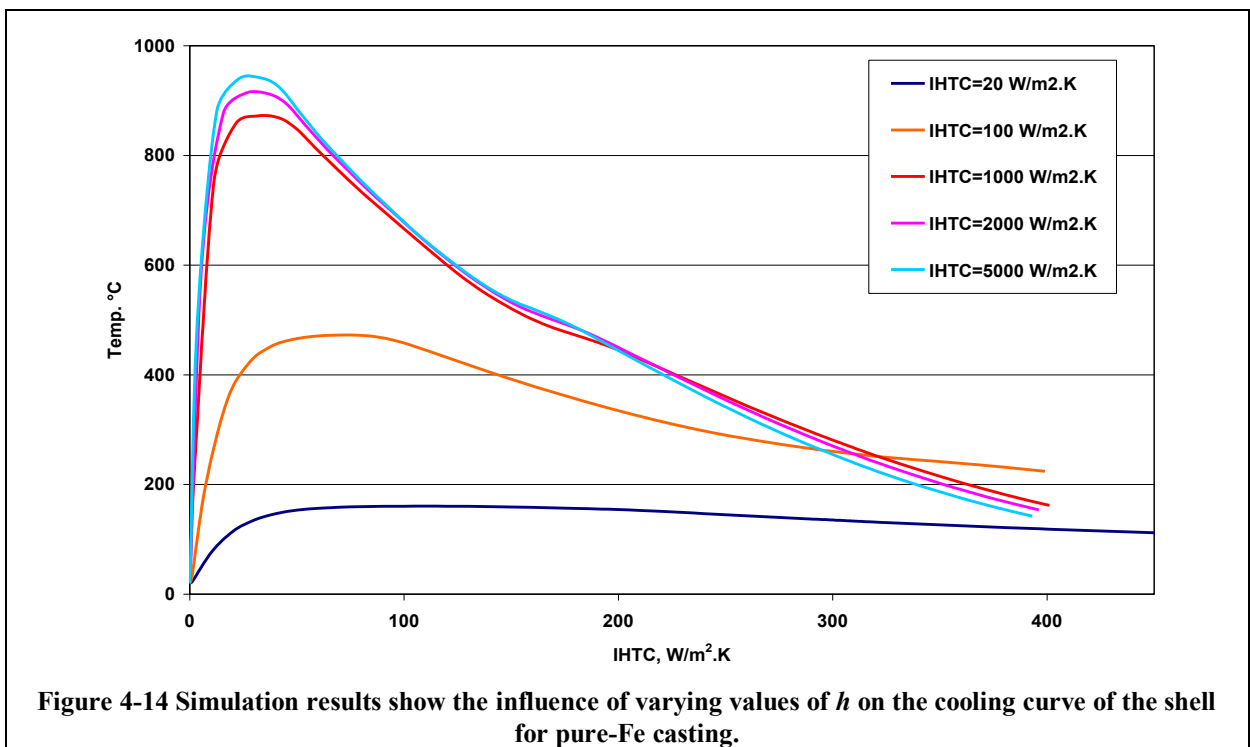
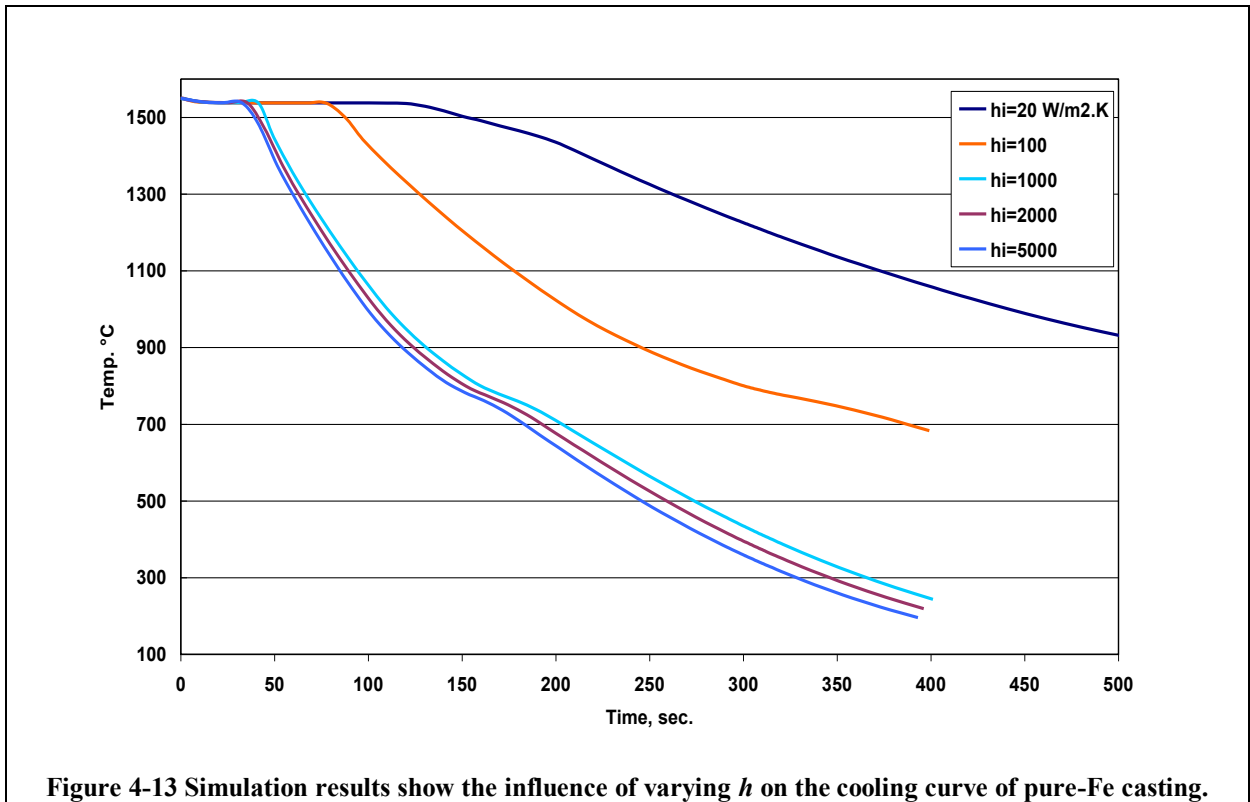
In this sensitivity analysis test the metal/mould interface heat transfer coefficient (h) was investigated in terms of its influence on the simulation results. Thus, constant values of h from 20 to 5000 W/m². K were used in several runs of the Pure-Fe test model, and the results are shown in Figures 4.13 and 4.14.

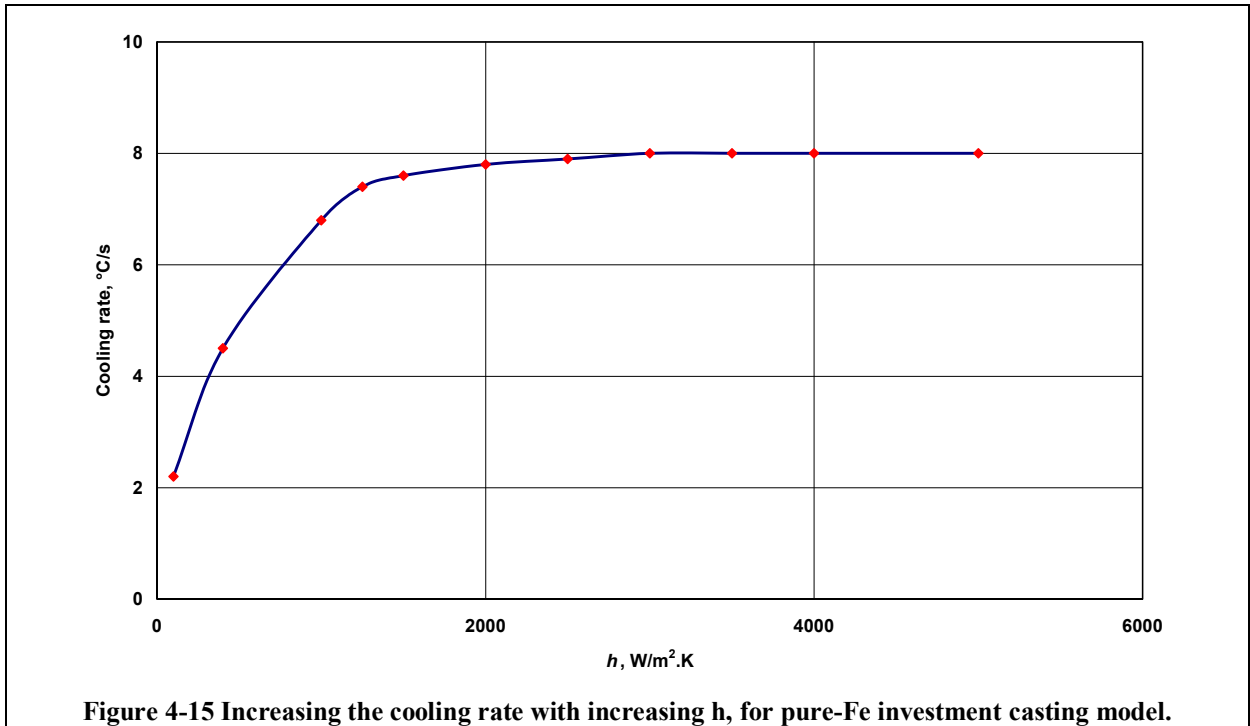
It is clearly shown in the plotted results that h significantly influenced the solidification time and the cooling rate of the casting in addition to affecting the thermal profile of the mould material. As h increased the solidification time decreased along with increasing cooling rate.

Figure 4.15 shows that the cooling rate of the casting increased as h increased from 20 to 2000 W/m². K, but is then almost constant between 2000 and 5000 W/m². K.

Additionally, the metal/mould interface heat transfer coefficient had a significant influence on the cooling curve of the shell, the maximum temperature that the mould material reached at

the middle of its thickness increased with higher h values, as shown in Figure 4.14. However, the cooling rate was almost constant as h increased in the range of 2000-5000 $W/m^2 \cdot K$.





4.4.5 Estimation of the Metal/Mould Interfacial Heat Transfer Coefficient

The heat transfer coefficient at the metal/mould interface can be defined as the ratio of heat flux to the temperature drop at that interface. As the molten metal is poured into the mould, a good contact at the metal/mould interface is expected. However, when solidification starts a solid skin is formed against the inner mould surface and the solidified metal contracts, pulling itself away from the interface creating a gap, which contains the ambient gases (Argon in this study).

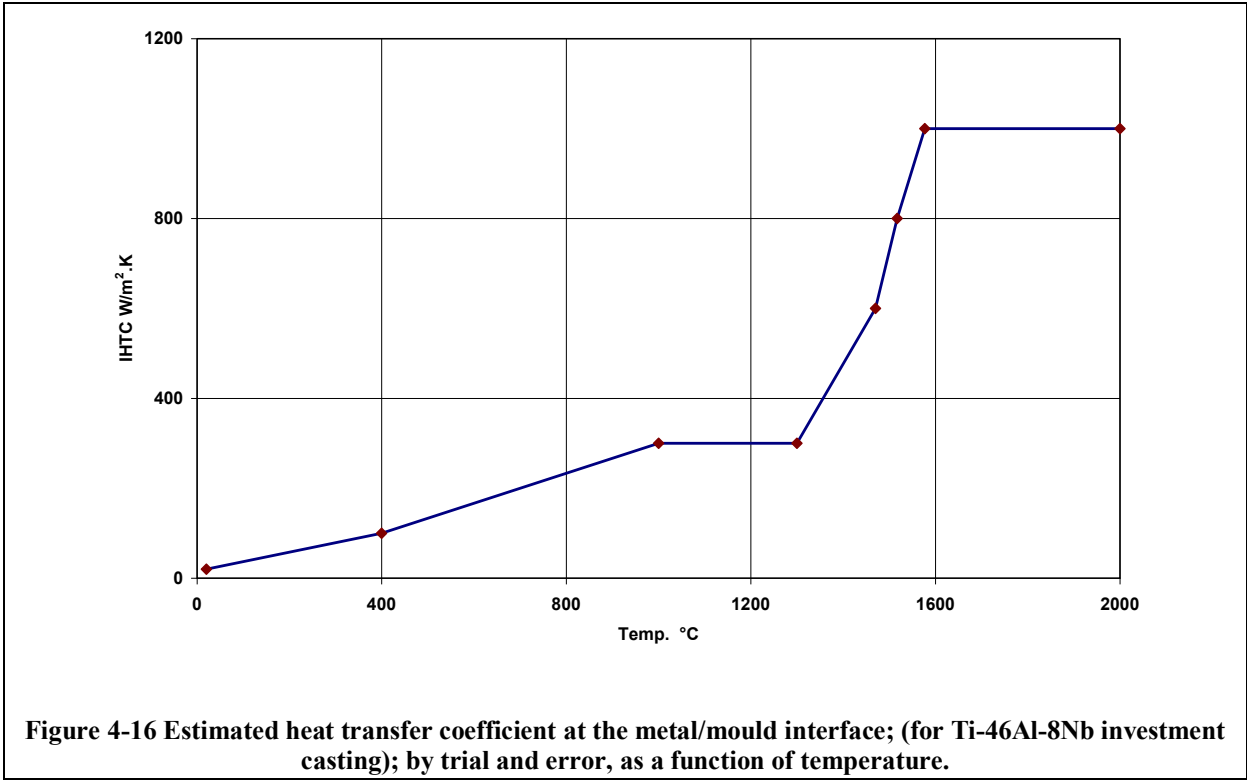
The size of this gap mainly depends on the roughness of both surfaces (the solid skin and the inner mould surface), and also depends on the metallostatic head pressure, and the coefficient of thermal expansion for the alloy and the mould [139]. The size of the gap is unknown and heat transfer through it is affected by its gas content and properties. The effect of that gap on h is considered and hence, the h is not a constant value, but is a function of time or temperature, and it is expected to vary with both according in the following stages:

- Pouring stage.
- During the mushy zone interval (T_1 to T_s); while the metal loses its sensible heat and the rate of heat transfer from the solidifying metal to the mould is high.
- During the formation of the gap between the solid skin and the mould wall, h decreases and it is continuing to decrease as the thickness of the solid increases.

Based on the available values of h in investment casting of comparable alloys and the previously discussed effect of the gap, h as a function of temperature was estimated by a trial and error method.

Several runs of the model of Ti-46A-8Nb temperature measurement experiments (of which the model geometry, meshing and parameters are given in section 4.6) were carried out and the model results were matched with the measured cooling curves.

Ultimately, the pattern of h shown in Figure 4.16 yielded a good convergence between the model results and the measured cooling curves. A maximum h of $1000 \text{ W/m}^2 \cdot \text{K}$ was assigned at the beginning of solidification, and then its value was decreased due to the formation of a gap between the solidified skin and the inner mould surface. A gradual decrease from 1000 to $300 \text{ W/m}^2 \cdot \text{K}$ associated with phase transformations during and after completion of solidification, was estimated to occur.



4.5 Modelling of the Ceramic Test

4.5.1 Solid Modelling and Meshing

The cooling of the ceramic shell experiments were simulated using the ProCast software.

A 5 mm diameter, 200 mm long cylindrical bar was created by using the commercial software Solid Edge. The surface mesh was generated with a cell size = 0.5 mm. A shell with 10 mm thickness was built up around the rod. The volume mesh was produced with a total number of nodes = 81186 and a total number of tetrahedral elements = 374780.

4.5.2 Model parameters and boundary conditions

Refractory Alumina was assigned as the core (the inner rod). The shell material was assigned as the mould with the database of (Ceramic Birmingham constant K). The cooling started from an initial mould temperature of 1000 °C, and the ambient temperature was set to 20 °C.

The heat transfer coefficient for the heat loss from the mould surface during cooling was calculated as a function of temperature using the measured cooling curves for the ceramic shell at 1000 °C in Argon atmosphere and in vacuum. Calculations of the boundary heat transfer coefficient are given in Chapter 5.

4.5.3 Verification of Mould/Surroundings Heat Transfer Coefficient

Three nodes were selected from the simulation model, at distances from the centre line of the rod which corresponded to the locations of the thermocouples. Cooling curves of these three nodes were plotted and consequently, matched with the measured cooling curves. Good agreement between measured and simulated cooling curves was found, as shown in Section 5.5.3.

4.6 Modelling of Solidification of Gravity Casting of Ti-46Al-8Nb

Two thermal-only gravity casting simulation models were validated using the measured cooling curves of Ti-46Al-8Nb investment casting in a mould at room temperature and in a preheated-mould at 1000 °C.

4.6.1 Geometry and Meshing

A solid model of cylindrical shape with 100 mm diameter and 150 mm height was created by using the commercial software Solid Edge. The surface mesh was generated with a cell size = 1.2 mm.

A shell of 10 mm thickness was added to the surface mesh, then the tetrahedral volume mesh was produced with a total number of nodes = 209714 and total number of elements = 911237.

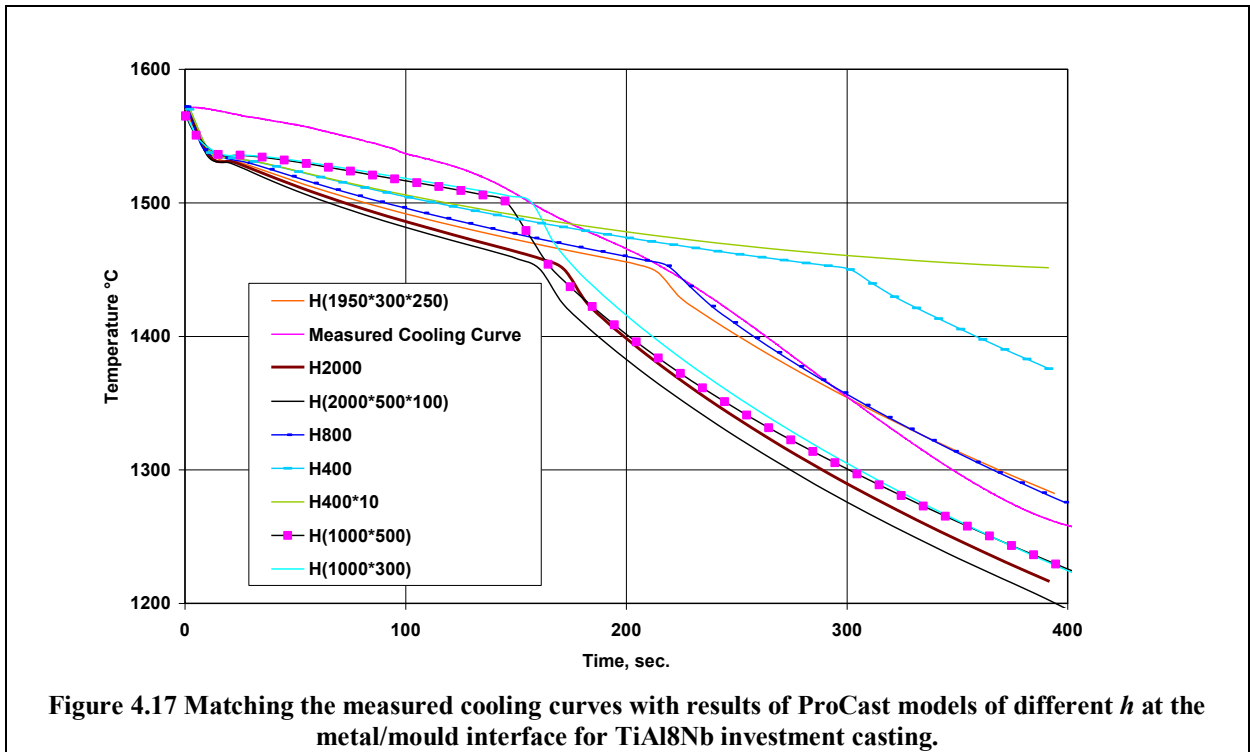
4.6.2 Initial temperatures and boundary conditions

The initial conditions of the model were assigned as the initial temperatures of the casting and the preheating temperature of the mould. The highest temperature recorded by the immersed thermocouple, 1572 °C, was assigned as the casting initial temperature.

The model was run twice, the first run with the mould temperature assigned to be 20 °C and the second run with the mould temperature of 1000 °C. The mould was initially 100% filled with molten metal at the initial temperatures. The database files which contained the calculated heat transfer coefficient and the estimated interface heat transfer coefficient as a function of temperature were assigned as the heat boundary conditions at the mould wall and at the metal/mould interface respectively.

The model was then used to estimate the interface heat transfer coefficient by using different h values as a function of temperature or as a constant value in several runs and the simulated

cooling curve at the position corresponded to the position of the thermocouple was matched with the measured cooling curve as shown in Figure 4.17.



4.7 Thermal Model of Ti-46Al-8Nb Test Casting

The ProCast thermal model solves the Fourier heat conduction equation, including the latent heat of solidification in order to obtain the temperature distribution, thermal gradient and solidification time.

4.7.1 Geometry and Meshing

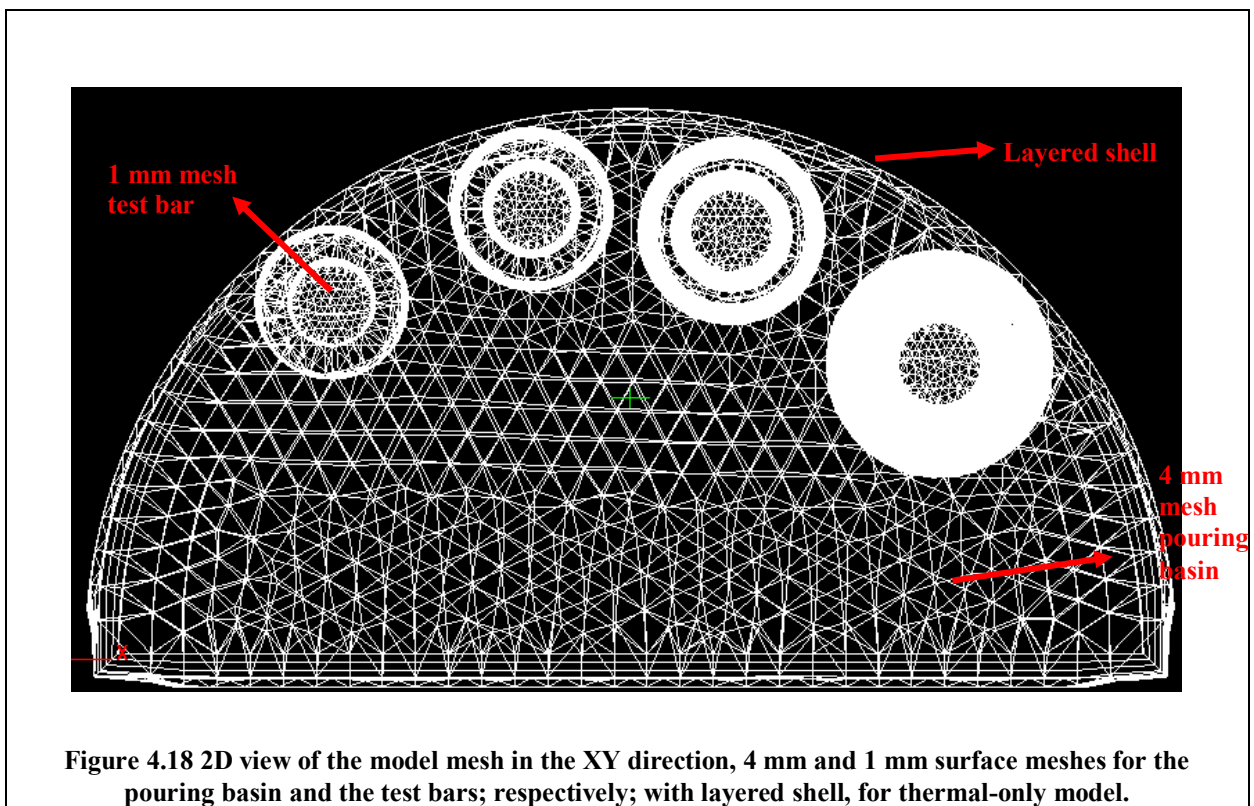
A Solid Edge model was produced with the actual dimensions of the test casting which composed of a pouring basin of the shape of a half-cylinder to which four 100 mm height bars were attached.

The bars were shaped with the taper angles and attached to the pouring basin in the order given in Table 3.3.

A coarse mesh with cell size = 4 mm was created for the pouring basin in order to reduce the computation time whilst a finer mesh of 1 mm cell size was created for the test bars.

A layered shell with 5 mm thickness was created and assigned as the mould material. A 2D view of the model mesh with the shell is shown in Figure 4.18. The model contained 73367 nodes and 228004 elements.

An enclosure with 27080 nodes and 54156 elements was created as a surface mesh and merged with the volume mesh of the model in a multiple-meshes PreCast file.



4.7.2 Boundary Conditions

A heat boundary condition was applied to the outer surface of the ceramic shell. The heat transfer coefficient between the mould surface and surroundings (Argon atmosphere at pressure of 200 mbar) was a function of temperature and had values in the range of 15 W/m². K at 20 °C to 100 W/m². K at 1200 °C, as measured for a ceramic shell in Argon atmosphere.

The interface heat transfer coefficient between the mould inner surface and the casting metal was set as a function of temperature as well, and had values from 20 W/m². K at 20 °C to 1000 W/m². K at 1600 °C (as previously estimated by trial and error using ProCast for the investigated alloy and casting conditions).

The initial casting temperature was set to 1580 °C, and the mould preheating temperature was set to 1000 °C in the first run, and then the model was rerun with a mould temperature = 500 °C.

The “view factor” parameter was used in order to consider the effect of radiation of the free surfaces of the test bars on temperature distribution and thermal gradient of the adjacent bars.

4.7.3 Analysis of the Model Results

The post-processor module "ViewCast" was used for visualizing the model results and for computation of the Niyama criterion function. Nodes were selected along the middle section of the test bars in the direction of pouring. Mapping factors M , temperature gradient G , cooling rate L and isotherm velocity V_s were calculated at 1523 °C, which corresponds to 90 % of the solidification interval of the investigated alloy. Mapping factors as calculated by using the constants: $a= 1$, $b= 0$, $c= 1$ and $d= -0.5$ were set to represent the Niyama criterion:

$$Nc = \frac{G}{\sqrt{L}} \quad \text{Eq. 4-7}$$

Where G is the magnitude of the temperature gradient in the three Cartesian directions, and is calculated using the following equation:

$$G = \sqrt{\left(\frac{dT}{dx}\right)^2 + \left(\frac{dT}{dy}\right)^2 + \left(\frac{dT}{dz}\right)^2} \quad \text{Eq. 4-8}$$

The cooling rate L is calculated as a “linear interpolation” between the upper temperature T_{upper} and lower temperature T_{lower} . In this study $T_{\text{upper}} = T_{\text{liquidus}} + 2$ and $T_{\text{lower}} = T_{\text{solidus}}$ [94].

The results of all bars were analysed individually and matched with the experimentally measured porosity contents (area percentage).

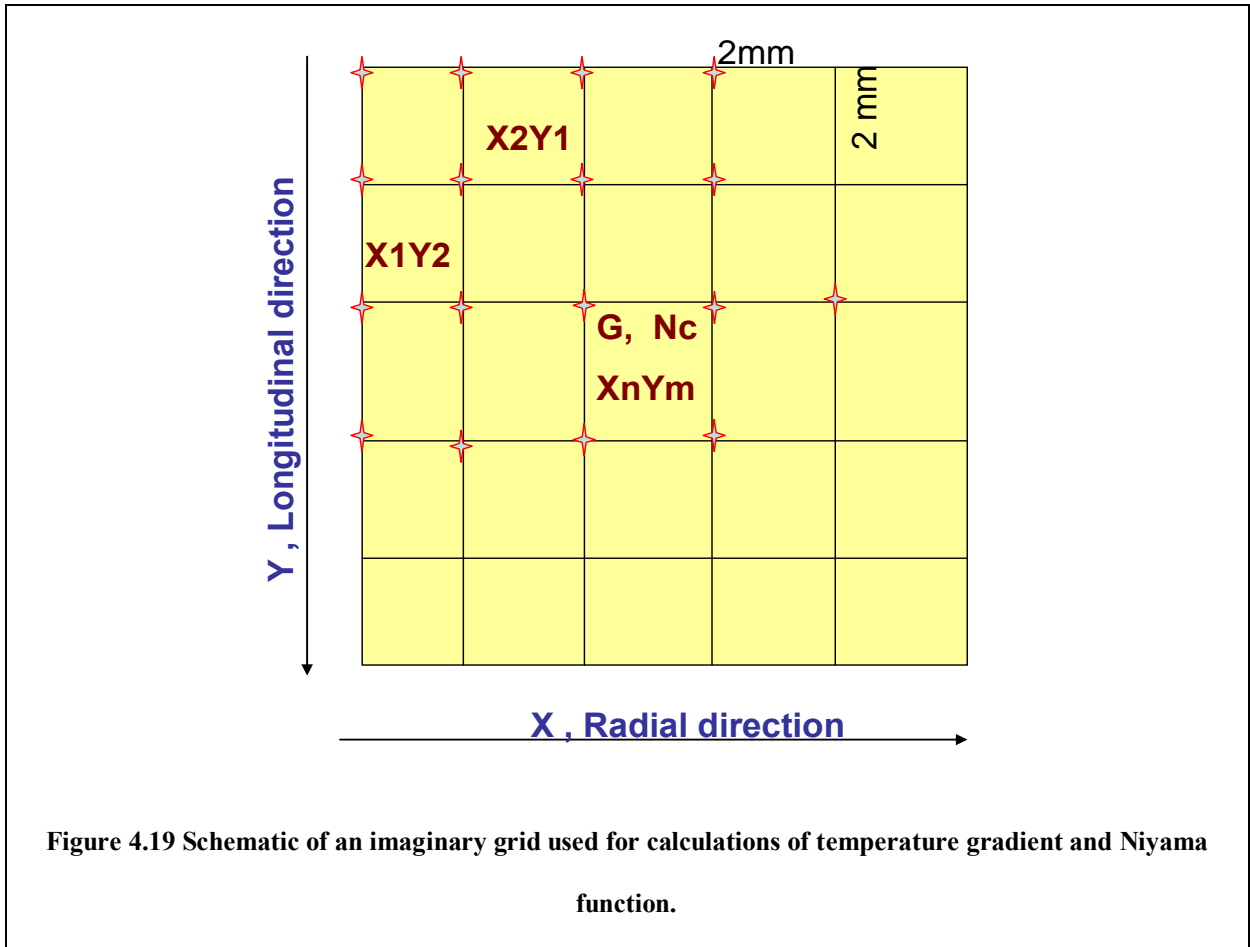
The following steps summarise how the mapping factor (and G for some test bars) was determined for any XY positions of the longitudinal middle sections of the test bars:

- Viewing the XY plane of the longitudinal cross sections of the test bars of the model
- An imaginary grid with a cell size of 2 x 2 mm (in the X and Y directions) was applied on each cross-section of the test bars.
- Nodes at the corners of each cell of the imaginary grid were chosen.
- The temperature gradient (magnitude of G) and the value of the Niyama function (N_c) for each node were recorded.
- Calculating the average values of G and N_c at all positions by calculating the average of these values at the corners of the $X_n Y_m$ cell.

Figure 4.19 shows schematically the imaginary grid applied on the longitudinal section of the parallel sided bar to calculate the average of N_c and G .

To compare the different criterion used to predict porosity, the feeding efficiency parameter (LCC): $G.t^{2/3}/V_s$ ($^{\circ}\text{C}.s^{5/3}.\text{mm}^{-2}$) was calculated for some of the test bars using the ProCast results of isotherm velocity, local solidification time and local temperature gradient at 1523 $^{\circ}\text{C}$.

Temperature gradient and Nc calculations



4.8 Tilt-filling Model of Ti-46Al-8Nb Test Casting

4.8.1 Geometry and Meshing

With the intention of simulating the filling process, the liquid metal (inside the crucible) has to be added to the model and has to be assigned an individual domain. Thus two surface meshes were created separately for the casting and for the liquid metal in an attached upside down crucible. The two meshes were assembled as two bodies separated by an equivalent surface.

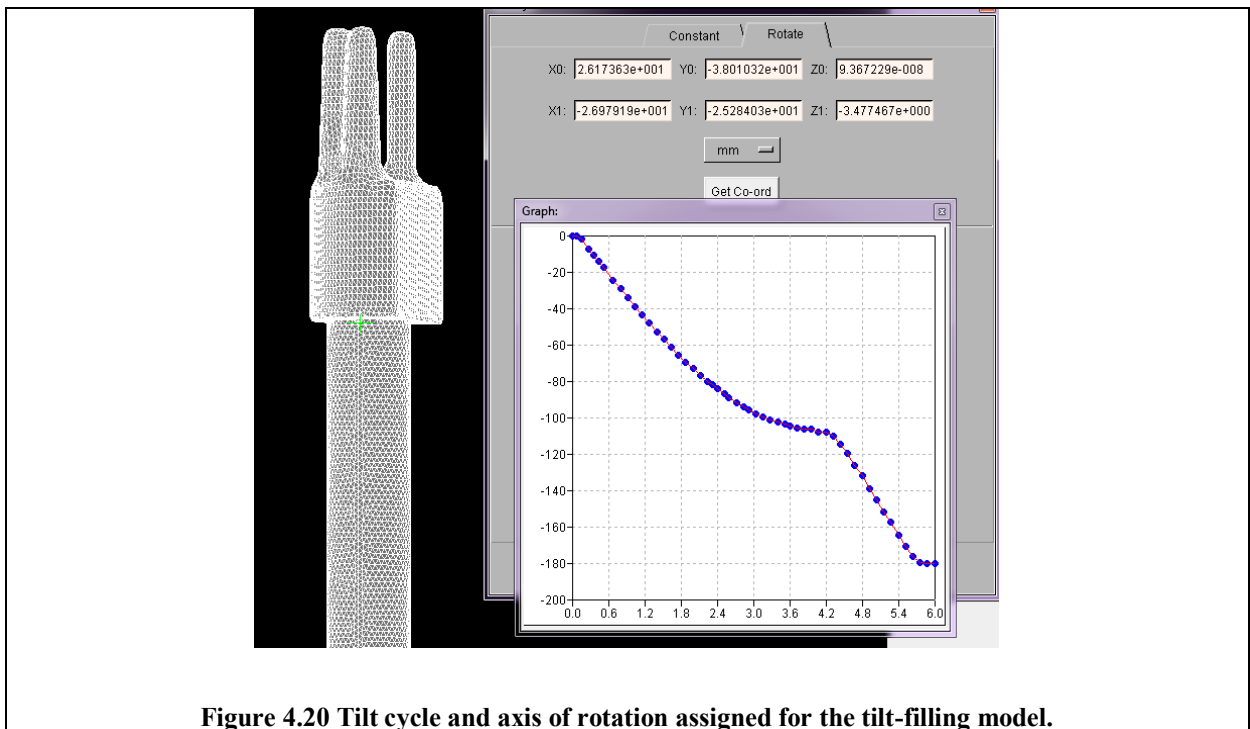
A coarse mesh with 4 mm cell size was created for the crucible and the pouring basin in order to reduce the computational time whilst a finer mesh with 1 mm cell size was created

for the test bars. A shell with 5 mm thickness was created and assigned as the mould material.

The tetrahedral volume mesh was then produced for the assembled surface meshes, consisting of 597329 nodes and 3018588 elements. An enclosure with 6771 nodes and 13538 elements was finally added to the model as a separate surface mesh. The geometry of the model is shown in Figure 4.20.

4.8.2 Boundary Conditions and Process Assignment

The model boundary conditions and initial temperatures were the same as in the thermal-only model, see section 4.7.2. The tilt-filling process was assigned for the model by choosing the axis of rotation and saving the rotation-cycle file as theta versus seconds as shown in Figure 4.20. The model results for 500 °C and 1000 °C mould temperatures were analyzed as described in section 4.7.3.

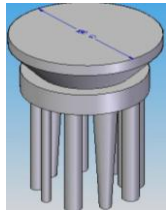


CHAPTER 5

PREDICTION OF SHRINKAGE POROSITY IN Ti-46Al-8Nb AND DETERMINATION OF THERMAL BOUNDARY CONDITIONS

The following table summarises the experimental castings and temperature measurements which have been carried out with the aim of investigating the effect of casting and cooling parameters on the formation of casting defects in Ti alloys.

Table 5.1: Summary of experimental work

Material	Casting/Cooling Process	Casting Design	Preheating Mould Temperature	Analysis of Results
C. P. Ti	Gravity-Casting 	200 mm long cylindrical bars of 10, 15, 20 and 30 Φ , one tapered bar of angle 2.25°	1000 °C	1. Assessment of casting defects by X-ray
Ti6Al4V				2. Examination of microstructure and macrostructure features by optical microscopy and SEM
Ti46Al8Nb				3. Quantitative analysis of porosity and macrostructure were determined by digital image analysis technique
Ti46Al8Nb	Tilt-Casting 	100 mm long bars: cylindrical bars of 10 and 20 mm Φ . tapered bars with angles of 0.5°, 1°, 1.5°, 2°, 2.5°	1000 °C	1. Assessment of casting defects by X-ray
			500 °C	2. Examination of microstructure and macrostructure features by optical microscopy and SEM 3. Quantitative analysis of porosity by digital image analysis technique 4. Quantitative analysis of macrostructure were determined by digital image analysis technique 5. Temperature measurements, cooling curves were used in thermal analysis and to determine interface heat transfer coefficient
Temperature measurements during cooling and solidification	<ul style="list-style-type: none"> • Ceramic shell of 16/30 Molochite • Gravity casting of Ti-46Al-8Nb • Tilt Casting of Ti-46Al-8Nb 	<ul style="list-style-type: none"> • Cooling in vacuum and in 200 mbar of Argon • Cooling curves at thermal centre, at interface, and in the mould. 	1000 °C	<ul style="list-style-type: none"> • Cooling curves were used to calculate interfacial heat transfer coefficient between mould material and its surroundings in Argon and in vacuum. • Thermal Analysis of the cooling curves.

5.1 Effect of Casting Parameters on the Formation of Casting Defects in Commercial Purity Titanium, Ti-6Al-4V and Ti-46Al-8Nb Investment Casting Alloys

The radiographs of the test bars of cylindrical shape with 10, 15, 20 and 30 mm diameters and 200 mm height, of commercially pure (CP) Ti, and Ti-6Al-4V, cast into moulds at 500 and 1000 °C are shown in Table 5.2. Radiographs of Ti-46Al-8Nb test bars, gravity cast into preheated moulds at 1000 °C under 200 mbar of Argon gas, are shown in Table 5.3.

5.1.1 Effect of Mould Temperature

Incomplete filling and cold laps were formed in case of C. P. Ti cast into moulds at 500 °C and at 1000 °C. On the other hand, as the mould temperature increased from 500 °C to 1000 °C all test bars of the Ti6Al4V were fully filled and no cold laps were formed.

The radiographs also show that the amount of gas bubbles in C. P. Ti and in Ti6Al4V decreased as the mould temperature increased from 500 °C to 1000 °C.

5.1.2 Effect of Castings' Size and Geometry

The smaller bars with diameters of 10 mm and 15 mm were severely misrun and contained cold laps with smooth round edges. Although a cold lap was found only in the 15 mm diameter bar of Ti-6Al-4V alloy with 500 °C mould temperature.

The radiographs of 20 and 30 mm diameter test bars clearly revealed the presence of internal gas bubbles in all of them. In addition, the 30 mm diameter bars contained fewer bubbles than the smaller diameter bars at both mould temperatures.

In addition, centreline shrinkage appeared in the larger bars with 20 and 30 mm diameters of all of the three alloys, with this type of defect being formed due to poor feeding, and hence did not resemble the type of regularly distributed (v-shaped) layer porosity.

The influence of casting geometry on cooling rate and temperature gradient and subsequently on the formation of casting defects in Ti and its alloys was studied by changing the geometry of the test bar in the same mould from a cylindrical to a tapered shape.

As can be seen in the radiographs of the tapered bars, no gas bubbles were found in the CP Ti and Ti-6Al-4V alloys at both mould temperatures. Other internal defects could not be detected in the radiographs, which implies that changing the bar geometry could minimize shrinkage porosity; this was investigated in more detail in the following sections.

5.1.3 Effect of Alloy Composition

The cylindrical bars of Ti-46Al-8Nb were prone to severe shrinkage porosity with a v-shaped repetitive distribution which is known as layer porosity. The x-ray of the tapered bar of 2.25° does not show evidence of layer porosity.

A comparison between the radiographs in Table 5.2 and 5.3 of the three investigated alloys; CP Ti, Ti-6Al-4V and Ti-46Al-8Nb, showed that cylindrical bars of Ti-46Al-8Nb contained severe layer porosity, while test bars of C. P. Ti and Ti-6Al-4V did not show layer porosity. Despite the fact that promoting directional solidification by using the tapered geometry effectively reduced the quantity of layer porosity, it wasn't completely eliminated, as will be discussed in more detail in section 5.4.

A close visual inspection of the longitudinal EDM sections of the three Ti alloys showed that macro shrinkage was found in both CP Ti and Ti-6Al-4V at the thermal centre of the cast bars, while layer porosity was very clear in the Ti-46Al-8Nb bar, as can be seen in Figure 5.1. Figure 5.2 shows polished and etched sections of 20 mm diameter bar of Ti-46Al-8Nb, the arrangement of the layer porosity was clearly shown in the etched macrograph where the pores were located and dispersed in the interdendritic regions and arranged in layers parallel to the direction of the advancing solidification front.

Table 5.2: Radiographs of the test bars of gravity casting (top pouring) of CP Ti and Ti6Al4V alloy in 500 °C and 1000 °C mould temperatures, different diameters cylindrical bars show casing defects while the tapered bars appear sound in the radiographs.

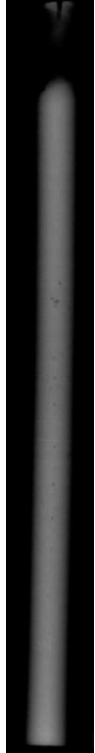
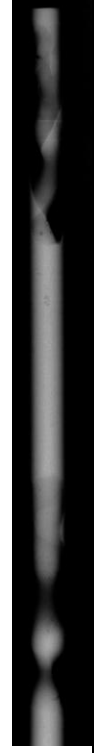
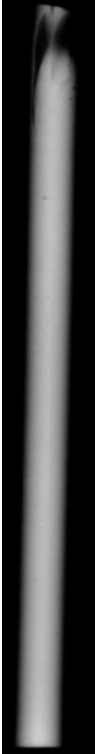
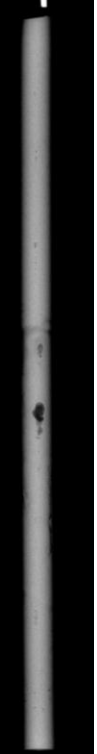
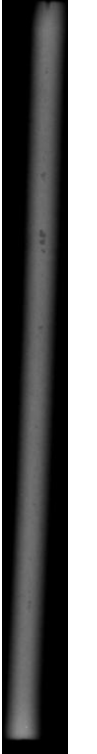
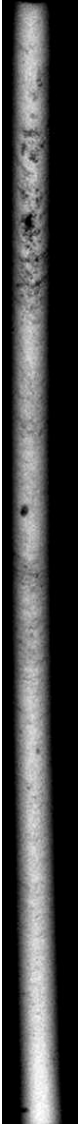
Alloy	CP Ti					Ti6Al4V				
Geometry	10 \varnothing	15 \varnothing	20 \varnothing	30 \varnothing	Tapered	10 \varnothing	15 \varnothing	20 \varnothing	30 \varnothing	Tapered
M. T.										
500 °C										
1000 °C										

Table 5.3: Radiographs of the test bars of gravity casting (top pouring) of Ti-46Al-8Nb alloy in 1000 °C mould temperature, different diameters cylindrical bars show layer porosity, while it is not appearing in the tapered bar.

				
10 mm \varnothing	15 mm \varnothing	20 mm \varnothing	30 mm \varnothing	Tapered

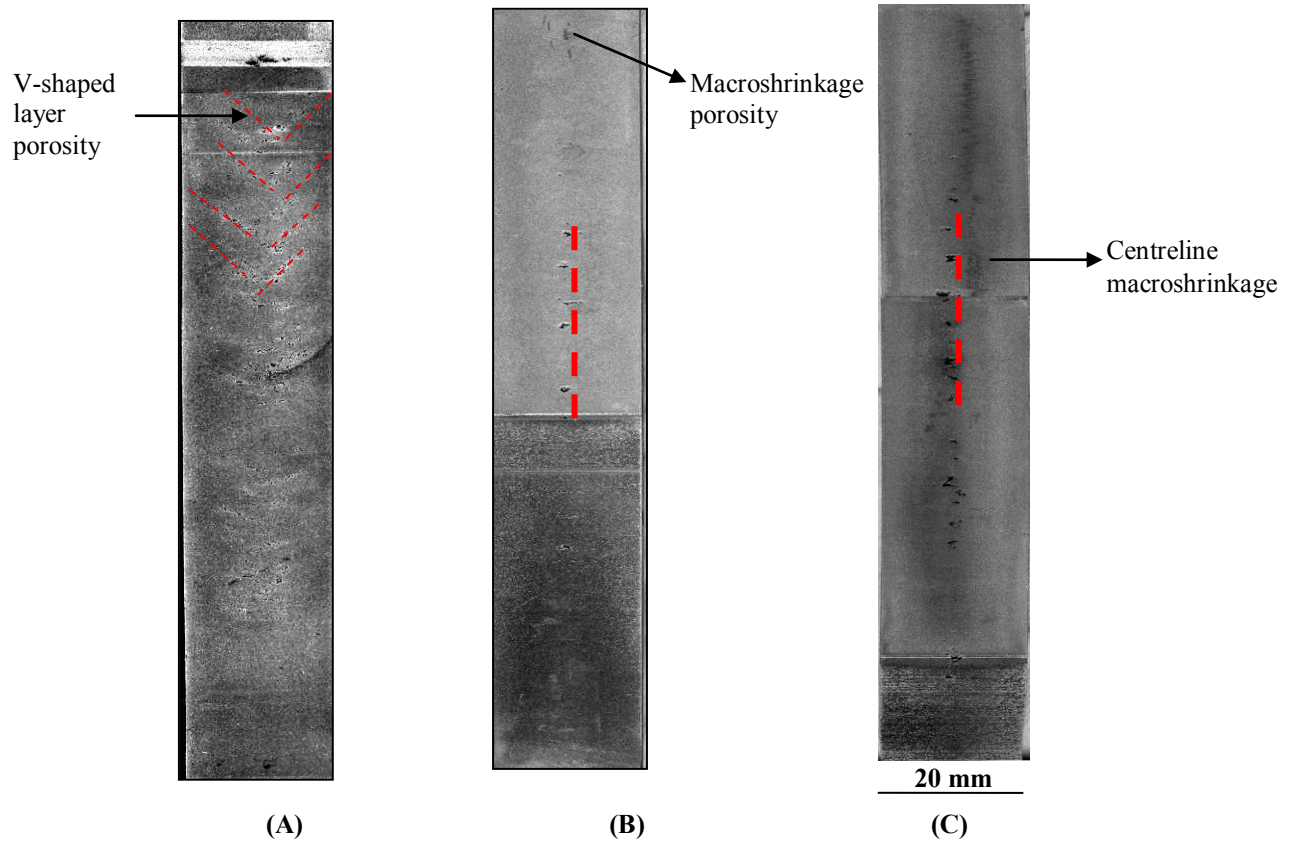


Figure 5.1 EDM sections of Ti-46Al-8Nb (A), CP Ti (B) and Ti-6Al-4V (C) of 20 mm diameter, 200 mm length gravity cast into preheated moulds at 1000 °C

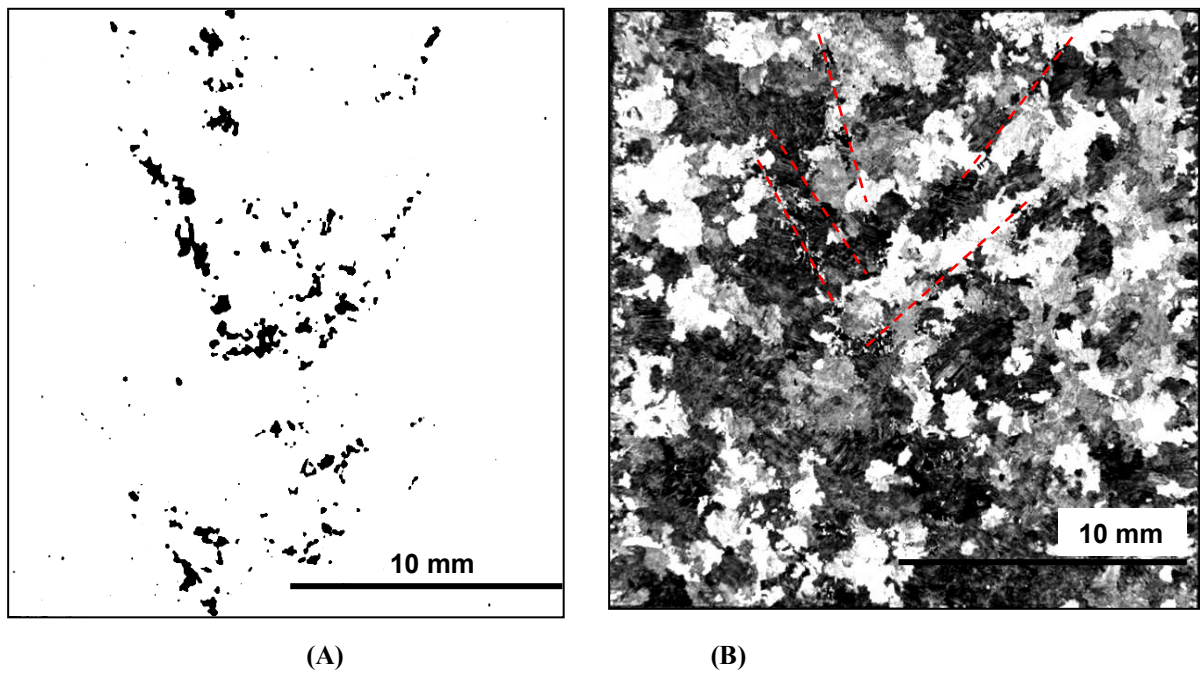


Figure 5.2 As-polished (A) and macrostructure (B) of the worst section of 20 mm diameter bar, (Sample A in Figure 5.1, of Ti-46Al-8Nb and mould at 1000 °C), in the direction of pouring, the red-dotted lines annotate some of the layer porosity in the etched section.

5.2 Microstructure and Macrostructure of the Investigated Alloys

5.2.1 Microstructure and Macrostructure of Commercial Purity Titanium

Figure 5.3 (a) shows the macrostructure of CP Ti, with the sample being taken from the 20 mm test bar, gravity cast into a mould at 500 °C. The thin chill zone at position (a) was followed by a columnar zone at (b), and a core of equiaxed grains at (c). The micrograph in Figure 5.3 (b) shows that the microstructure of commercial purity titanium consisted mainly of coarse α platelets.

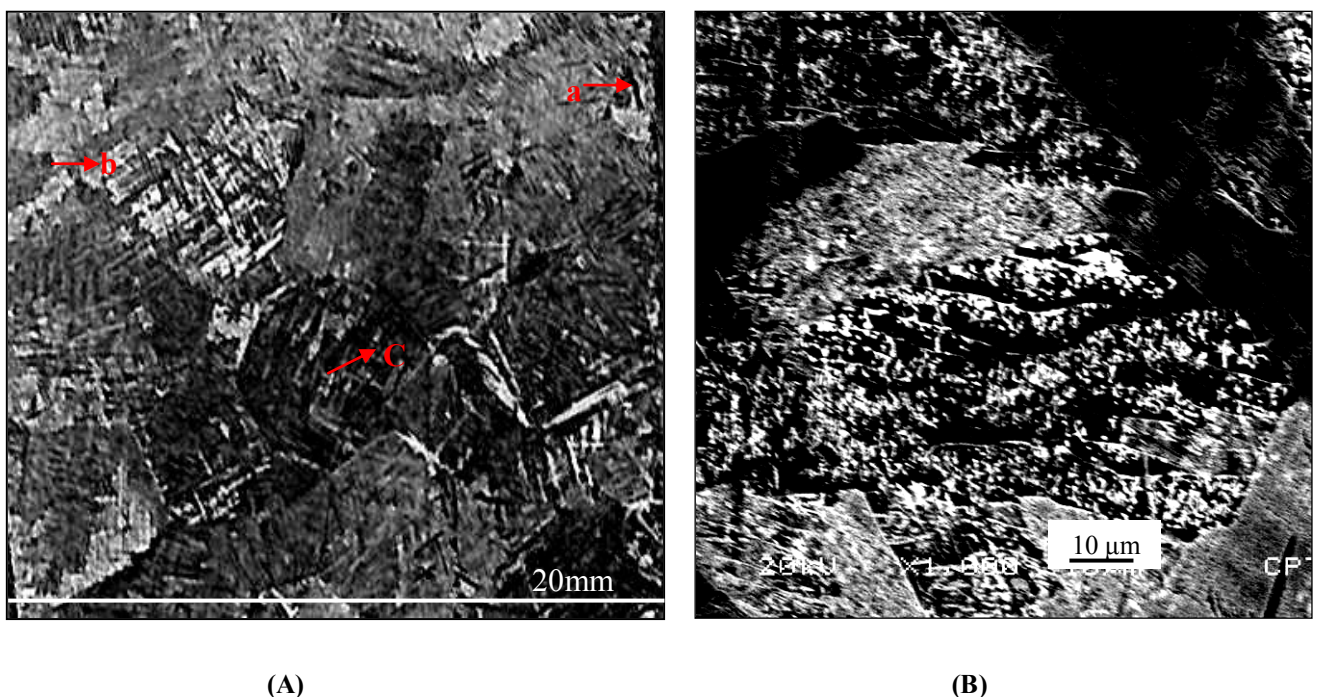


Figure 5.3 Macrostructure of CP Ti, gravity casting in mould preheated to 500 °C, (A) macrostructure of longitudinal section of a sample from the 20 mm diameter bar and (B) SEM image of microstructure.

5.2.2 Microstructure and Macrostructure of Ti-6Al-4V

The predominant feature that characterized the microstructure of the Ti-6Al-4V alloy was the (basket-weave) pattern, constituted of coarse plates of α -phase with thin dark regions of β phase, as shown in the micrographs in Figures 5.4 and 5.5. This arrangement resulted from the transformation of the bcc (β) titanium into hcp (α) titanium, whereas α lamellar nucleated and grew inside the prior β grains, corresponding to the twelve orientation relationships as

discussed in Chapter 2. The macrostructure, as shown in Figure 5.5 (a) consisted mainly of coarse columnar grains and a central equiaxed zone, the chill zone was not clear in the transverse section.

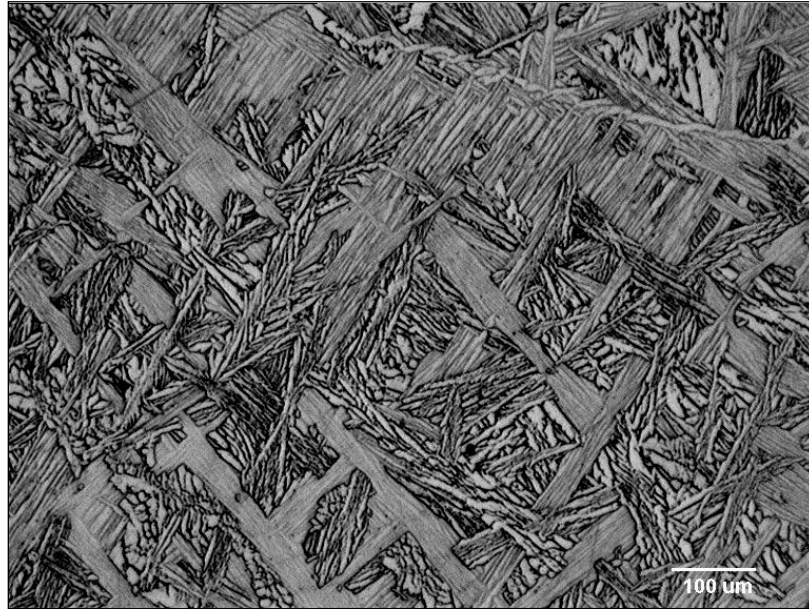
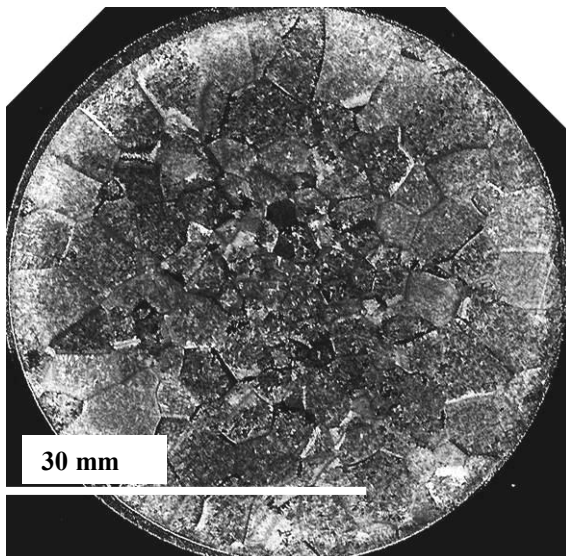
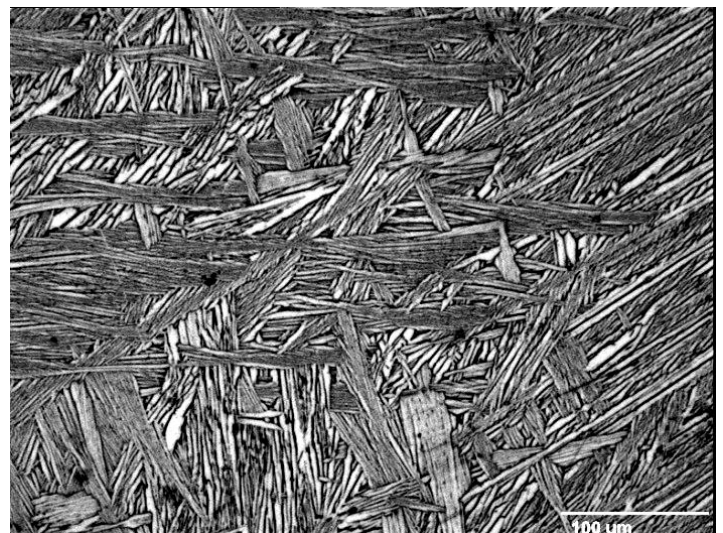


Figure 5.4 Microstructure of Ti-6Al-4V; sample from 20mm diameter test bar, mould preheating temperature was 500 °C.



(A)



(B)

Figure 5.5 Microstructure of Ti-6Al-4V; sample from 30 mm diameter test bar, mould preheating temperature is 1000 °C.

5.2.3 As-Cast Structure of Ti-46Al-8Nb Gravity Casting

Figure 5.6 shows the as-cast structure of a longitudinal section from the middle length of the cylindrical bar with 15 mm diameter cast with 1000 °C mould temperature, gravity cast.

The macrograph shows that the chill zone occurred on both sides of the structure, where fine grains were formed against the mould walls in a perpendicular direction. Coarse columnar grains aligned in a preferred orientation can be seen extended from both sides of the macrostructure. In addition, relatively fine equiaxed grains can be observed too, dispersed in the interior zone of the as-cast structure.

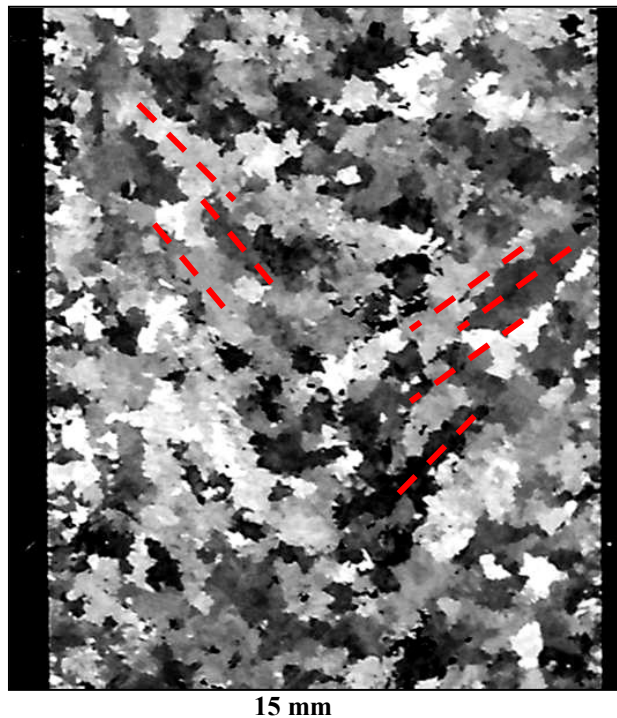


Figure 5.6 Macro-camera image of longitudinal section of Ti-46Al-8Nb gravity casting, M.T is 1000°C, sample from the middle of 15 mm diameter bar in the direction of pouring, red-dotted lines show the direction of some columnar grains ended by the CET.

Aiming to study the macrostructure of the Ti-46Al-8Nb gravity cast bars in more detail, macrographs the whole longitudinal sections of three bars of 10, 15, and 20 mm diameters, from the top to the end of the bars, in the direction of pouring, were examined and are shown in Figure 5.7.

The macrographs are presented at a one-to-one scale, the thin chill zone can be detected on both sides of the structure of the three bars. However, the samples were examined by using image analysis software which provided closer examination under higher magnifications. It was observed that the equiaxed grains formed the structure just below the feeder. As the equiaxed zone expanded downwards, the predominant feature of the macrostructure was the equiaxed grains in the 20 mm diameter bar.

The macrostructure in the smaller bars of 10 mm and 15 mm diameter consisted of columnar grains extended from the free end and from both sides along the vertical section of the bar, and relatively fine equiaxed grains at the centre. In addition, inspection of the macrostructure of etched transverse sections, (Figures 5.10 to 5.14), showed the expected increase in grain size as the bar diameter increased.

The mean grain size increased from 0.69 grain/mm^2 in the 10 mm diameter bar to 0.32 grain/mm^2 in the 30 mm diameter bar. As for the tapered bar of 2.25° angle, the average grain size decreased gradually from 0.3 grain/mm^2 at the top to 0.59 grain/mm^2 at the middle, and the finest grains of 0.68 grain/mm^2 at the smallest cross-section of the bar.

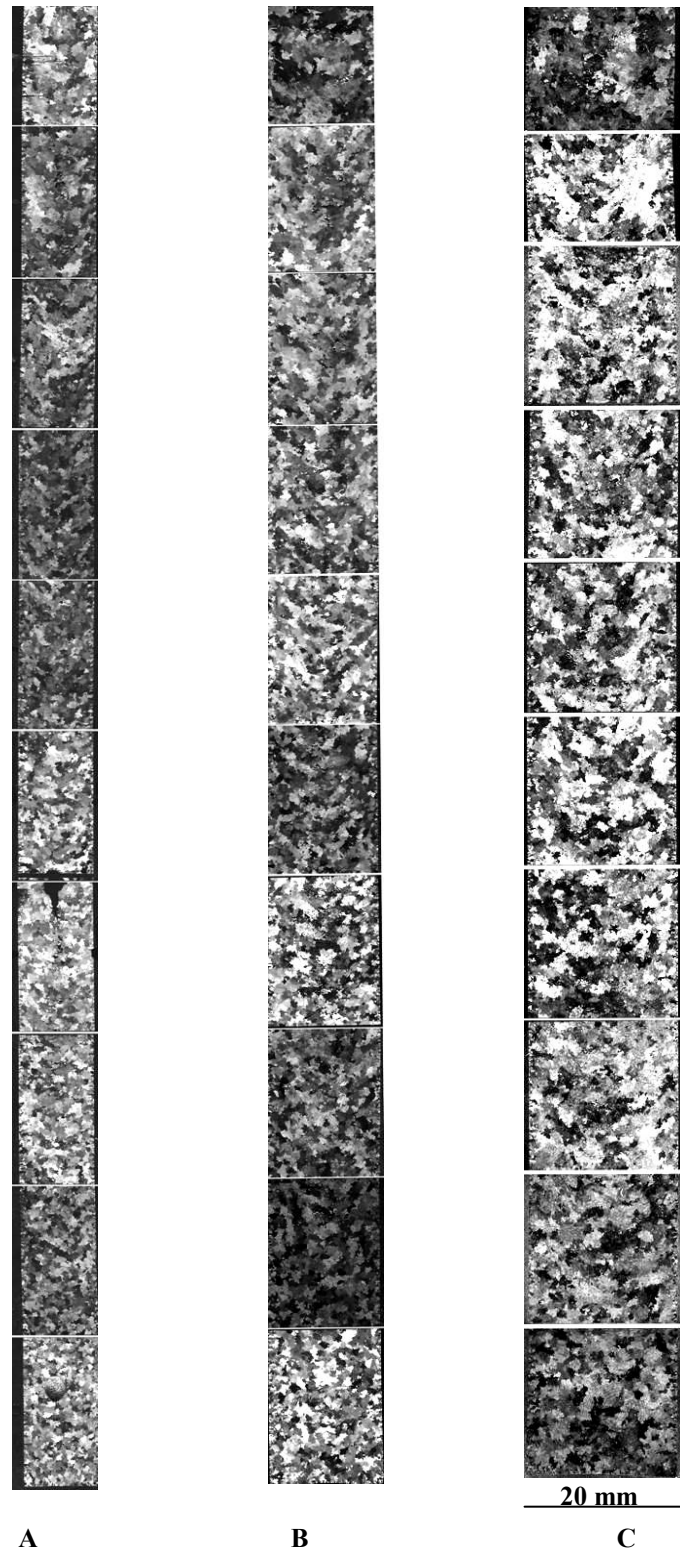


Figure 5.7 Macro-camera images of longitudinal sections in the direction of pouring of 10 mm diameter (A), 15 mm diameter (B) and 20 mm diameter bars, gravity casting of Ti-46Al-8Nb in preheated mould at 1000 °C.

5.2.4 Microstructure and EDS Analysis of the Ti-46Al-8Nb Gravity Casting

Figure 5.8 shows the microstructure of the Ti-46Al-8Nb alloy, which consisted of lamellar eutectoid, bright regions enriched with Nb, and a darker phase of interdendritic γ enriched with Al. A fine lamella eutectoid ($\alpha_2 + \gamma$ TiAl), as was expected from the Ti-Al phase diagram, (see Figure 5.44).

The EDS analysis of some selected points and areas at different positions of the samples revealed the heterogeneity of the as-cast structure, as shown in Figure 5.9, with the results also shown in Table 5.4. Microsegregation of Nb could be observed at the bright regions, for instance, at the position of spectrum 2. The Nb was enriched in the core of the dendrites with a segregation coefficient of 0.21 %. While the Al segregation coefficient was 0.15 % in the interdendritic γ phase. However, detecting microsegregation is a complicated process that requires extensive experiments and EDS analysis. QDS (quenching during directional solidification), provides more reliable information about microsegregation of Al and Nb in different phases than the information that could be provided by the as-cast microstructure examination.

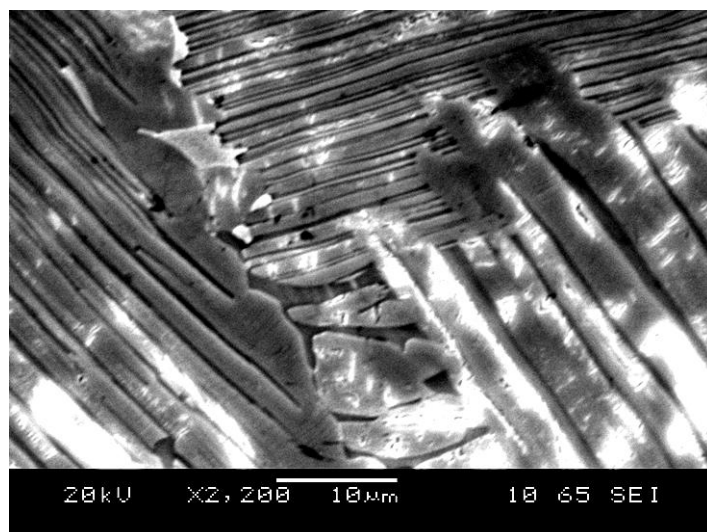


Figure 5.8 Microstructure of Ti-46Al-8Nb shows lamellar eutectoid ($\alpha + \gamma$).

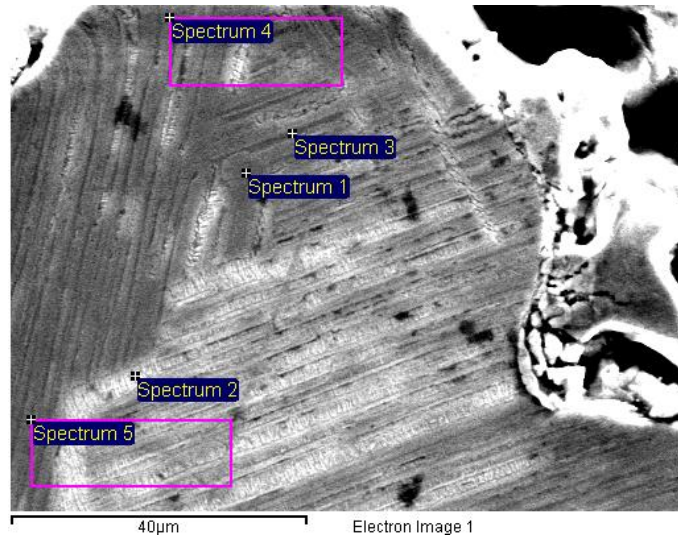


Figure 5.9 EDS area and point analysis of Ti-46Al-8Nb sample show the heterogeneity of the as-cast structure.

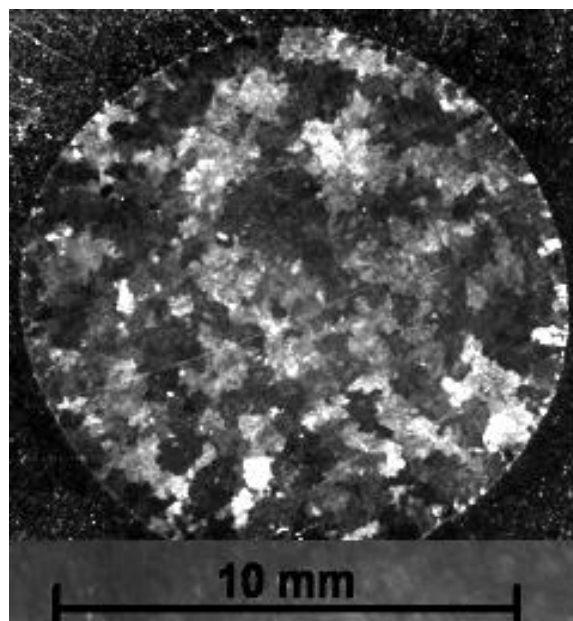
Table 5-4: EDS analysis of Ti-46Al-Nb sample in atomic % and weight %.

Spectrum	Al	Ti	Nb	Al	Ti	Nb
	Atomic %			weight %		
Spectrum 1	42.33	49.80	7.87	26.80	56.00	17.17
Spectrum 2	41.64	49.65	8.71	26.00	55.16	18.80
Spectrum 3	41.33	50.72	7.95	26.00	56.70	17.25
Spectrum 4	40.62	51.10	8.17	25.42	56.76	17.82
Spectrum 5	40.92	50.97	8.11	25.70	56.78	17.53

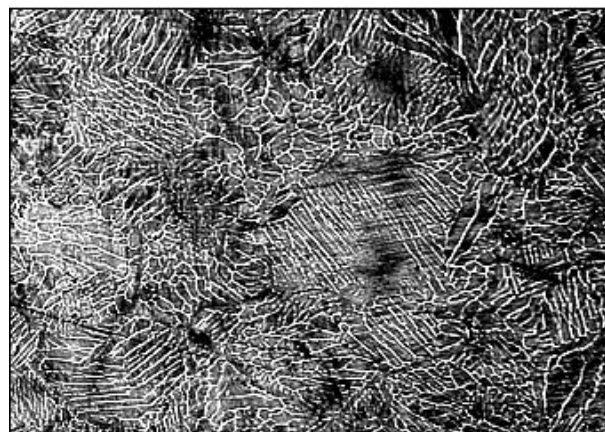
5.3 Shrinkage Porosity in Ti-46Al-8Nb Gravity Casting

5.3.1 Visual Inspection and Qualitative Comparisons

Figures 5.10 to 5.14 show a selection of micrographs of samples from the middle of the test bars which were used for visual and microscopic inspection, and quantitative analysis of porosity and grain size. Optical microscopy of transverse sections revealed that the amount of porosity increased with increasing bar diameter from 10 to 30 mm, as will be discussed quantitatively in Section 5.3.2.

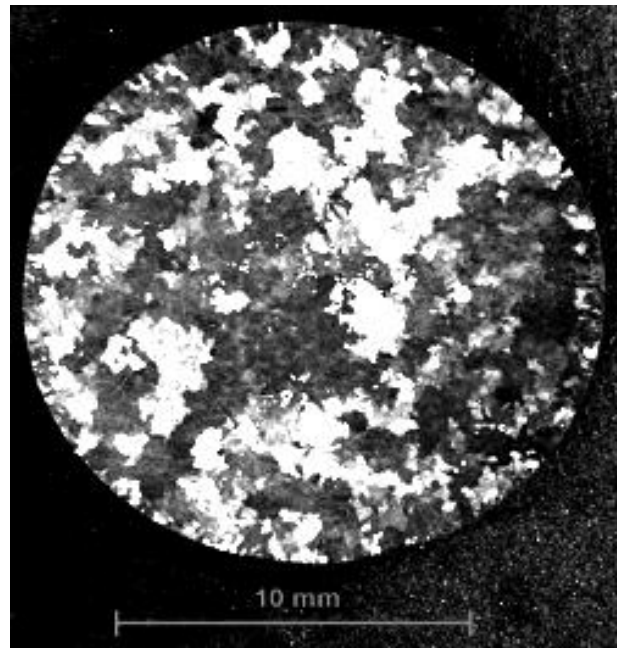


(A)

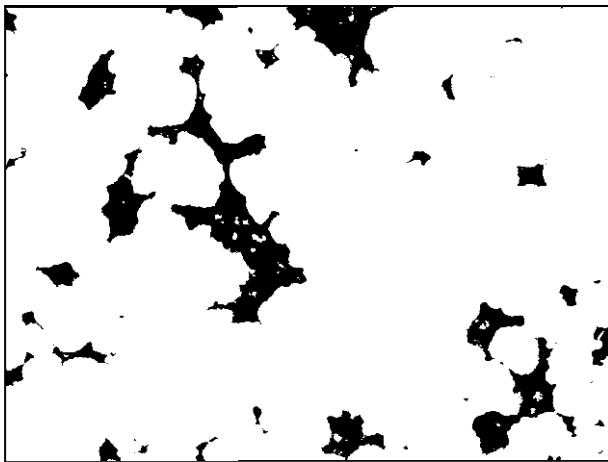


(B)

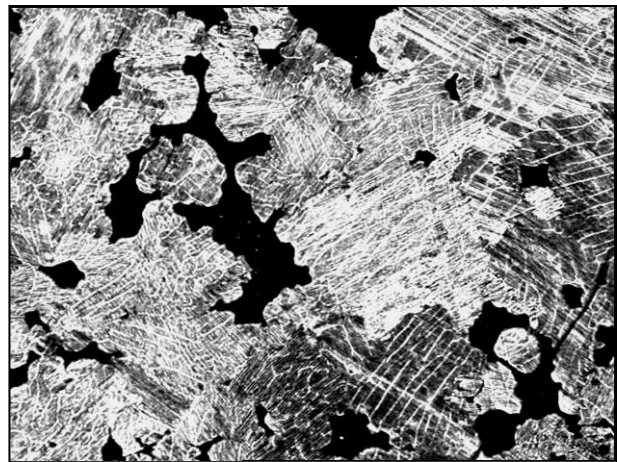
Figure 5.10 Macrograph (A) of etched middle section of the cylindrical bar (10 mm ϕ), Ti-46Al-8Nb gravity cast into mould at 1000 °C and optical micrograph (B) of the worst field at 50x magnification.



(A)

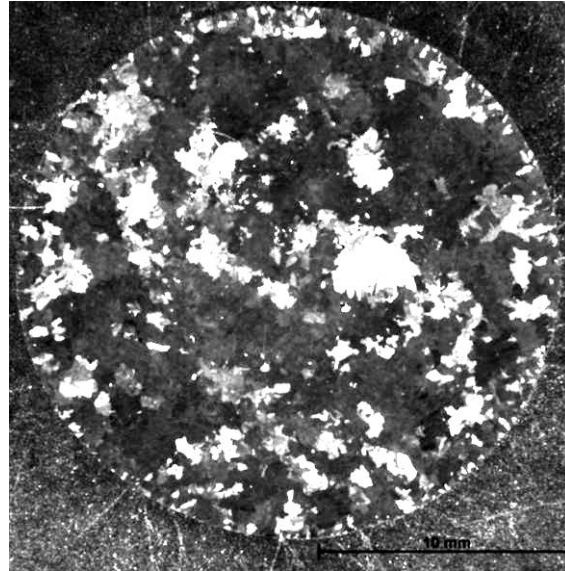


(B)

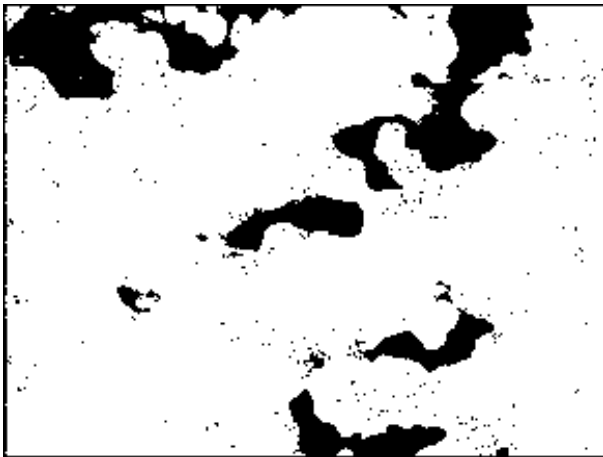


(C)

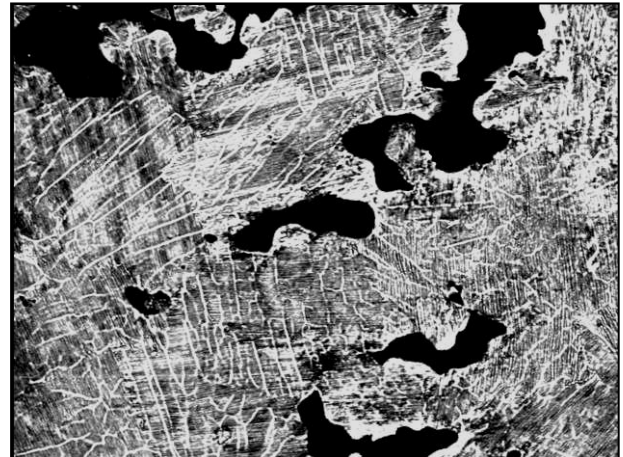
Figure 5.11 Macrograph (A) of etched middle section of the cylindrical bar (15 mm ϕ), Ti-46Al-8Nb gravity cast into mould at 1000 °C, as-polished (B) and etched (C) optical micrographs show the worst field at 50x magnification.



(A)

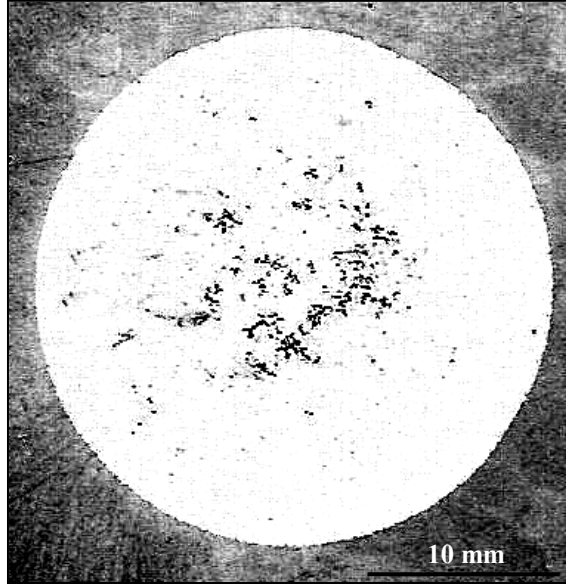


(B)

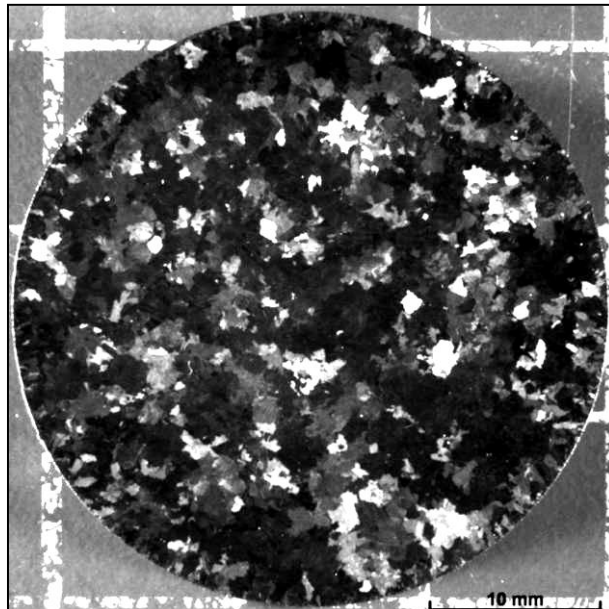


(C)

Figure 5.12 Macrograph (A) of etched middle section of the cylindrical bar (20 mm ϕ), Ti-46Al-8Nb gravity cast into mould at 1000 °C, as-polished (B) and etched (C) optical micrographs show the worst field at 50x magnification.

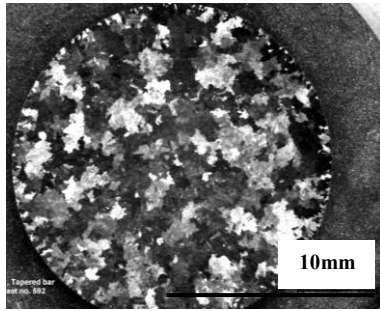


(A)

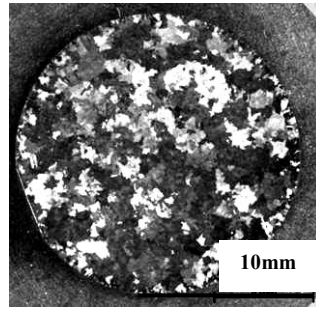


(B)

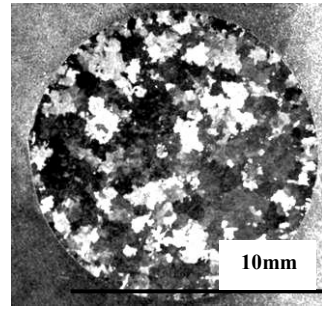
Figure 5.13 As-polished (A) of etched middle section of the cylindrical bar (30 mm ϕ), Ti-46Al-8Nb gravity cast into mould at 1000 °C and etched (B) optical macrograph at 50x magnification.



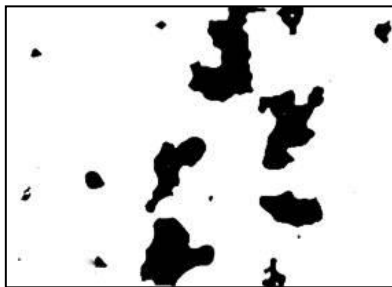
(A)



(B)



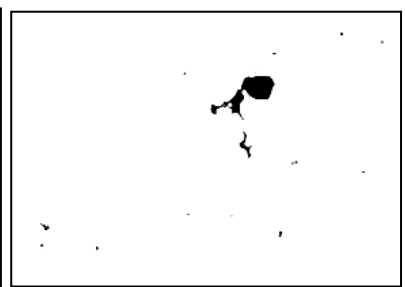
(C)



(D)



(E)



(F)

Figure 5.14 Macrographs (A), (B), (C) of etched top, middle and bottom sections and (D), (E), (F) show optical micrographs of the worst field at 50x magnification of the tapered bar, Ti-46Al-8Nb gravity cast into mould at 1000 °C.

5.3.2 Quantitative Distribution of Porosity

Area percentage of porosity was measured in five longitudinal sections, each of 20 mm length, in all test bars. Thus, the values given here are the area of porosity related to the area of the inspected 20 mm length section, (20×10 , 20×15 , 20×120 and 20×30 for the 10, 15, 20 and 30 mm diameter bars, respectively). Area percentages of porosity as functions of position along the longitudinal sections of the test bars are shown in Figure 5.15.

Generally, the area of porosity tended to decrease with increasing bar diameter. The highest porosity content was found in the 10 mm diameter bar whereas the maximum measured area of porosity was 11 % at a position of between 40 to 60 mm from the feeder. The maximum area of porosity in the 30 mm diameter bar was 3% at a distance of 80 mm from the feeder. The tapered bar contained the smallest area of porosity with a maximum value of 0.95% at a position between 160 and 180 mm from the feeder where the thin section of the tapered bar (at about 150 mm from the feeder) had a cross section of approximately 10 mm diameter.

The end effect can be described by heat was extracted from three surfaces instead of two.

The cooling effect of the end surface, (the penetration of the end effect extended into the bar), was in the region of 20 mm from the free end of the 10 mm diameter bar, increased to about 40 mm in the 20 and 30 mm diameter bars.

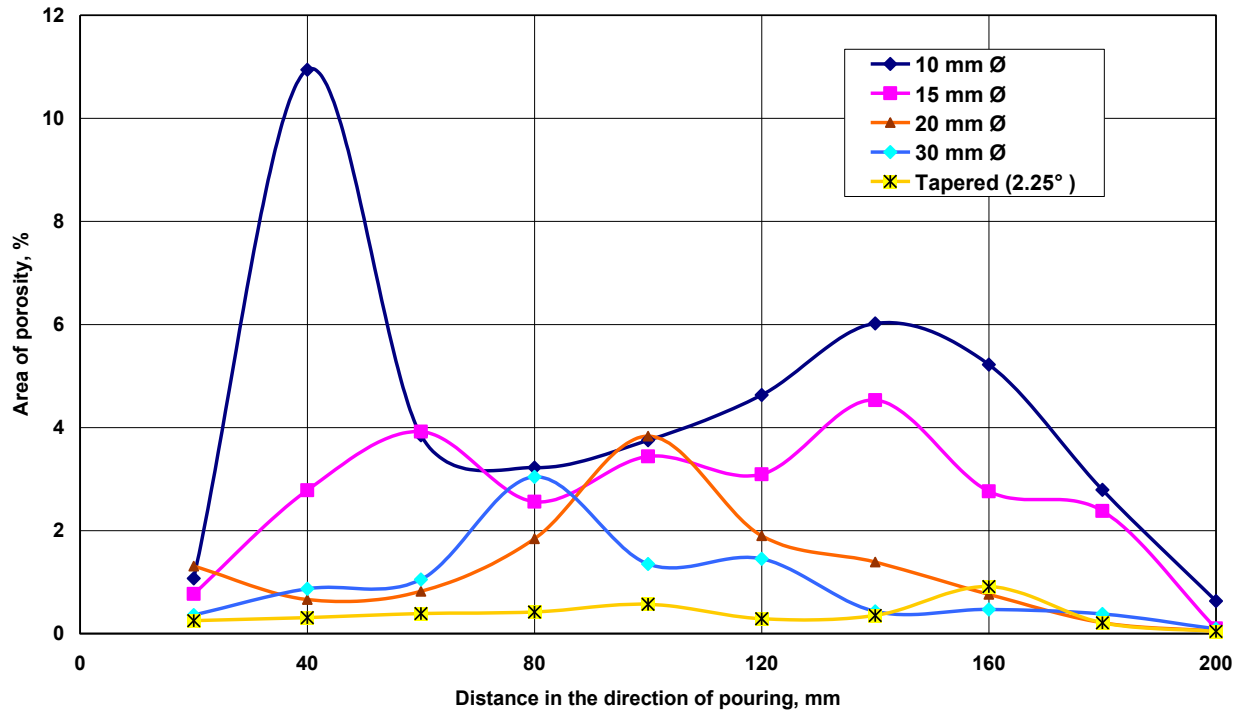


Figure 5.15 Comparison of area of porosity in the longitudinal sections of the test bars, Ti-46Al-8Nb gravity cast into mould at 1000 °C.

5.4 Shrinkage Porosity and Macrostructure in Ti-46Al-8Nb Tilt Casting

5.4.1 Visual Inspection and Qualitative Comparisons

Examination of radiographs shown in Figures 5.16 and 5.17 along with further inspection of the polished longitudinal sections of all test bars revealed that the shrinkage appeared in the form of centreline shrinkage cavities in conjunction with layer porosity in the cylindrical bars, while the tapered bars contained only centreline shrinkage. In addition there was a noticeable decrease in the amount of shrinkage as the taper angle increased from 0.0° to 2.5° for both preheating mould temperatures; 500 °C and 1000 °C. Quantitative description of porosity in tilt-cast bars is given in Section 5.4.3.

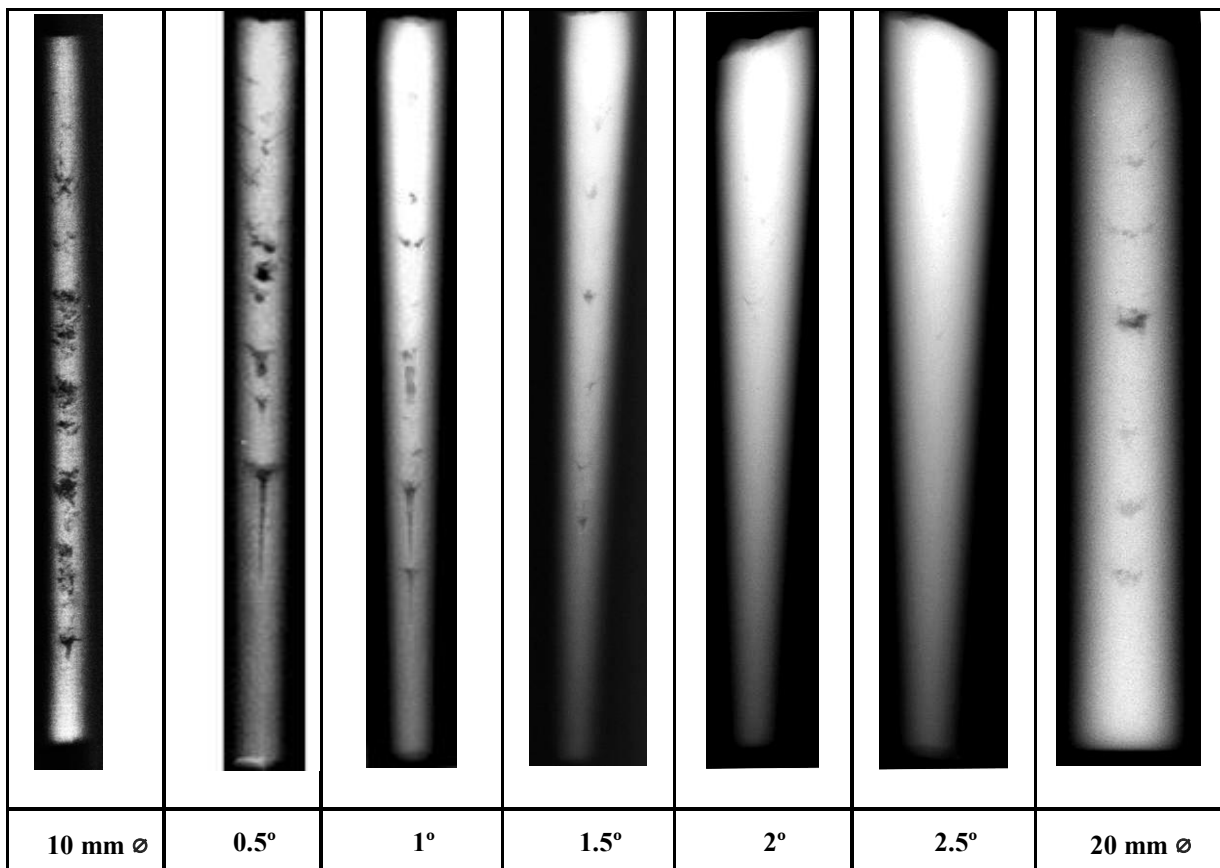


Figure 5.16 Radiographs of the different geometry test bars, Ti-46Al-8Nb tilt casting, preheating mould temperature 500 °C.

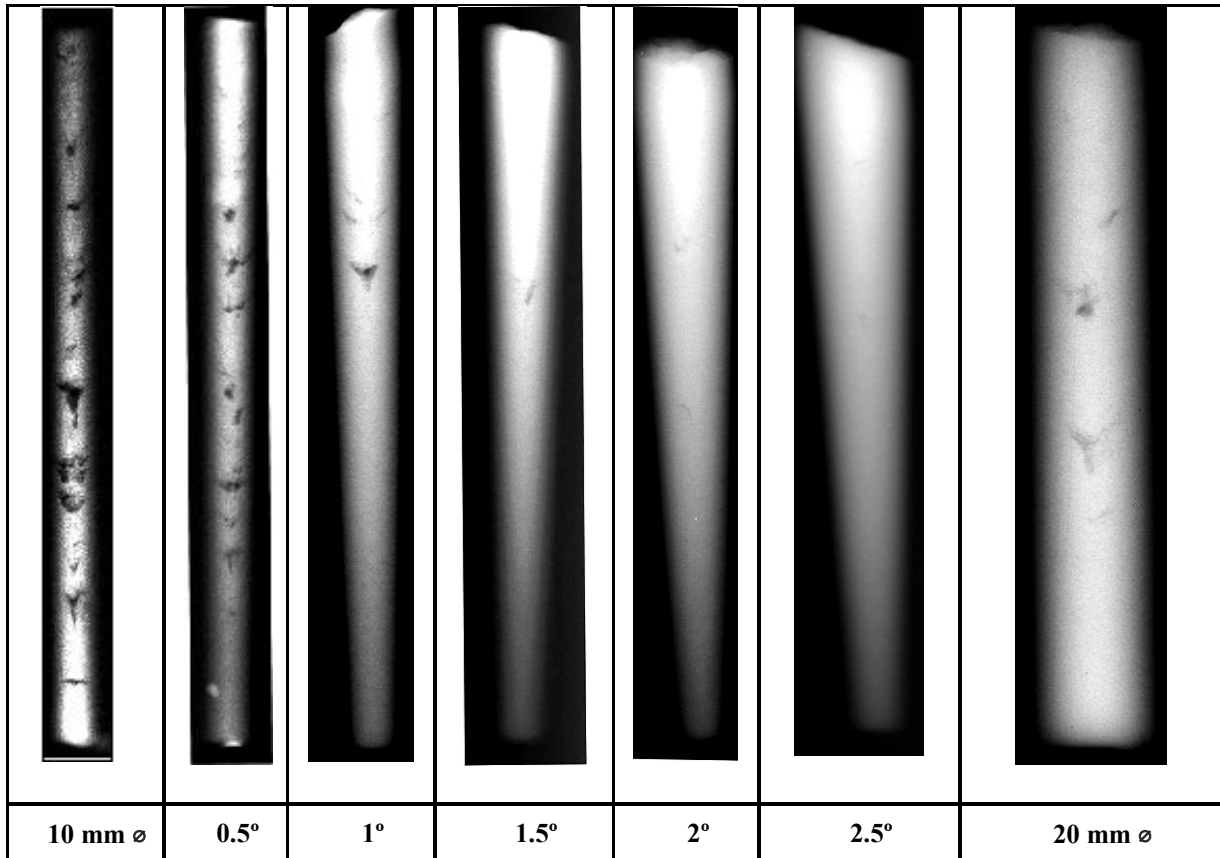


Figure 5.17 Radiographs of the different geometry test bars, Ti-46Al-8Nb tilt casting, preheating mould temperature 1000 °C.

5.4.2 Macrostructure of Tilt Cast Cylindrical and Tapered Bars

Figures 5.18 to 5.21 show the macrostructure of longitudinal sections of the tilt casting test bars. Generally, a columnar structure was the predominant feature of the macrostructure and the zone of equiaxed grains occupied almost the first fifth of the bar length (about 20 mm from the feeder) then diminished gradually downward, (in the direction of pouring). The average area of the equiaxed zone along the vertical sections of different geometry bars are shown in Figures 5.22 and 5.23, the plots show that the 2.5° bar contained the lowest average area of the equiaxed grains, (the mean area was 40% at the middle length), while the 0.5° tapered bar contained the highest value among the tapered bars, (the mean area was 58 % at

the middle length). The equiaxed zone narrowed as the tapering of the bars increased in accordance with increasing directional solidification.

On the other hand, the cylindrical bars of 10 and 20 mm diameters contained the largest equiaxed zones, (70% and 78% respectively), in both mould temperatures. Figure 5.24 summarizes these comparisons of mean area of the equiaxed zone in different bar geometries and different mould temperatures.

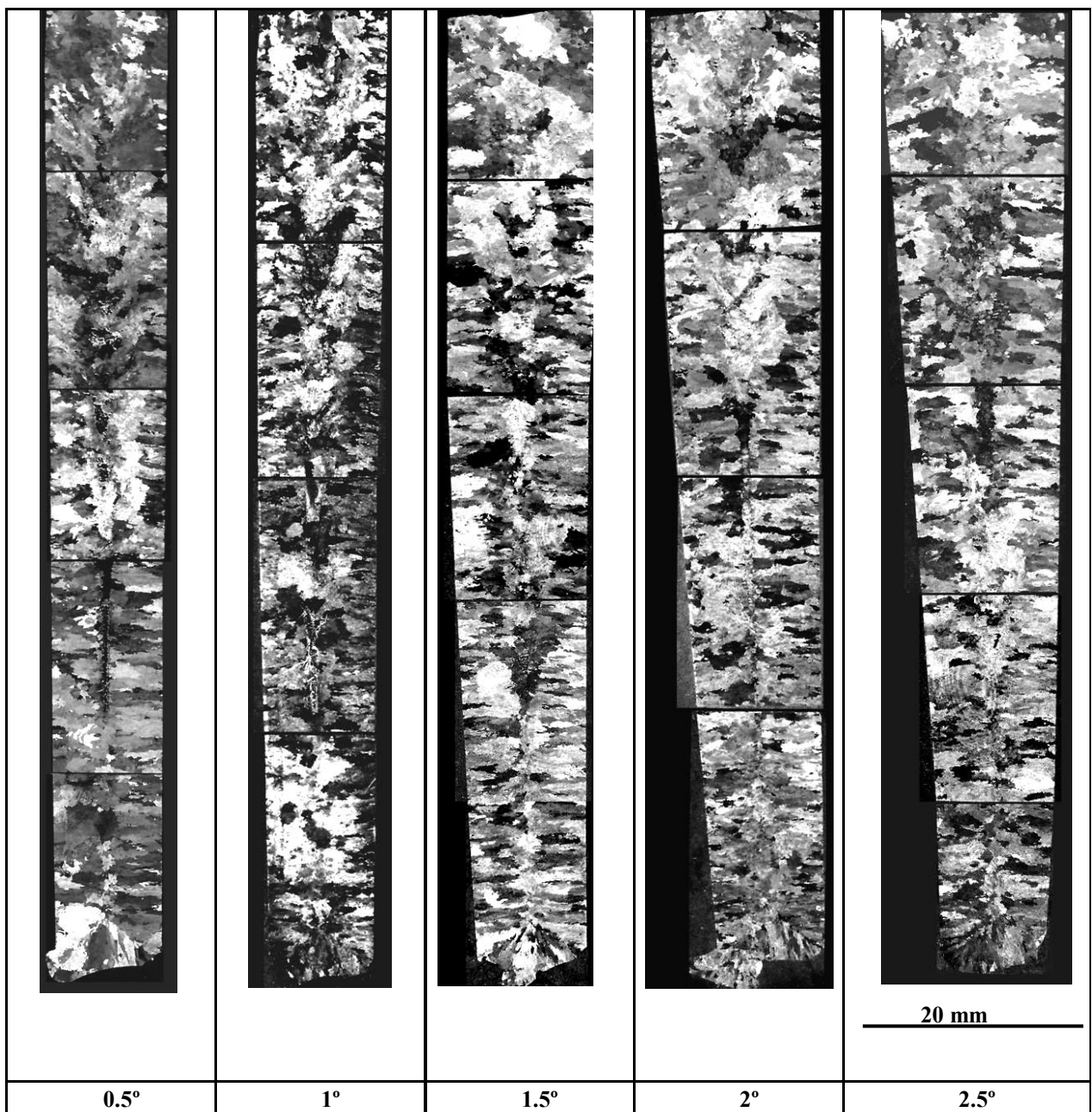


Figure 5.18 Macrographs of tapered bars, Ti-46Al-8Nb tilt casting, preheating mould temperature 500 °C.

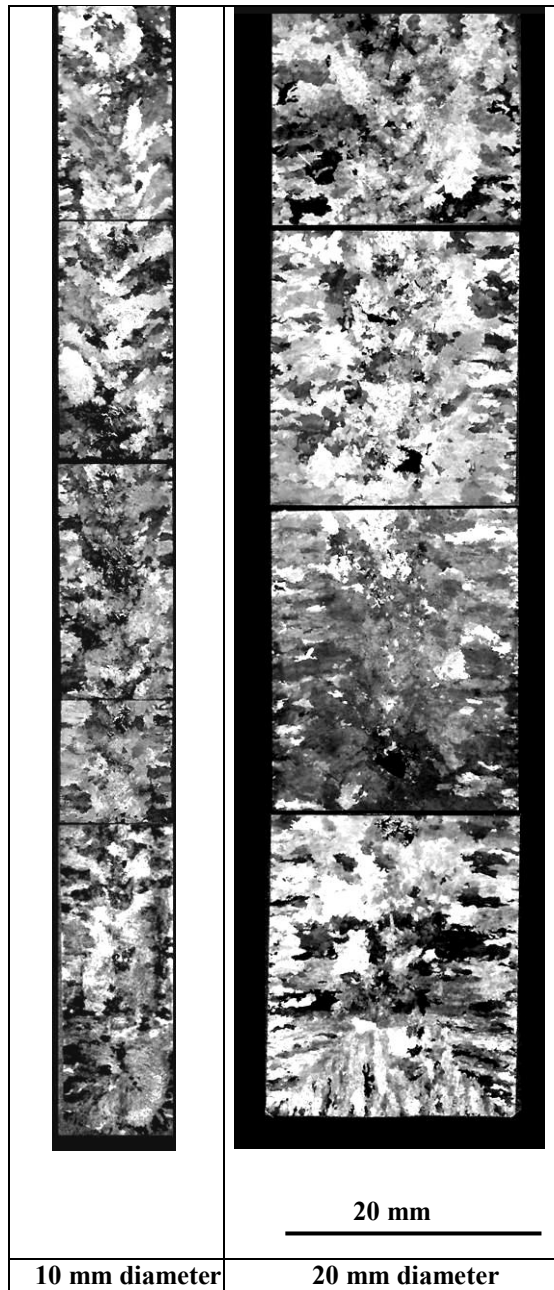


Figure 5.19 Macrographs of Cylindrical bars, Ti-46Al-8Nb tilt casting, preheating mould temperature 500 °C.

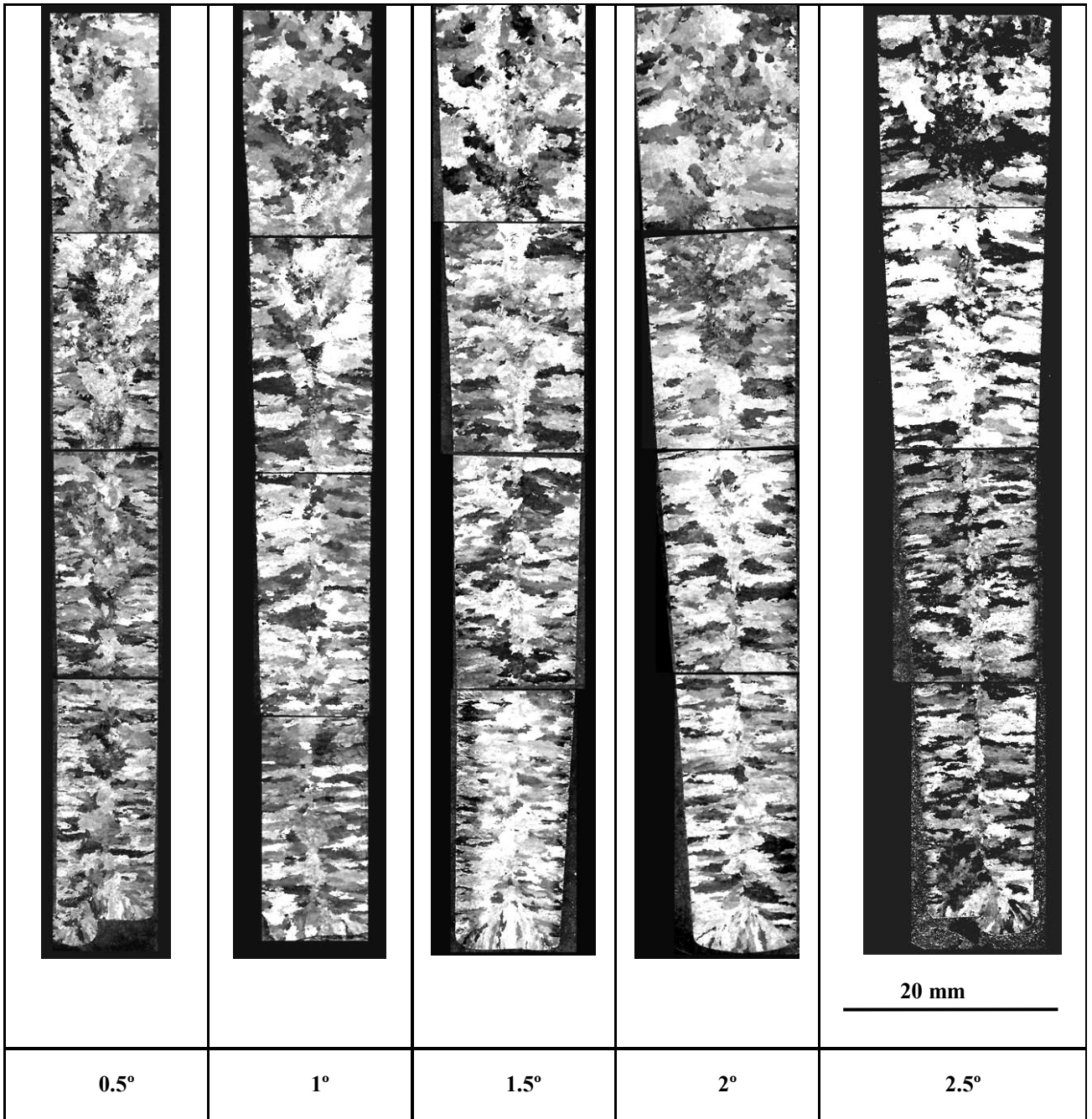


Figure 5.20 Macrographs of tapered bars, Ti-46Al-8Nb tilt casting, preheating mould temperature 1000 °C.

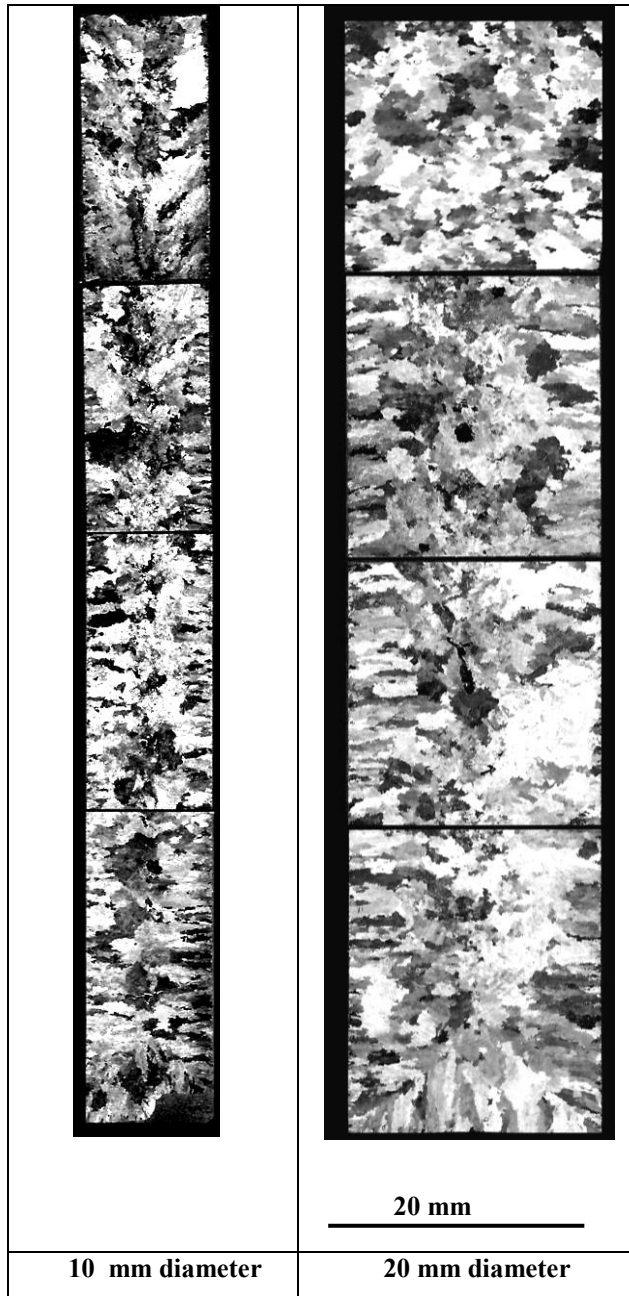
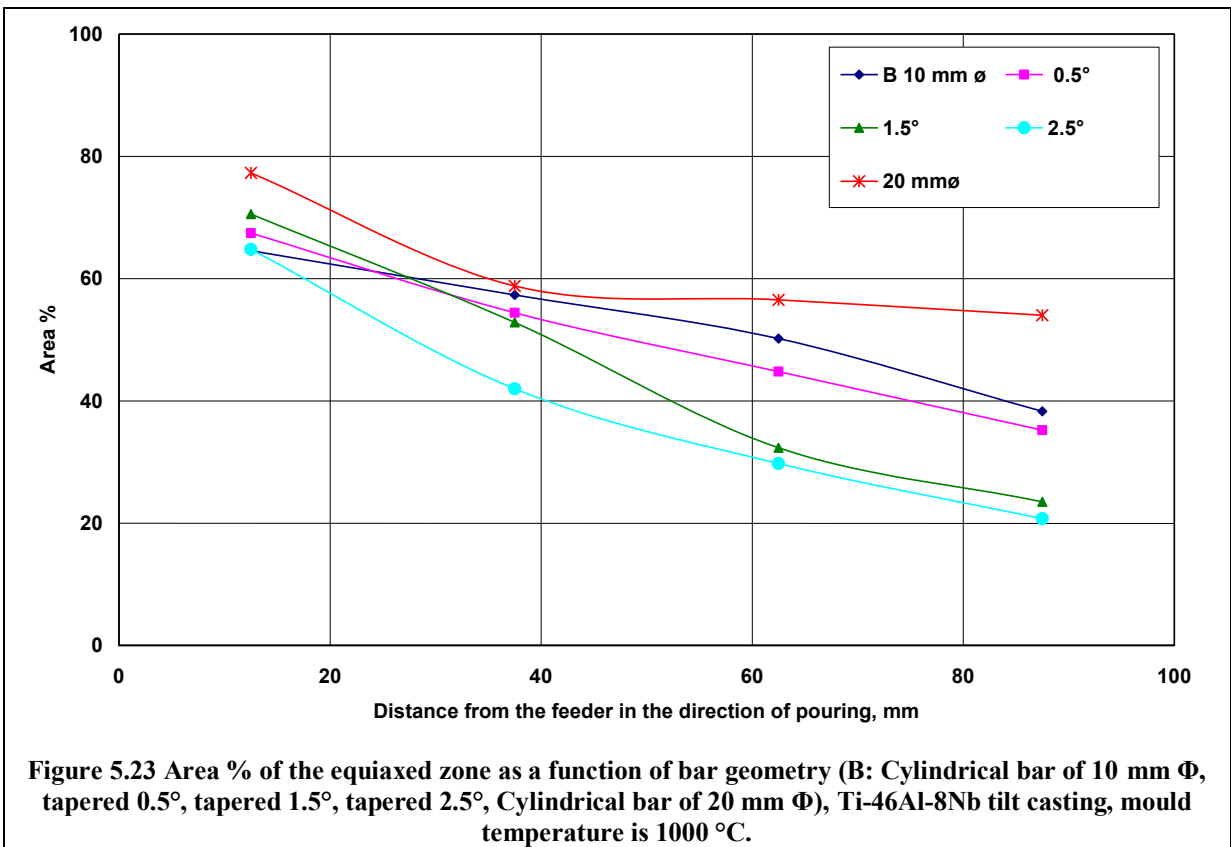
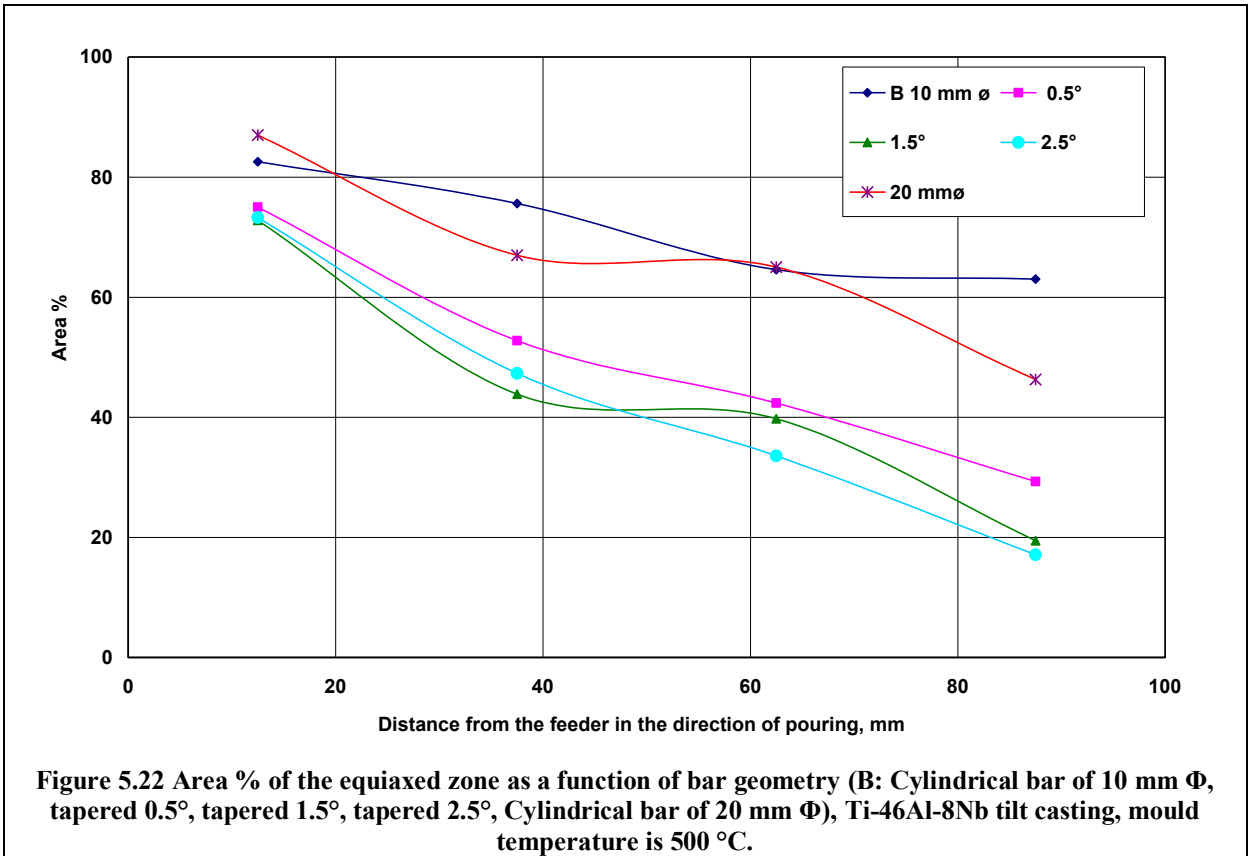
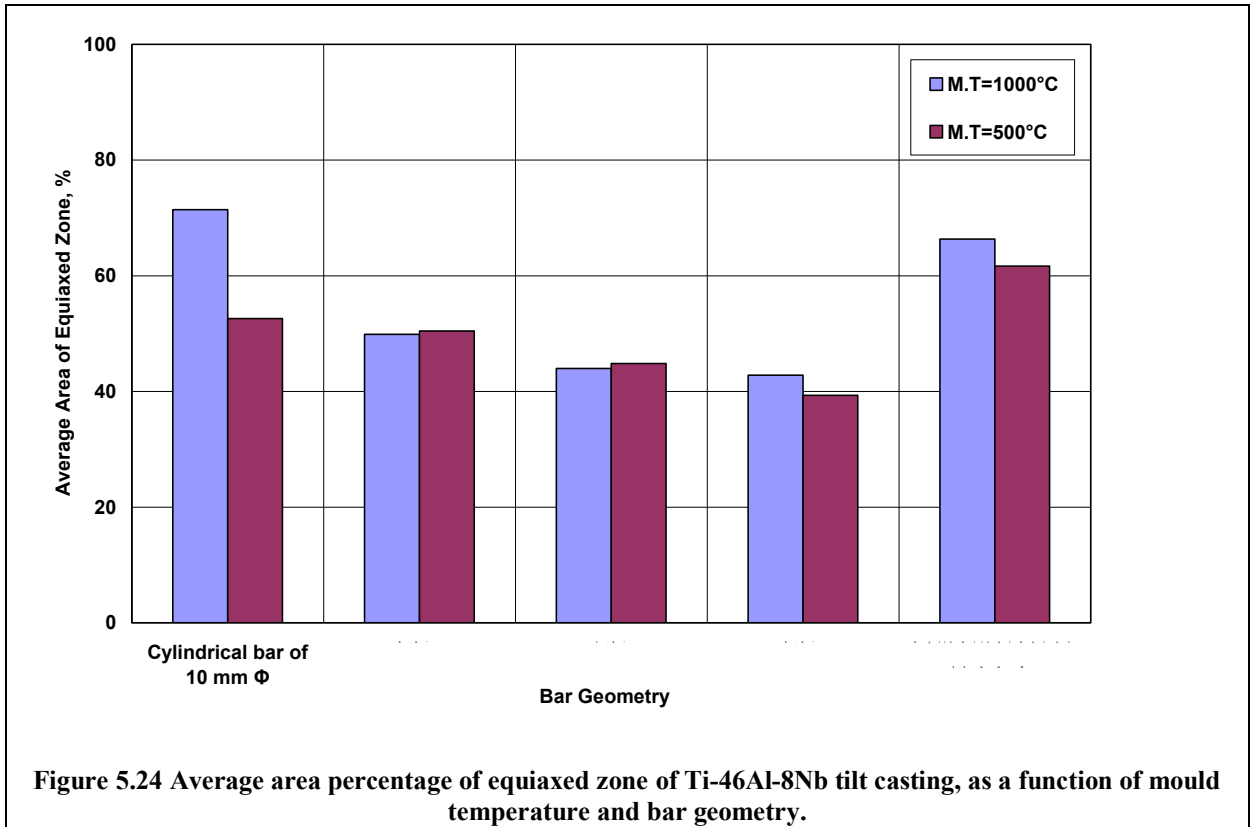


Figure 5.21 Macrographs of Cylindrical bars, Ti-46Al-8Nb tilt casting, preheating mould temperature 1000 °C.





5.4.3 Effect of Bar Geometry on Shrinkage Porosity

A noticeable decrease in the average amount of shrinkage porosity associated with increasing the taper angle of the test bars, as seen in Figures 5.25 and 5.26.

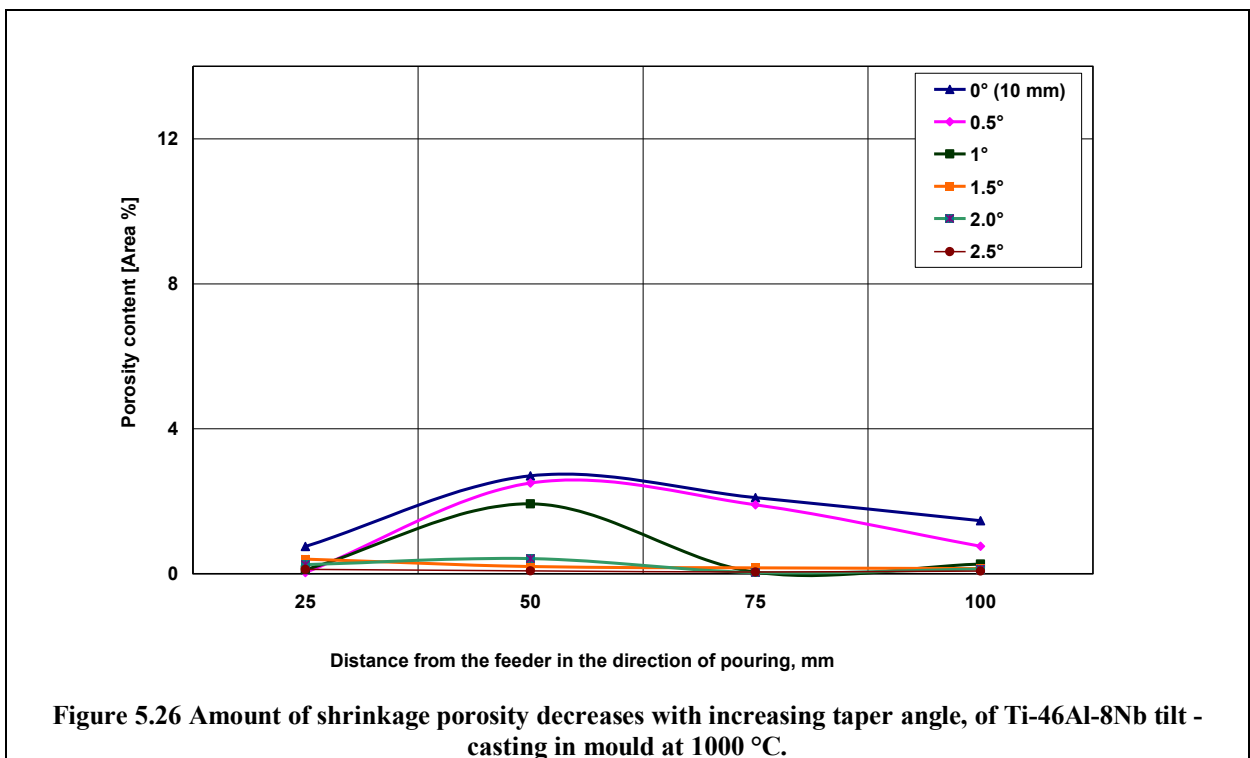
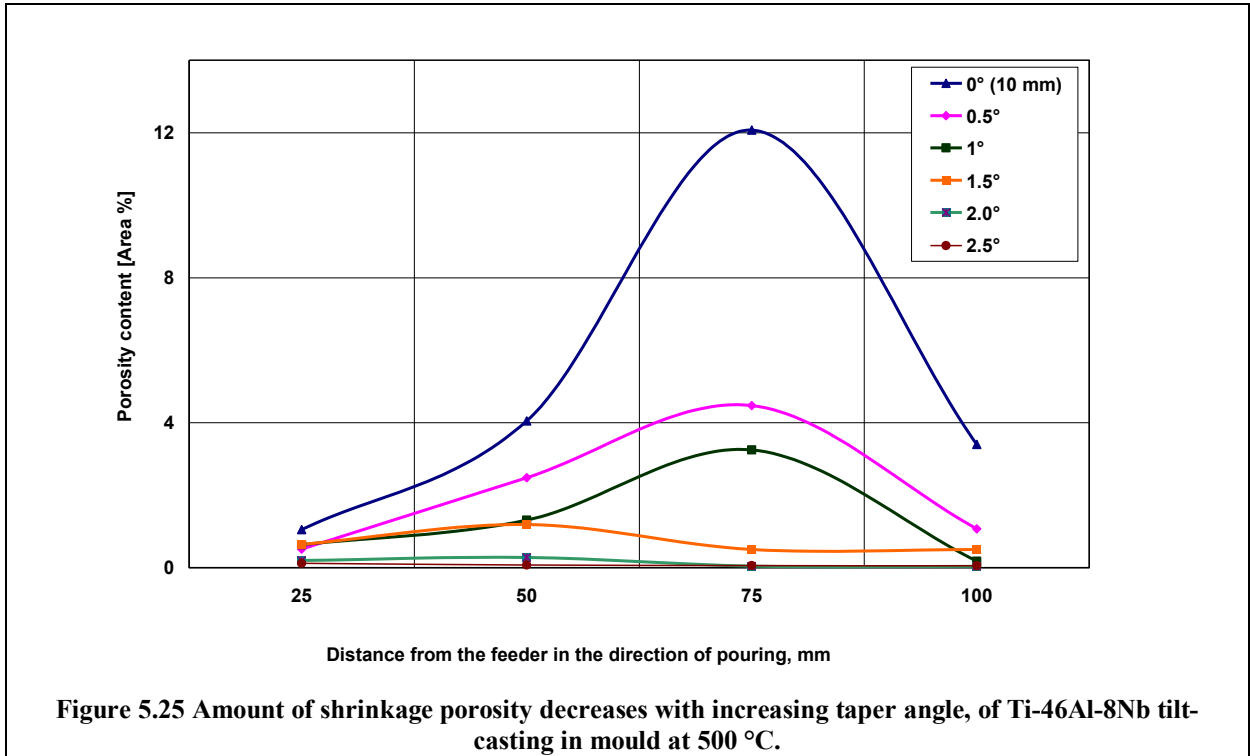
In addition, the porosity decreased with increasing bar diameter in the cylindrical bars, in the case of both the 500 °C and 1000 °C mould temperatures.

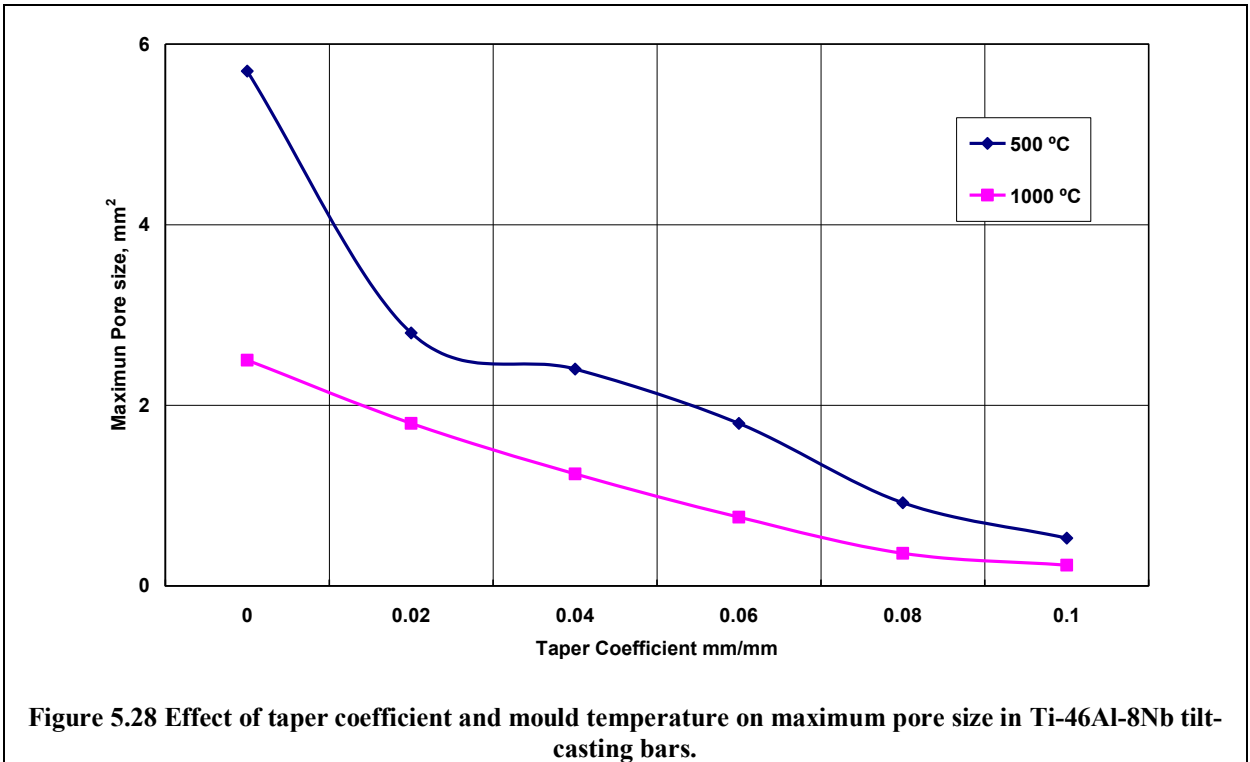
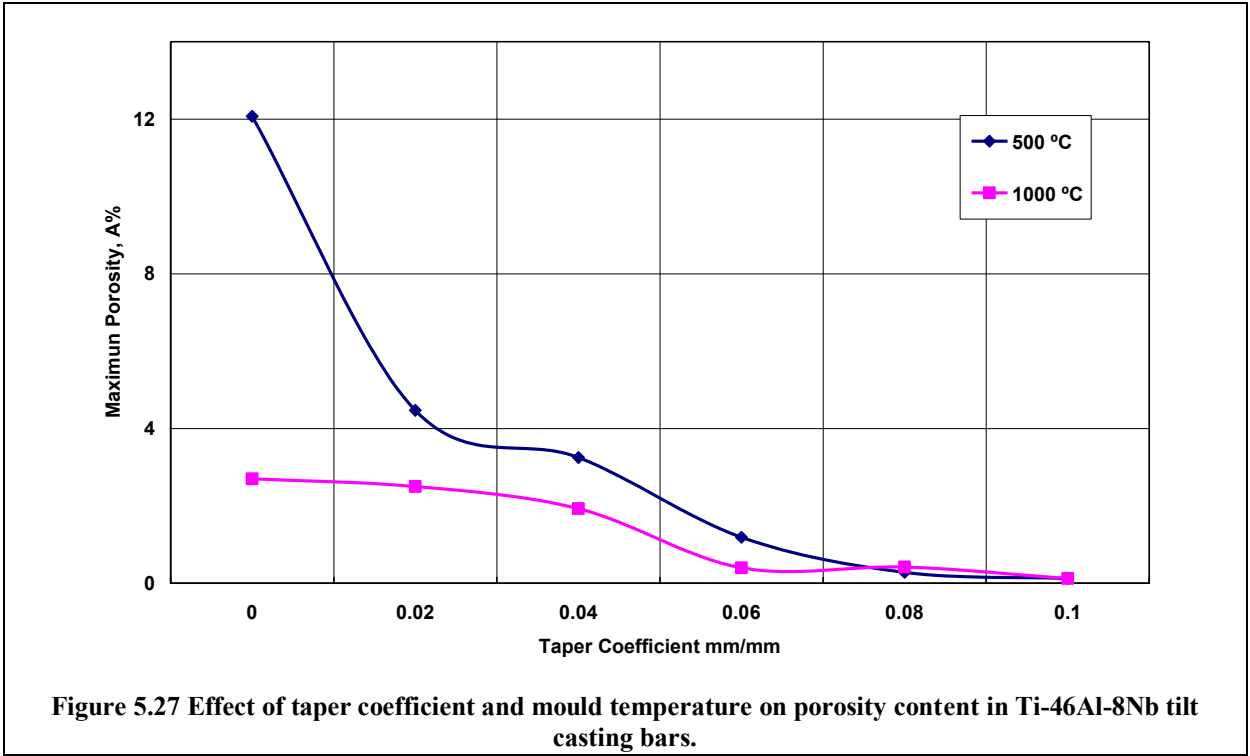
However, the average shrinkage porosity decreased from a maximum value of 12 % of the examined area in the case of casting into a 500 °C preheated mould, to less than 3 % of the examined area in the case of casting into 1000 °C preheated mould.

Figures 5.27 and 5.28 show the effect of the taper of the test bars on the maximum area of porosity, as a percentage of the total area of the central longitudinal section and the maximum pore size, respectively.

The average area of porosity generally decreased as the taper coefficient increased from 0 to 0.1 mm/mm in mould temperatures, 500 °C and 1000 °C.

The maximum pore size also decreased from 5.5 mm² to 0.65 mm² and from 1.7 mm² to 0.13 mm² as the taper angle increased from 0.5° to 2.5°, in the 500 °C and 1000 °C mould temperatures, respectively.





5.5 Determination of the Heat Transfer Coefficient for Mould/Surrounding Interface

As described in section 3.4, cooling of the ceramic test-piece in a vacuum, in Argon and in the air was studied. Temperatures were recorded at three positions, which gave enough data to fit an equation for the temperature distribution across the ceramic shell/bar. In addition, there was no source of heat and there were no phase changes expected to take place during cooling and hence a simple heat content analysis was applied.

5.5.1 Calculation of the Surface Temperature of the Ceramic Test Bar

The rate of heat loss can be determined by the drop of the surface temperature (T_s) of the cooled body. However, surface temperature of the ceramic test piece could not be accurately measured because it was not possible to fix a thermocouple precisely on the surface. Hence, T_s was estimated from the three temperatures, T_1 , T_2 and T_3 , measured within the bar.

A pseudo steady state was assumed as the rate of temperature variation with time ($\frac{\partial T}{\partial t}$) was very small, (close to zero), this was detected by calculating the first derivative at the initial stage of the measured cooling curves. Once steady state cooling was established T_1 , T_2 and T_3 would lie on a parabola with an origin at a distance (a) from the thermal centre of the bar (since the core was made of a different material) and the thermal centre of the ceramic bar was assumed to be at T_0 . Figure 5.29 shows the temperature distribution across the ceramic bar at any position (x) from the centreline of the Alumina core. Three simultaneous parabolic equations can be written:

$$T_1 = T_0 - b(a + x_1)^2 \quad \text{Eq.5.1}$$

$$T_2 = T_0 - b(a + x_2)^2 \quad \text{Eq. 5.2}$$

$$T_3 = T_0 - b(a + x_3)^2 \quad \text{Eq. 5.3}$$

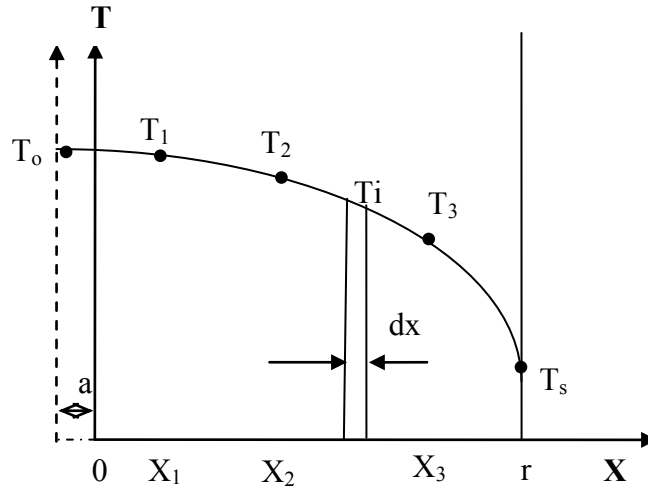


Figure 5.29 Temperature distribution across the bar diameter r .

Where T_0 , a and b are constants, and x_1 , x_2 and x_3 are the positions of the thermocouples, measured from the centre of the Alumina rod core given in Table 4.5. These three equations were solved in terms of the measured values of T_1 , T_2 and T_3 and hence T_0 , a and b were determined. The expressions for these unknowns are given below:

$$a = \frac{x_1^2 - x_2^2 + \left(\frac{T_1 - T_2}{T_2 - T_3}\right)(x_3^2 - x_2^2)}{2\left(\frac{T_1 - T_2}{T_2 - T_3}\right)(x_2 - x_3) + 2(x_2 - x_1)} \quad \text{Eq. 5.4}$$

$$b = \frac{T_2 - T_1}{(a + x_1)^2 - (a + x_2)^2} \quad \text{Eq. 5.5}$$

And from equation Eq. 5.1

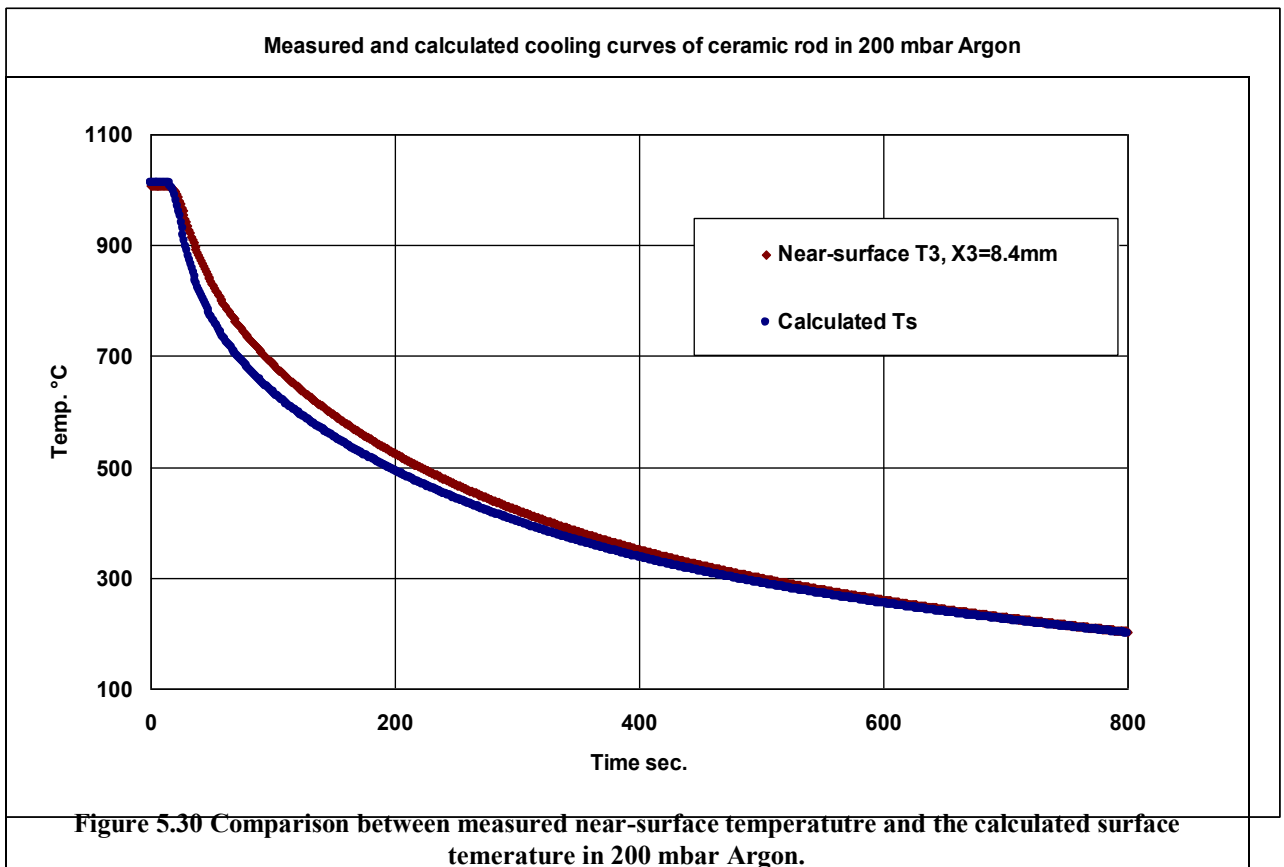
$$T_0 = T_1 + b(a + x_1)^2 \quad \text{Eq. 5.6}$$

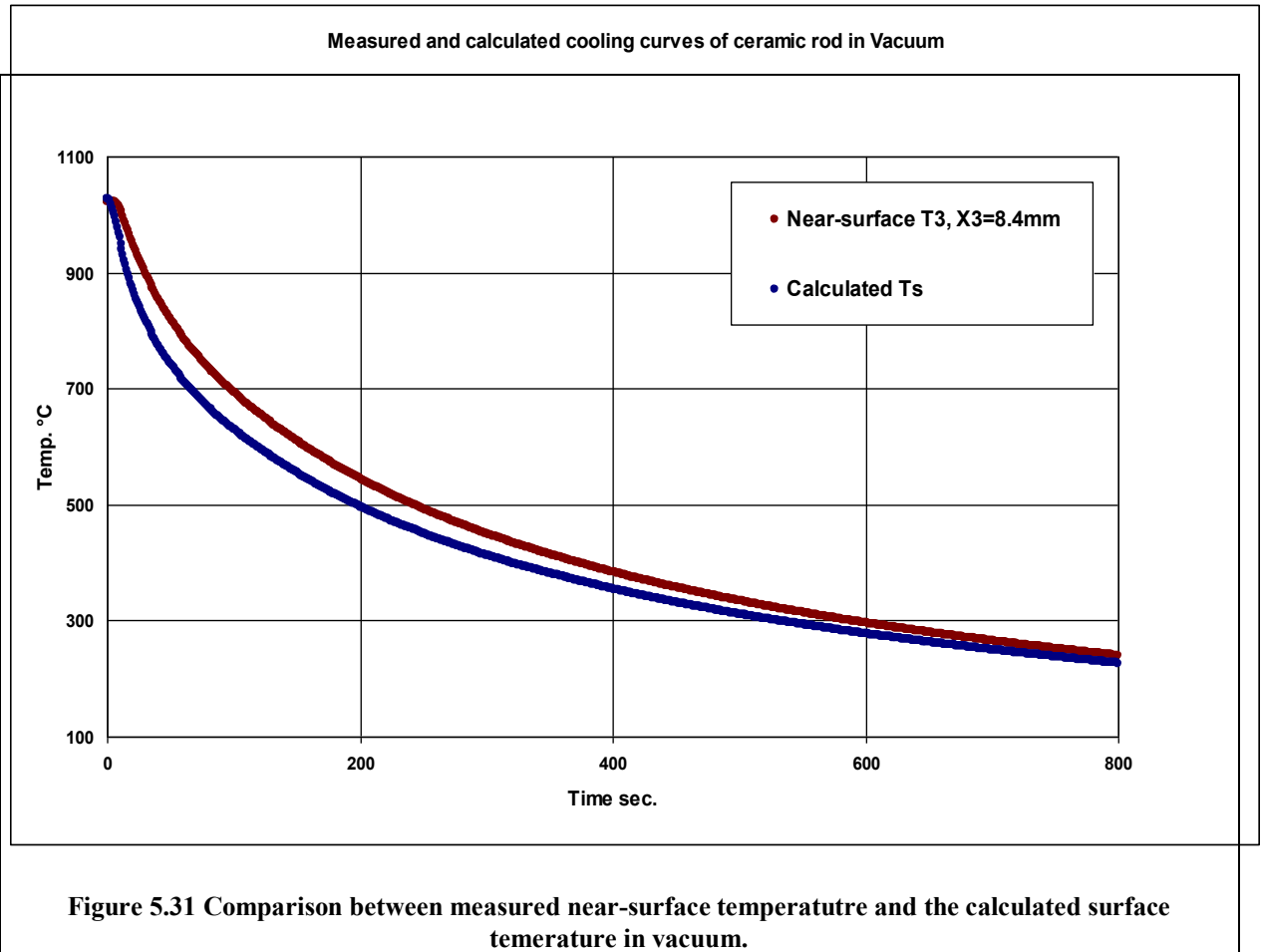
By substituting r (the radius of the ceramic bar) for x in the temperature distribution equation, T_s is calculated as follows:

$$T_s = T_0 - b(a + r)^2 \quad \text{Eq. 5.7}$$

T_1 , T_2 and T_3 were measured as functions of time and thus $T_o(t)$, $a(t)$, and $b(t)$ were computed, and subsequently T_s as a function of time was determined.

The measured near-surface temperatures $T_3(t)$ were compared with the calculated $T_s(t)$ in both experimental conditions, casting in 200 mbar of Argon and in a vacuum. Figures 5.30 and 5.31 show these comparisons. The average difference between the calculated T_s and the measured near-surface T_3 was 5% of the measured T_s in case of cooling in the Argon atmosphere, while this difference was 7% in the case of cooling in the vacuum.





5.5.2 Calculation of the Heat Transfer Coefficient at the Ceramic Mould/Surrounding Interface

The ratio of the length to the diameter of the test bar was around 10 so heat flow in the longitudinal direction can be ignored and the only heat flow is in the radial direction. The heat flow equation can be solved based on the following analysis. As illustrated by the schematic diagram in Figure 5.32, a slice with a unit height was divided into n annular slices, each of thickness dx and volume dV . The heat content of any small annular volume dV rotated around the T axis is;

$$Q_i = m * C_p * T_i \quad \text{Eq. 5.8}$$

Where m is the mass = $2.\pi.x.dx.\rho$ (where ρ = density, C_p = specific heat)

And from the parabolic equation of the temperature distribution:

$$T_i = T_0 - b(a + x)^2 \quad \text{Eq. 5.9}$$

Where T_0 , b and a were derived from the cooling curve data

The total heat content of the slice is Q_i where;

$$Q_i = \int_0^R 2 \cdot \pi \cdot \rho \cdot C_p \cdot x \cdot T_i \cdot dx \quad \text{Eq. 5.10, a}$$

$$= \int_0^R 2 \cdot \pi \cdot \rho \cdot s \cdot x (T_0 - c(a + x)^2) dx$$

$$= \int_0^R 2 \cdot \pi \cdot \rho \cdot C_p \cdot x (T_0 - b(a + x)^2) dx \quad \text{Eq. 5.10, b}$$

Substituting for T_i from Eq. 5.9 and integrating gives;

$$Q_i = \pi \cdot \rho \cdot C \cdot R^2 (T_0 - b \cdot a (a - \frac{4}{3}R) - \frac{b}{2}R^2) \quad \text{Eq. 5.10, c}$$

The total heat content of the specimen Q is calculated at each time step by substituting for $a(t)$, $b(t)$ and $T_0(t)$.

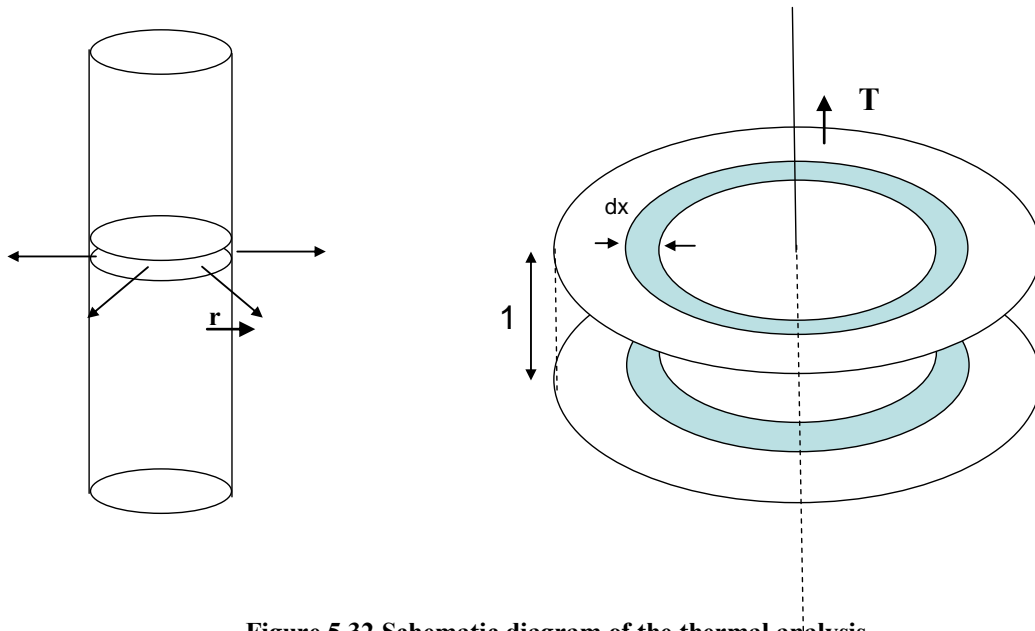


Figure 5.32 Schematic diagram of the thermal analysis

Assume no heat flow along length of specimen, i.e. 2D heat flow
Divide the 2D slice (unit height) into n annular slices, each dx thick

The heat transfer coefficient h of a surface can be defined by the rate of heat loss through its surface area. Thus the heat lost (dQ/dt) from a surface of area A in a given time interval was calculated and divided by the difference between the surface temperature T_s and the ambient temperature T_∞ ($= 20$ °C) to obtain h , as shown in the following equations;

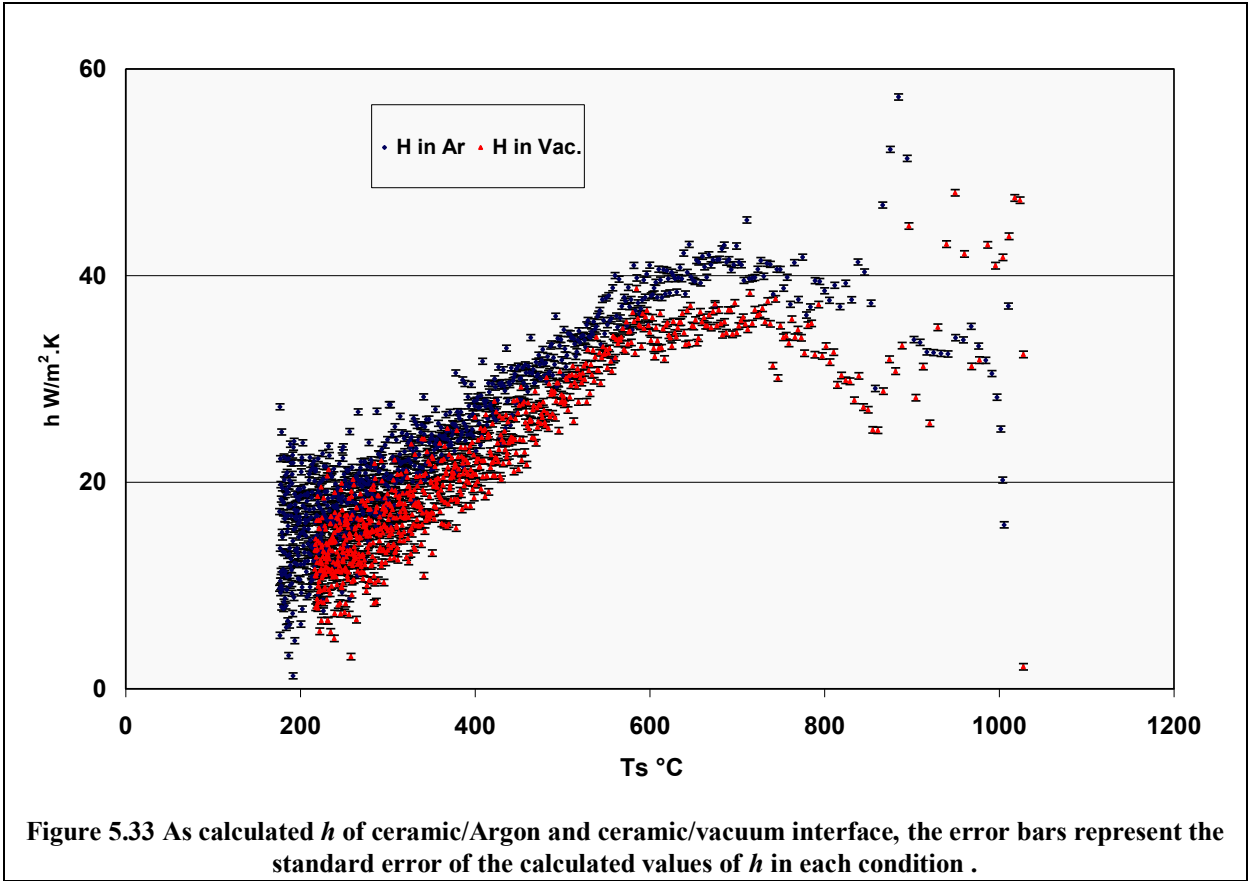
$$Q = 2 * \pi * \rho * C_p * \int_0^R x(T_0 - C(a + x))^2 dx$$

$$\frac{dQ_i}{dt} = \frac{Q_{i+1} - Q_{i-1}}{t_{i+1} - t_{i-1}} \quad \text{Eq. 5.11, a}$$

$$h = \frac{dQ}{dt} / A * (T_s - T_\infty) \quad \text{Eq. 5.11, b}$$

h was calculated by using the cooling curves data recorded for cooling in Argon and in vacuum, and a comparison between values of h as a function of the calculated surface temperature in both conditions is given in Fig. 5.33. As shown in the figure the values of h in the Argon atmosphere were slightly higher than in vacuum.

In the case of the ceramic bar being cooled down from 1000 °C in the Argon atmosphere heat was expected to be transferred from the surface by convection through the Argon gas, in addition to heat being transferred by radiation. In the early stages of cooling, two heat transfer mechanisms contribute simultaneously in raising the rate of heat removal from the surface. When cooling was taking place in a vacuum the only mode of heat transfer is radiation, which depends mainly on the temperature of the ceramic surface. Thus the heat transfer coefficient h in Argon, which combines the effects of both convection and radiation throughout the cooling process, was higher than h in vacuum.



For the cooling conditions where the ceramic shell was cooled from 1000 °C under a pressure of 200 mbar Argon, used in the Ti-46Al-8Nb casting experiments and the modelling in this research, the values of h in the range from 200 °C to 700 °C were fitted to a straight line, characterized by the following equation;

$$h = 0.0572 * T_s + 3.6072 \quad \text{Eq. 5.12}$$

This equation was used to extrapolate the $h(T)$ curve over an extended temperature range, as shown in Figure 5.34, and was subsequently stored in the boundary conditions database of the modelling software ProCastTM.

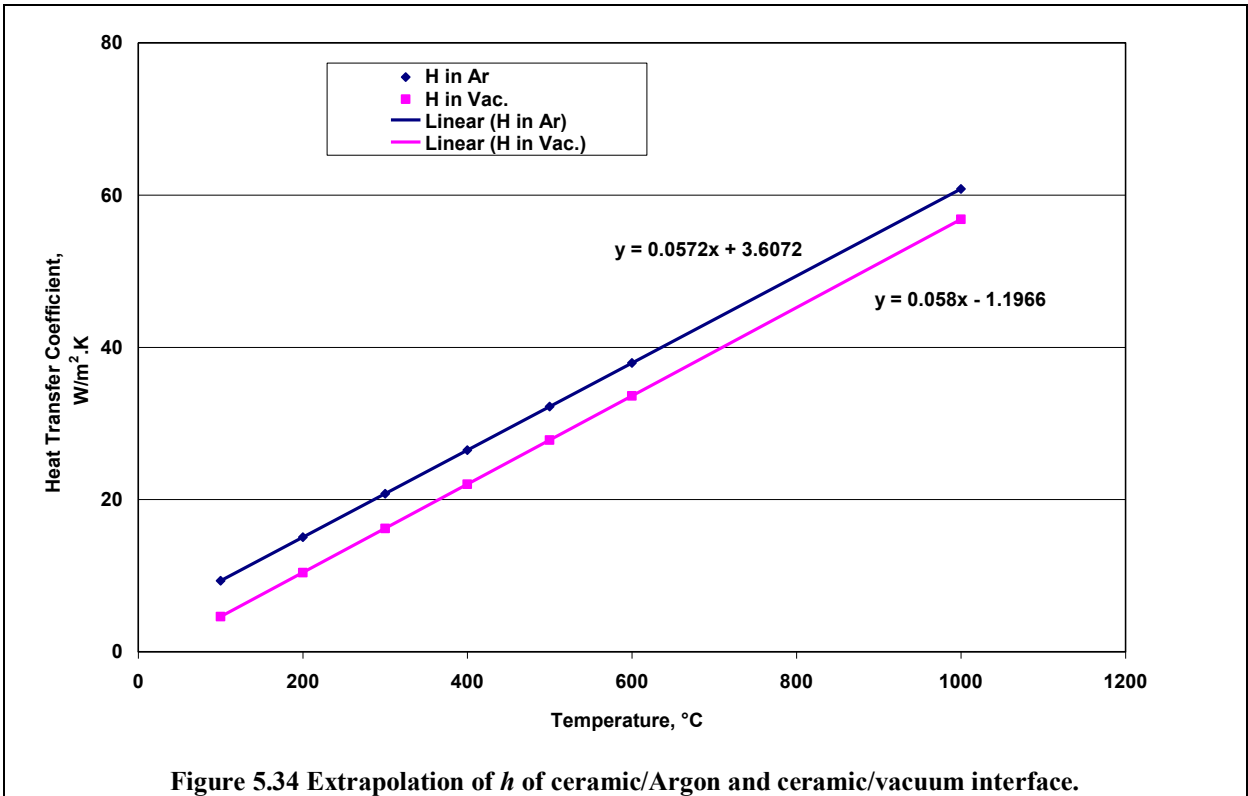
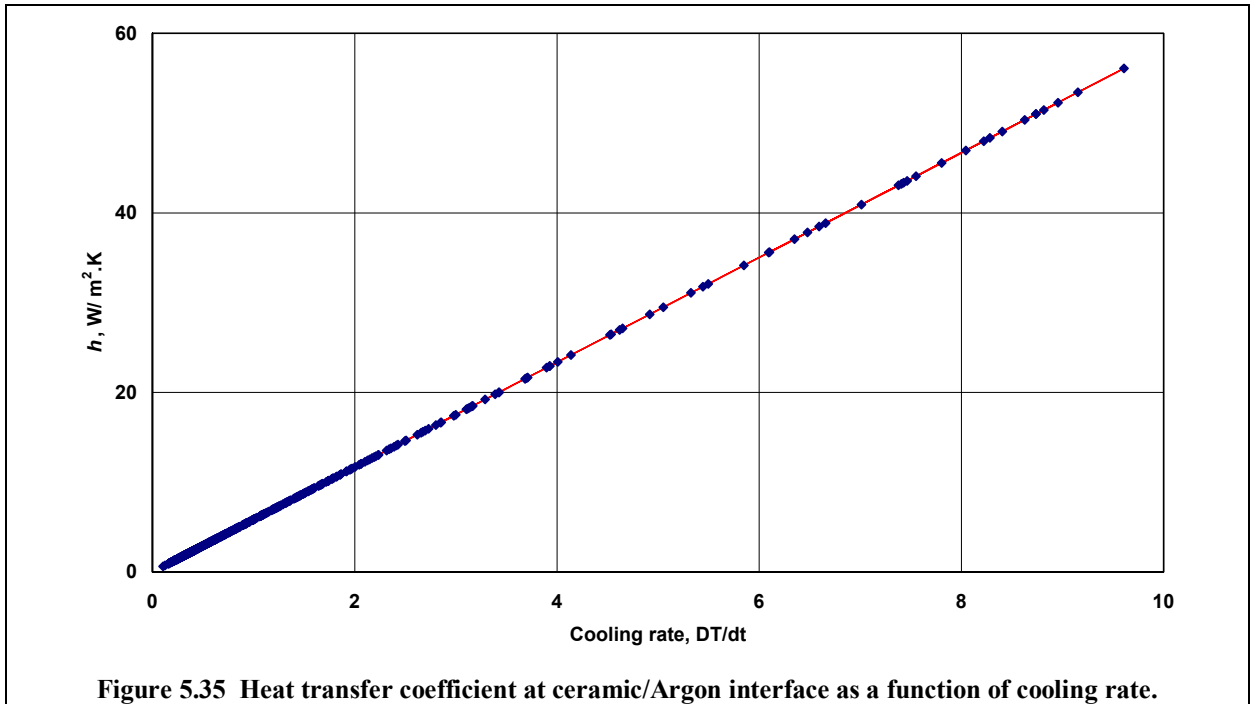


Figure 5.34 Extrapolation of h of ceramic/Argon and ceramic/vacuum interface.

According to Newton's Law of Cooling, the rate of heat loss from the solid body into its surroundings is proportional to the surface area A of the heat transfer and the temperature drop between the body and the ambient temperature. Since there was no source of heat generation during cooling of the ceramic bar, and with the assumption that the material properties were constants, Newton's Law of Cooling can be written in the form;

$$\frac{dT}{dt} = -h \frac{A}{m \cdot C_p} (T - T_\infty) \quad \text{Eq. 5-13}$$

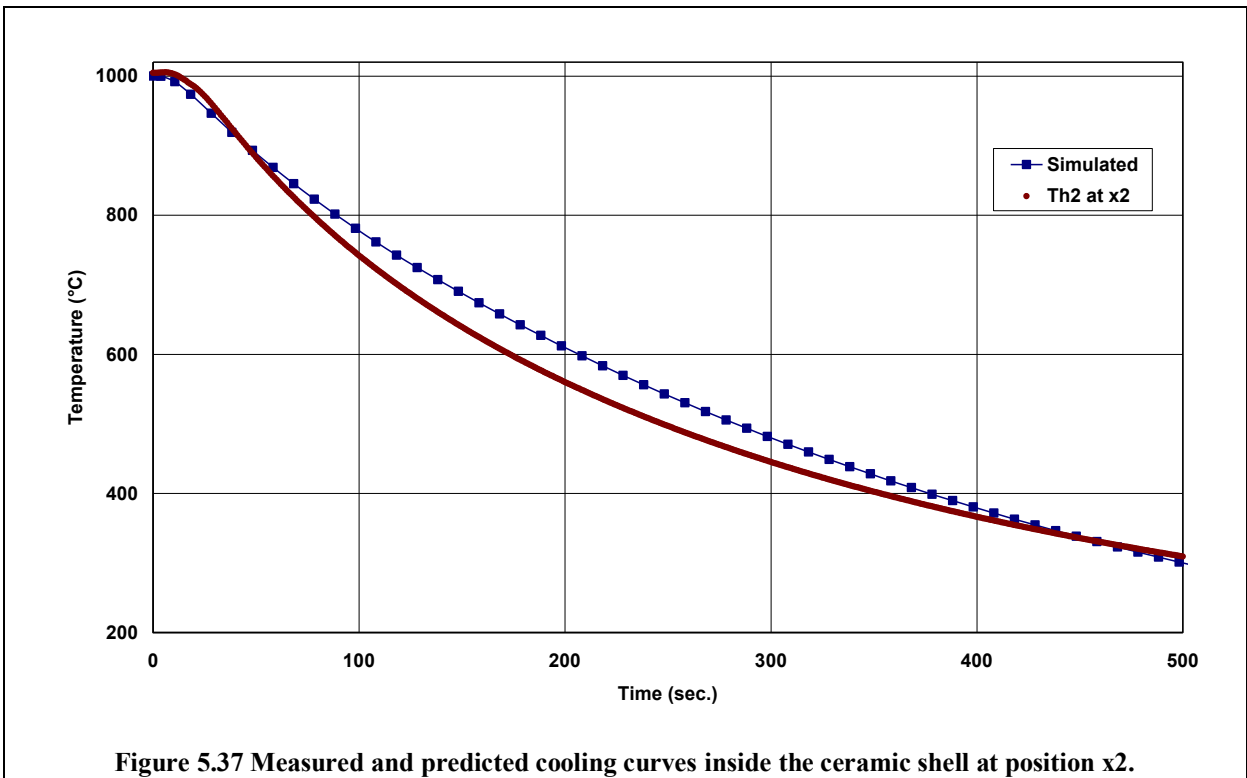
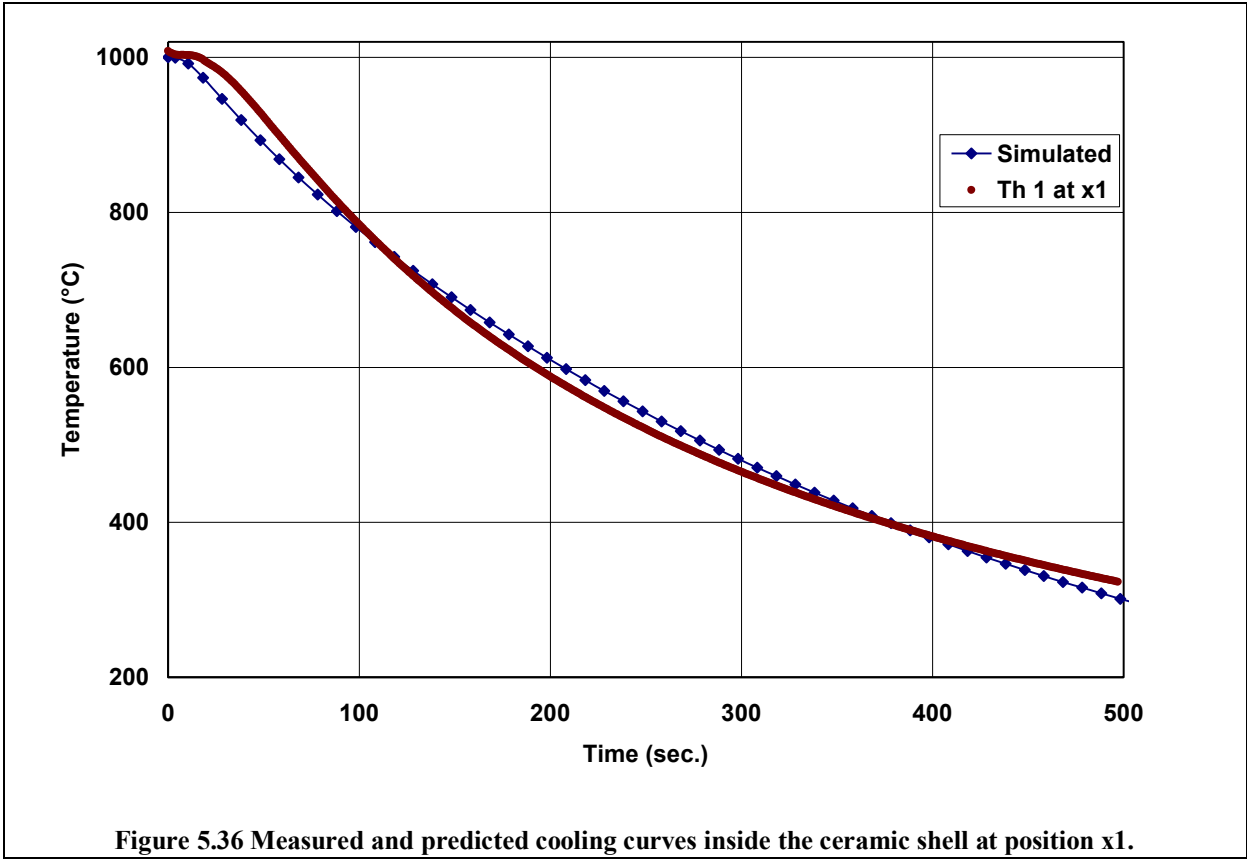
The relationship between the cooling rate and the heat transfer coefficient h is shown in Figure 5.35, which shows that h was directly proportional to the cooling rate. However, at the beginning of cooling from 1000 °C the cooling rate was relatively high and h had distracted values as functions of the surface temperature, (see Figure 5.33), this could be due to the noise in the thermocouple measurements recorded during the initial few seconds of cooling, which in turn led to scatter in the calculated T_s , and subsequently in the calculated h .

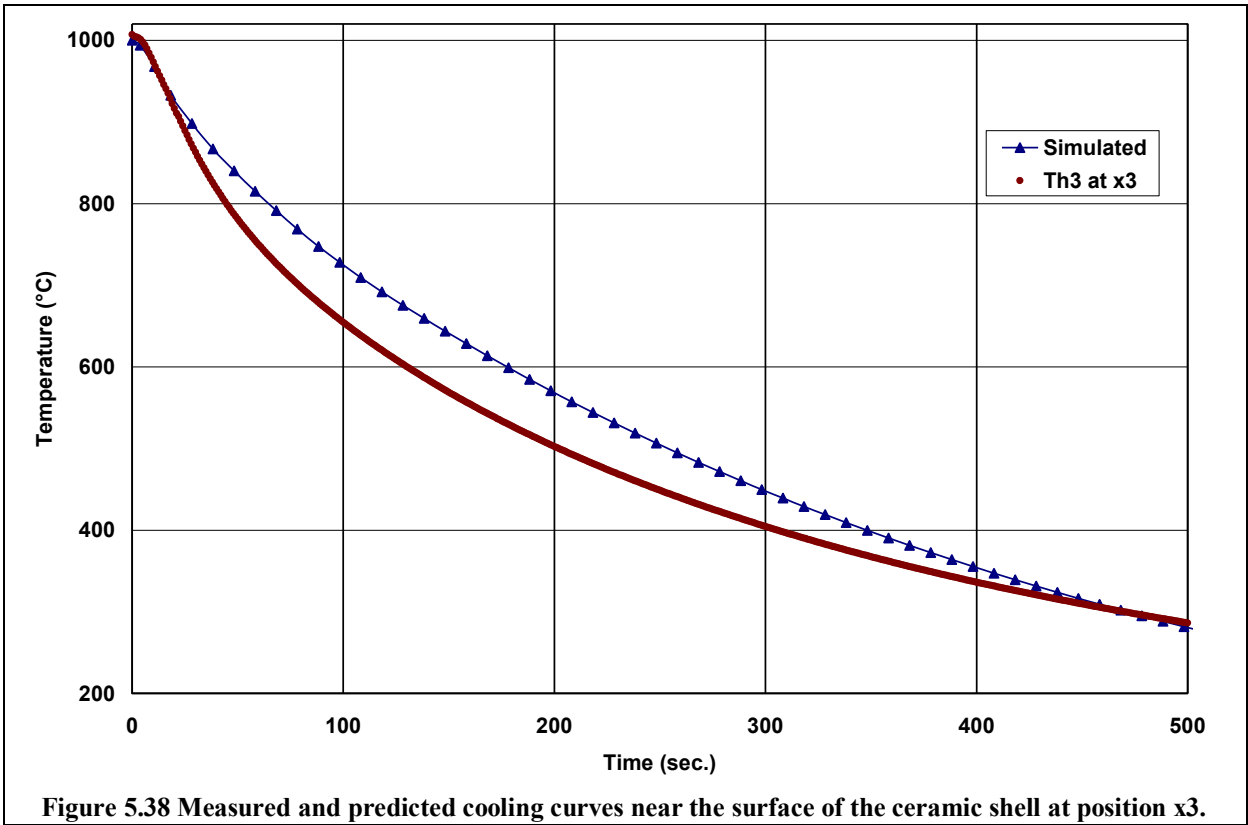


5.5.3 Verification of the ProCastTM Model of the Ceramic Test with the Measured Data

Experiments of the cooling of the ceramic test bar were modelled using the ProCastTM software, aiming to verify the database created by comparing the simulation results with the recorded cooling curves. Figures 5.36, 5.37 and 5.38 show a good agreement between the measured cooling curves and the predicted curves of the simulation modelling which validated the use of the created database for the ceramic material properties and the boundary conditions of cooling in an atmosphere of 200 mbar of Argon gas.

However, the predicted cooling curves were very sensitive to the position of the selected nodes which represented the positions of thermocouples. Many trials to predict the cooling curves at the required nodes showed that as the position of the selected node was slightly shifted from the actual thermocouple position a different cooling curve resulted.





5.6 Analysis of the Cooling Curve of Ti-46Al-8Nb Alloy

The cooling curves of the alloy measured during gravity and tilt casting were analysed in terms of inflexion points which represent the liquidus and solidus points and start and end points of any phase transformation that the solidifying metal undergoes during cooling.

Figure 5.39 shows the recorded cooling curve of the Ti-46Al-8Nb alloy during gravity casting into a 100 mm diameter cylindrical mould at ambient temperature. The R-type thermocouple was positioned at the thermal centre of the casting. The highest recorded temperature was 1563 °C.

Figure 5.40 shows the measured cooling curve during tilt casting into a 50 mm diameter cylindrical mould preheated to 1000°C. The B-type thermocouples TC1 and TC2 were positioned at 37.5 mm above and below the centre point of the casting respectively. Both measured curves showed a slight difference in the recorded temperatures, as the upper thermocouple responded earlier and hence recorded a slightly higher curve in the initial 18 seconds, which included the time of the tilting cycle, (7 seconds). Then the lower thermocouple, TC2 recorded temperatures 2 to 4 K higher, (see Figure 5.41). The maximum temperatures on the curves were 1571.6 and 1572.2 °C from TC1 and TC2 respectively. These recorded (maximum) temperatures could be lower than the actual pouring temperature due to the effect of the alumina sheath and the response time of the thermocouple.

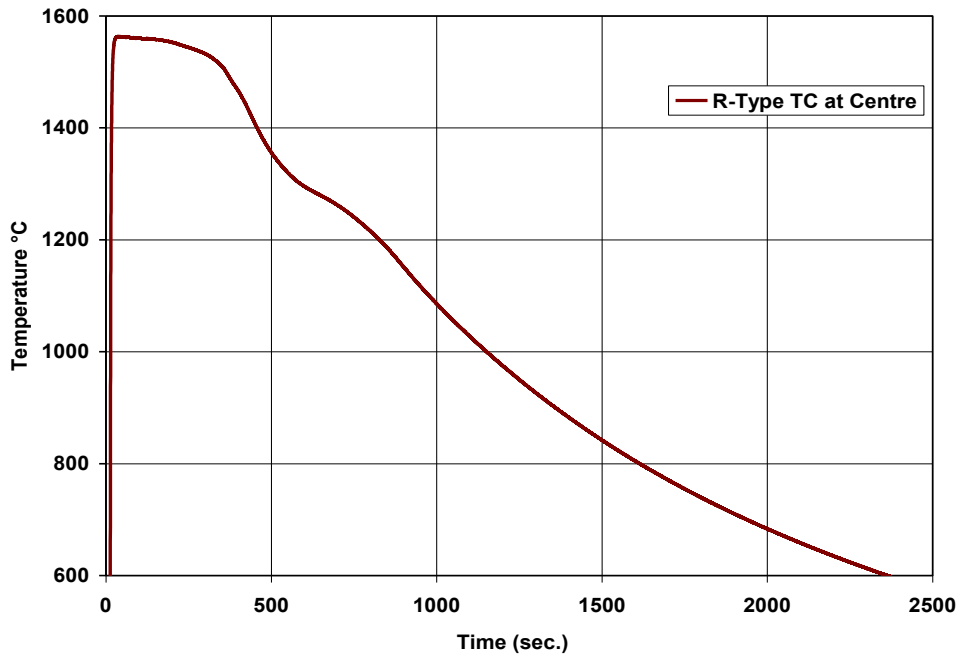


Figure 5.39 Experimental cooling curve at the thermal centre of Ti-46Al-8Nb alloy in gravity casting, RT mould.

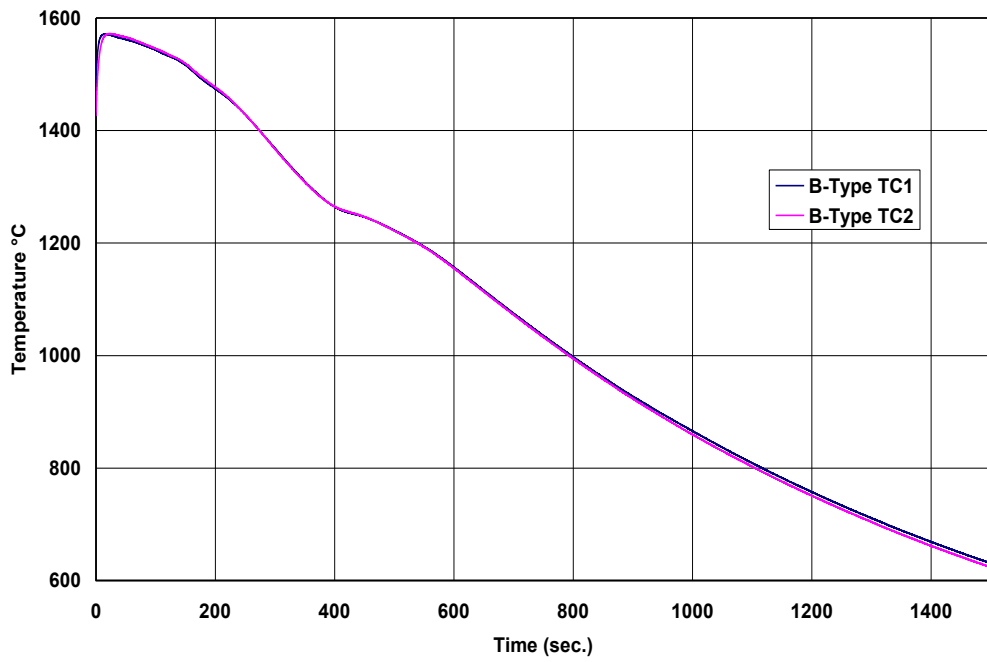
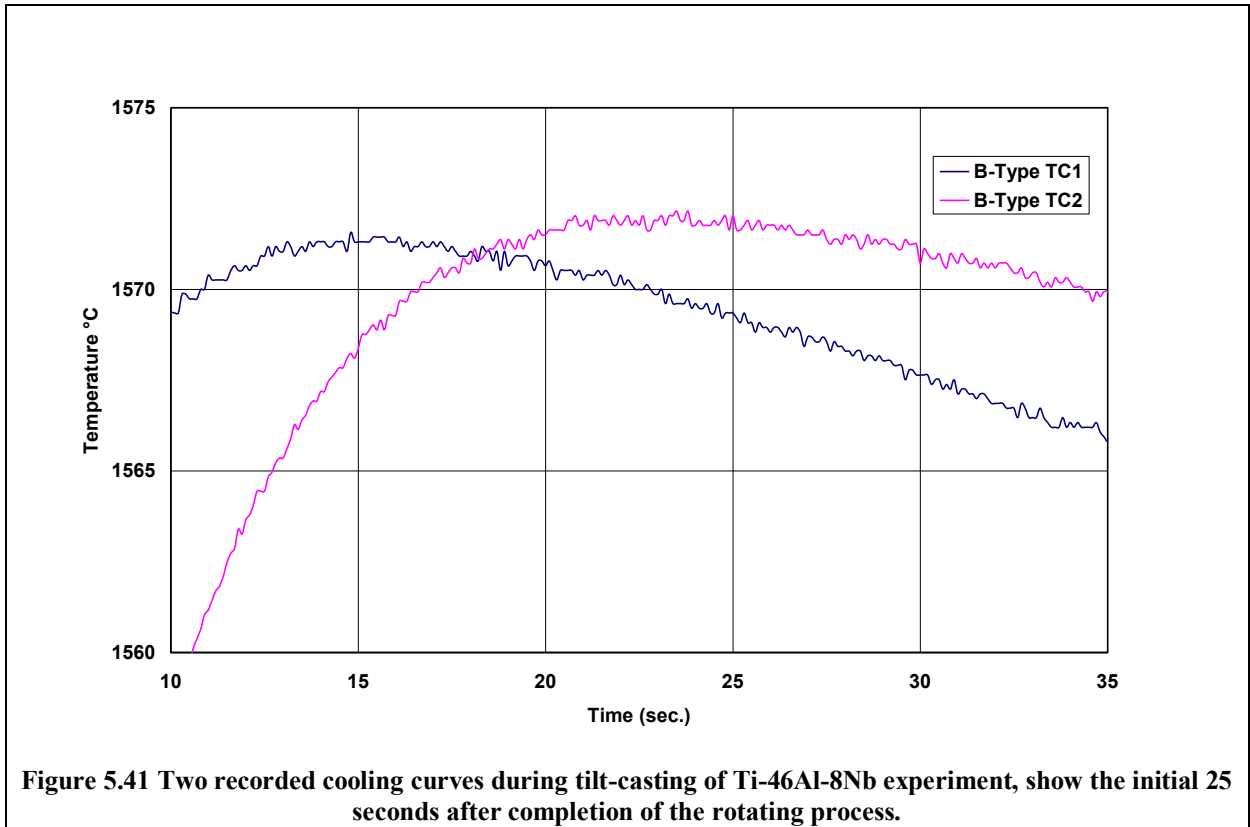
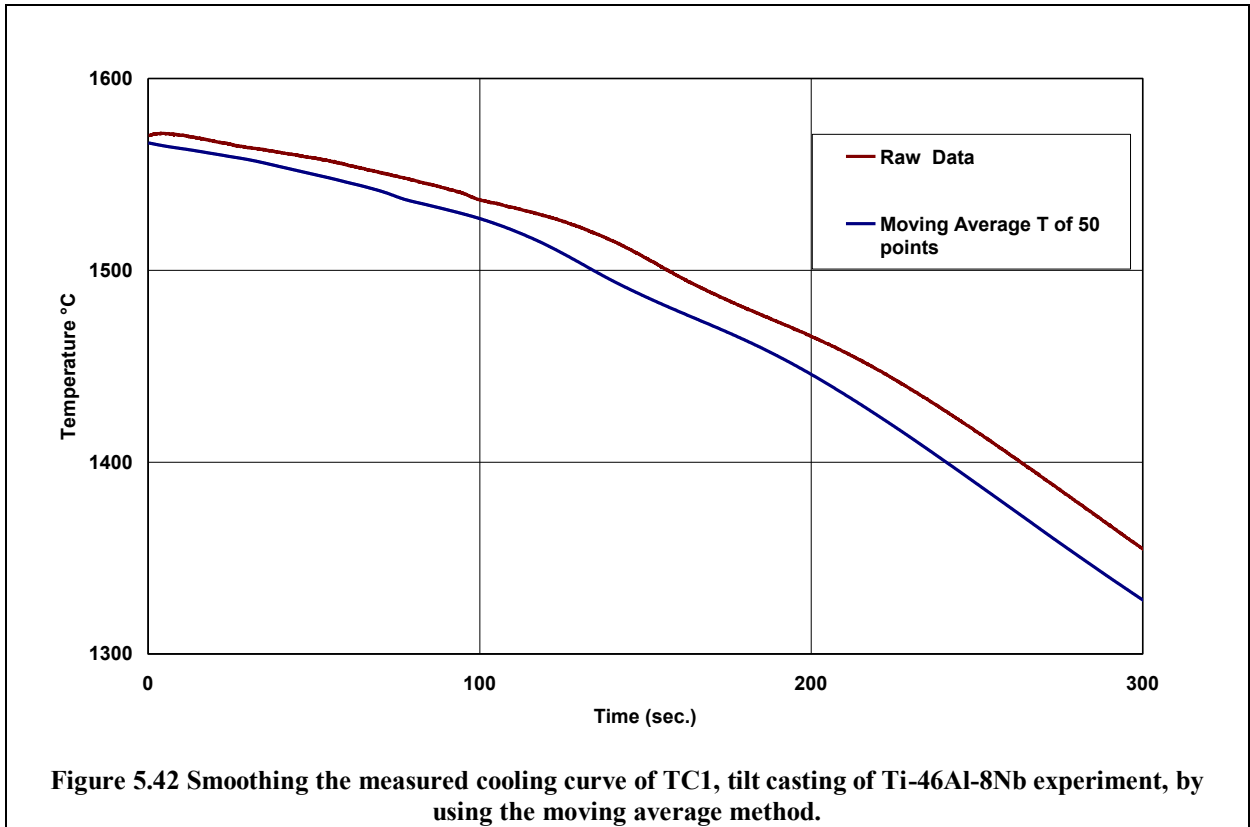


Figure 5.40 Experimental cooling curves at the thermal centre of Ti-46Al-8Nb alloy in tilt casting into 1000 °C preheated mould.



The raw data from the thermocouples contained a considerable amount of noise, as shown in Figure 5.41, which required the necessity of smoothing the measured data by applying numerical methods. Two numerical methods were applied and compared in order to obtain a convenient procedure to minimise the background noise.

Firstly, a moving average of 10 points was applied and repeated up to five times on the cooling curves measured by TC1 during the tilt casting experiment; the resulting curve is shown in Figure 5.42. The noise was significantly reduced, but the cooling curve was undervalued with an average of 20 K. Although the obtained cooling curve was significantly underestimated, (lower value of temperature as a result of taking the average of several points), the moving average algorithm resulted in a considerable reduction in noise.



The first and second derivatives of the smoothed curve were calculated in order to identify the peak points which coincided with inflexions on the cooling curve corresponding to phase transformations during solidification. The first differential (dT/dt) showed several peaks, although the inflexion points in the cooling curve were not clear, and thus the main peaks in the second differential curve (d^2T/dt^2) were used, along with the peaks in the first derivative curve, to identify inflexion points on the cooling curve.

The main peak points on the first derivative curve coincided with positions of maxima and minima peaks in the second derivative curve, as shown in Figure 5.43. These were matched with the phase diagram of Ti-46Al-8Nb which combined calculated and experimentally measured data by Witusiewicz et al. [14]. Figure 5.44 shows the phase diagram and the red line represents the investigated alloy at 0.458 Al (mole fraction), the average composition of the investigated alloy is given in Table 3-4.

The liquidus temperature on the phase diagram is 1577 °C and due to the uncertainty of the measured cooling curve, (as will be discussed in Section 5.6.1); the liquidus point was not clear on the cooling curve or on the first and second derivative curves. The first peak on both the first and second derivatives could be the solidus temperature, which occurred at 1517 °C on the phase diagram.

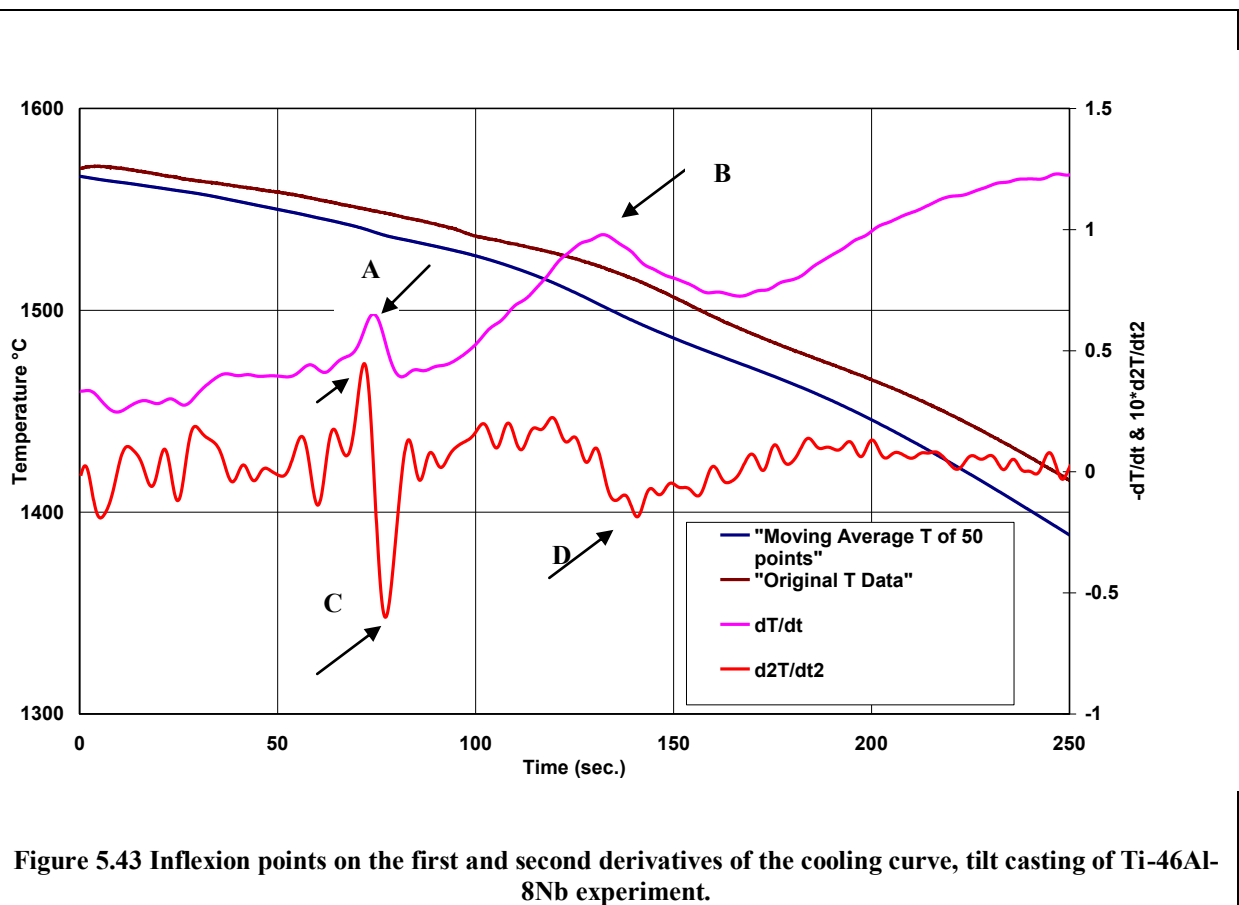


Figure 5.43 Inflexion points on the first and second derivatives of the cooling curve, tilt casting of Ti-46Al-8Nb experiment.

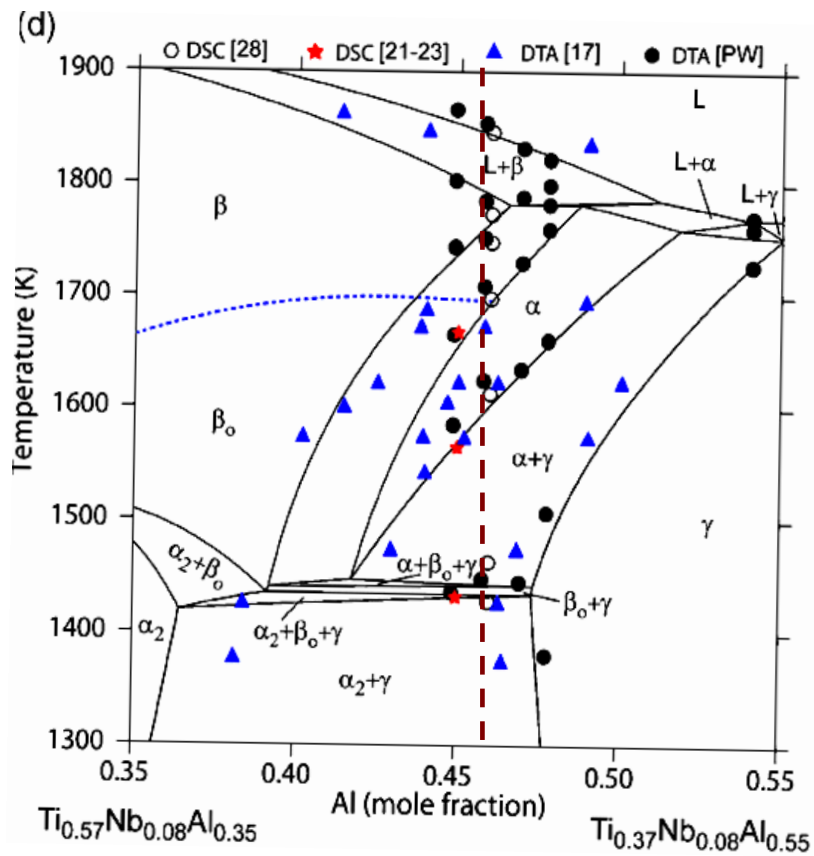
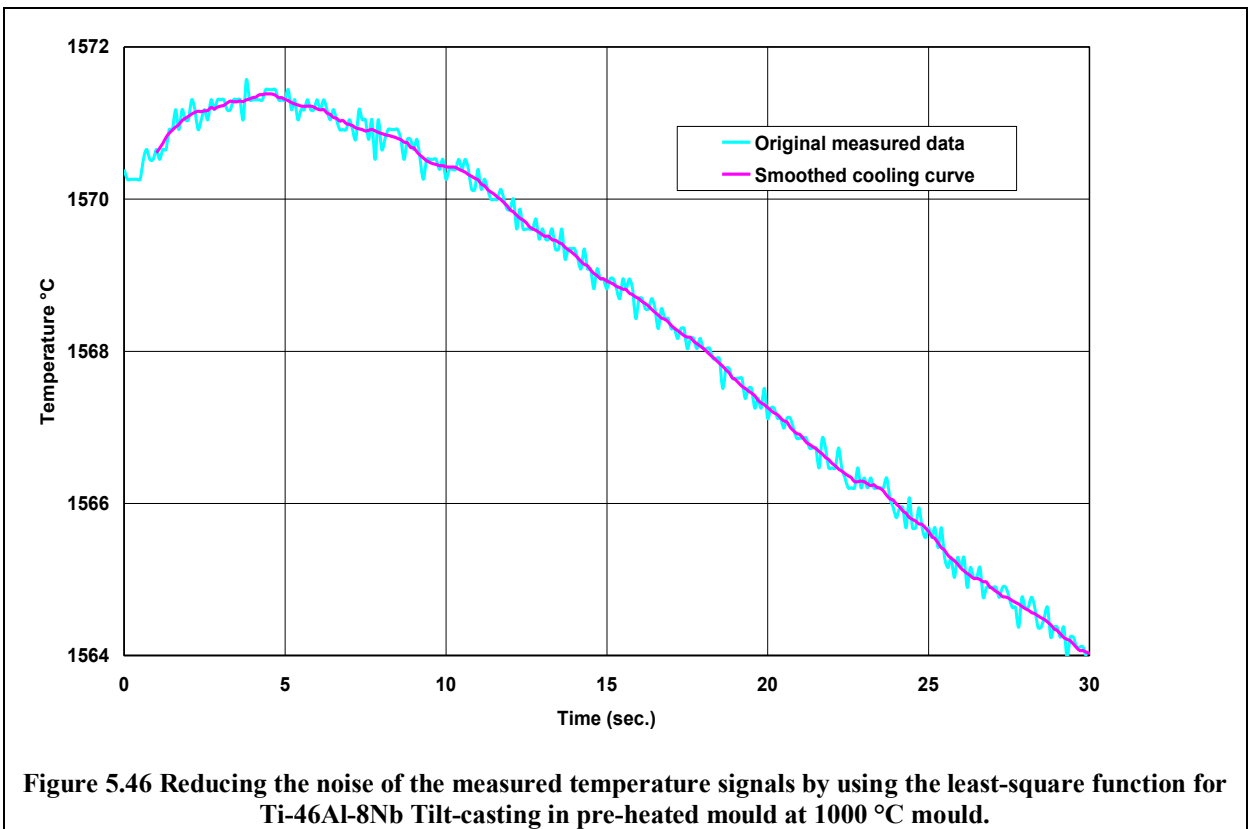
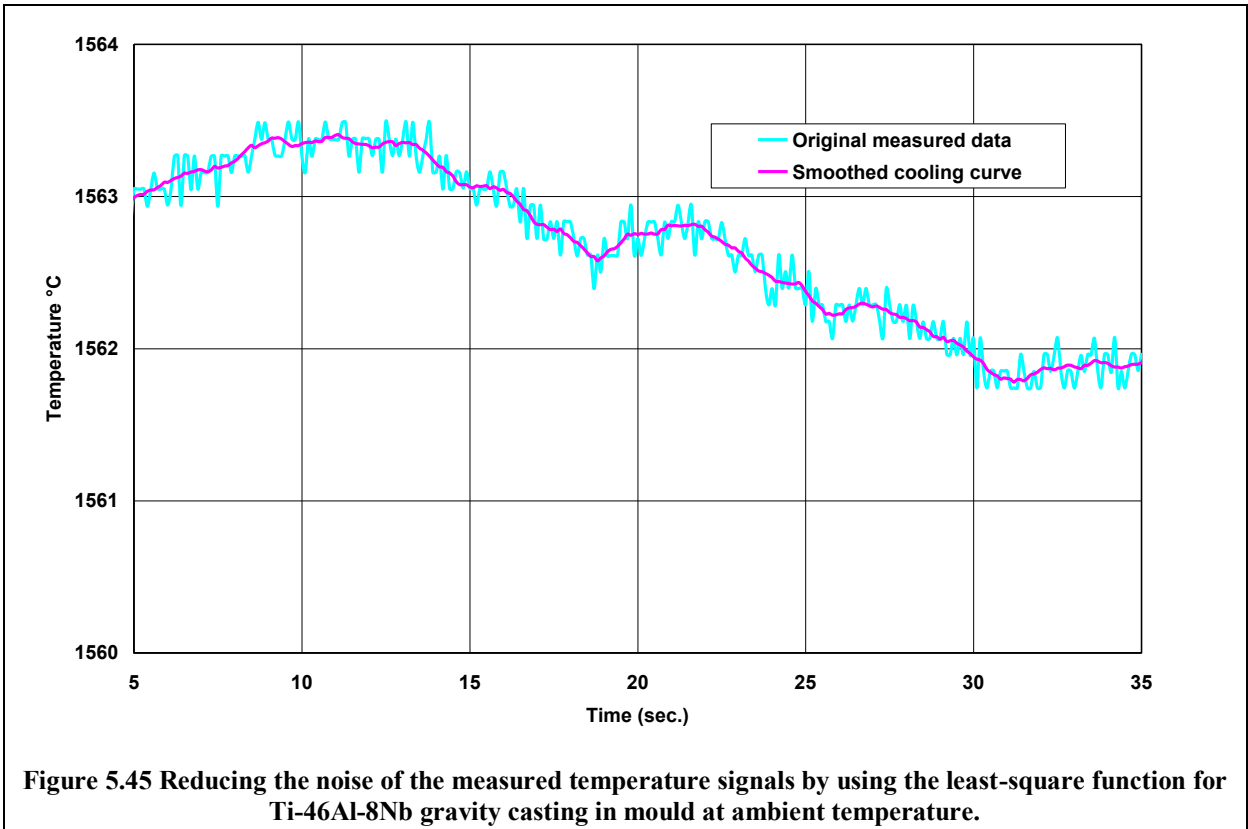
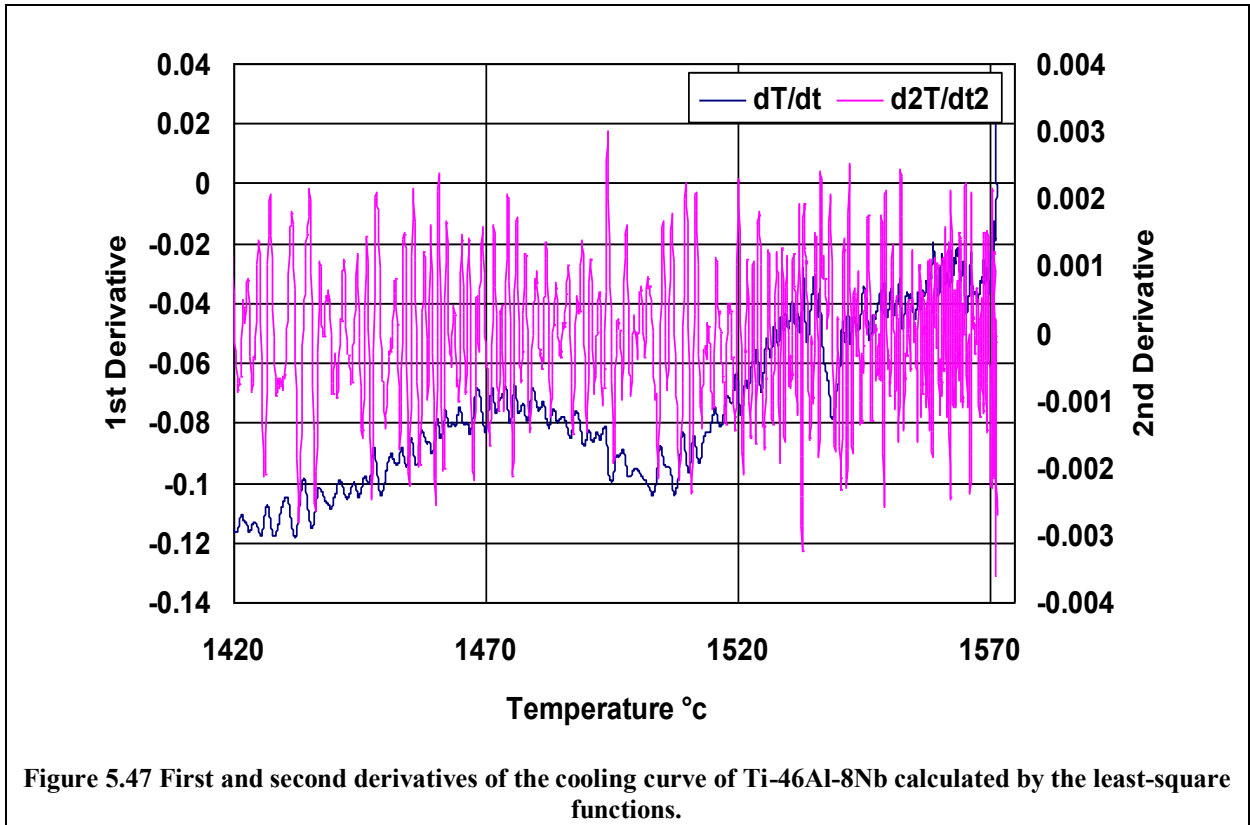


Figure 5.44 Phase diagram of TiAl8%Nb combines calculated and experimentally measured data, Witusiewicz et al. [14].

The least square algorithm [130], (as discussed in Section 3.7.1), was also used to minimize the noise of the recorded cooling curves. Figures 5.45 and 5.46 show a considerable reduction in the noise without underestimation of the measured data. However, the first and second derivatives, Figure 5.47, as calculated by the least square functions, still showed a large amount of noise and thus could not be used to detect any inflexion points.





5.6.1 Sources of Errors and Uncertainty of Measurements

Sources of errors during the temperature measurement experiments were various and related to the experimental conditions and the type of thermocouple used. Although the positioning of the thermocouples were carried out with a considerable care, however, an uncertainty in the position of the thermocouples is expected, especially for those in which their tips were embedded inside the ceramic shell which was characterised by a high roughness and a varying thickness around its circumference.

As stated in Section 3.6, the accuracy of the thermocouples' positions in the ceramic shell was checked by X-ray imaging, and the uncertainty of the positions was estimated to be about ± 0.5 mm.

In addition there was an uncertainty in the thermocouple position at the centre of the solidifying cylinder, due to inserting the thermocouple into an alumina sheath where the tip of the thermocouple did not exactly touch the inner end of the tube.

The response time of the TC could reach 5 seconds [140]; also, the presence of the alumina sheath was expected to cause a further delay in the response of the thermocouples.

The R and B type thermocouples used had had an accuracy of ± 1.4 to 1.6 K, [141].

Regarding the calculations of the mould/surroundings heat transfer coefficient the source of the uncertainty was limited to the extrapolation of the calculated curve of the heat transfer coefficients of the ceramic shell to a higher temperature range, in both the Argon atmosphere and in vacuum.

5.7 Using Criteria Functions for Predicting Shrinkage Porosity in Ti-46Al-8Nb Alloy

5.7.1 Analysis of Results

The results of the thermal-only model were used to compare the effectiveness of different criteria in predicting porosity in the titanium aluminide alloy. The model assumptions and boundary conditions are given in Chapter 4. The mould temperature was 1000 °C and the initial metal temperature was 1580 °C.

Each bar of the model was sectioned through its diameter at the vertical X-Y plane where the radius of the bar was in the X direction and the height was in the Y direction. Nodes were selected along the vertical sections of the test bars in the direction of pouring, (see Figure 4.18).

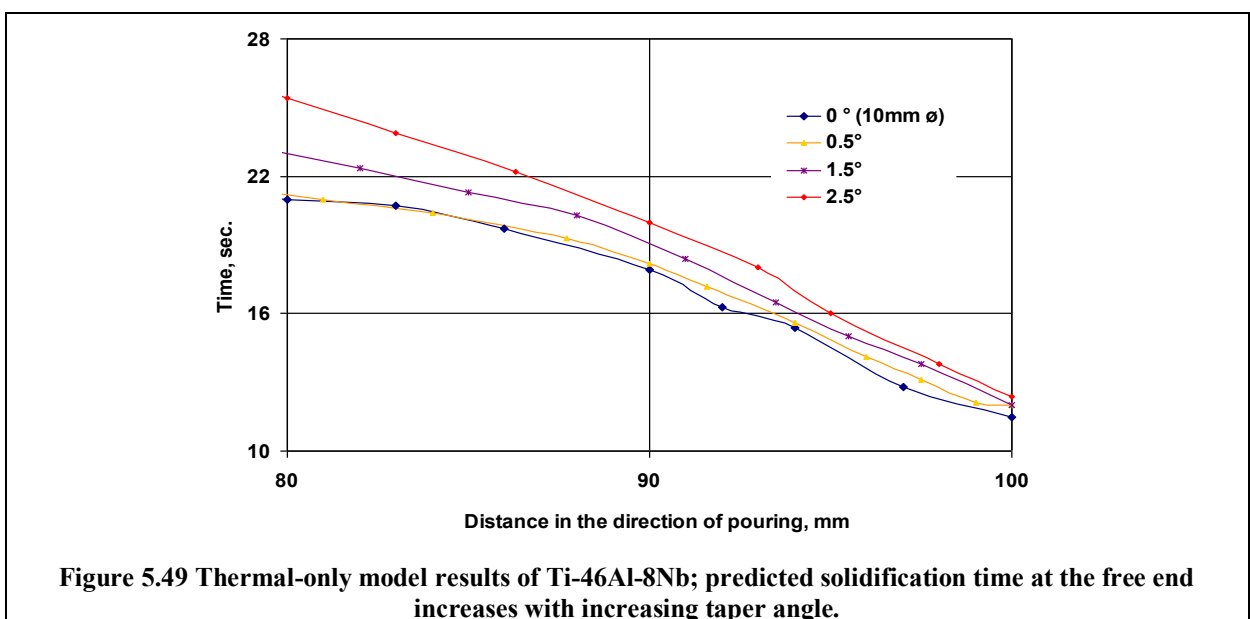
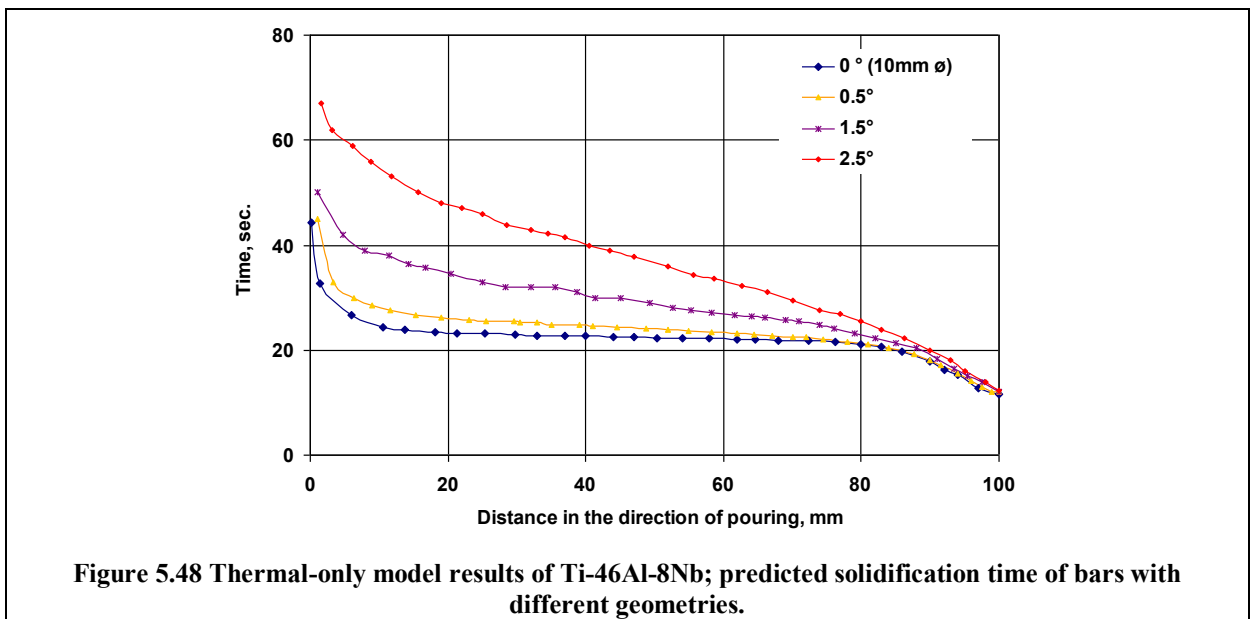
The temperature gradient G was calculated twice, first at a temperature corresponding to 100% solid at any point along the bars, and secondly at 1523 °C, which corresponds to 90 % of the solidification interval of the alloy. The values of G at any node of the model were computed as the total of the components of the temperature gradient in the X, Y and Z directions.

The cooling rate L and the isotherm velocity V_s were also calculated at 1523 °C. The mapping factors M , (the mapping factor is a mathematical formula used to calculate criterion function based on thermal parameters), were also calculated by the post-processor module (ViewCast) using the following constants: $a = 1$, $b = 0$, $c = 1$ and $d = -0.5$, which represent the Niyama criterion: $Nc = G/L^{1/2}$ ((°C^{0.5}. min^{0.5}.cm⁻¹) or (K^{0.5}.s^{0.5}.mm⁻¹)), at 1523 °C as well.

The feeding efficiency parameter (LCC): $G.t^{2/3}/V_s$ (K.s^{5/3}. mm⁻²) was calculated for each node using the ProCast results of the isotherm velocity, local solidification time and local temperature gradient at 1523 °C. The results of all bars were analysed individually and matched with the experimentally measured porosity contents (area percentage).

5.7.2 Predicted Solidification Time

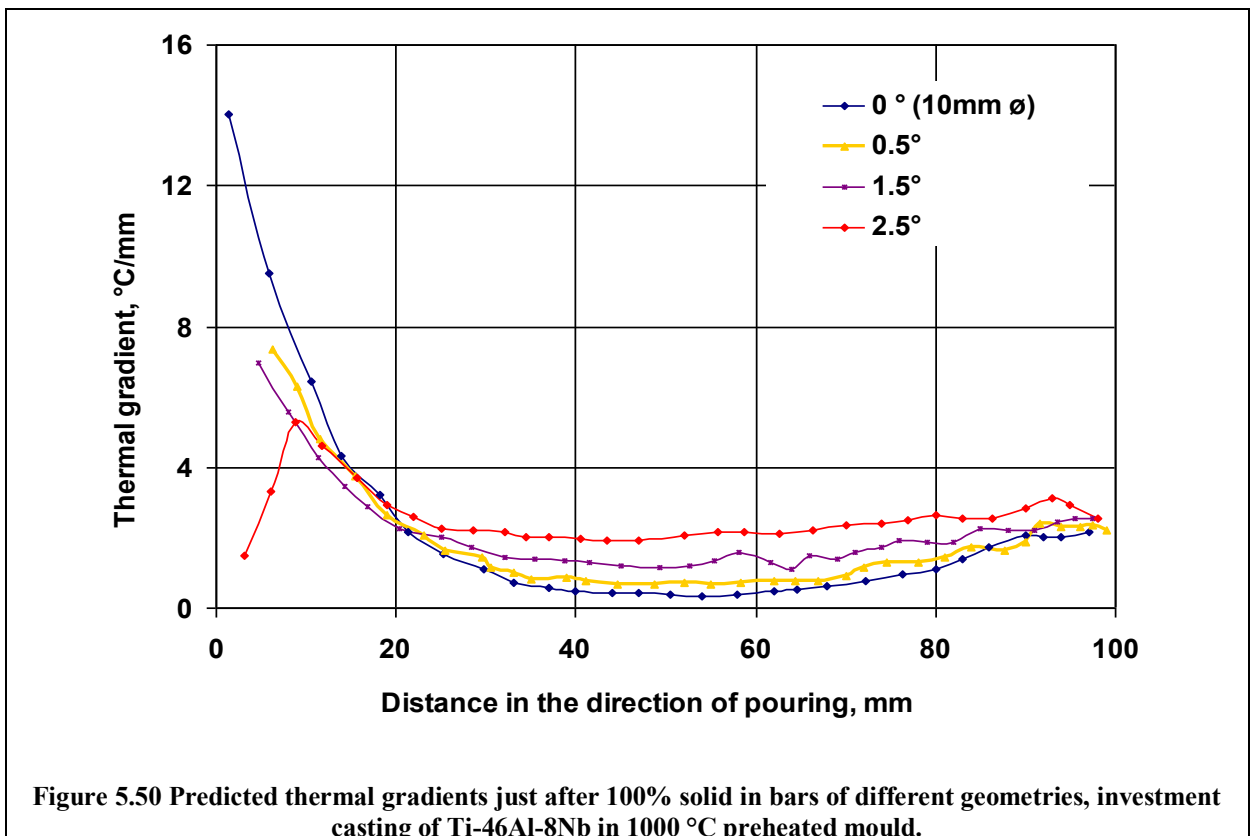
The solidification time along the central cross section of the bars showed a shallow change in the cylindrical bar and in the 0.5° tapered bar. A slight increase in the slope of the time-distance curve was noticed in the 1.5° tapered bar while the 2.5° tapered bar showed a steeper change in the (solidification time vs. distance) curve, as shown in Figure 5.48. The local solidification time at the free end of the bars increased with increasing taper angle, as shown in Figure 5.49.



5.7.3 Thermal Gradient

The thermal gradients at 100 % solid were plotted against distance from the top, along the centre line of the bars, in order to show the effect of casting geometry, (taper angle of the bars), on the general trend of thermal gradient. Figure 5.50 shows this comparison. The cylindrical 10 mm diameter bar has the highest thermal gradient over the first 10 mm from the top of the bar, and then G decreased with distance in all bars until about 20 mm from the top. At this point, G in the cylindrical bar had the lowest value along the centre line and then it started to increase again at about 80 mm from the feeder.

As the taper angle increased the thermal gradient increased, particularly in the middle (between 20-80 mm) height of the bars. The bar with the largest taper angle (2.5°) had the lower G at the top where it had the largest diameter, and then G increased and reached an almost constant value in the middle height between 20 to 80 mm, which was higher than the thermal gradients in the bars with lower taper angle.



Local thermal gradients, as predicted by the model at 90% of the solidification interval (1523 °C), fluctuated with position along the centre line of the bars, as depicted in Figure 5.51.

Generally, the local thermal gradient increased from the free end of the bar to a position where it reached a maximum value, after which the free-end effect faded. Then, the thermal gradient decreased until at the position where the effect of the feeder on the top of the bar was strong enough to encourage the thermal gradient to increase again.

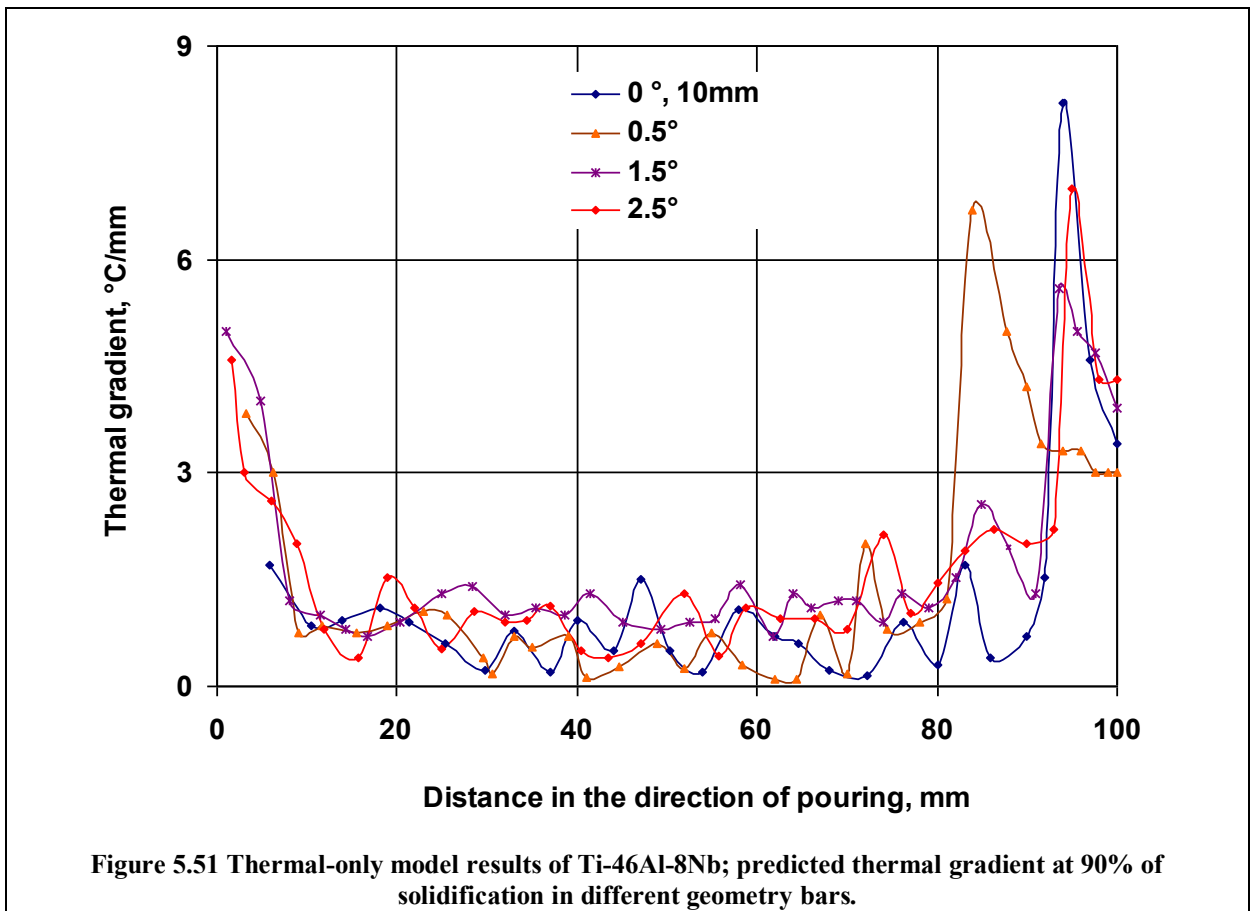
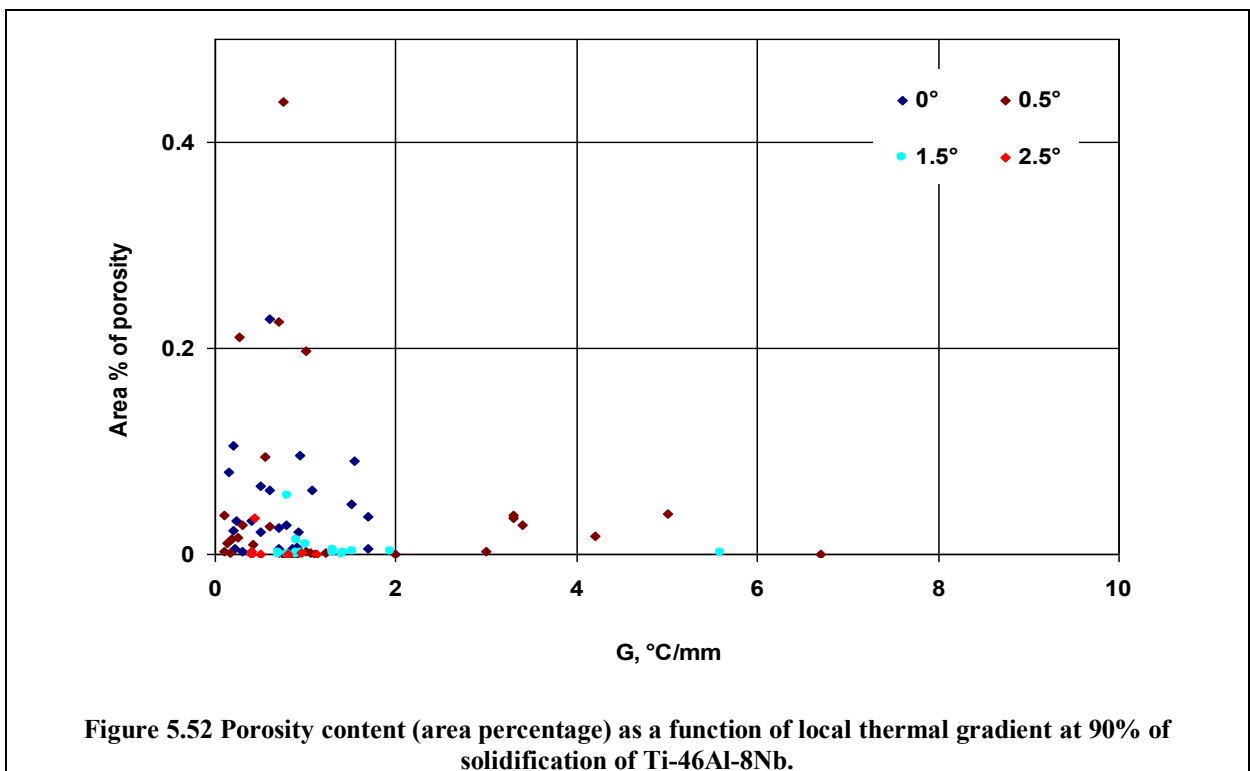


Figure 5.52 shows the measured porosity along the centre line of the test bars plotted against the predicted temperature gradient at selected nodes which corresponded to the position of the porosity as calculated by ProCastTM software at 90% solidification (1523 °C).

The higher values of porosity were mainly associated with low temperature gradient regions in the range between 0.1 to 2 °C/mm. In addition, the cylindrical 10 mm diameter (0°) bar had the most scattered distribution of porosity as predicted by the temperature gradient, while the 2.5° tapered bar showed the least scattered distribution among the (0°, 0.5°, 1.5° and 2.5°) tapered bars tested.



5.7.4 Feeding Efficiency Parameter

The feeding efficiency parameter (known in some research works that used ProCastTM as the LCC parameter) is a more complicated criterion used to predict porosity in long freezing range alloys. It was developed by Lee et al. [83] and is denoted $G.t^{2/3}/V_s$ ($^{\circ}\text{C}\cdot\text{sec}^{5/3}/\text{mm}^2$), where G is the local thermal gradient, t is the local solidification time and V_s is the solidus velocity (or solidification rate (R) as defined in ProCast). G , t and V_s were obtained from the results of the thermal model, and values of the feeding efficiency parameter were calculated at each selected node. Figures 5.53, 5.54, 5.55 and 5.56 show the correlation between the feeding efficiency parameter, (LCC will be used hereafter to refer to this parameter), and the measured area percentage of porosity along the thermal centre of some of the test bars; the 10 mm cylindrical bar, the 0.5° tapered bar, the 1.5° tapered bar and the 2.5° tapered bar.

In the case of the 10 mm cylindrical bar the LCC parameter fluctuated between high and low values at the positions of high porosity content. Likewise, the LCC values fluctuated between low and high values in the 0.5° tapered bar, while they showed less scatter in the case of the 1.5° and 2.5° tapered bars whereas most of the lower values of the LCC were associated with positions of high porosity content.

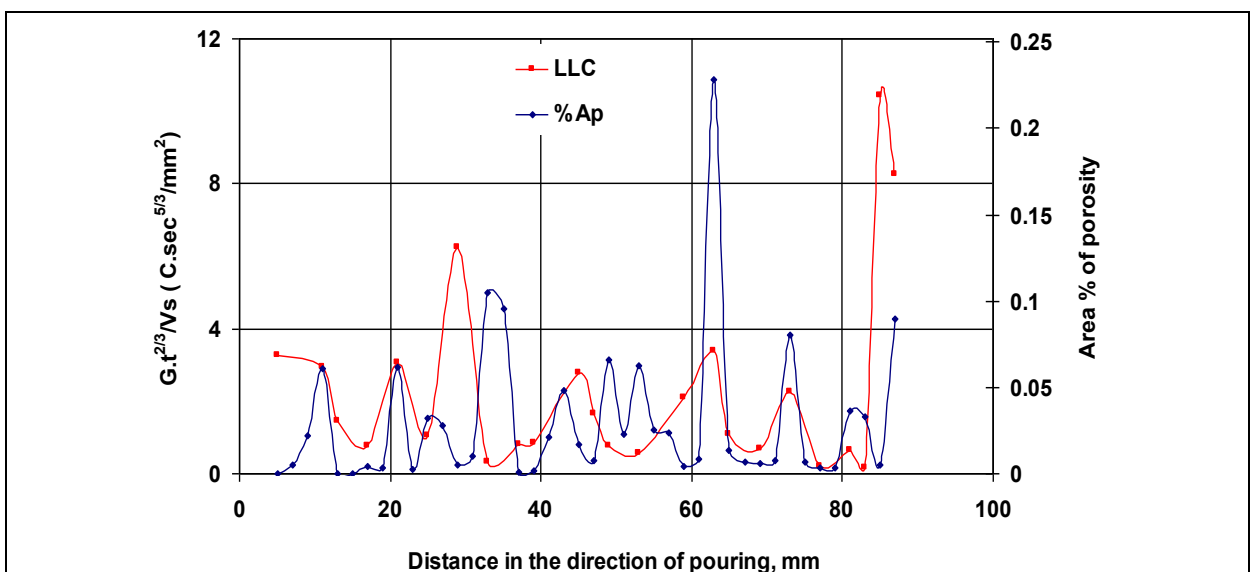


Figure 5.53 Model results of investment casting of Ti-46Al-8Nb in 1000 °C preheated mould; prediction of porosity by feeding efficiency parameter along the thermal centre of the cylindrical 10 mm diameter bar.

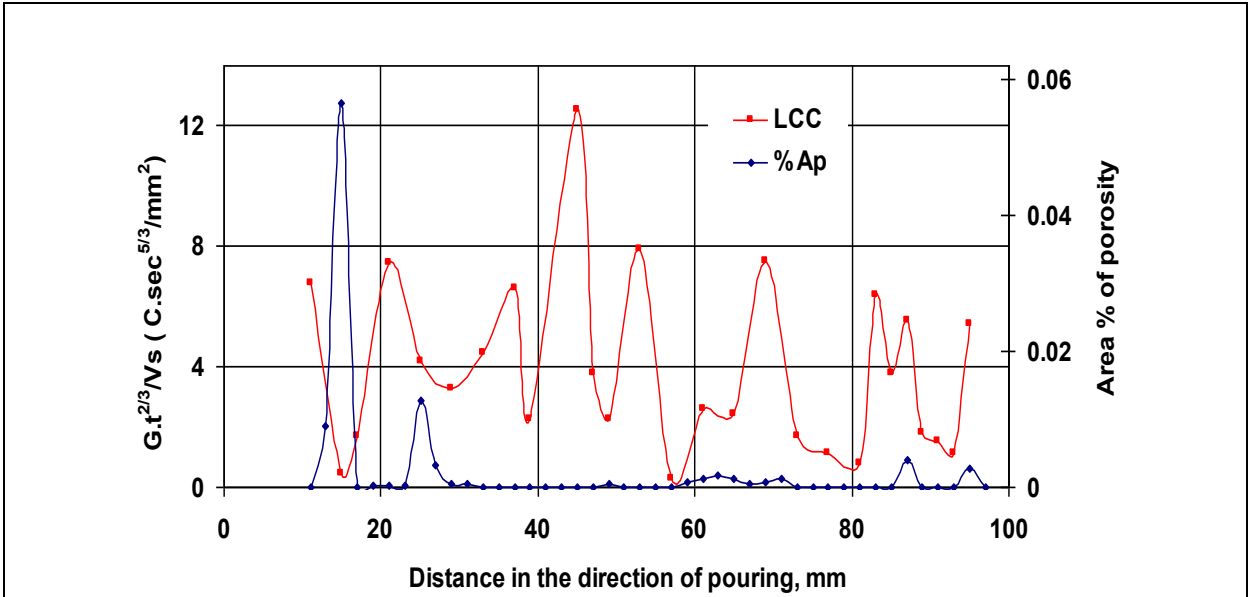


Figure 5.54 Model results of investment casting of Ti-46Al-8Nb in 1000 °C preheated mould; prediction of porosity by feeding efficiency parameter along the thermal centre of the 0.5° tapered bar.

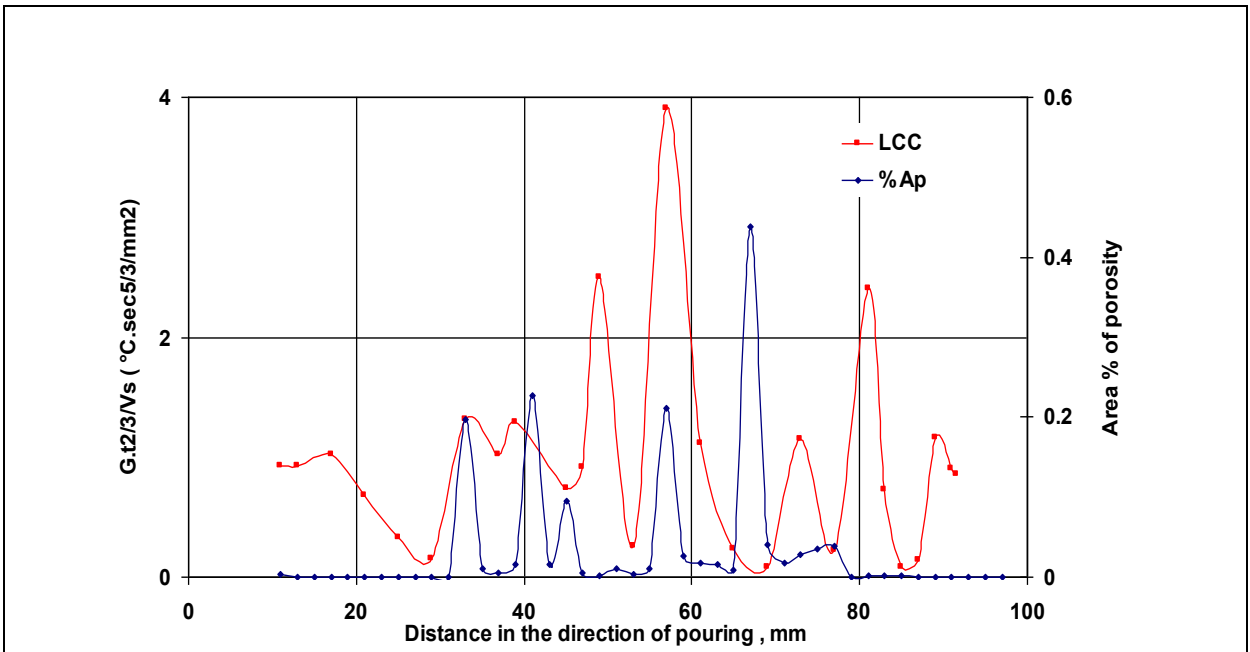


Figure 5.55 Model results of investment casting of Ti-46Al-8Nb in 1000 °C preheated mould; prediction of porosity by feeding efficiency parameter along the thermal centre of the 1.5° tapered bar.

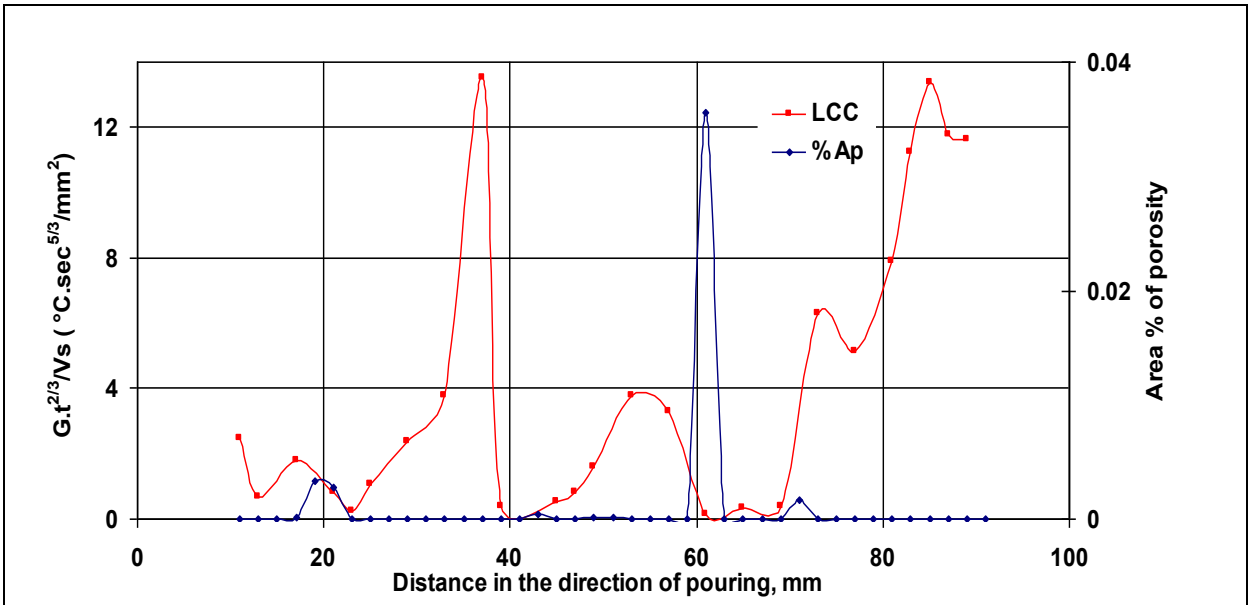
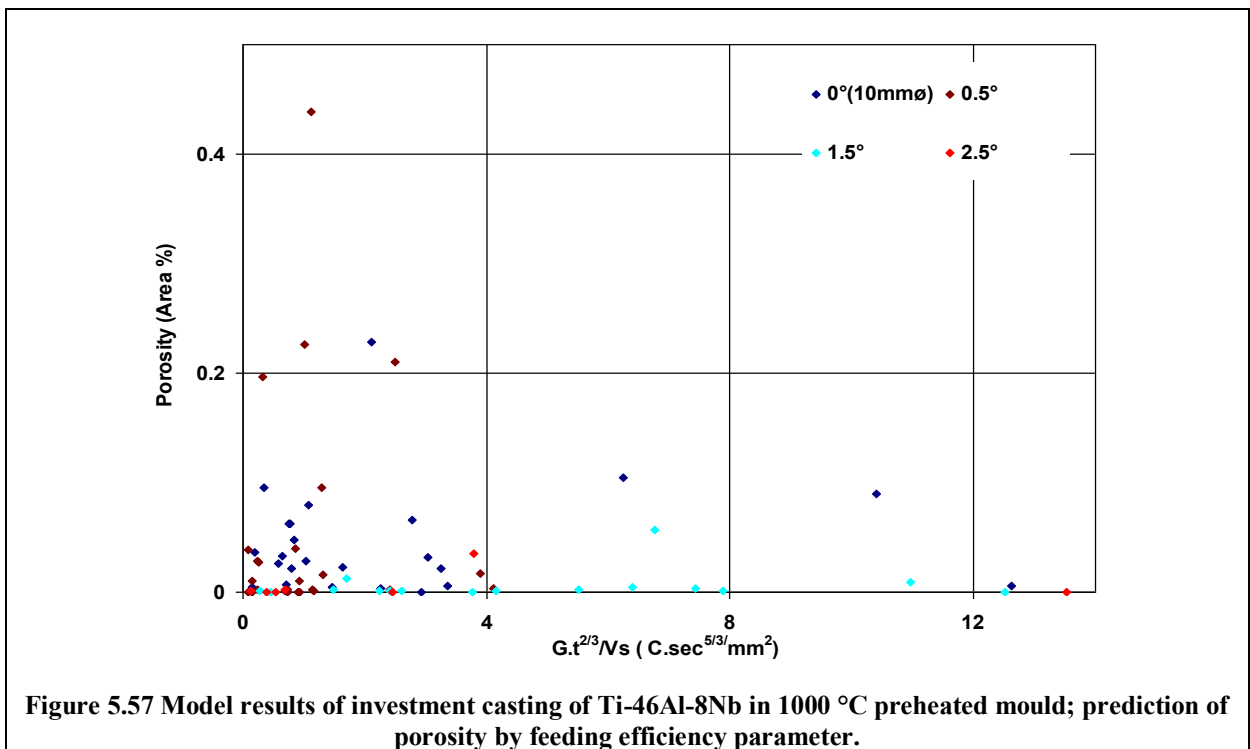


Figure 5.56 Model results of investment casting of Ti-46Al-8Nb in 1000 °C preheated mould; prediction of porosity by feeding efficiency parameter along the thermal centre of the 2.5° tapered bar.

In order to illustrate a direct correlation between the LCC parameters and the distribution of the porosity Figure 5.57 shows porosity content against corresponding values of LCC at the same position along the thermal centre of the test bars.

Although the porosity can be very low even with LCC values as low as 0.13, there was a general trend of the porosity to decrease gradually as the LCC increased. The scatter in porosity distribution, especially in the cylindrical bar and the smaller tapered bars when it was matched with LCC, reflects that the criterion is a geometry dependant function.

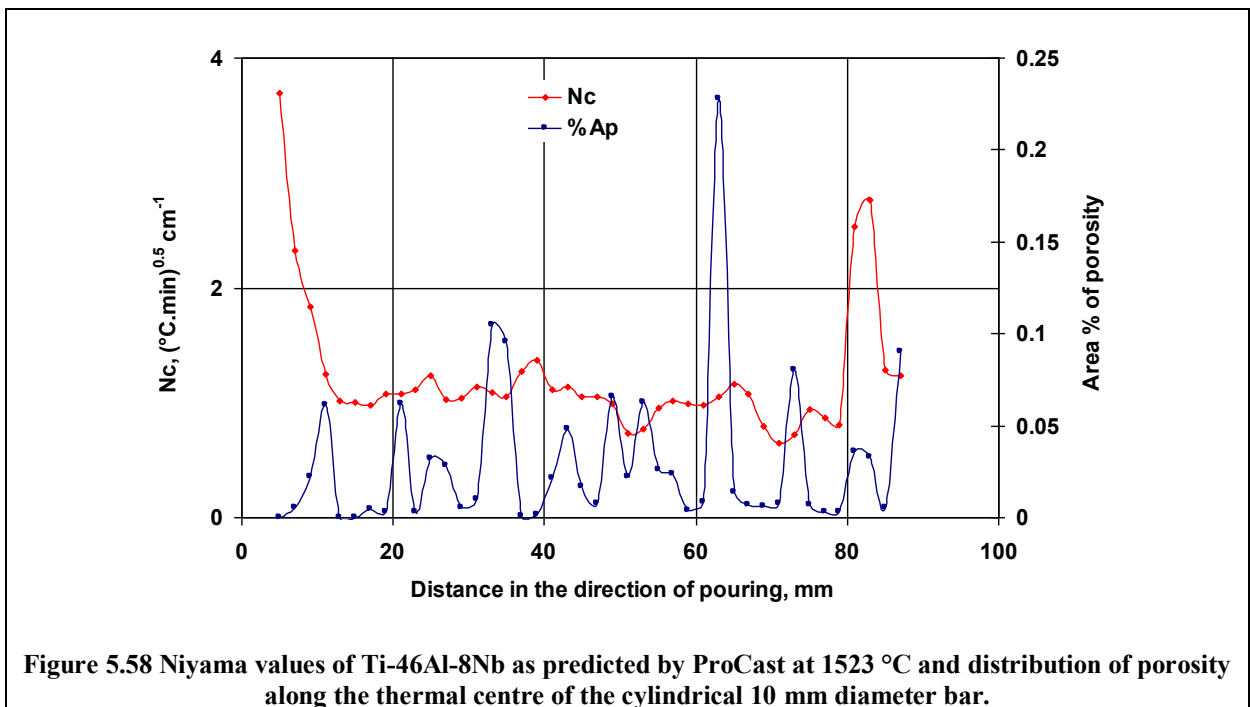


5.8 Correlation between Niyama Criterion and Porosity Distribution

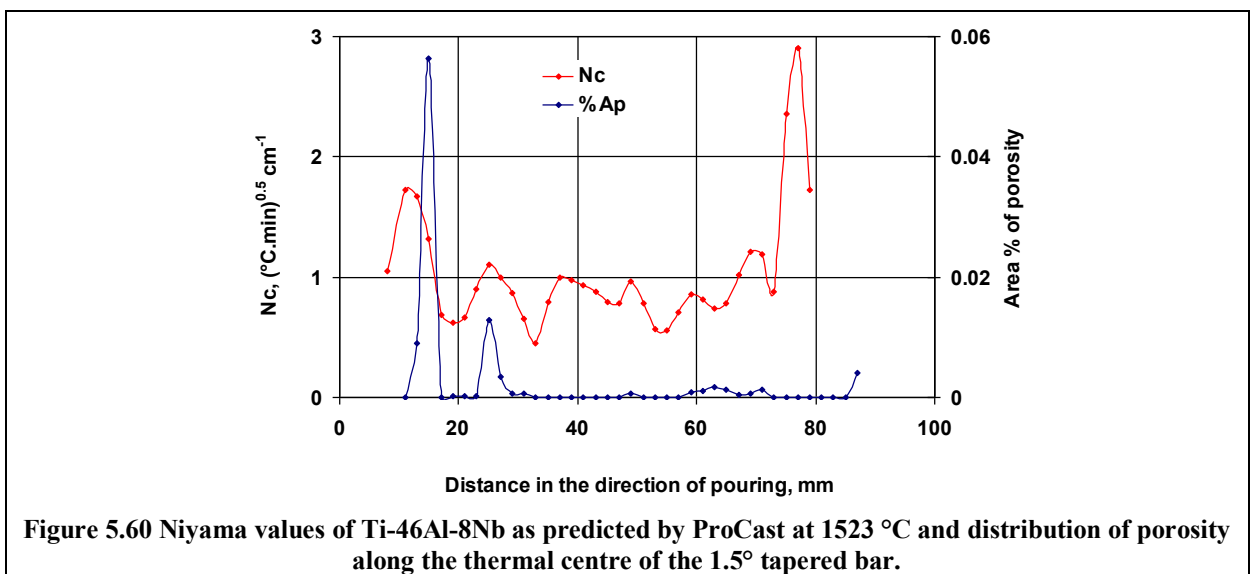
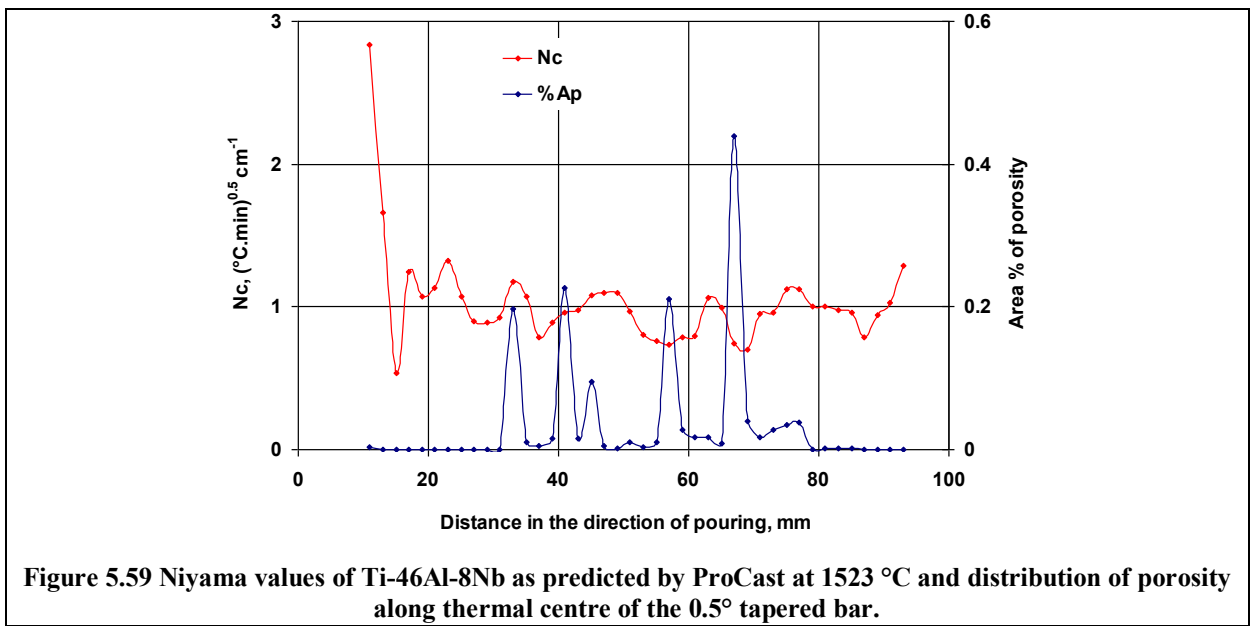
5.8.1 Distribution of Porosity along the Central Line of the Test Bars

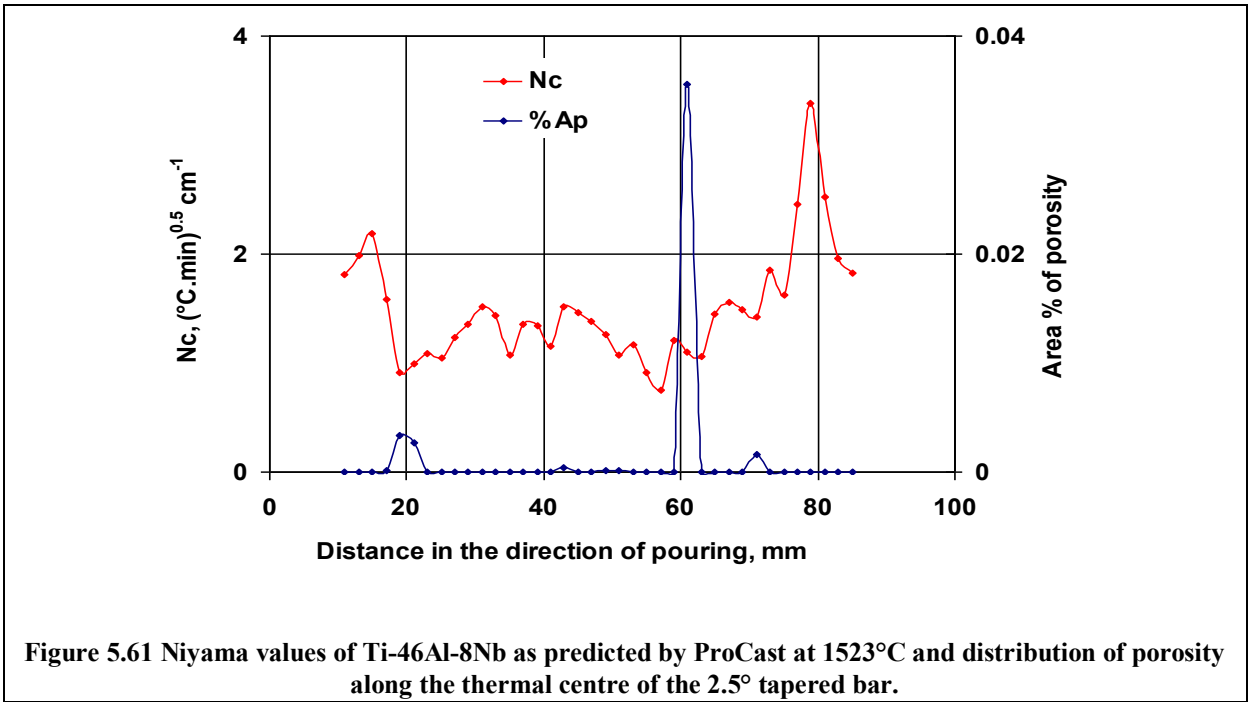
Niyama criterion values (N_c) were computed by the ProCastTM model at selected nodes along the central lines of the investigated bars, separated by 2 mm. The values of N_c were sensitive to the temperature at which they were calculated. Therefore, the distributions of the measured porosity along the central line of the bars were plotted against Niyama values at corresponding positions, calculated at 90% solidification (1523 °C).

As can be seen in Figure 5.58, most of the positions of high porosity content in the 10 mm diameter cylindrical bar corresponded to lower values of N_c , particularly between the (30-70 mm) of the length.

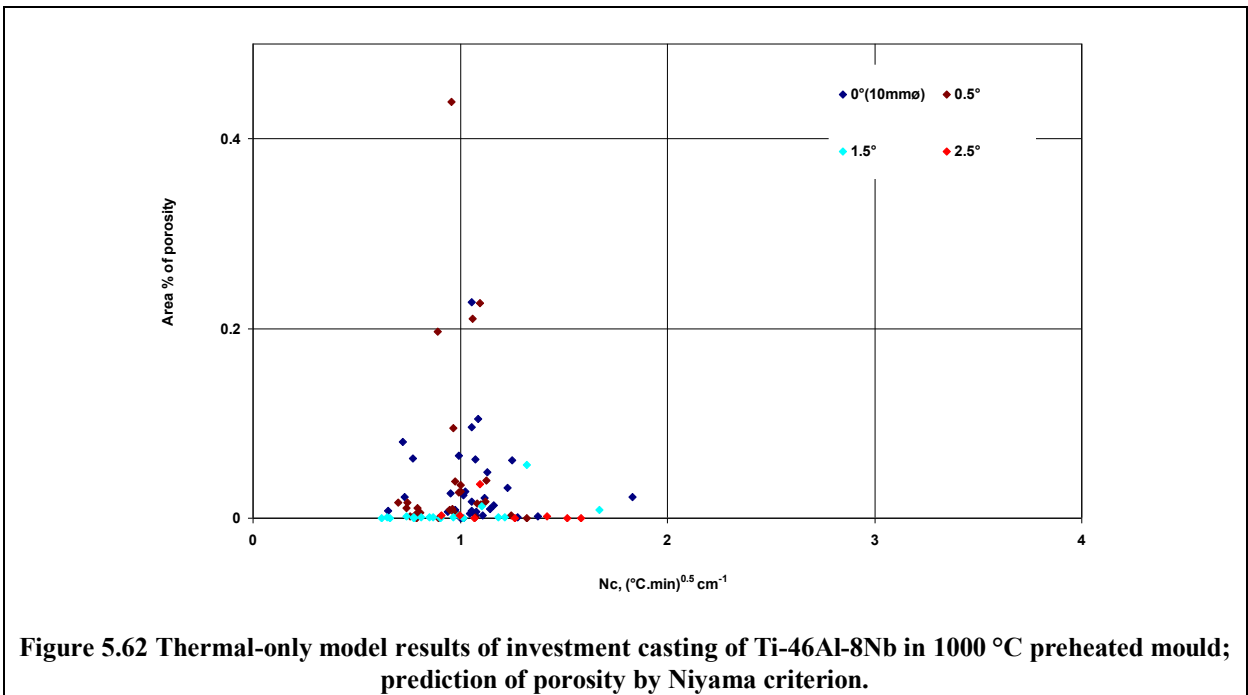


The same observation applied to the 0.5° tapered bar, as shown in Figure 5.59. Regarding the 1.5° and 2.5° tapered bars, the level of porosity was generally low (between 0 to 0.6 area %) and the position of the maximum value of Nc corresponded to an almost zero porosity position in the 1.5° bar, as shown in Figure 5.60. Just one position in the central line of the 2.5° tapered bar contained a relatively high porosity, specifically at about 61 mm from the top of the bar where % Ap =0.036, whereas Nc= 1.09 (°C.min)^{0.5} cm⁻¹ as shown in Figure 5.61.





To summarize the above results, the Niyama function versus the porosity content at the central line is shown in Figure 5.62. The higher porosity values were associated with low values of N_c in the range of 0.7 to 1.1 $(^{\circ}\text{C}\cdot\text{min})^{0.5}\text{cm}^{-1}$. The results of the 2.5° bar showed that points of very low porosity corresponded to N_c of 3.7 $(^{\circ}\text{C}\cdot\text{min})^{0.5}\text{cm}^{-1}$.



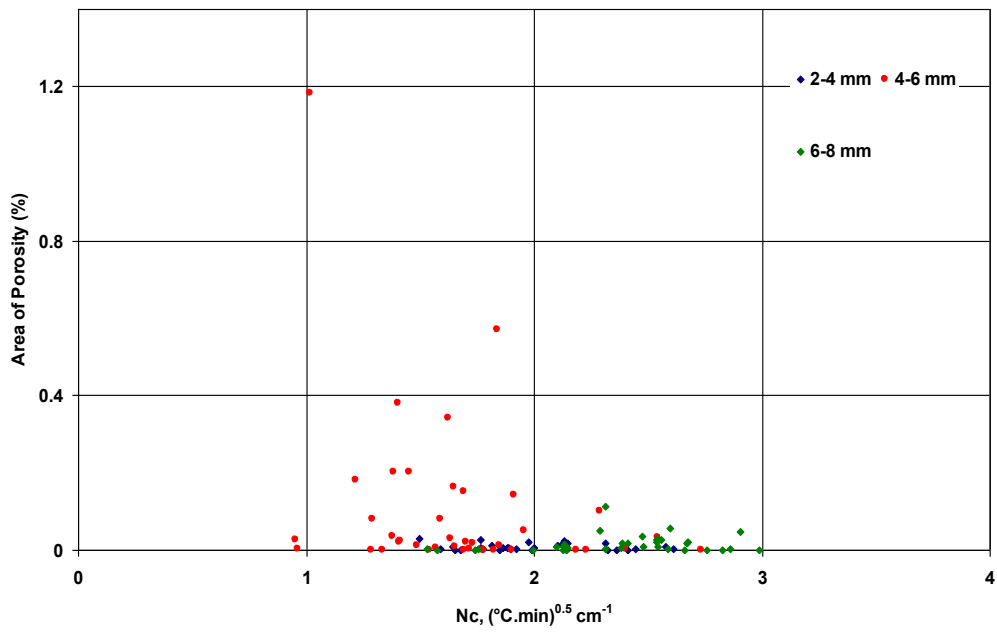
In the following sections the use of the Niyama criterion is presented in more detail by predicting the positions of maximum porosity in the geometries investigated, through using a more precise matching of the measured porosity with the N_c values calculated by two ProCast models with preheat mould temperatures of 1000 °C and 500 °C, respectively, in 2×2 mm cells in the radial and longitudinal directions, as described in Chapter 4.

5.8.2 Distribution of Porosity in the Longitudinal Section of the Test Bars

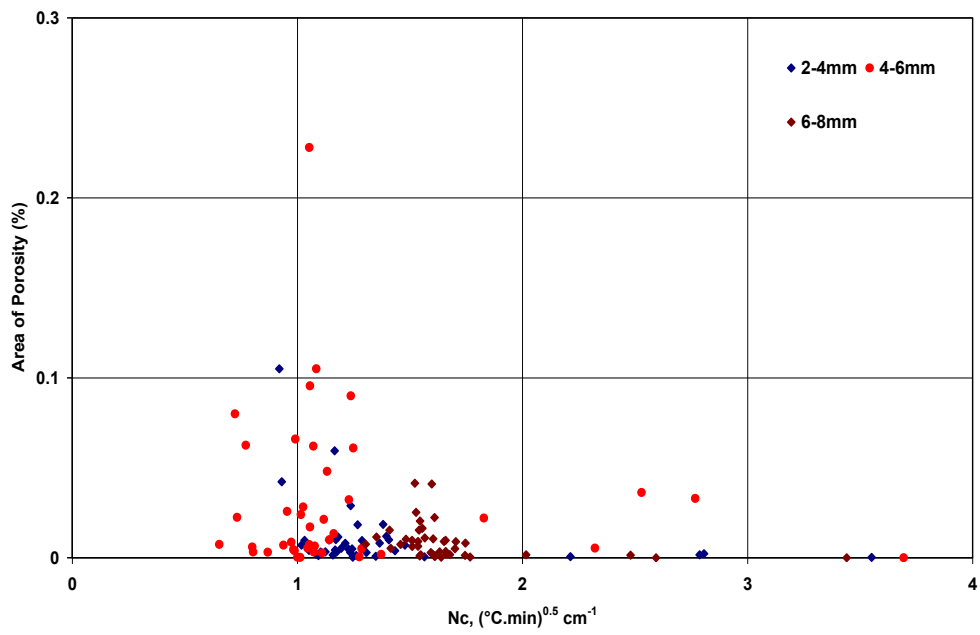
The values of the Niyama criterion (N_c) were calculated as the average of N_c at four nodes at the corners of the 2 mm x 2 mm cells in the X and Y directions of the centre cross-section of the model bars. The edges of the test bars were excluded from the calculations and the nodes were selected 2 mm away from the edges. The measurements of porosity at these sections (0-2 mm from both edges) were also excluded. The values of measured porosity were matched with the calculated N_c at the corresponding positions.

Figures 5.63 to 5.66 show the matching of average values of the measured porosity in cylindrical and tapered bars cast in 500 °C and 1000 °C preheated moulds with the calculated average of N_c at the corresponding positions.

As a general observation, in all test bars and in both preheating mould temperatures, the porosity occurred in the range of N_c between 0.5 to 4 (°C.min)^{0.5} cm⁻¹. Additionally, the high porosity levels corresponded mainly to N_c values in the range of 1 to 2 (°C.min)^{0.5} cm⁻¹.

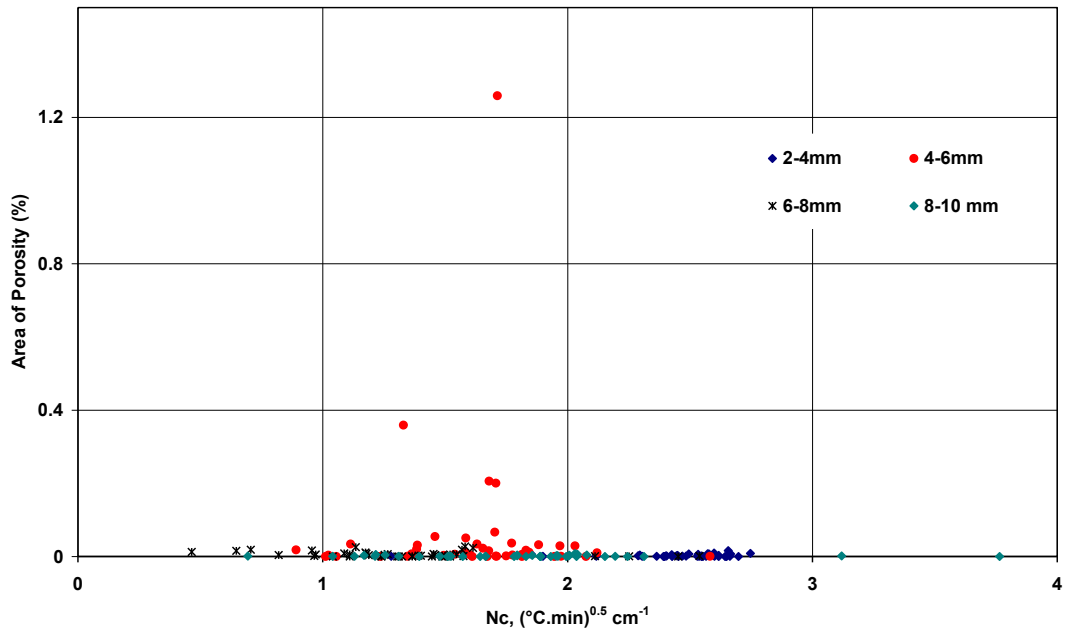


(A)

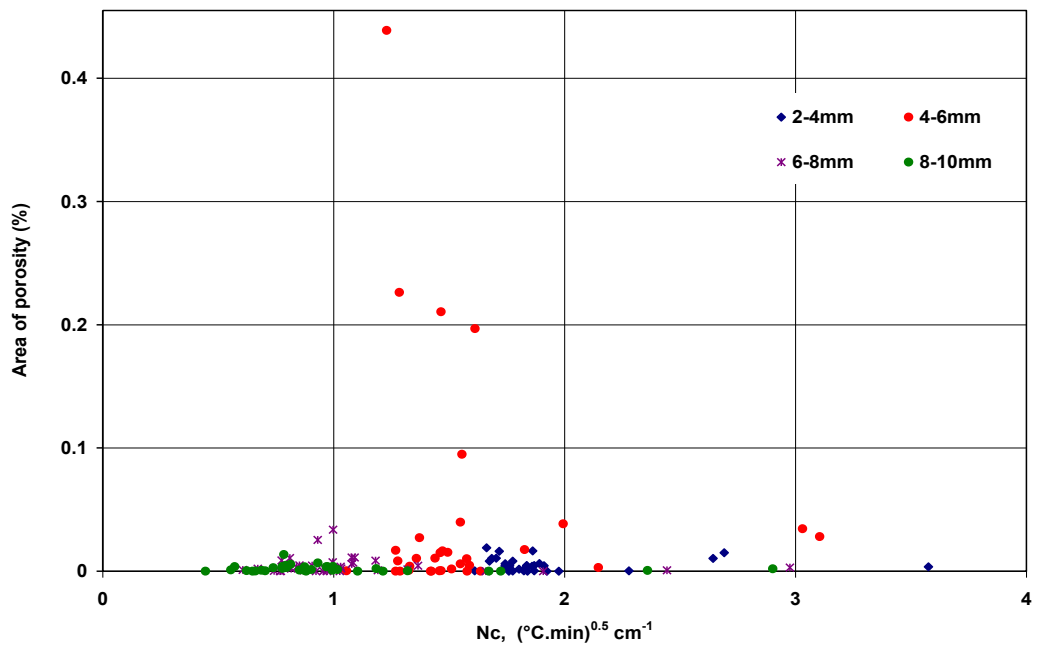


(B)

Figure 5.63 Distribution of porosity of Ti-46Al-8Nb in the longitudinal cross- section of the 10 mm diameter cylindrical bar in 500 °C (A) and 1000 °C (B) mould temperature as a function of Nc Values.



(A)



(B)

Figure 5.64 Distribution of porosity of Ti-46Al-8Nb in the longitudinal cross- section of the 0.5° tapered bar in 500 °C (A) and 1000 °C (B) mould temperature as a function of Nc Values.

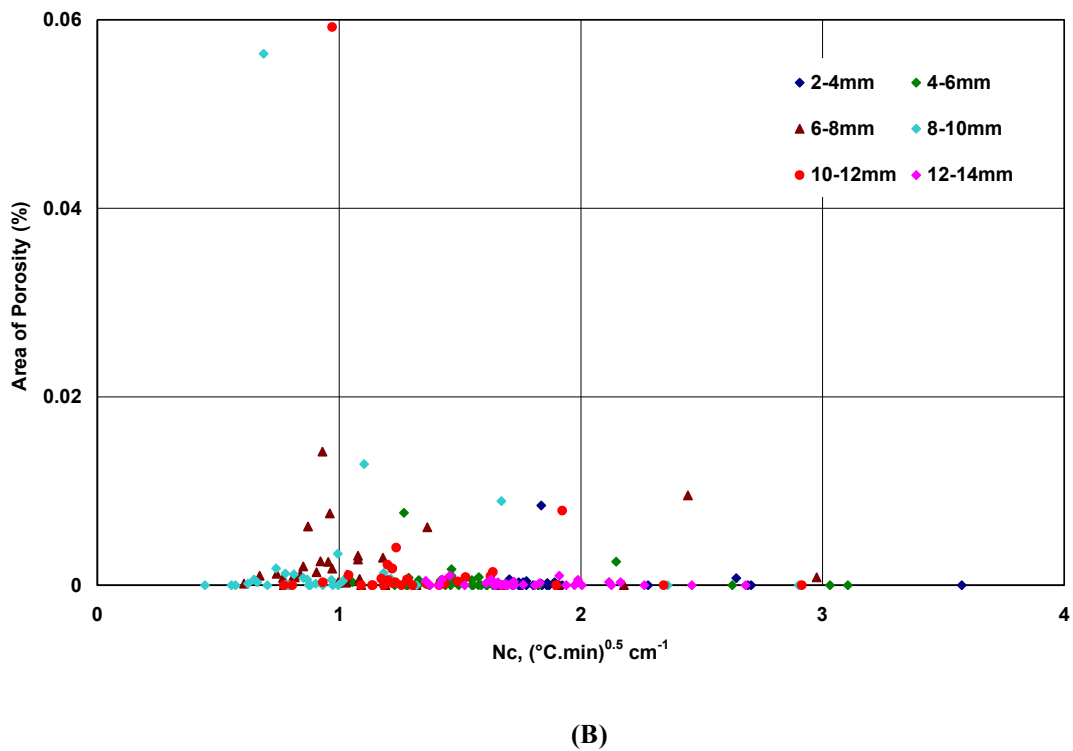
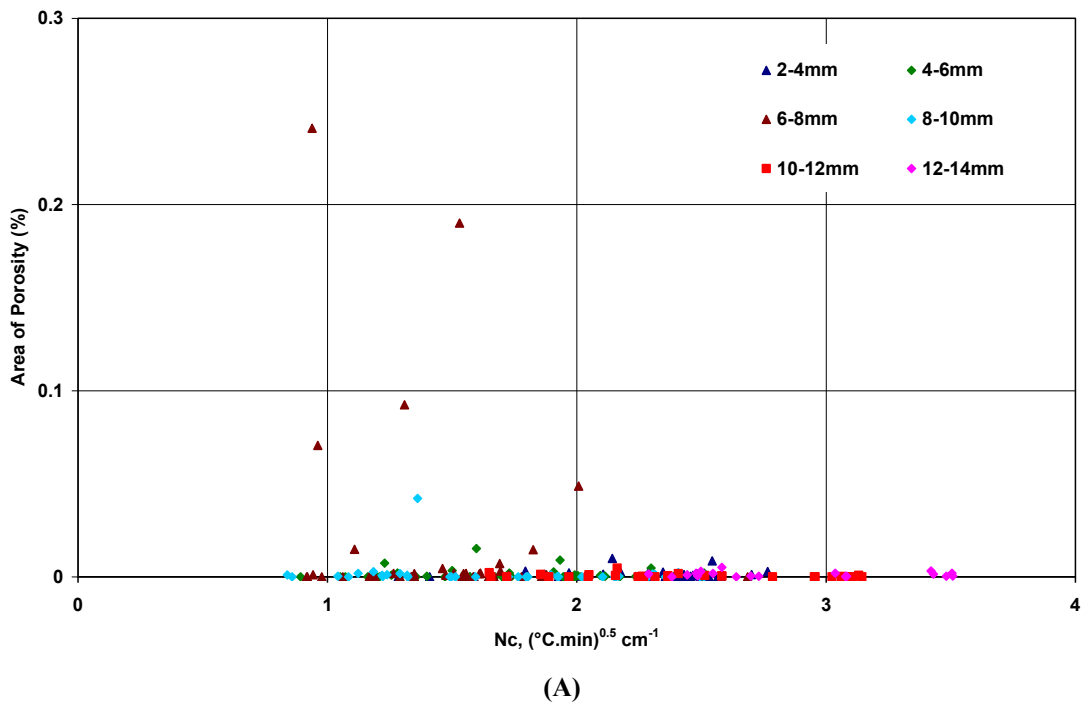


Figure 5.65 Distribution of porosity of Ti-46Al-8Nb in the longitudinal cross-section of the 1.5° tapered bar in 500 °C (A) and 1000 °C (B) mould temperature as a function of Nc Values.

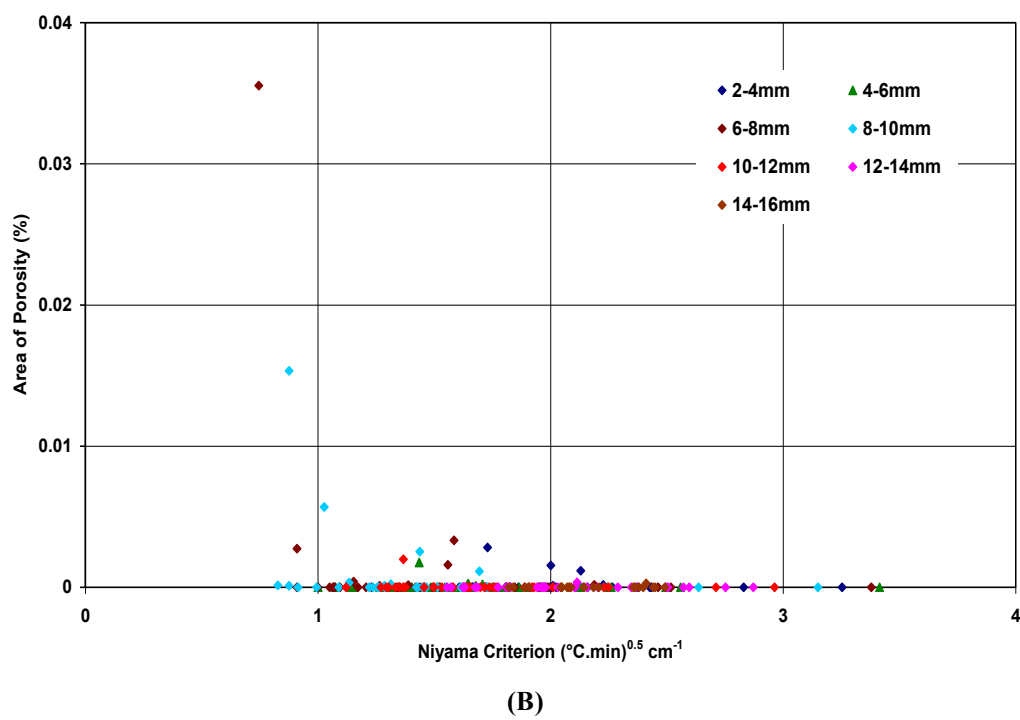
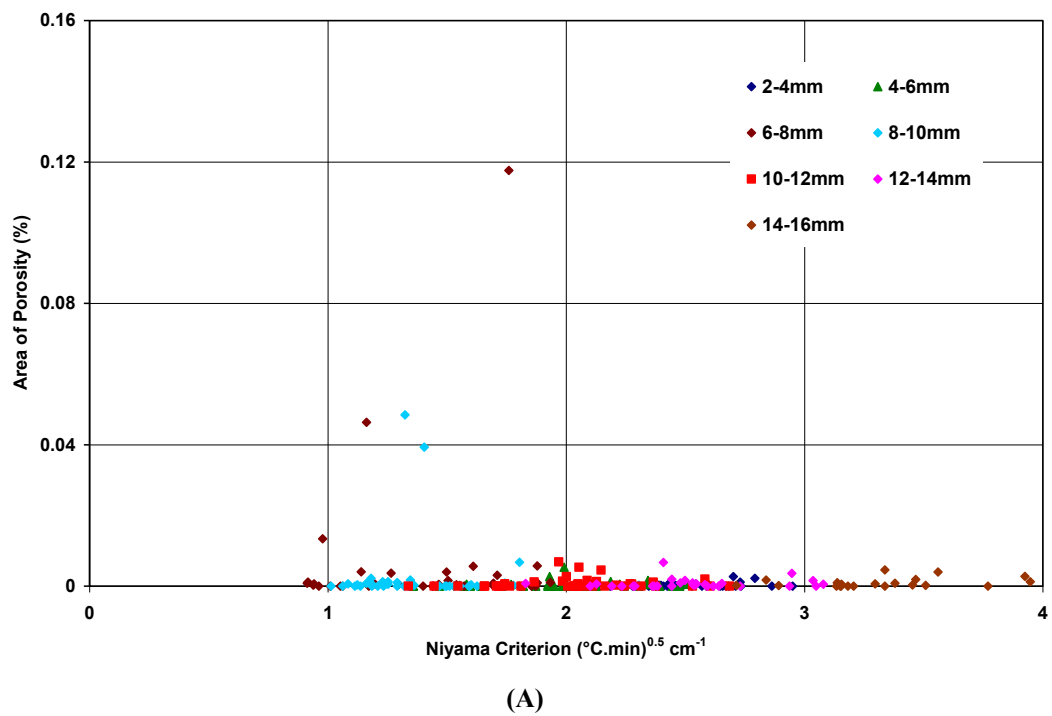
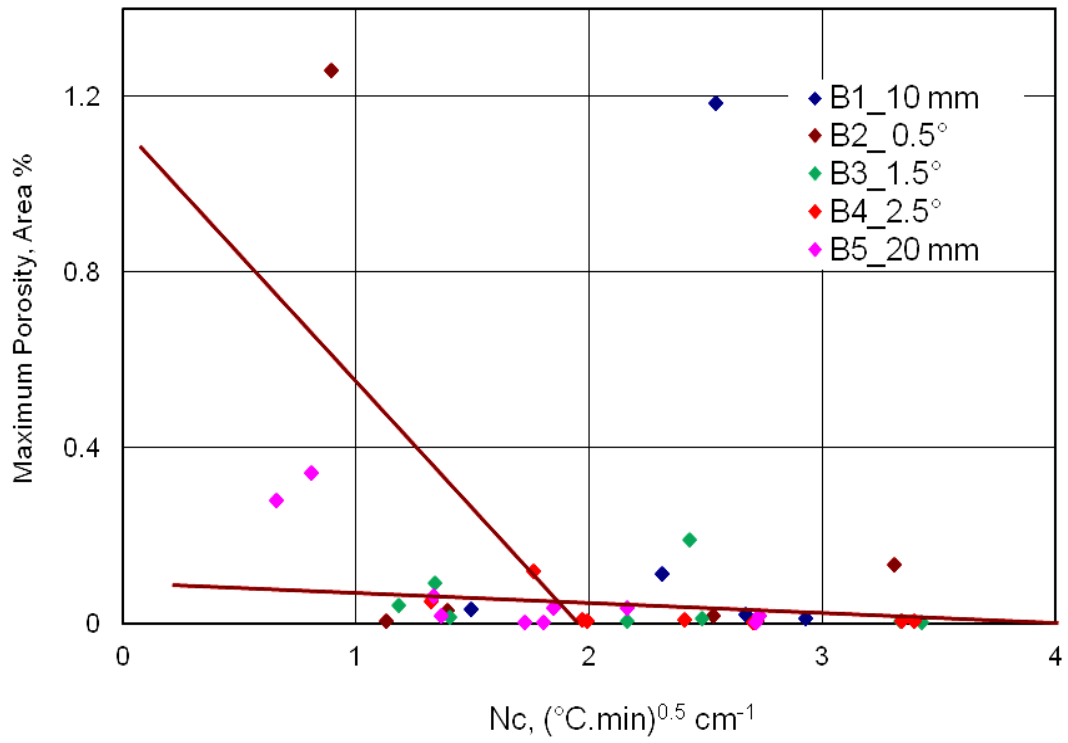
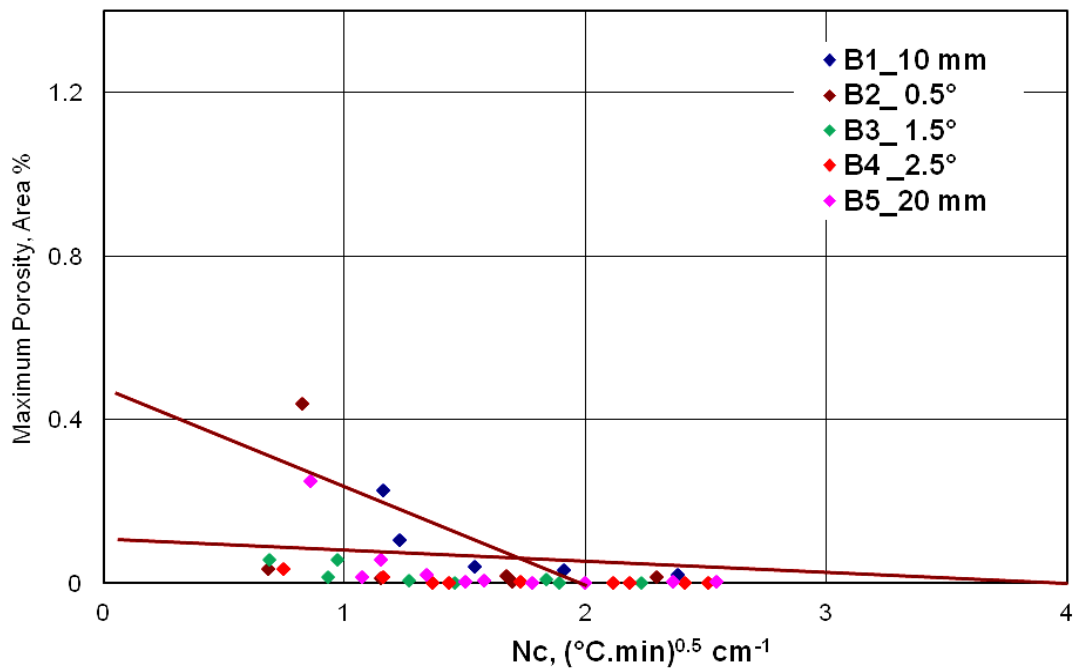


Figure 5.66 Distribution of porosity of Ti-46Al-8Nb in the longitudinal cross- section of the 2.5° tapered bar in a 500 °C (A) and 1000 °C (B) mould temperature as a function of Nc Values.

The maximum porosity contents in each longitudinal 2 mm wide stripe (excluding 2 mm from each side) of the sections of the model bars were plotted against the corresponding values of N_c , with the aim of determining the critical values of N_c above which shrinkage porosity could not form under the investigated casting conditions and is shown in Figures 5.67 (A) and (B). The red lines mediate the maximum and minimum values of the porosity contents, intersect the x-axis at two points which represent two values of the Niyama criterion function, these two points determine the critical values of the Niyama function.



(A)



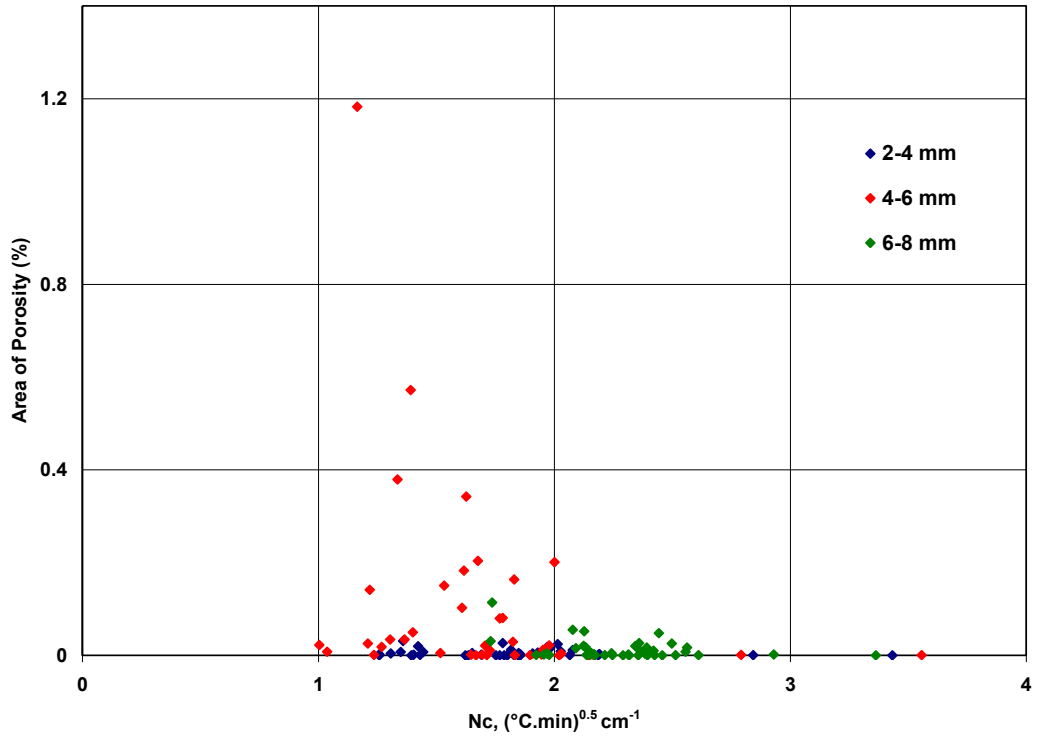
(B)

Figure 5.67 Comparison of maximum porosity of Ti-46Al-8Nb in bars of different geometries and mould temperatures 500 °C (A) and 1000 °C (B) as a function of average values of N_c calculated by thermal-only model.

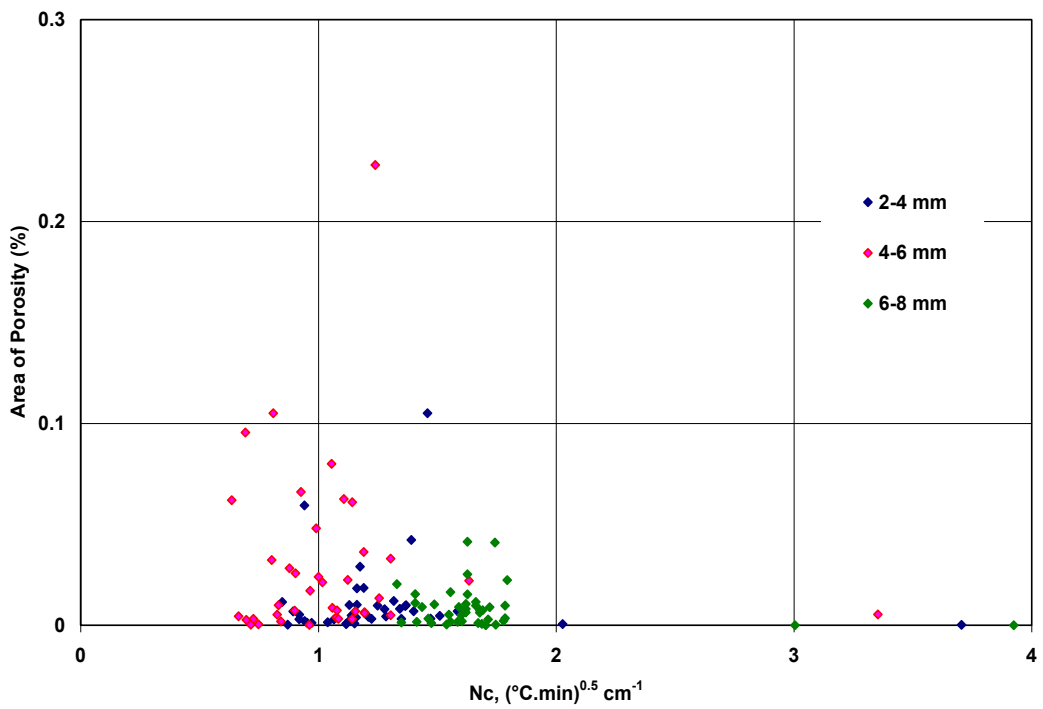
5.8.3 Porosity Distribution as Predicted by Niyama Criterion using the Tilt-Filling Model

Figures 5.68 to 5.71 (A) and (B) display the correlation between porosity distribution and average N_c , calculated using the results of the tilt-filling model, in the cylindrical and tapered bars cast into 500 °C and 1000 °C preheated moulds, respectively.

Commonly, in all test bars and in both preheating mould temperatures, the porosity ranged between $N_c \approx 0.5$ to $N_c \approx 4$ ($^{\circ}\text{C}\cdot\text{min}$)^{0.5} cm^{-1} . In addition, the high porosity levels in the 10 mm diameter cylindrical bar and the 0.5° tapered bar corresponded mainly to N_c values in the range of 1 to 2 ($^{\circ}\text{C}\cdot\text{min}$)^{0.5} cm^{-1} . The 1.5° and 2.5° tapered bars had the lowest porosity content; the relatively high porosity in these bars (≈ 0.04 to 0.06 %) in the 1000 °C mould temperature ranged between $N_c = 0.9$ to 2 ($^{\circ}\text{C}\cdot\text{min}$)^{0.5} cm^{-1} and 1.5 to 2.5 ($^{\circ}\text{C}\cdot\text{min}$)^{0.5} cm^{-1} in the case of mould temperature = 500 °C.



(A)



(B)

Figure 5.68 Distribution of porosity in the longitudinal cross- section of the 10mm ϕ cylindrical bar in 500 °C (A) and 1000 °C (B) mould temperature as a function of Nc Values (Tilt-filling model).

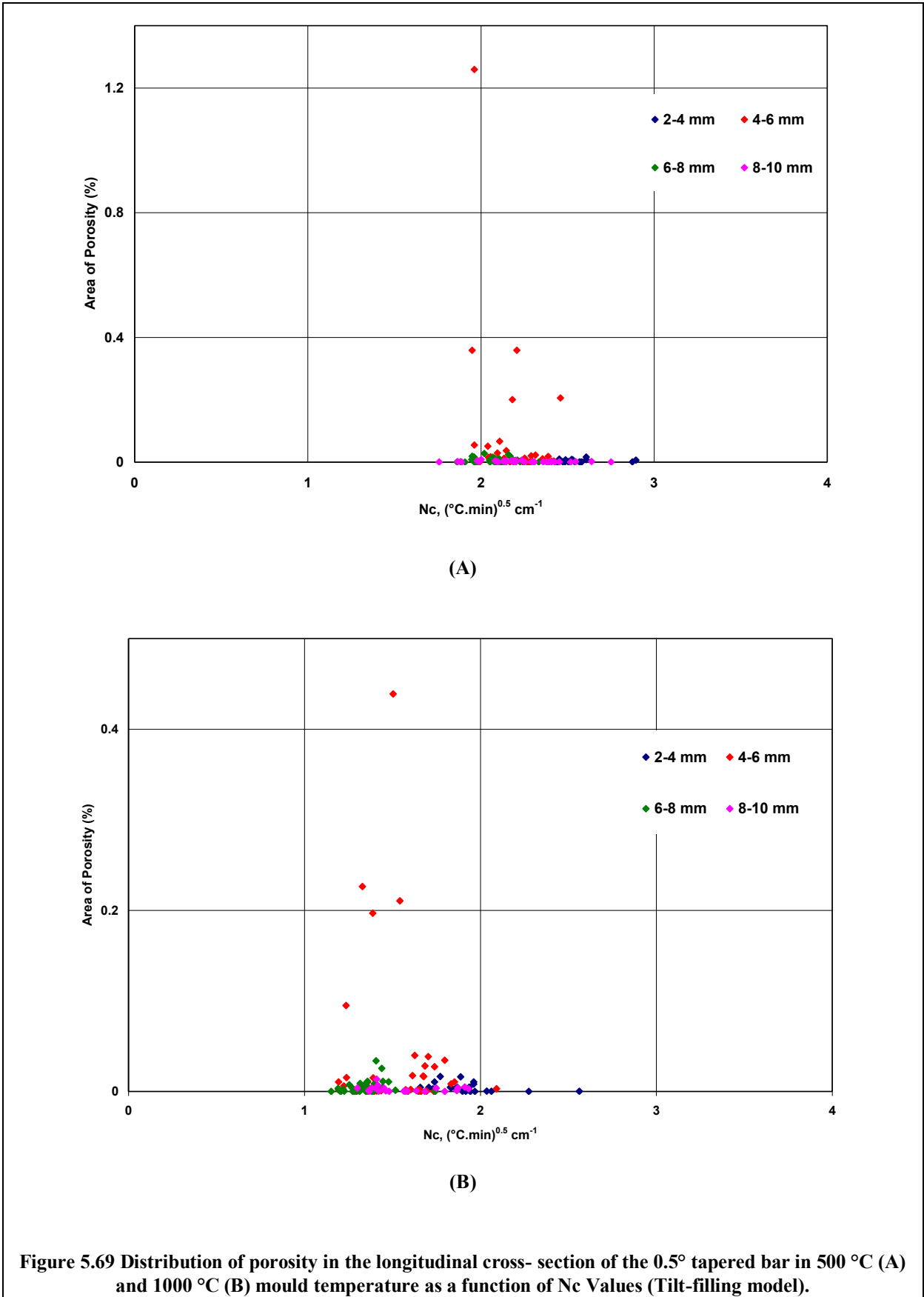
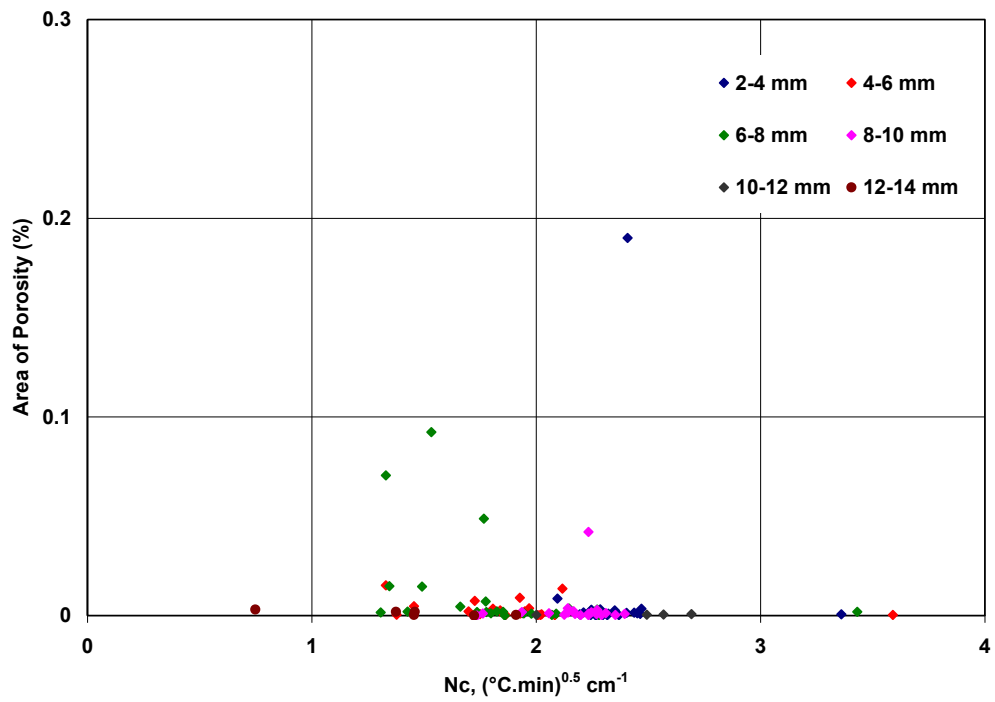
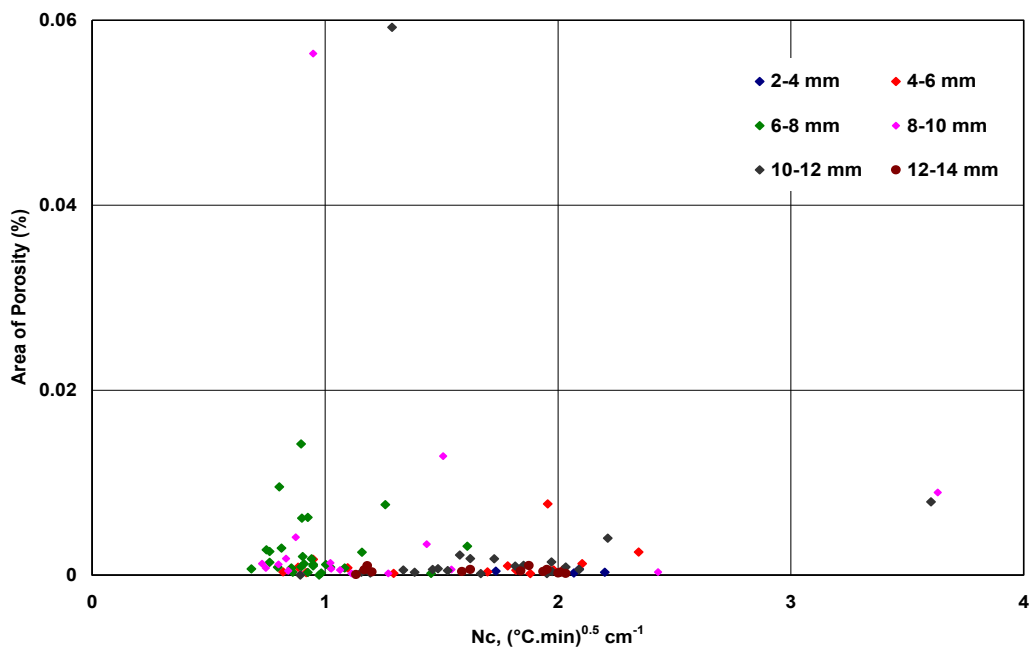


Figure 5.69 Distribution of porosity in the longitudinal cross- section of the 0.5° tapered bar in 500 °C (A) and 1000 °C (B) mould temperature as a function of N_c Values (Tilt-filling model).

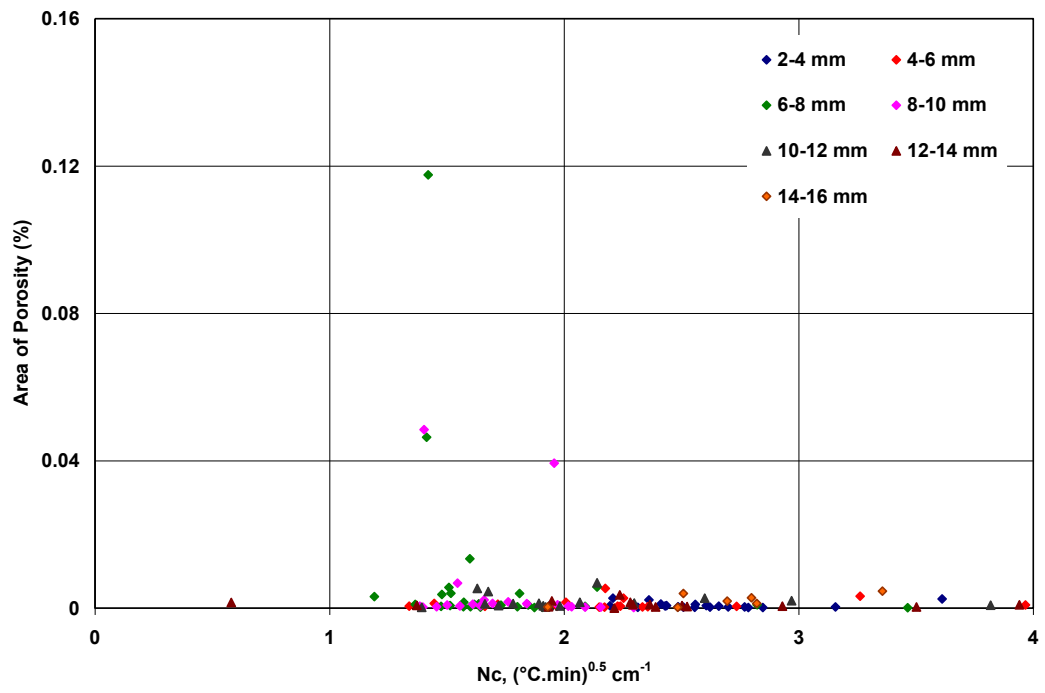


(A)

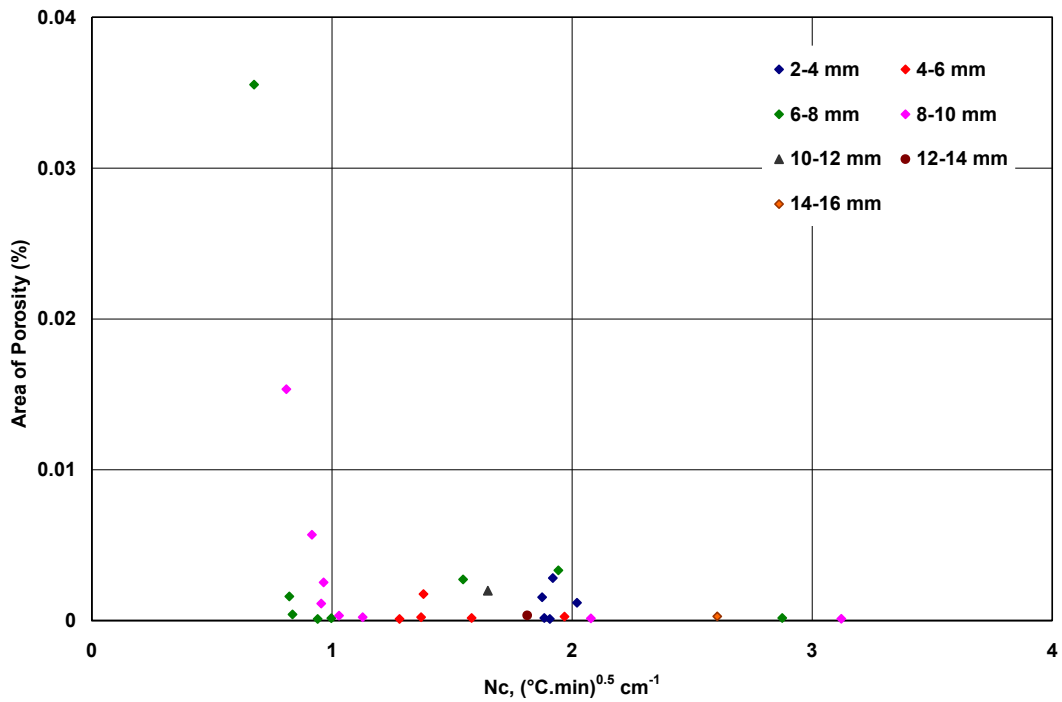


(B)

Figure 5.70 Distribution of porosity in the longitudinal cross- section of the 1.5° tapered bar in 500 °C (A) and 1000 °C (B) mould temperature as a function of Nc Values (Tilt-filling model).



(A)



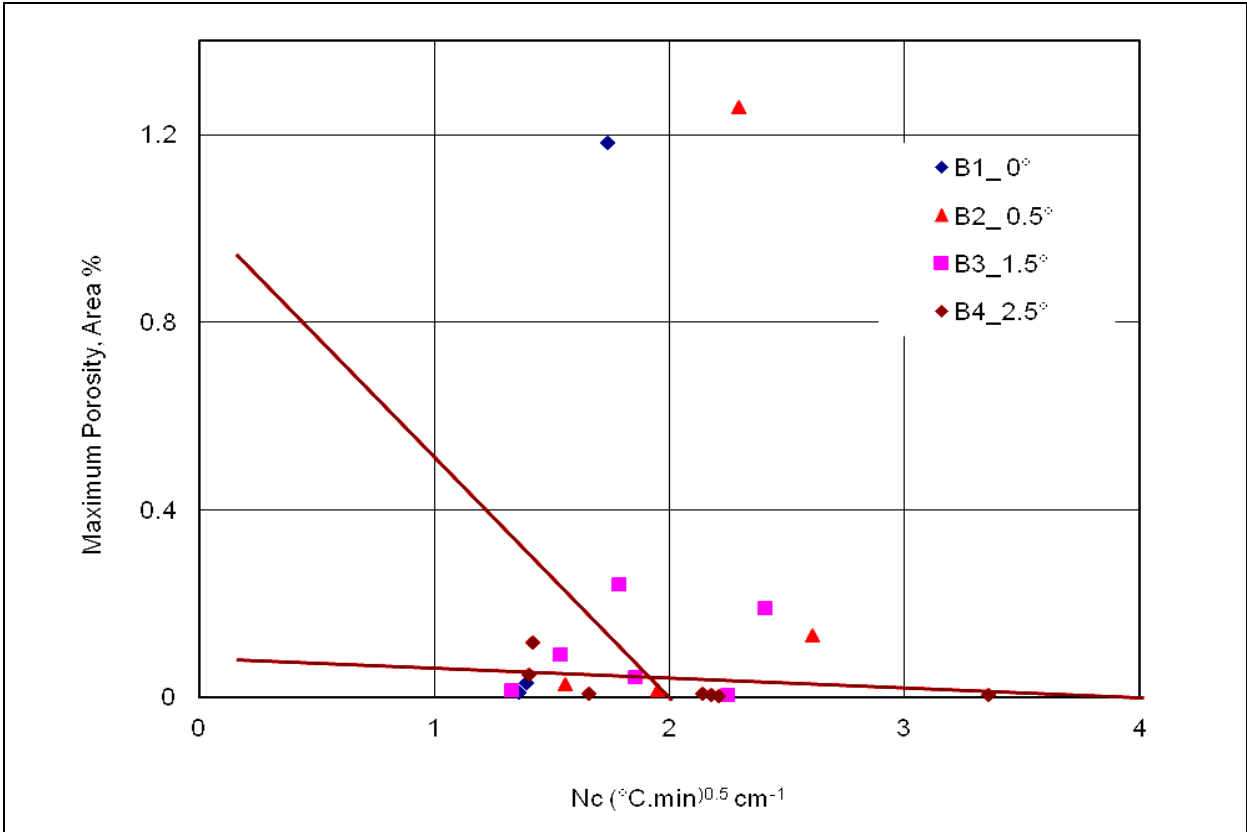
(B)

Figure 5.71 Distribution of porosity in the longitudinal cross- section of the 2.5° tapered bar in 500 °C(A) and 1000 °C (B) mould temperature as a function of Nc Values (Tilt-filling model).

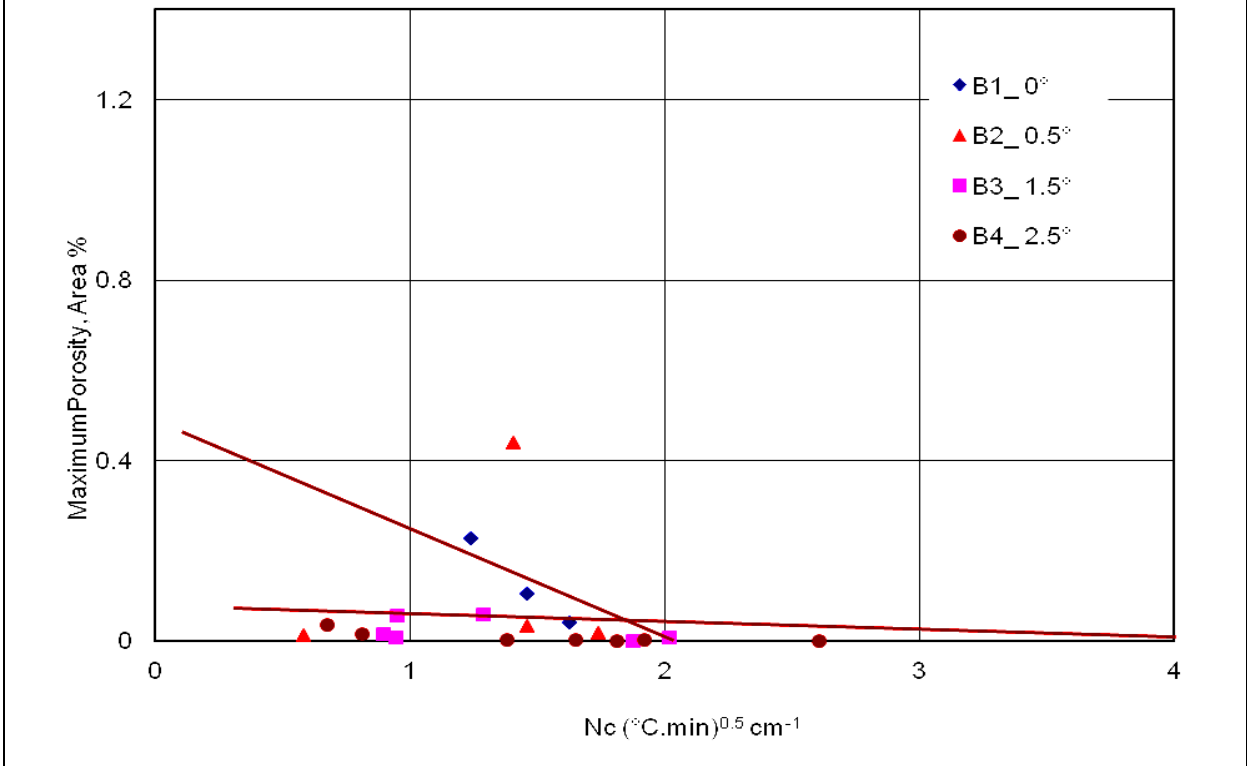
Figures 5.72 (A) and (B) shows the maximum porosity in each 2 mm wide longitudinal section (again excluding 2 mm from each side) against the corresponding values of average N_c calculated from the results of the ProCast tilt-filling model. The red lines mediate the maximum and minimum values of the porosity contents, in order to determine the critical values of the Niyama function.

As can be depicted in the plots, the highest content of shrinkage porosity in the 0.5° tapered bar and in the case of the mould at 500 °C, was associated with $N_c \approx 1.9 (\text{°C}\cdot\text{min})^{0.5} \text{ cm}^{-1}$, while the highest content of shrinkage porosity in the 10 mm diameter cylindrical bar was associated with the minimum value of $N_c (\approx 1.2 (\text{°C}\cdot\text{min})^{0.5} \text{ cm}^{-1})$. In the case of the 1000 °C mould, the 0.5° tapered bar contained the highest porosity which was associated with $N_c \approx 1.4 (\text{°C}\cdot\text{min})^{0.5} \text{ cm}^{-1}$.

Figures 5.73 (A) & (B) show comparisons between the results of the thermal model and the tilt-filling model for calculation of the critical value of the Niyama criterion in the test bars in the case of 500 and 1000 °C mould temperatures, respectively. The comparisons revealed that both results had the same approach with a slight shift in the N_c values, with the mean of differences between N_c calculated from both models being $\pm 0.04151 (\text{°C}\cdot\text{min})^{0.5} \text{ cm}^{-1}$ in case of the 500 °C mould, and ± 0.087 in the case of the 1000 °C mould.

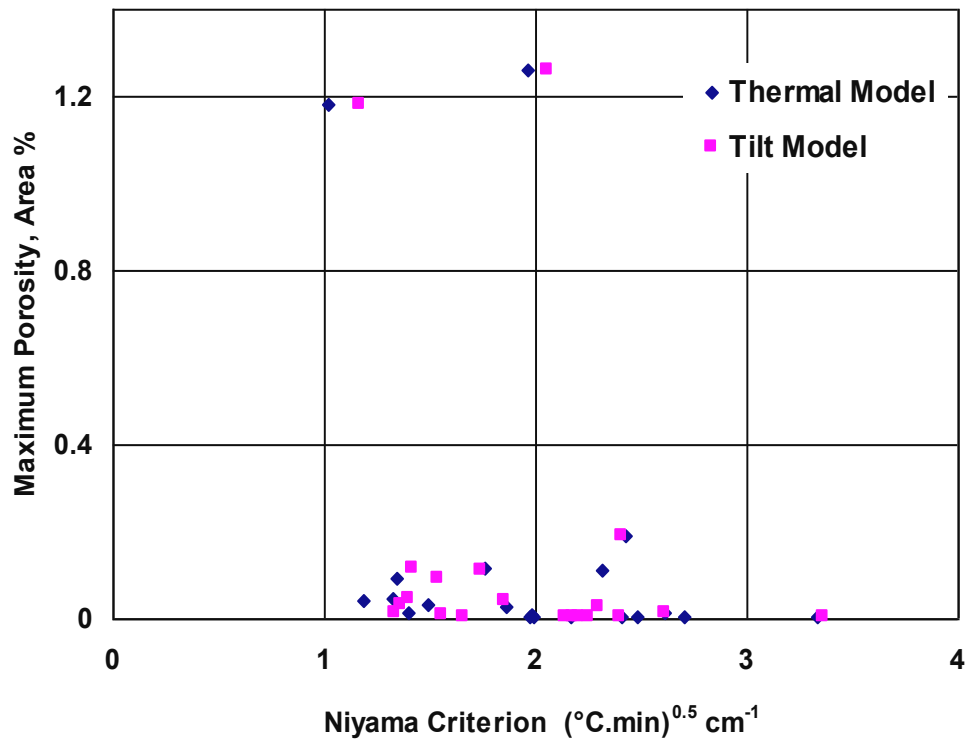


(A)

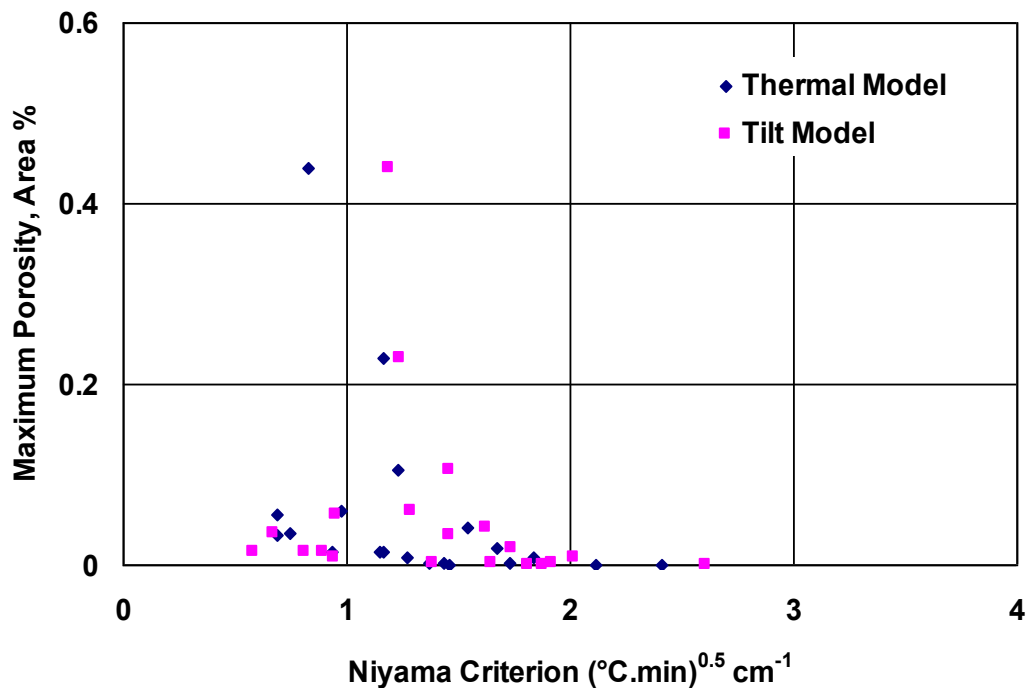


(B)

Figure 5.72 Comparison of maximum porosity of Ti-46Al-8Nb in bars of different geometries and mould temperatures 500 °C (A) and 1000 °C (B) as a function of average values of Nc calculated by tilt-filling model.



(A)



(B)

Figure 5.73 A comparison between using thermal model and the tilt-filling model to predict critical N_c at maximum porosity positions in all test bars of Ti-46Al-8Nb, (A) M.T=500 °C and (B) M.T=1000 °C.

CHAPTER 6

DISCUSSION

6.1 Boundary Conditions for Ti-46Al-8Nb Investment Casting

6.1.1 The Heat Transfer Coefficient at the Ceramic Mould/Surroundings Interface

The surface heat transfer coefficient of the ceramic shell used for investment casting was measured in a 200 mbar argon atmosphere, and in vacuum, to resemble the conditions of the investment casting process for titanium aluminide. The data obtained were then used in a thermal model to simulate the cooling process of the ceramic shell. The verification of measurements and calculations was carried out by comparing the results of the simulation with measured cooling curves in a series of experiments and hence the reliability of the data was validated.

The temperature dependent heat transfer coefficients of the ceramic shell surface in argon and in vacuum are shown in Figure 5.34. For both conditions, the heat transfer coefficient increased linearly with temperature, and the average difference between the heat transfer coefficient in argon and in vacuum was only 5 W/m².K due to the effect of convection in argon gas, as discussed in Section 5.5.2. The surface heat transfer coefficient was in the range of 10 ± 3.5 W/m².K at 100 °C to 60 ± 3.5 W/m².K at 1000 °C.

Despite the importance of the mould/atmosphere heat transfer coefficient in obtaining reliable casting simulation results, these data are very limited in the literature and are mainly estimated rather than measured. However, the data obtained in this research were found to be in the same range as the results given by O'Mahoney et al. [96] for a comparable shell mould system measured in air, as shown in the following table:

Table 6.1 Mould/atmosphere heat transfer coefficient

Researcher/Condition	300 °C	600 °C
Current Work/ Measured in Argon	21 W/m ² .K	38 W/m ² .K
Current Work/ Measured in Vacuum	16 W/m ² .K	33.6 W/m ² .K
O'Mahoney et al. [96] in Air	22 W/m ² .K	34 W/m ² .K

6.1.2 Interfacial Metal/Mould Heat Transfer Coefficient

a) Pure-Iron Test Model

With the aim of studying the effect of the interface heat transfer coefficient on the model results, any variation of the model result due to the uncertainty of the thermophysical properties of the casting alloy, such as thermal conductivity and heat capacity of Ti46Al8Nb alloy, should be avoided. And hence, pure-iron, because it has a well established thermophysical data file in the ProCastTM software, and the solidification temperatures were similar, was chosen as a casting alloy in the sensitivity study of the interface heat transfer coefficient. The results of the pure-iron model were analysed in terms of the effect of changing the initial value of h at the metal/mould interface on the cooling curves of points at the thermal centre of the casting and the ceramic shell.

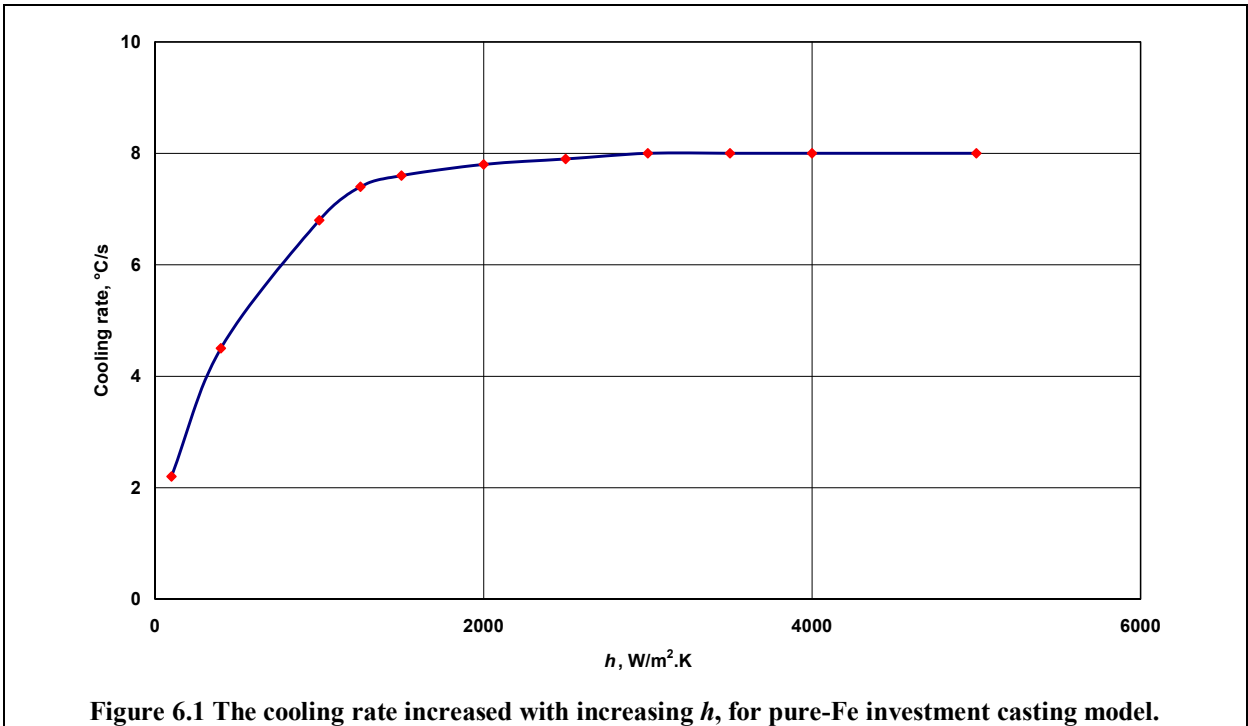
As described in Section 4.4.4, simulations of pure iron investment casting process were carried out with different interfacial metal/mould heat transfer coefficient (h) to study its effect on the cooling rate of the casting. The sensitivity analysis test showed a significant effect of h on the cooling rate, as shown by the investment casting model results.

For a ceramic mould with low thermal conductivity, 1.4 W/m. K, the mould can be considered as an insulating medium [142] which implies that the temperature at the interface can reach the metal temperature upon pouring while the mould temperature is still low, i.e.

the temperature difference at the interface is high and the cooling rate is dominated by the interfacial heat transfer coefficient. Moreover, solidification against the mould walls takes place simultaneously during pouring, which creates a close contact at the interface between the solidified metal and the mould material.

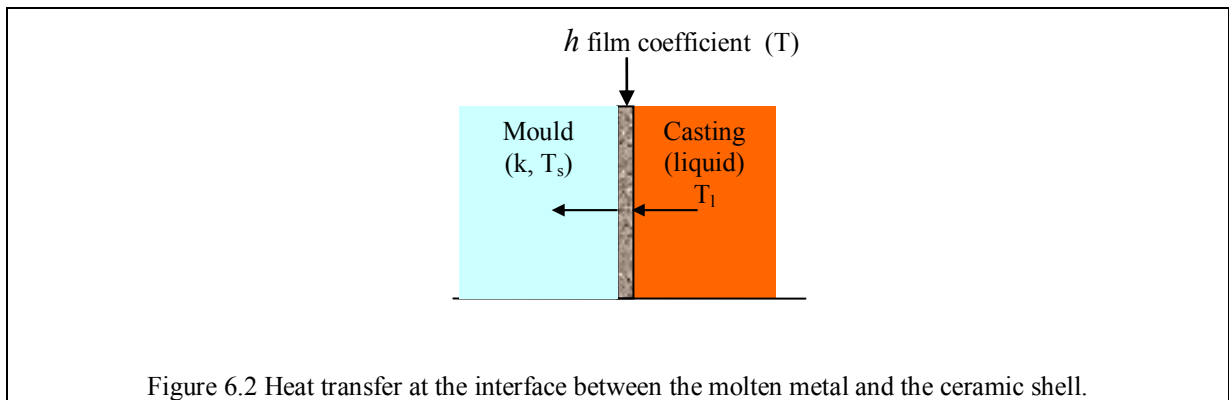
Based on these assumptions the relationship between the cooling rate of the casting and the interfacial heat transfer coefficient in the case of pure-Fe metal can be discussed as follows.

The heat transfer coefficient defines the quantity of the heat transferred through the interface between the solidified casting surface and the mould, and hence the cooling rate was expected to increase as the rate of heat transfer through the interface increased. As can be seen in Figure 6.1, (a copy of Figure 4.15 is included here for ease of discussion), the cooling rate increased from 2.2 K/s to 7.8 K/s with increasing h from 100 W/m².K to 1500 W/m². K. Afterwards, at a certain point when the cooling rate reached a maximum value, at which any further increase of h would not have an influence on the cooling rate, this was when the heat was transferred easily through the interface and the cooling rate was dominated by the heat convection.



The problem of the heat transfer at the interface can be analyzed as follows: just after the complete filling of the mould, the interface separates between the liquid metal and the mould internal surface, and the heat transfer from the internal liquid to the mould shell is controlled by heat resistance at the interface.

In this case, the Biot number; represented by equation 6.1, (a dimensionless parameter that compares the relative resistance to heat transfer at a surface between two materials), gives an indication of the heat resistance at the interface and inside the shell, (see schematic diagram in Figure 6.2).

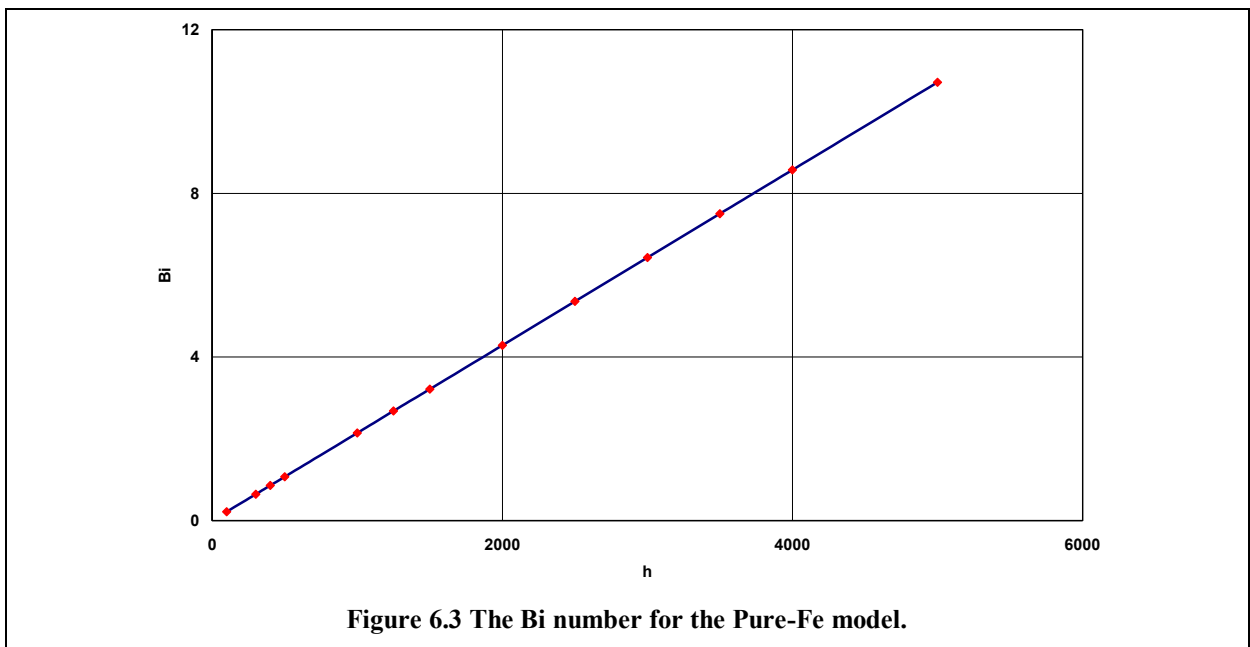


$$Bi = \frac{hL}{k} \quad \text{Eq. 6.1}$$

Where h is the interfacial heat transfer coefficient or the film coefficient, L is the shell thickness; (characteristic length), and k is the thermal conductivity of the mould.

The Bi number as a function of the assigned values of h , (in the Pure-Fe test model), is given in Figure 6.3.

The given data show that the $Bi \geq 1$ as $h \geq 500 \text{ W/m}^2\cdot\text{K}$, this could indicate that the heat convection started to dominate the heat transfer process at the interface. As h exceeded $1000 \text{ W/m}^2\cdot\text{K}$ the Bi was $\gg 1$ which may imply that the interface was approaching an equilibrium state with the internal bulk temperature. In this case the cooling rate became constant with increasing h , with the cooling rate reached a steady state value of 8 K/s , when h was $2000 \text{ W/m}^2\cdot\text{K}$.



b) Estimation of h for Ti-46Al-8Nb Investment Casting Model

Based on the preceding discussion about the effect of the interface heat transfer coefficient on the cooling rate of the casting, and in light of the understanding of different stages of the interface heat transfer coefficient as a function of temperature, as conducted by analysing the results of the pure-iron model, the interface heat transfer coefficient, in the case of investment casting of Ti-46Al-8Nb, was estimated as follows.

The interfacial heat transfer coefficient during solidification of the Ti-46Al-8Nb investment casting, was studied as a temperature-dependant parameter.

The values of the interfacial heat transfer coefficient are determined by several casting factors [148]. These factors include preheating mould temperature, thermal conductivity and surface roughness of the mould surface or the mould coating, pouring temperature, casting size, and the formation of the gap that separate the two surfaces apart. Thermal resistance through this gap is determined by the thermal conductivity of the gas content along with the gap size which in turn is influenced by the roughness of both surfaces. In the case of the current work the gap is expected to contain mainly Argon which has a very low thermal conductivity which increased thermal resistance at the interface and subsequently reduced the value of the interfacial heat transfer coefficient.

During the first stage of heat transfer, upon pouring of the liquid metal into the mould, the interfacial heat transfer coefficient is expected to be high due to the initial contact with the mould wall and the metal is expected to release its superheat. However, the initial value of h was assumed to be constant down to the liquidus temperature, since the superheat was insignificant due to the “Induction Skull” melting technique used.

The second step, during which the metal loses its latent heat of fusion, in this stage, the interfacial heat transfer coefficient is expected to increase with increasing the mushy zone

length, as the liquid feeding provides a compensation for the solidification shrinkage and hence resists the formation of the gap, and the solidifying metal maintains a good contact with the mould surface [143]. In the case of Ti-46Al-8Nb, the metal was expected to release its latent heat of fusion during a solidification range of 60 K, (see the phase diagram in Figure 5.44), which can be considered as an intermediate mushy zone.

Then h was expected to decrease as solidification proceeded due to the formation of a gap (a gas layer) separating the two surfaces, by which the resistance to heat transfer could be increased, (as discussed in Section 4.4.5).

In view of the preceding discussion, the temperature-dependant h curve for Ti-46Al-8Nb investment casting was determined by trial and error through several simulation runs, with the results of each run matched with measured cooling curves.

The results of the trial and error tests showed that the cooling rate of the metal increased by 65% as the maximum h increased from 1000 W/m². K to 2000 W/m². K. However, h of 1000 W/m². K provided the best curve fit. And, increasing h above 300 W/m². K just below the solidus temperature resulted in a faster cooling rate than the measured curve, while decreasing it to 100 W/m². K gave a very slow cooling rate.

As shown in Figure 6.4, (a copy of Figure 4.16), the maximum value of the interface heat transfer coefficient between the casting surface and the inner surface of the mould wall was 1000 W/m². K in the liquid zone down to the solidus temperature, and decreased to 300 W/m². K just below the solidus temperature.

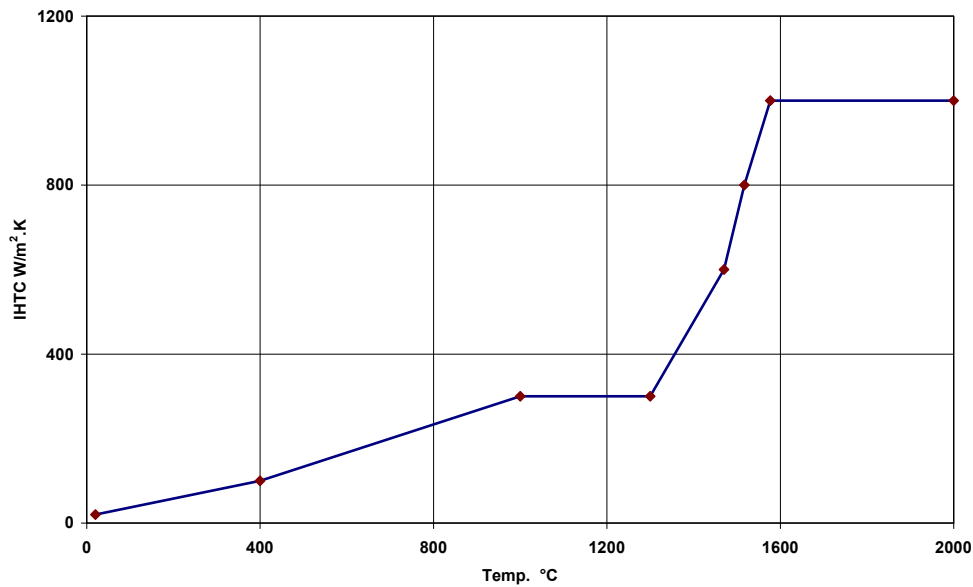


Figure 6.4, (A copy of Figure 4.16), Estimated heat transfer coefficient at the metal/mould interface; (for Ti-46Al-8Nb investment casting); by trial and error, as a function of temperature.

These values of h are in agreement with the range of values that have been used in titanium aluminide computational simulation studies, in some of which a constant value was used of $1000 \text{ W/m}^2 \cdot \text{K}$ [35], and in some studies where the interfacial heat transfer coefficient was suggested to be a function of time, a maximum value of $1000 \text{ W/m}^2 \cdot \text{K}$ was used [91].

However, reports of the interfacial heat transfer coefficient of titanium aluminide in investment casting are very limited, so it was beneficial to compare the suggested curve of h vs. temperature with other values reported for alloys with similar solidification range, such as Al-base and Ni-base alloys cast in investment moulds. For the Al-base alloys, h was determined by using numerical and inverse modelling techniques as discussed in Chapter 2, and the maximum h was reported to be very high at the initial stage of solidification, and then decreased to $400 \text{ W/m}^2 \cdot \text{K}$ during the second stage of cooling [144]. For a Ni-base superalloy, h was $1000 \text{ W/m}^2 \cdot \text{K}$ in the liquid stage then decreased to $500 \text{ W/m}^2 \cdot \text{K}$ below the solidus temperature [99].

6.2 The Features of the As-Cast Macrostructure of Ti-46Al-8Nb Casting

6.2.1 The Macrostructure of the Ti-46Al-8Nb Gravity-Castings

As illustrated in Section 5.2.3, the as-cast macrostructure of the Ti-46Al-8Nb gravity casting samples can be described by three features: a fine chill zone, columnar grains and a central zone of equiaxed grains.

However, it is apparent from the examination carried out on the vertical sections of the gravity cast test bars that the equiaxed zone is the major characteristic of the macrostructure. This can be attributed to two casting conditions, turbulent convection encountered in top-pouring, and the fact that the cooling process took place inside the mould-heating furnace. The expected liquid convection resulting from the turbulent pouring plays an important role in dissipating the superheat in the bulk liquid, and also in carrying fragmented dendrite arms within it, where they can grow to form equiaxed grains [145, 35].

The presence of a chill zone against the mould walls shows that liquid convection during the initial stage of solidification dissipated the low superheat (resulting from the induction skull melting technique) which gave rise to a relatively fast cooling rate against the mould walls. Heterogeneous nucleation took place on the mould internal surfaces soon after pouring due to the fast undercooling action of the mould walls. This provided many sites for heterogeneous nucleation and as a result a thin layer of fine, randomly oriented grains was formed as shown in the macrographs in Figures 5.6 and 5.7.

In addition, as a consequence of a long solidification time combined with a general slow cooling rate a shallow temperature gradient was developed in the bulk liquid which in turn promoted constitutional undercooling and subsequently equiaxed grain solidification. As a result of these casting and solidification conditions, the coarse equiaxed structure was the predominant grain structure in the gravity casting test bars. However, the bars with smaller

diameters contained a variable amount of the columnar structure, (as will be discussed in Section 6.3).

6.2.2 The Macrostructure of the Ti-46Al-8Nb Tilt-Castings

In contrast to the gravity cast test bars, the vertical sections of the tilt-cast cylindrical bars showed that the equiaxed zone was not a predominant structure and the columnar zone occupied a considerable area of the macrostructure.

As discussed in Chapter 2, tilt casting technique provides a tranquil filling of the mould with a maximum velocity of 0.5 m/s, while the liquid velocity during gravity filling can reach 1.6 m/s at the bottom of the downsprue, [124, 146].

This highlights the role of liquid convection in the solidification and growth of equiaxed grains, as the tilt filling technique reduced the turbulence and hence reduced the fluid flow velocity, which hindered the formation of equiaxed grains, and consequently enhanced columnar growth.

6.3 The Columnar-To-Equiaxed Transition in Ti-46Al-8Nb

As can be seen in Figures 5.18 to 5.21, the lower ends of the test bars contained a fully columnar structure while the upper parts had a fully equiaxed one, and a columnar plus equiaxed macrostructure occupied the middle parts, between the limits of the feeder effect and the end effect, and in which the equiaxed area tended to decrease linearly with distance from the feeder. Thus, the columnar-to-equiaxed transition of Ti-46Al-8Nb casting is the leading solidification mechanism under the casting and solidification conditions studied.

6.3.1 The Effect of Superheat on Columnar-To-Equiaxed Transition

According to the constitutional supercooling hypothesis of the columnar to equiaxed transition [26], the lower temperature at the tips of the columnar grains leads to undercooling of the bulk liquid, where the concentration of the solute elements exceeds the alloy composition and consequently heterogeneous nucleation of equiaxed grains is expected to take place on any nucleants in the supercooled liquid ahead of the columnar tips.

As discussed in Section 2.4, a low superheat is the main disadvantage of the induction skull melting technique and in these experiments a melt with low superheat was poured into a preheated mould either at 1000 °C or 500 °C, and subsequently a low temperature gradient was the prevalent thermal condition in the bulk liquid in all of the cylindrical test bars. A low temperature gradient in turn encouraged the growth of the equiaxed grains in the supercooled liquid and subsequently the equiaxed zone extended to obstruct the progressive growth of the columnar grains.

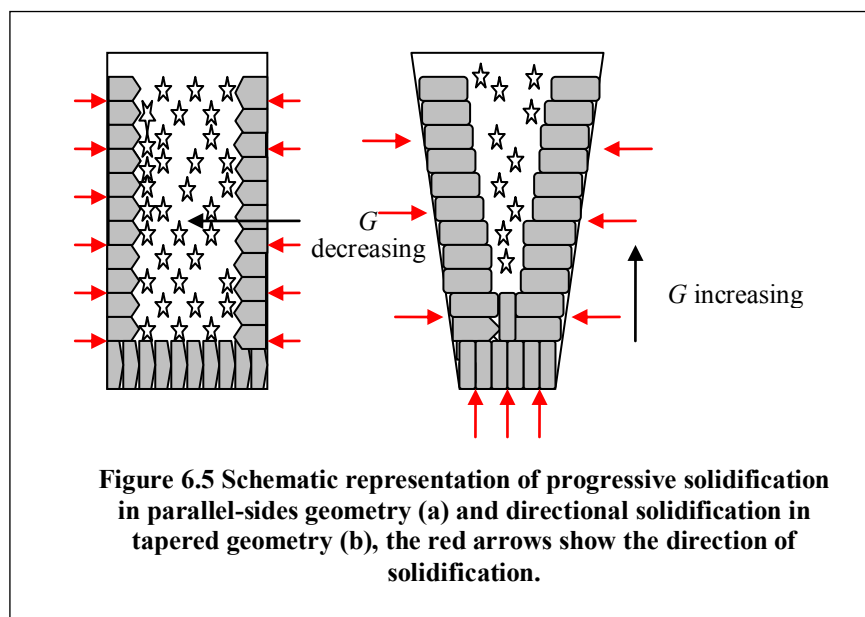
However, other casting parameters can interfere with the expansion of the equiaxed zone, for instance, a change in the cooling rate can occur as a result of changing the casting size, and the influence of directional solidification on the columnar-to-equiaxed transition.

6.3.2 The Effect of Taper Geometry on the Columnar-To-Equiaxed Transition

The effect of improving the temperature gradient on the macrostructure is obvious in the light of changing the casting geometry from cylindrical to tapered bars, with different taper angles.

The macrographs of the vertical cross-sections of the tapered bars, (see Figures 5.18 and 5.20), showed that the tendency to the formation of a columnar structure increased with increasing taper angle, with the mean area of the equiaxed zone in the cylindrical bars ranging between 70-65% in 10 mm and 20 mm diameter bars respectively, while it ranged

between 50-40% in the tapered bars. This is attributed mainly to the fact that the tapered geometry of the casting created thermal conditions that favoured directional solidification. The geometrical shape of the tapered test bars encouraged solidification to start at the smallest section, that is at the free end of the bar, and then solidification proceeded upwards, with directional solidification prevailing over the nucleation associated with constitutional undercooling, and over the growth of equiaxed grains in the supercooled bulk liquid, (see the diagram in Figure 6.5).



Consequently, large columnar grains grew inwards and the equiaxed zone diminished. It was also apparent that the area of the columnar grains gradually increased with increasing taper angle from 0.5° to 2.5° .

The effect of the taper angle on promoting columnar growth and decreasing the area of the equiaxed zone was demonstrated by the relationship between the area of the equiaxed zone and the position along the vertical cross-sections of the investigated test bars.

The mean percentage area of the equiaxed zone decreased by 40% and 25% as the taper angle was increased from 0° in a cylindrical bar of 10 mm diameter to a 2.5° tapered bar in preheated moulds at 500 °C and 1000 °C respectively, see Figures 5.22 and 5.23.

At lower positions of the tapered bars, the high temperature gradient at the advancing solidification front of the columnar grains could delay equiaxed grain nucleation and/or growth, and consequently the columnar zone expanded at the expense of the equiaxed zone.

However, as the temperature gradient decreased with distance up the bar towards the feeder, the cooling rate reduced, and so the growth rate of the columnar grains decreased also. Therefore, the equiaxed zone expanded at the middle positions and reached a maximum value at the upper end of the bars; the average area of the equiaxed zone in the last 20 mm from the feeder was 87% in the cylindrical bar and 73 % in the 2.5° tapered bar in 500 °C mould, while average values were 77% in the cylindrical bar and 64 % in the 2.5° tapered bar in 1000 °C mould.

Due to the limited number of samples, (one test bar for each geometry and mould temperature) because of the high cost of the material, these values could be non reproducible. However, the comparisons could give reliable information about the macrostructure features despite of the difficulty of estimating the error in these measurements.

6.3.3 The Effect of Preheat Mould Temperature on the Columnar-To-Equiaxed Transition

The comparison between the area of the equiaxed zone for two mould preheating temperatures, 500 °C and 1000 °C, as shown in Figure 5.24, revealed that the mould temperature had no obvious effect on the area of the equiaxed zone in the tapered bars. This effect appeared more clearly in the 10 mm cylindrical bar where the average area of the

equiaxed zone increased by 36 % as preheating mould temperature increased from 500 °C to 1000 °C.

The higher mould temperature was expected to reduce the cooling capacity of the mould and hence produce a lower cooling rate and lower temperature gradient at the metal/mould interface, all of which conditions would promote the columnar-to-equiaxed transition by reducing the velocity of the columnar front, and as a result the 1000 °C mould was expected to produce an as-cast structure with a larger equiaxed area. However, the high temperature gradient created by the tapered geometry seems to have overcome this effect of the mould temperature.

Based on these observations, the columnar-to-equiaxed transition in Ti-46Al-8Nb was found to be mainly controlled by the temperature gradient at the advancing solidification front, and therefore the influence of high mould temperature on the growth of the equiaxed zone was insignificant in the tapered bars.

6.4 Effect of Thermal Parameters on Feeding Mechanisms

The varying porosity distribution in terms of position and maximum pore size observed over the range of casting conditions and geometries studied revealed that both casting and solidification parameters significantly affected the formation of porosity in the investigated titanium aluminide alloy. Moreover, not only the general solidification conditions but also local conditions including cooling rate, temperature gradient and solidification time all determined the position at which a pore can form and grow.

However, understanding the feeding mechanism of such a mushy freezing alloy is also important for studying the tendency of shrinkage porosity formation. In addition, the role that criterion functions can play in predicting quantity and position of porosity is also considered

in order to develop a comprehensive understanding of shrinkage phenomenon in the titanium aluminide alloy investigated. These points are discussed in the following sections.

6.4.1 Feeding-related Shrinkage Porosity in Gravity-Casting Ti-46Al-8Nb alloy

Generally, as the radiographs in Table 5.3 show V-type or layer porosity is a characteristic distribution of shrinkage porosity in the gravity cast test bars. The V-type distribution can be attributed to the mechanism proposed by Campbell [49, 60], as discussed in Section 2.6. The negative pressure (internal gas pressure and shrinkage resistance tension) increases severely in the mushy zone to a point where it exceeds the required pressure for a pore formation, and this is where the pore can form and grow in the interdendritic channels of the progressive solidifying layer. The radius of the interdendritic channels decreases with the continuous solidification and thus the hydrostatic tension increases again and consequently a new pore is formed. As the solidification proceeds, further pores are nucleated and grown to produce the following layers.

Additionally, as described in Section 5.3.2 and as shown in Figure 5.15, the percentage area of porosity was generally high in these test bars, (compared to the porosity content in tilt casting test bars), and it had a tendency to increase in smaller diameter bars, the maximum area of porosity was 11 % in the cylindrical bar of 10 mm diameter and decreased to 3 % in the 30 mm diameter bar.

This result can be explained in terms of the thermal parameters that the casting experienced during solidification. Initially, as discussed earlier, the temperature gradient encountered in the gravity casting experiment was generally low, and hence the long solidification time could be considered to have a major effect on the porosity content in this case. Solidification time was generally long as cooling took place inside the mould heater, and it is well known that porosity is expected to increase with increasing solidification time as isolated pockets of

liquid can form readily in the last-to-solidify positions. Consequently, interrupting liquid feeding to these positions results in macroshrinkage cavities and centreline porosity.

At late stages of solidification the pressure drop of the liquid in the dendritic network increases as a result of the increasing solidus velocity. Accordingly, the residual liquid accelerates away from the feeder in the direction of low pressure in order to compensate for the pressure drop, and experiences high frictional resistance with increasing solid fraction, and thus the pressure drop increases even more as the liquid channel gets smaller, and a negative pressure can develop causing rupture of the remaining liquid and porosity. Consequently the isolated pockets of liquid cannot get adequate feeding to compensate for solidification shrinkage.

Conversely, the 2.25° tapered bar in the same casting experiment contained the lowest amount of porosity where the maximum area of porosity was 0.9%, (Figure 5.15), which reflects the tendency of decreasing shrinkage porosity formation as a result of directional solidification despite low overall temperature gradient and a long solidification time in the gravity cast test bars. This is attributed to the taper geometry which promotes directional solidification from the free end of the bar to the feeder and hence a tapered feeding path is formed which in turn provides effective liquid feeding throughout the late stages of solidification, (since the pressure drop is inversely proportional to the taper, and as the pressure drop of the feeding liquid decreases the capability of feeding the dendritic network increases and no centreline cavities can form).

This analysis of results agrees well with the approach developed by Walther et al. [54], for pure metal where it was suggested that the shape of the liquid region during the late stage of solidification determined the capacity for feeding, they developed a relationship to determine

the pressure drop as a factor of the taper factor of the feeding liquid, as discussed in Section 2.6.3.

Although that approach was developed based on the solidification mechanism of a pure metal, however, it can be used to describe the improvement of feeding in a casting with a tapered geometry and a mushy solidification alloy, but bearing in mind that the frictional resistance is expected to be higher due to the presence of a coherent dendrite network in the mushy solidification alloys. A taper factor of 0.065 mm per mm in a 200 mm long bar with 13 mm diameter at the small end was required to minimize the porosity by 73 % of that in the 10 mm diameter cylindrical bar.

6.4.2 Feeding-related Shrinkage Porosity in Tilt-Casting Ti-46Al-8Nb alloy

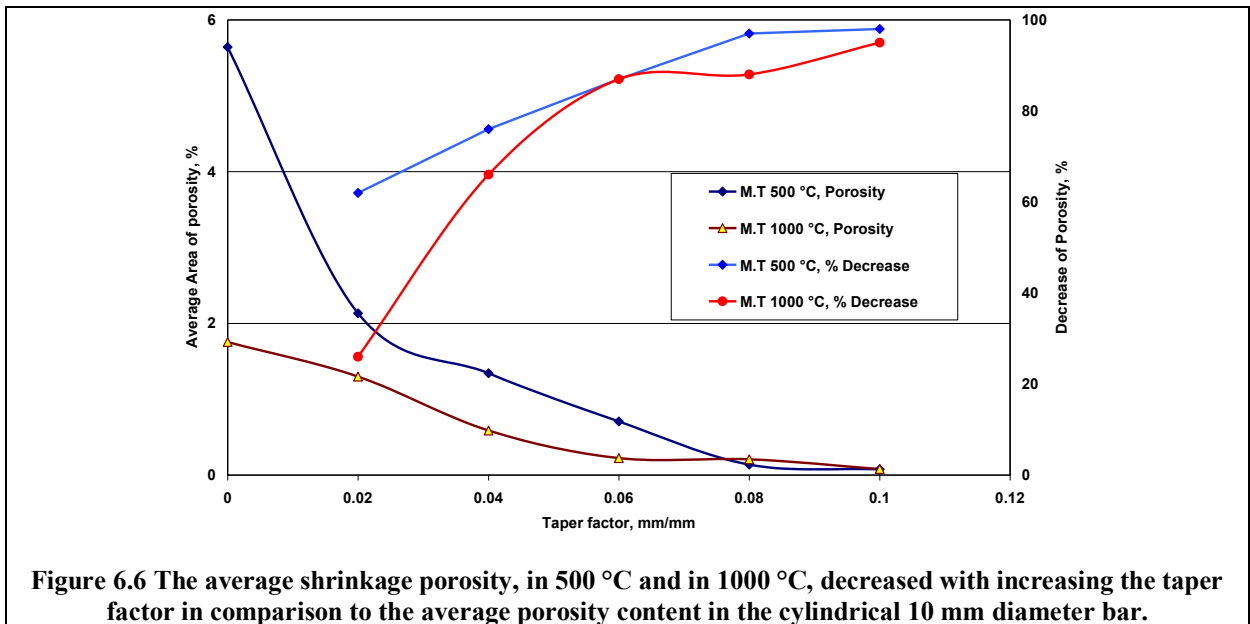
The significant influence of promoting directional solidification achieved by using a tapered geometry on the formation of shrinkage porosity is comprehensively studied in the tilt-cast test bars. As discussed in Section 6.3.3, the enhanced temperature gradient condition promoted columnar growth and delayed the CET and hence the area of the equiaxed zone was smaller and resistance to feeding decreased. Thus, liquid feeding and subsequently interdendritic feeding can proceed readily during the late stages of freezing, i.e., the feeding distance is longer under the condition of directional solidification. In light of the preceding discussion, the influence of enhanced feeding on shrinkage porosity in Ti-46Al-8Nb was investigated.

First, an overall comparison among cylindrical bars and tapered bars showed an obvious reduction in the amount of shrinkage porosity in the tapered bars generally, and it decreased with increasing the taper angle from 0.5° to 2.5° for both mould preheat temperatures.

As can be seen in Figure 6.6, a total decrease of porosity of up to 98% could be achieved by applying a taper factor of 0.1 mm per mm in a 100 mm long bar with 10 mm diameter at the small end.

Generally, the soundness of the casting was gradually increased by more than 10% as the taper factor, (in the range of 0.0 to 0.1 mm/mm), increased by 0.02 mm/mm.

The influence of the temperature gradient appeared to be stronger in tapered bars with larger angles; 1.5°, 2°, 2.5°. This result agrees with the Niyama criterion to predict porosity, as will be discussed later.



On the other hand, it was noticed that the area percentage of porosity was slightly higher in the mould preheated to 500 °C in comparison to the area percentage of porosity in the mould preheated to 1000 °C, (see Figure 6.6), in particular with the bars with smaller angles (0° (the cylindrical bar with 10 mm diameter), 0.5° and 1° tapered bars), as also shown in Figures 5.25, 5.26 and 5.27.

This can be attributed to the fact that the lower the initial mould temperature the higher the amount of heat it can transfer out of the casting in the initial stages of cooling, which means that the mould preheated to 500 °C has a higher cooling capacity than that preheated to 1000 °C. The test bars cast in the 500 °C mould therefore had a higher cooling rates than those cast in the 1000 °C mould, and as a result of the higher cooling rate, the solidus velocity increased, and as discussed earlier the liquidus velocity increased and led to a greater pressure drop along the feeding path which implies that the tendency to porosity formation increased too.

As Campbell [49] proved by Equation 2.6, (Chapter 2), the pressure drop along the interdendritic feeding channels is directly proportional to the cooling rate, which deduced that as the cooling rate increases the pressure drop along the feeding liquid increases too. Furthermore, as the pressure drop increases the remaining liquid accelerates towards the regions of the critical low pressure which causes a build up of the pressure drop in the interdendritic paths which in turn results in the formation of interdendritic microshrinkage porosity.

6.5 Prediction of Factors affecting Shrinkage Porosity in Ti-46Al-8Nb using a ProCastTM Modelling

6.5.1 The Local Solidification Time

The distribution of solidification time for vertical cross-sections of each bar of the casting as predicted by ProCastTM is shown in Figure 6.7, (the model conditions are given in Section 5-8 and the initial mould temperature was 1000 °C). The plots show the variation of local solidification time with position along the different tapered bars, and it is clear that the local solidification time tended to increase with increasing taper angle of the test bar. This is to be expected as the bars were tapered upward from 10 mm diameter at the free end to the larger diameter connected with the feeder.

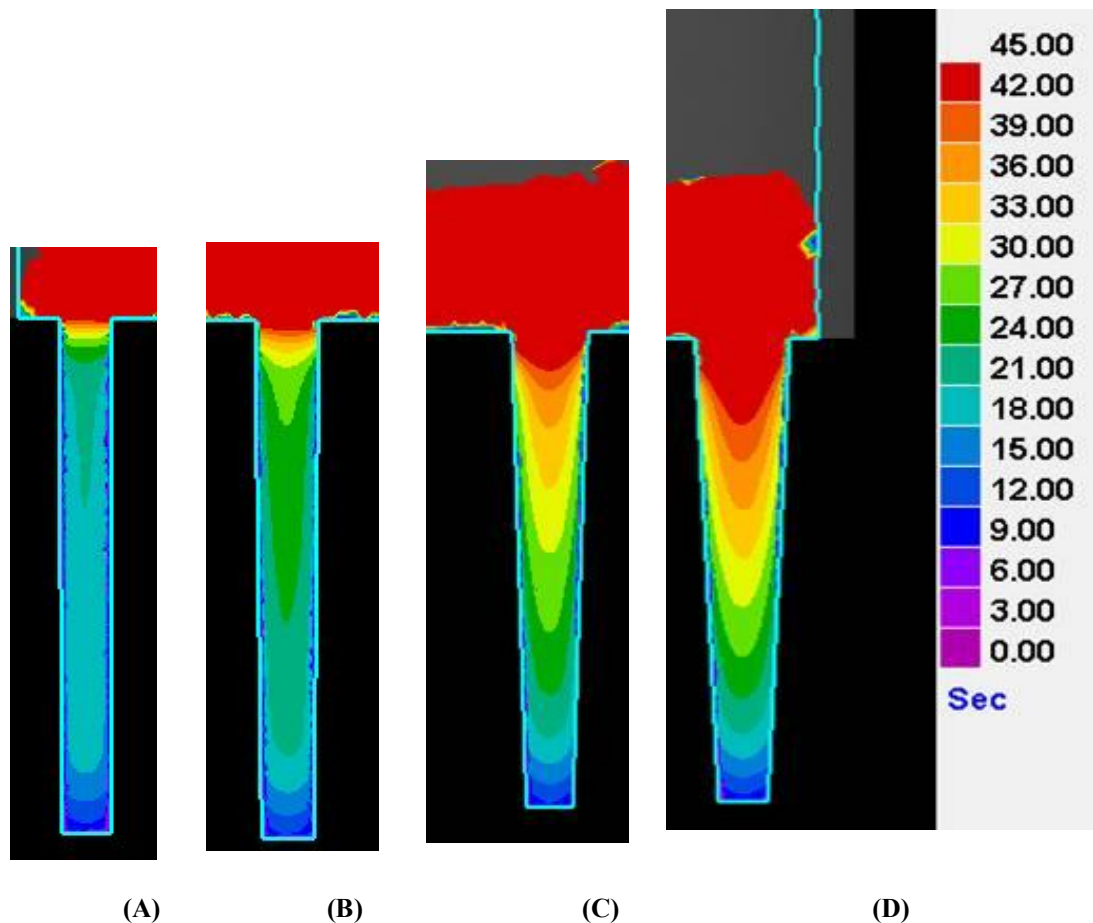


Figure 6.7 Predicted local solidification time in four vertical sections of the tilt-casting model; (A) 10 mm diameter cylindrical bar, (B) 0.5° Tapered bar, (C) 1.5° Tapered bar and (D) 2.5° Tapered bar (Mould initial temperature; 1000 °C).

Longer local solidification time can be observed at the centre of 1.5° and 2.5° tapered bars, while the free ends of all bars remained at lower values. Figure 5.48 shows local solidification time along the centreline of each bar versus distance from the feeder, (the results are from a thermal-only model). At the bottom end of the bars the solidification time was generally low due to the fast cooling rate, known as the end effect. This effect tends to fade sooner as the taper angle increased, as shown in Figure 5.49.

As discussed earlier, the shrinkage porosity decreased significantly with increasing taper angle, this is in agreement with the higher local solidification time (predicted by the model) at the thermal centre of the tapered bars, which is consistent with the approaches of shrinkage formation based on Darcy's law. The expectation is that the dendrite arm spacing (DAS)

increases with local solidification time and consequently the permeability of the dendritic network increases too, which would lead to improved interdendritic feeding.

6.5.2 The Cooling Rate

The distribution of cooling rate in the vertical sections of each bar of the casting, predicted by the ProCast model is shown in Figure 6.8. Zones of lower cooling rate can be observed at the centre of each bar whereas the highest values extending in wider zones from the free end in the smaller bars, the 10 mm diameter cylindrical bars and the bars with 0.5° taper. This distribution is to be expected due to the size variations in the test bars. In general, the larger bars with higher taper angle produced the lower cooling rates than those of smaller sizes and smaller taper angles. Consequently, the larger bars were expected to have the minimum porosity content, as porosity is expected to decrease with decreasing cooling rate.

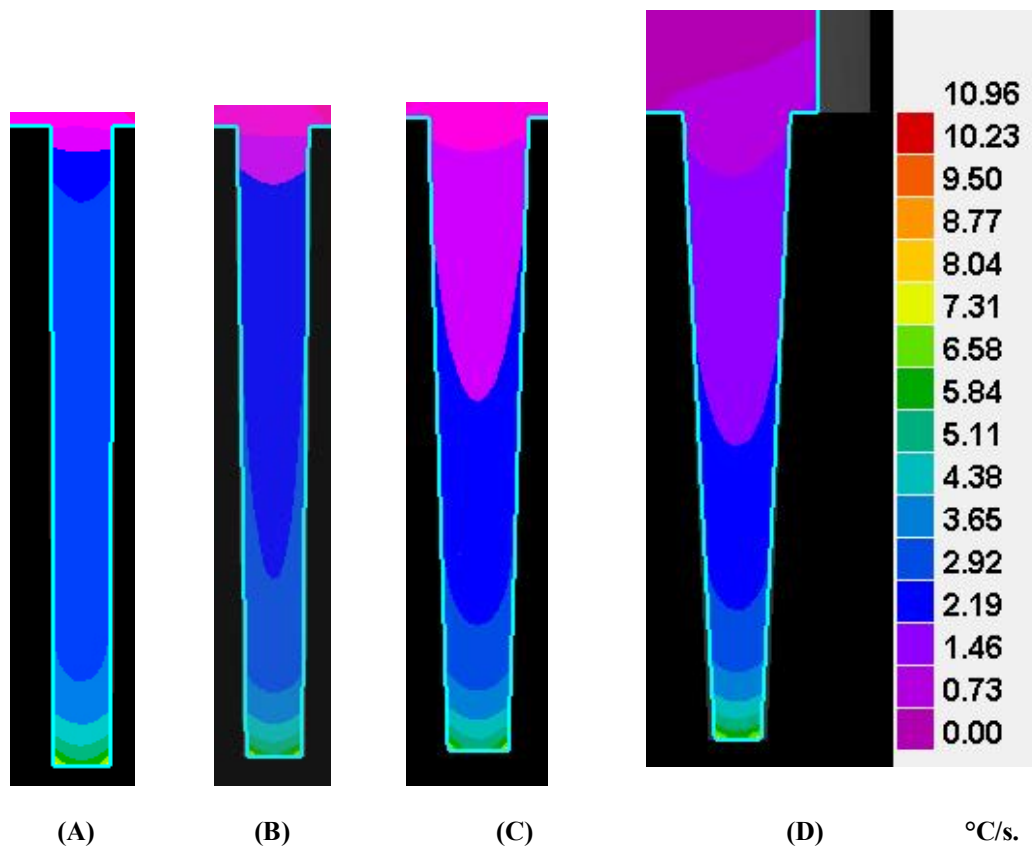


Figure 6.8 Predicted cooling rate in four vertical sections of the tilt-casting model; (A) 10 mm diameter cylindrical bar, (B) 0.5° Tapered bar, (C) 1.5° Tapered bar and (D) 2.5° Tapered bar (Mould initial temperature; 1000 °C).

6.5.3 The Temperature Gradient

The role that enhanced temperature gradient plays in improving the feeding mechanism of a mushy-freezing alloy has already been pointed out in Section 6.4.2. However, it is necessary to highlight the importance of local temperature gradient in achieving soundness in the titanium aluminide alloy.

Figure 5.50 shows the predicted local temperature gradients versus distance from the feeder, just after 100 % solidification. After completion of solidification the temperature gradient was generally shallow away from the top end connected to the feeder. And as expected, higher values were observed in the bars with larger angles.

It is commonly agreed that feeding reaches its most difficult stages at 90 % of the solidification process, that is when the dendritic network attains high coherency in the mushy zone [72]. As shown in the model results calculated at 90% of solidification, Figure 6.9, the central zones of each section have lower values of temperature gradients, while the larger tapered bar had higher values of temperature gradient.

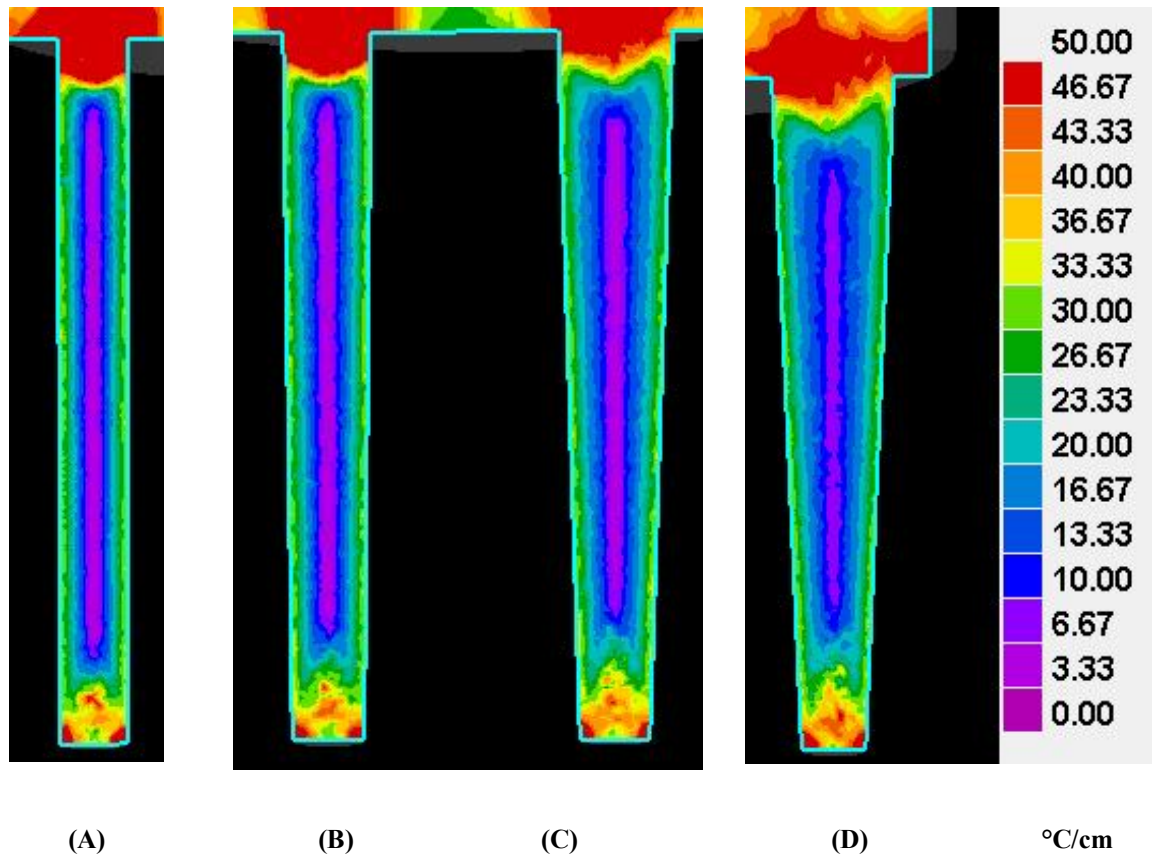


Figure 6.9 Predicted temperature gradient in four vertical sections of the tilt-casting model; (A) 10 mm cylindrical bar, (B) 0.5° Tapered bar, (C) 1.5° Tapered bar and (D) 2.5° Tapered bar (Mould initial temperature; 1000 °C).

This observation shows the improvement of temperature gradient in the tapered geometry generally and in the bar with a 2.5° taper angle particularly. Subsequently, directional solidification, and also improved feeding during the last stages of solidification, was expected to be the strongest in this bar.

The values of local temperature gradients along the centreline of the test bars at 90 % of solidification were also used to plot percentage porosity as a function of temperature gradient, as shown in Figure 5.52. The higher porosity percentages were found in the lower temperature gradient zones (0 to 2 K. mm⁻¹), and porosity decreased significantly with increasing taper angle.

It can be seen from these results that the temperature gradient could predict shrinkage porosity in the investigated alloy, based on the fact that it can be considered to be the strongest, most influential thermal parameter in the castings studied, where the geometry of the casting dominated other parameters.

However, using temperature gradient to predict shrinkage porosity could be a general qualitative function, and could be used for comparison in certain cases limited to effective geometric variations that promote directional solidification, (otherwise other thermal and solidification parameters like cooling rate and local solidification time are interdependent and could not be overlooked). Plus, local values of temperature gradients could not be used to predict amount and position of porosity, as these values did not give a smoothly varying curve with distance from the feeder, and hence no precise value could be determined to quantitatively predict porosity, see Figures 5.51 and 5.52.

More complicated criterion function, (the Niyama Criterion Function), which accounts for temperature gradient along with cooling rate is discussed in the following section.

6.6 Prediction of Shrinkage Porosity Using the Niyama Criterion Function

6.6.1 Factors Influencing the Niyama Function

As mentioned in Chapter 2, the Niyama criterion was developed based on Darcy's Law, in which interdendritic feeding in a two-phase solidification (mushy) alloy is considered in a function that uses thermal conditions, i.e., the temperature gradient and cooling rate, to predict shrinkage porosity. The simplicity of using the Niyama criterion makes it very popular in predicting porosity in most casting simulation software, e.g. for steel alloys and for non-ferrous alloys as well.

The distribution of porosity along the centre line in the test bars, Figures 5.58 to 5.61, showed that positions of high porosity corresponded to lower values of the Niyama function, and it was also observed that porosity was generally found along the centreline between 0.7 and 2 °C. min^{0.5}cm⁻¹, (see Figure 5.62), which can reflect a critical value of the Niyama function at the thermal centre of the casting where a lower temperature gradient was expected and also a higher solidus velocity, at the last stage of solidification, combined with a pressure drop.

However, the centre line cannot characterize the global conditions across the casting, and hence an extended study was carried out to investigate the critical values of the Niyama function which corresponded to maximum porosity at any position in the vertical cross-sections of the bars.

Firstly, comparing the values of Niyama function (N_c) which corresponded to the porosity in the cylindrical bars with two mould temperatures highlighted the role of the cooling rate in porosity formation as the role of the temperature gradient is decreased in the cylindrical shape in both cases. The porosity in the 10 mm cylindrical bar, in the case of a mould preheat temperature of 500 °C, was generally dispersed in positions corresponding to a Niyama function value of between 1 to 3 (°C.min)^{0.5}cm⁻¹, the high porosity values were mainly distributed in a 2 mm wide strip in the middle of the cross-section, where the corresponding values of the Niyama function were between 1.4 and 2.4 (°C.min)^{0.5}cm⁻¹, as shown in Figure 5.63 (a).

In the case of the mould preheated to a temperature of 1000 °C the high porosity values were found to be between 0.8 and 2 (°C.min)^{0.5}cm⁻¹ and the porosity extended to positions corresponding to 3.8 (°C.min)^{0.5}cm⁻¹ as shown in Figure 5.63 (b).

This variation in the Niyama function values reflects the differences in solidification conditions in both castings, in particular the lower values of N_c were associated with porosity in the lower mould temperature and could be attributed to the higher cooling rate as discussed in Sections 6.4 and 6.5.2.

Moreover, the lower Niyama function values could be considered as a sign of feeding difficulties in the mushy zone where the critical value of the Niyama function could be interpreted as a critical pressure drop in the mushy zone which in turn is the driving force for shrinkage formation [72].

In contrast, the effect of temperature gradient on the Niyama values (N_c) is shown clearly in the results of the tapered bars. As shown in Figures 5.64 to 5.66, porosity values were generally dispersed in positions corresponding to N_c between 1 to 4 $(^{\circ}\text{C}\cdot\text{min})^{0.5}\text{cm}^{-1}$, and tended to increase with decreasing Niyama criterion values where the highest porosity values were associated with a N_c in the range of 1 to 2 $(^{\circ}\text{C}\cdot\text{min})^{0.5}\text{cm}^{-1}$.

As discussed in Sections 6.4.1 and 6.4.2, the improved temperature gradient which was achieved by increasing the taper angle encouraged directional solidification and consequently postponed the columnar-to-equiaxed transition, all of which improved feeding and hindered porosity formation. As the taper angle increased the temperature gradient increased and subsequently the Niyama values increased too, while the porosity decreased, (see Figure 5.67). These factors dominated the solidification process for both mould temperatures and overcame the differences in solidification time and cooling rate.

6.6.2 Critical Values of the Niyama Criterion to Predict Shrinkage Porosity in Ti-46Al-8Nb Investment Castings

As shown in Chapters 4 and 5, two simulations with different approaches were executed, a thermal model and a tilt-filling model, in order to investigate the effect of convection and the dynamic pressure of the liquid on porosity prediction. The ProCast thermal model performs heat transfer calculations which include the latent heat of solidification by solving the Fourier heat conduction equation, while the filling model performs free surface calculations based on the fluid flow equation. The results of the tilt-filling model were analyzed, as shown in Figures 5.68 to 5.72, and compared with the results from the thermal-model, (see Figures 5-73).

The comparisons show that there was an acceptable agreement between the Niyama values obtained from both models. This can be attributed to the fact that the thermal model can predict the thermal parameters accurately enough to calculate the Niyama criterion, and the impact of convection and the dynamic pressure of the liquid on thermal parameters would be of less significance in these calculations.

On the other hand, the accuracy of the heat boundary conditions is mandatory to achieve a reliable model, and these conditions were experimentally measured as a part of this study, (Sections 6.1 and 6.2), and were assigned to both models. Figures 6.10 and 6.11 show the predicted volume percentages of shrinkage porosity from the tilt-filling model and the thermal model, respectively.

Clear differences between the two models can be found in the location and volume of the pipe-shrinkage, with a large macroshrinkage cavity in the tilt-filling model located at a lower position than the open shrinkage pipe in the thermal model. This could be due to the filling model taking into account the pressure head of the remaining liquid above the feeder.

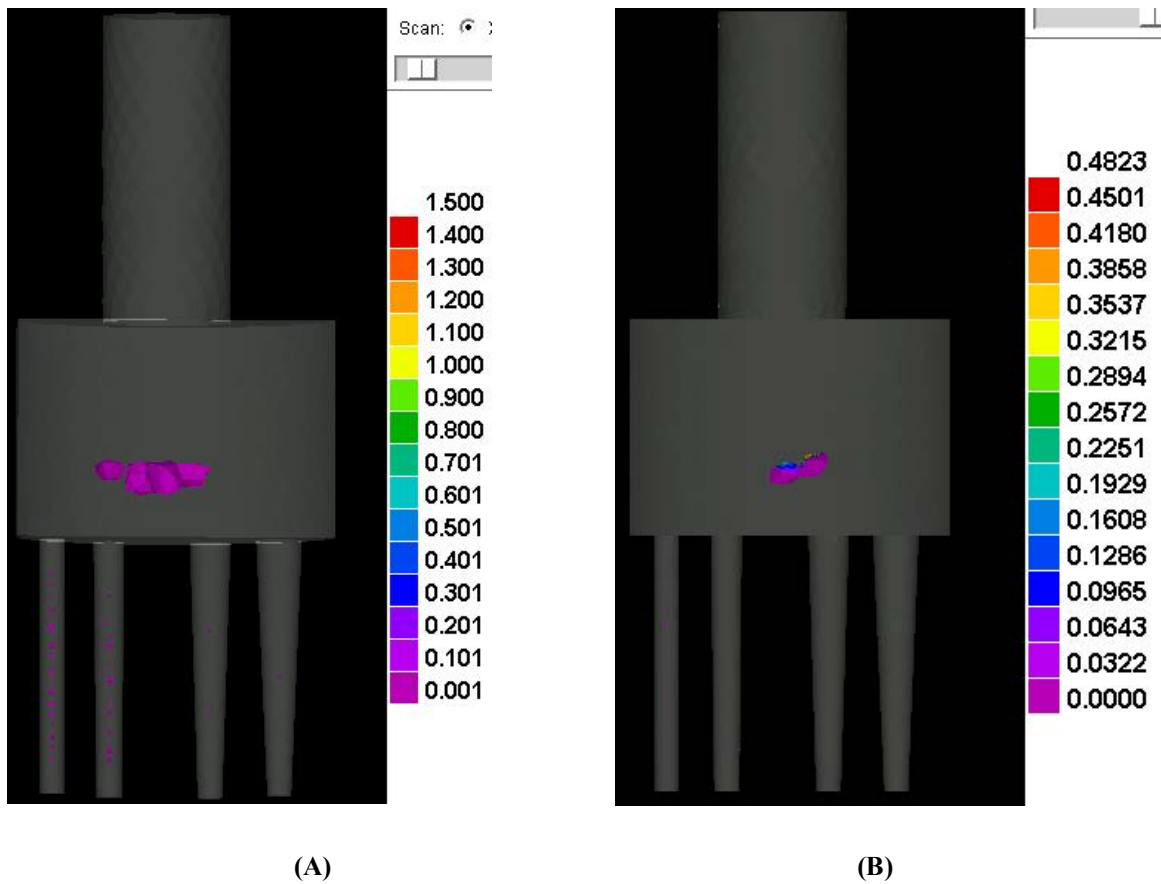
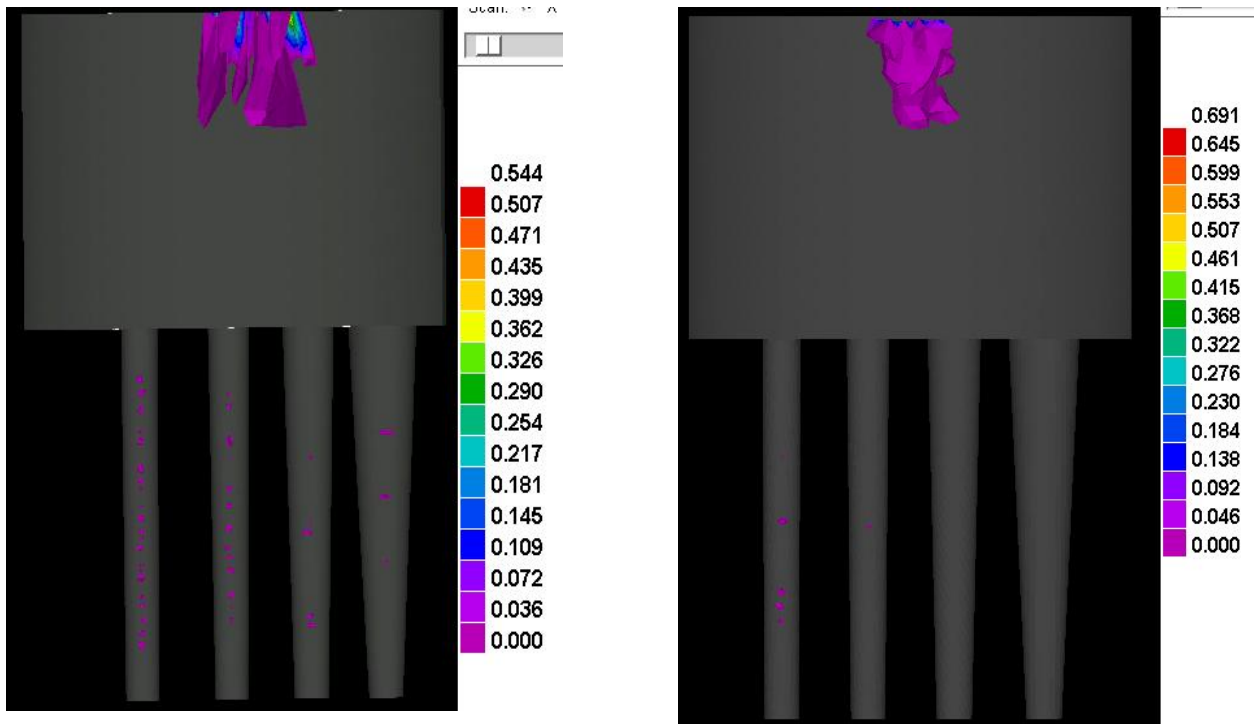


Figure 6.10 Volume percentages of shrinkage as predicted by the tilt-filling ProCast™ model (A) 500 °C and (B) 1000 °C.



(A) (B)
Figure 6.11 Volume percentage of shrinkage as predicted by the thermal-only ProCast™ model (A) 500 °C and (B) 1000 °C.

However, both models could predict shrinkage porosity for both mould temperatures. The 500 °C mould-temperature model predicted a larger volume of porosity than the 1000 °C mould-temperature model, which agreed well with the experimentally measured porosity, (see Figure 5.73), and shows that the prediction of shrinkage porosity, under the investment casting conditions investigated, can be achieved based on thermal parameters only.

As mentioned in Chapter 2, there have been many attempts to investigate whether the Niyama criterion is capable of predicting shrinkage in non-ferrous alloys, and to determine threshold values for these alloys. Some of these recent studies concerned the applicability of the Niyama criterion in TiAl based alloys, (although these studies have been limited), and it was therefore important to determine a threshold value for the Niyama criterion in the TiAlNb alloy in this research.

The results have shown that the relationship between shrinkage porosity in Ti-46Al-8Nb and the Niyama criterion can be divided into three intervals, (see Figures 5.68 to 5.72). For sufficiently high Niyama values; above $4 \text{ (}^\circ\text{C}\cdot\text{min)}^{0.5}\text{cm}^{-1}$, all the locations tested in the casting can be considered completely sound. As the Niyama function decreased to a value less than 4, where $4 > N_c > 2 \text{ (}^\circ\text{C}\cdot\text{min)}^{0.5}\text{cm}^{-1}$, the tested part is expected to contain microshrinkage porosity with an area percentage not larger than 0.05 %. The critical value of the Niyama function is $2 \text{ (}^\circ\text{C}\cdot\text{min)}^{0.5}\text{cm}^{-1}$, below which macroshrinkage porosity with a percentage area that could be as large as 1.3 % of the whole area of the tested section could occur.

This could mean that improving the thermal parameters of the casting process, i.e. the temperature gradient and the cooling rate, can be used to keep the Niyama values high enough to achieve soundness of the Ti-46Al-8Nb investment castings.

According to the results of this study, the temperature gradient alone can ensure soundness throughout the casting. The reliability of these values originates from the comparisons made between the measured results and the analysis of the model results, where areas with the maximum porosity were located in the same positions that exhibited minimum values of the Niyama criterion.

Plus, the results showed a good agreement between the increased temperature gradient and the distribution of porosity in the structure progressively solidified towards the feeder with the distribution of equiaxed grains along the investigated sections, which implies that the feeding difficulties due to the columnar-to-equiaxed transition are attributable to thermal parameters. Consequently, thermal-parameter based criterion, such as the Niyama criterion, can be used to predict shrinkage porosity directly related to thermal conditions, and can correlate porosity with the feeding mechanisms occurring during solidification of the castings.

6.7 A Comparison between Casting Defects in CP Ti, Ti-6Al-4V and Ti-46Al-8Nb Investment Casting Alloys

6.7.1 Misrun and Cold Laps in CP Ti and Ti-6Al-4V

Incomplete mould filling was caused by a low metal temperature as a result of low superheat due to Induction Skull melting. The maximum superheat as determined from the thermocouple and pyrometer readings (Table 3.2) did not exceed 50 °C. Thus the melt started to solidify before complete filling of the mould had occurred, and incomplete bars of 10 mm and 15 mm diameter are shown in Table 5.1. Cold laps with smooth round edges can be explained in terms of rapid filling of the mould cavities which were already filled by the argon gas, leading to a pressure build up inside the narrow cavities of the 10 mm diameter bars.

The increasing pressure of the mould atmosphere strongly resisted the stream of the poured melt and causing the formation of a back wave. Solidification was accelerated due to a low superheat at the tip of the advancing streams and the two streams of the melt met each other, and subsequently two convex surfaces with smooth round edges were formed.

By preheating the investment mould to 1000 °C cold laps and miss-run were avoided in the thinnest bars of 10 mm and 15 mm diameter of the Ti-6Al-4V alloy, (see the radiographs in Table 5.2). While these defects could not be avoided in C. P. Ti cast in a 1000 °C preheated mould, even though the castability of the metal was expected to increase with increasing the mould temperature.

Castability can be defined by the ability to produce a quality casting with minimum cost, which depends on the metal physical properties and the casting process conditions. Accordingly, castability is not a material property but it controlled by the casting parameters (mould design, casting design, primary coating, the mould temperature and the amount of

superheat) along with the metal properties like alloying elements and fluidity. Since all the casting parameters which affected the castability of CP Ti and Ti-4Al-6V in these experiments were fixed, then the low castability of C. P. Ti should be attributed to the solidification behaviour of the pure metal, where the planer solidification took place, while the α -laths with irregular grain boundaries, as can be seen in the microstructure and the macrographs in Figure 5.3, are indicative of the rapid cooling of the pure Ti during the casting process.

The fluidity of CP Ti at 1000 °C and a possible reaction with the Ytria coating which produces the α -case (which can reduce the fluidity as well by increasing the melt viscosity due to the formation of the inclusions [147]) are also important factors that need to be investigated in order to establish a complete understanding of the castability of C. P. Ti in 1000 °C preheated investment mould. (the α -case was observed on the surface of the test bars)

6.7.2 Gas Bubbles

By comparing the radiographs of all test bars it was noticed that, while the gravity-cast bars contained several gas bubbles, the tilt-cast bars did not contain any gas bubbles. It was concluded that the tilt filling process could significantly reduce or even eliminate the formation of gas bubbles by reducing or eliminating surface turbulence which would entrap surrounding gases inside the casting cavity during mould filling.

However, other casting parameters can also contribute to minimize the possible occurrence of gas bubbles, like casting size and the mould temperature. It was found that the amount of gas bubbles decreased with increasing bar size and mould temperature, and this can be seen in the radiographs of the commercial purity Ti and Ti-6Al-4V gravity casting test bars.

The effect of casting size and high mould temperature on the formation of this defect can be explained in terms of the fact that both factors cause a slow cooling rate which would provide additional time for entrapped gas bubbles to float to the surface of the melt.

6.7.3 Layer Porosity

Comparing the radiographs and the EDM and polished sections of samples from the same mould temperature (1000 °C), for the three investigated alloys Ti-46Al-8Nb, CP Ti and Ti-6Al-4V, (see Figures 5.1 and 5.2), showed that cylindrical bars of Ti-46Al-8Nb contained severe layer porosity. However, promoting directional solidification by using the tapered shape effectively reduced the quantity of layer porosity but did not completely eliminate it. On the other hand, commercial purity Ti and Ti-6Al-4V test bars did not show evidence of layer porosity in this study conditions.

CHAPTER 7

CONCLUSIONS

The aim of this study has been to develop a better understanding of the role of different casting parameters on the formation of shrinkage defects in Ti-46Al-8Nb investment castings through experimental and modelling techniques. This raises the significance of developing reliable boundary conditions, to contribute to the improvement of simulation modelling of the Ti-46Al-8Nb investment casting process. Optimization of mould temperature, casting design, and finite element analysis approaches in combination with materials characterization techniques were employed to correlate casting variables and macrostructural features to shrinkage defects in the investigated alloy. The conclusions obtained from the research are as follows:

1. Within the limitations of this study, for example the casting design and mould initial temperatures, there was no evidence of layer porosity formation in the commercial purity Ti and Ti-6Al-4V alloys, for the casting sizes studied and the mould temperatures used, (500 °C and 1000 °C).
2. Titanium aluminide, (Ti-46Al-8Nb), is prone to the formation of extensive layer porosity, this was attributed to the columnar-to-equiaxed transition which is promoted by low superheat and low temperature gradient conditions. It can be presumed that the nucleation and growth of equiaxed grains in front of the advancing columnar tips obstruct feeding especially the interdendritic feeding in the mushy zone, and pores are formed in the interdendritic spaces between the progressive solid layers.
3. Based on practical measurements and computer simulation, a tapered geometry of the test bars was found to be effective in decreasing the amount of shrinkage porosity in Ti-

46Al-8Nb alloy. The average area percentage of porosity was reduced by 95% by applying a taper factor of 0.1 mm per mm in a 100 mm long bar with 10 mm diameter at the small end. The soundness of the casting tested was improved by 10% as the taper factor was increased by 0.02 mm/mm in a 100 mm length. This is due to an improved temperature gradient which promoted directional solidification and hence more effective liquid feeding. In addition, it delayed the columnar-to-equiaxed transition which improved interdendritic feeding during the last stages of solidification.

4. The effect of mould preheating temperature on the columnar-to-equiaxed transition in Ti-46Al-8Nb was significant with low temperature gradient conditions. The average area of the equiaxed zone was increased by 36% as the mould temperature was increased from 500 °C to 1000 °C. A low temperature gradient combined with low superheat in the bulk liquid, both encouraged the constitutional nucleation of the equiaxed grains ahead of the columnar tips, which obstructed further growth of the columnar grains. However, as the temperature gradient was enhanced in the tapered test bars the columnar-to-equiaxed transition was hindered. Hence, the average area of the equiaxed zone was decreased by 40% for the mould at 500 °C, and 25% for the mould at 1000 °C, by applying a taper coefficient of 0.1 mm/mm in a 100 mm long bar with 10 mm diameter at the small end.

5. Increasing the mould preheating temperature significantly decreased the amount of shrinkage porosity in Ti-46Al-8Nb. A high initial mould temperature reduced the cooling rate of the casting and hence decreased the pressure drop of the feeding slurry in the interdendritic paths during the last stages of solidification, which improved feeding and hindered porosity formation. As a result, the average amount of porosity was decreased by a value of between 40 to 70 %.

6. Based on the experimental measurements of thermal boundary conditions of the investment mould, the interfacial heat-transfer coefficient of the ceramic shell was determined using measured cooling curves in 200 mbar of Argon and in vacuum.

The ceramic mould/surroundings interfacial heat transfer coefficient was in the range of $10 \text{ W/m}^2\cdot\text{K}$ at $100 \text{ }^\circ\text{C}$ to $60 \text{ W/m}^2\cdot\text{K}$ at $1000 \text{ }^\circ\text{C}$. The heat transfer coefficient of a ceramic shell cooling down from 1000°C in 200 mbar of argon was higher by $5 \text{ W/m}^2\cdot\text{K}$ than the heat transfer coefficient in vacuum. This was due to the contribution of convection in argon to the overall heat transfer mechanisms on the ceramic surface.

7. The interfacial heat transfer coefficient (h) between Ti-46Al-8Nb alloy and the inner surface of the ceramic investment mould was determined, by trial-and-error modelling, as a temperature dependant function. A value of $1000 \text{ W/m}^2\cdot\text{K}$ was assigned for the liquid interval down to the solidus temperature, which decreased to $300 \text{ W/m}^2\cdot\text{K}$ just below the solidus temperature, then gradually decreased to $20 \text{ W/m}^2\cdot\text{K}$ at room temperature, to reflect the consecutive intervals of solidification and the subsequent solid phase transformations, during which contraction of the casting metal takes place and a gap is expected to form at the interface and increase the resistance to heat transfer.

8. Temperature gradient alone cannot predict shrinkage porosity in Ti-46Al-8Nb, as feeding mechanisms in the mushy freezing alloy are dominated not only by local temperature gradient but also by local cooling rate and solidification time.

9. Thermal-only and tilt-filling ProCastTM models were developed and used to predict thermal parameters and criterion functions in different test bars with different taper angles, with $500 \text{ }^\circ\text{C}$ and $1000 \text{ }^\circ\text{C}$ mould temperatures.

The Niyama Criterion can be used to predict shrinkage-related porosity in Ti-46Al-8Nb castings. In particular, for positions in a casting with Niyama values above $4 (\text{°C}\cdot\text{min})^{0.5}\text{cm}^{-1}$, the casting can be considered completely sound. As for local areas with Niyama values in the range of 4 to $2 (\text{°C}\cdot\text{min})^{0.5}\text{cm}^{-1}$, the tested position was expected to contain microshrinkage porosity with an area percentage not larger than 0.05 %. The critical value of the Niyama function was $2 (\text{°C}\cdot\text{min})^{0.5}\text{cm}^{-1}$, below which the local area of a casting would be susceptible to macroshrinkage porosity.

10. Either a thermal model or a filling model can be used to calculate the Niyama criterion function to predict shrinkage porosity in Ti-46Al-8Nb alloy.

CHAPTER 8

FUTURE WORK

The results obtained in this study have shown the influence of the macrostructure on the formation of shrinkage porosity in Ti-46Al-8Nb alloy. The following future work can be undertaken as an extension to this project:

- It would be useful to use a computer modelling (cellular automaton-finite element, CAFE model) to predict macrostructure of this alloy in order to establish a correlation between macrostructure and shrinkage porosity in a wide range of different casting and solidification conditions.

- The current results have also shown that liquid and interdendritic feeding in the Ti-46Al-8Nb alloy can be improved through optimization of thermal conditions during the solidification process, thus a correlation between thermal parameters and feeding can be established through the investigation of the pressure drop along the feeding path in different temperature gradient and cooling rate. Therefore, in future research it would be significant to consider predicting the pressure drop by using a fully-coupled (three phases; liquid, gas and solid) mould filling and solidification simulation.

- The effect of initial mould temperature on castability of CP Ti metal during investment casting process needs to be investigated further, in terms of the effect of high mould temperature (1000 °C and higher) on the fluidity of the melt due to interaction with the mould coating and the formation of the α -case.

REFERENCES

1. R. Boyer, G. Welsh, E. Collings, "Materials Properties Handbook: Titanium Alloys", ASM International, 1994.
2. C. Leyens, M. Peters, "Titanium and Titanium Alloys Fundamentals and Applications", Betz-druck GMBH, 2005, pp 5-7, 9-11, 19-23, 89-93.
3. M. J. Donachie, Jr., "Titanium: A Technical Guide", Second Edition, ASM International, 2000.
4. Titanium Alloy Guide, RMI Titanium Company, 2000, pp 3-5.
5. D. Eylon, A. Vassel, Y. Combres, R.R. Boyer, P.J. Bania, and R.W. Schutz, "Issues in the Development of Beta Titanium Alloys", JOM, 1994, pp. 14-15.
6. Y. Kim, "Intermetallic Alloys Based on Gamma Titanium Aluminide", JOM, 1989, pp 24-30.
7. www.calphad.com/titanium-aluminum.html , Aug.2008.
8. N. Saunders, "Phase Equilibria in Multi-Component γ -TiAl Based Alloys", In "Gamma Titanium Aluminides 1999" eds. Y-W. Kim et al. (TMS Warrendale, PA), pp.183-187.
9. J. P. Lin, L. L. Zhao, G. Y. Li, L. Q. Zhang, X. P. Song, F. Ye, G. L. Chen, "Effect of Nb on oxidation behaviour of high Nb containing TiAl Alloys", Intermetallics, Vol. (19), 2011, pp.131–136.
10. Y. Liu, Hong Li, S. Wang, H. Ye, "Nb Effects on the Structural and Mechanical Properties of TiAl alloy: Density-functional Theory Study", Journal of Materials Research, Vol. 24, 2009, pp 3165-3173.
11. U. R. Kattner, W. J. Boettinger, "Thermodynamic calculation of the ternary Ti-Al-Nb system", Materials Science and Engineering, A 152, 1992, vol.(9), pp 17 9.

12. L. A. Bendersky, A. Roytburd, W. J. Boettinger, "Transformation of BCC and B2 High Temperature Phases to HCP and Orthorhombic structures in the Ti-Al-Nb System- Part I: Microstructural Predictions Based on a subgroup Relation between Phases", *Journal of Research of the National Institute of Standards and Technology*, vol. 98, 1993.
13. N. V. Kazantseva, S. V. Lepikhin, "Study of the Ti-Al-Nb Phase Diagram", *The Physics of Metals and Metallography*, Vol. 102, No. 2, 2006, pp. 169-180.
14. V. T. Witusiewicz, A. A. Bondar, U. Hecht, T. Ya. Velikanova, "The Al-B-Nb-Ti system, IV. Experimental study and thermodynamic re-evaluation of the binary Al-Nb and ternary Al-Nb-Ti systems", *Journal of Alloys and Compounds*, Vol. 472, 2009. pp. 133-161.
15. A. V. Kartavykh, "On the Primary Phase Microstructure of Solidifying Ti-46Al-8Nb Refractory Intermetallic Alloy", *American Journal of Materials Science*, 2012, pp. 28-33.
16. J. P. Kuang, R. A. Harding, J. Campbell, "Microstructure and Properties of Investment Castings γ -Titanium Aluminide", *Materials Science & Engineering*, A329-331, 2002.
17. L. L. Rishel, N. E. Biery, R. Raban, V. Z. Gandelsman, T. M. Pollock, A. W. Cramb, "Cast Structure and Property Variability in Gamma Titanium Aluminides", *Intermetallics*, Vol. 6, 1998, pp 629-636.
18. R. V. Ramanujan, "Phase Transformations in γ based Titanium Aluminides", *International Materials Reviews*, Vol. 45, No. 6, 2000, pp. 217-240.
19. M. Sujata, H. H. Sastry, C. Ramachandra, "Microstructural Characterization and Creep Behaviour of As-Cast Titanium Aluminide Ti-48Al-2V", *Intermetallics*, vol.12, 2004, pp 691-697.

20. A. K. Singh, K. Muraleedharan, D. Banerjee, "Solidification Structure in a Cast γ Alloy", *Scripta Materialia*, Vol. 48, 2003.
21. J. Zollinger, J. Lapin, D. Daloz, H. Combeau, "Influence of Oxygen on Solidification Behavior of Cast TiAl-Based Alloys", *Intermetallics*, vol. 15, 2007.
22. J. Barbosa, C. Silva Ribeiro, A. Caetano Monteiro, "Influence of Superheat on Casting of γ -TiAl", *Intermetallics* 15, 2007, pp 945-955.
23. A. Duarte, F. Viana, Henrique M. C. M. Santos, "As-Cast Titanium Aluminides Modification", *Materials Research*, Vol. 2, No. 3, 1999.
24. M. Charpentier, D. Daloz, A. Hazotte, E. Gautier, G. Lesoult, M. Grange, "Study of Microstructure and Solute Partitioning in a Cast Ti-48Al-2Cr-2Nb Alloy by Quenching during Directional Solidification Technique", *Metallurgical and Materials Transactions A*, Vol. 34A, 2003, pp 2139-2148.
25. O. Shuleshova, T. G. Woodcock, H.G. Lindenkreuz, R. Hermann, W. Loser, B. Buchner, "Metastable Phase Formation in Ti-Al-Nb Undercooled Melts", *Acta Materials* 55, 2007, pp 681-689.
26. J. A. Spittle, "Columnar to equiaxed grain transition in as solidified alloys", *International Materials Reviews*, Vol. 51, No. 4, 2006, pp. 247-269.
27. W. A. Tiller, K. A. Jackson, J. Rutter, B. Chalmers, "The Redistribution of Solute Atoms During the Solidification of Metals", *Acta Metallurgical*, 1953, pp. 428-437.
28. R. D. Doherty, P. D. Cooper, M. H. Bradbury, F. J. Honey, "On the Columnar to Equiaxed Transition in Small Ingots", *Metallurgical Transactions A*, Vol. 8A, 1977, pp. 397-402.
29. M. Wu, G. Nunner¹, A. Ludwig, J. Li, P. Schumacher, "Evaluation of a mixed columnar-equiaxed solidification model with laboratory castings." *IOP Conference Series: Materials Science and Engineering*. Vol. 27. No. 1. IOP Publishing, 2012.

30. H. Jung, N. Mangelinck-Noel, H. Nguyen-Thi, B. Billia, "Columnar to Equiaxed Transition during Directional Solidification in Refined Al-Based Alloys", *Journal of Alloys and Compounds* 484, 2009, pp 739-746.
31. M. A. Martorano, C. Beckermann, C. A. Gandin, "A Solutal Interaction Mechanism for the Columnar-to Equiaxed Transition in Alloy Solidification", *Metallurgical and Materials Transactions A*, Vol. 34A, 2003, pp 1657-1674.
32. C. A. Siqueira, N. Cheung, A. Garcia, "Solidification Thermal Parameters Affecting the Columnar to Equiaxed Transition", *Metallurgical and Materials Transactions A*, Vol. 33(A), 2002, pp. 2107-2118.
33. W. Shi-ping, L. Dong-rong, G. Jingjie, F. Heng-zhi, "Effect of Process Variables on Grain Growth in Simulating Solidification Microstructure of Ti-45% Al Alloy Ingot by Stochastic Model", *Trans. Nonferrous Met. Soc. China*, Vol. (15), No. 5, 2005, pp. 1096-1102.
34. S. Witzke, J. P. Riquet, F. Durand, "Diffusion Field Ahead of A growing Columnar Front: Diffusion of the Columnar-Equiaxed Transition", *Acta Metallurgical*, Vol. 29, 1980, pp. 365-374.
35. D. R. Liu, J. J. Guo, S. P. Wu, Y.Q. Su, H.Z. Fu, "Stochastic Modelling of Columnar-to-Equiaxed Transition in Ti-(45-48) Al Alloy Ingots", *Materials Science And Engineering A* 415, 2006, pp. 184-194.
36. Z. Gabalcová, J. Lapina "Experimental Study of Columnar to Equiaxed Transition during directional solidification of intermetallic Ti-46Al-8Nb Alloy", *Hradec nad Moravici, Metal* 2009, pp. 19-21.
37. M. M. Franke, M. Hilbinger, A. Heckl, R. F. Singer, "Effect of Thermophysical properties and processing conditions on primary dendrite arm spacing of nickel-base

- superalloys– numerical approach”, *Advanced Materials Research* Vol. 278, 2011, pp 156-161
38. J.D. HUNT, “Steady State Columnar and Equiaxed Growth of Dendrites and Eutectic”, *Mater. Sci. Eng.*, vol. 65, no. 1, 1984, pp. 75-83.
 39. S. C. Flood, J. D. Hunt, “Columnar and Equiaxed Growth: II Equiaxed Growth A head of Columnar Front”, *Journal of Crystal Growth*, Vol. (82), 1987, pp. 552-560.
 40. R. A. Harding, M. Wickins, Y.G. Li, “Progress Towards the Production of High Quality γ -TiAl Castings”, *Structural Intermetallics*, 2001
 41. N. Sakuma, H. Kurabe, T. Tsujimoto, “TiAl Melting in CaO Crucible and its Mechanical Properties”, *Tetsu to Hagane*, 1992, pp 172-179.
 42. A. Choudhury, M.Blum, “Economical Production of Titanium Aluminide Automotive Valves Using Cold Wall Induction Melting and Centrifugal Casting in a Permanent Mould”, *Vacuum*, Vol. 47, No.6-8, 1996, pp 829-831.
 43. R. A. Harding, M. Wickins, “Temperature Measurements During Induction Skull Melting of Titanium Aluminide”, *Materials Science and Technology*, Vol. 19, 2003.
 44. F. Gomes, J. Barbosa, C. S. Ribeiro, “Aluminium Evaporation During Ceramic Crucible Induction Melting of Titanium Aluminides”, 6th International Materials Symposium (MATERIALS 2011)/15th Meeting of SPM, Vol. 730-732, 2013
 45. H. Wang¹, G. Djambazov, K. A. Pericleous, “Numerical Study of Crucial Parameters in Tilt- Casting for Titanium Aluminides”, *China Foundry, Research and Development*, Vol. (8), No. (3), 2011, pp 274-280
 46. K. Pericleous, V. Bojarevics, R. A. Harding, M. Wickins, “Experimental and Numerical Study of the Cold Crucible Melting Process”, *Applied Mathematical Modelling*, vol. (30), 2006, pp 1262–1280

47. "Handbook of Metallurgical Process Design", Edited by George E. Totlen, Kiyoshi Unatani, Lin Xie, USA, 2004.
48. J. Campbell, "Castings", Butterworth-Heinemann, 1994
49. J. Campbell, "Complete Casting Handbook Metal Casting Processes, Techniques and Design", Vol. : Casting metallurgy, 2011, pp 187–253,
50. Li Y, M. Jolly, J. Campbell, "Internal and external porosity in short, medium and long freezing range aluminium alloy castings", In: Thomas BC, Beckermann C, editors. Modelling of Casting, Welding and Advanced Solidification Processes VIII, The Minerals, Metals & Materials Society; 1998, pp 1241-1253.
51. D.M. Stefanescu, "Computer Simulation of Shrinkage Related Defects in Metal Castings – A review", International Journal of Cast Metals Research, Vol. 18 No. 3, 2005.
52. Ch. Pequet, M. Gremaud, M. Rappaz, "Modelling of Microporosity, Macroporosity, and Pipe- Shrinkage Formation during the Solidification of Alloys Using a Mushy-Zone Refinement Method: Applications to Aluminium Alloys", Metallurgical and Materials Transactions A Vol. 33A, 2002.
53. M. Ross, I. Peter, " Defect Control on Al Casting for Excellent Quality and Improved Performance through Novel Rheocasting Processes", "Supplemental Proceedings Volume 2: Materials Properties and Characterization and Modelling", TMS 2012.
54. W. D. Walther, C. M. Adams, H. F. Taylor, "Mechanism for Pore Formation in Solidifying Metals", Trans. AFS, 1956, Vol. 64, pp 658-664.
55. H. Meidani, A. Jacot, "Phase-field simulation of micropores constrained by the dendritic network during solidification", Acta Materialia, Vol. 59, 2011, pp 3032–3040.
56. G. Couturier, M. Rappaz, "Modelling of Porosity Formation in Multicomponent Alloys in the Presence of Several Dissolved Gases and Volatile Solute Elements", Symposium

- of Simulation of Aluminium Shape Casting Processing , Edited by Qigui Wang, TMS (The Minerals, Metals & Materials Society), 2006.
57. J. Mi, R. A. Harding, M. Wickins, J. Campbell, “Entrained Oxide Films in TiAl Castings”, *Intermetallics*, Vol. 11, 2003.
 58. C. Reilly, N.R. Green, M.R. Jolly, “The present state of modelling entrainment defects in the shape casting process”, *Applied Mathematical Modelling*, Vol. 37, 2013, pp 611–628.
 59. J. Donea, A. Huerta, J.-Ph. Ponthot, A. R. Ferran, “Arbitrary Lagrangian–Eulerian Methods, Volume 1: Fundamentals”, *Encyclopaedia of Computational Mechanics*, Edited by Erwin Stein, Ren´e de Borst and Thomas J.R. Hughes, 2004
 60. J. Campbell, “Layer Porosity”, *The British Foundryman*, 1969, pp 147-158
 61. M. P. Groover, “Fundamentals of Modern Manufacturing: Materials, Processes and Systems”, 4th Edition, WILEY, USA, 2010.
 62. D.M. Stefanescu, “Science and Engineering of Casting Solidification”, 2nd Edition, Congress Library, USA, 2009.
 63. B. Ravi and M. N. Srinivasan, “Casting Solidification Analysis by Modulus Vector Method”, *Int. Cast Metals Res.*, 1996.
 64. Foseco Ferrous Foundryman’s Handbook, Edited by John R. Brown, Foseco International Ltd, 2000, pp 344-346.
 65. Thomas and C. Beckerman, *Modelling of Casting, Welding and Advanced Solidification Processes*, Warrendale, PA, TMS, 1998, pp 1071.
 66. J. Lu Battaglia, Jose Manuel Rozoto, “A Predictive Model for the Micro-porosity Quantitative in Al-Si Alloy”, *The Proceeding of the COMSOL Multiphysics User’s Conference*, Paris, 2005.

67. Z. Xu, A. Reis, Rob Van Tol, "A Feeding Flow Related Model for Modelling Shrinkage Defects", Modelling of Casting, Welding and Advanced Solidification Process-XII, TMS (The Minerals, Metals and Materials Society), 2009.
68. T. S. Piwonka, "Shrinkage Related Porosity in Steel Castings: A State of the Art Review", AFS Transactions 02-113, 2002.
69. H. Yildirim Erbil, "Surface Chemistry of Solid and Liquid Interfaces", Blackwell Publishing Ltd, 2006, pp 308-310.
70. P. K. Sung, D. R. Poirier, S. D. Felicelli, "Continuum Model for Predicting Microporosity in Steel Castings", Modelling Simul. Mater. Sci. Eng., Vol. 10, 2002
71. C. A. Monroe, C. Beckermann, J. Klinkhammer, "Simulation of Deformation and Hot Tear Formation Using A Visco-Plastic Model with Damage", Modelling of Casting, Welding and Advanced Solidification Process-XII, TMS (The Minerals, Metals and Materials Society), 2009.
72. I.E. Niyama, T. Uchida, M. Morikawa, M. Saito, "Predicting Shrinkage in Large Steel Castings from Temperature Gradient Calculation," AFS International Cast Metals Journal, Vol. 6, No. 2, 1981.
73. K. C. Carlson, C. Beckermann, "Prediction of Shrinkage Pore Volume Fraction Using a Dimensionless Niyama Criterion", Metallurgical and Materials Transactions A, Vol. 40A, 2009.
74. G. K. Sigworth, "Discussion of "Prediction of Shrinkage Pore Volume Fraction using a Dimensionless Niyama Criterion"". Metallurgical and Materials Transactions B, No. 40A, 2009.
75. K. C. Carlson, C. Beckermann, "Reply: Authors' reply to Discussion of Prediction of Shrinkage Pore Fraction using a Dimensionless Niyama Criterion", Metallurgical and Materials Transactions B, No. 40A, 2009.

76. R. A. Hardin, X. Shen, J. P. Gu, C. Beckermann, "Progress in the Development of Improved Feeding Rules for the Riser of Steel Castings", in Proceeding of the 52nd SFSA Technical and Operating Conference, Chicago, IL, 1998, Paper No. 4.
77. R. A. Hardin, S. Ou, K. Carlson, C. Beckermann, "Relationship Between Niyama Criterion and Radiographic Testing in Steel Casting", AFS Transactions, Vol. 108, 2000.
78. K. C. Carlson, C. Beckermann, "Use of the Niyama Criterion to Predict Shrinkage-Related Leaks in High-Nickel Steel and Nickel-Based Alloy Castings". In Proceedings of the 62nd SFSA Technical and Operating Conference, Steel Founders' Society of America, 2008.
79. E. Liotti, B. Previtali, "Study of the Validity of the Niyama Criteria Function Applied to the Alloy Al-7Si-Mg", La Metallurgia Italiana, 2006, pp 33-37.
80. V. Laurent, C. Rigaut, "An Experimental and Numerical Study of Criteria Functions for Predicting Microporosity in Cast Aluminium Alloys", AFS Transactions, 1992.
81. J. A. Spittle, S. G. R. Brown, J. G. Sullivan, "Application of Criteria Functions to the Prediction of Microporosity Levels in Castings", Proceedings of the 4th Decennial International Conference, Sheffield, 1997, pp 251-255.
82. V. K. Suri, A. J. Paul, N. El-Kaddah, J. T. Berry, "Determination of Correlation Factors for Prediction of Shrinkage in Castings-Part 1: Prediction of Microporosity in Castings; A Generalized Criterion", AFS Transactions, Vol. (138), 1994.
83. Y. W. LEE, E. Chang, "The Role of Solidus Velocity in the Feeding Behaviour of Al-7Si-0.3Mg Alloy Plate Castings", Materials Science and Engineering, A124, 1990.
84. J. Jakumeit, S. Jana, B. Böttger, R. Laqua, M. Y. Jouani, A. Bührig-Polaczek, "Simulation-Based Prediction of Micro-Shrinkage Porosity in Aluminium Casting: Fully-Coupled Numerical Calculation vs. Criteria Functions", The 3rd International

- Conference on Advances in Solidification Processes IOP Publishing, Materials Science and Engineering 27, (2011), 012066 doi:10.1088/1757-899X/27/1/012066
85. J. P. Kuang, R. A. Harding, J. Campbell, “ Examination of Defects in Gamma Titanium Aluminide Investment Casting”, *Int. J. Cast Metals Res.*, Vol. 13, 2000, pp 125-134.
 86. R. A. Harding, M. Wickins, “The Effect of Some Process Variables on Defects in Titanium Aluminide Castings”, 11th World Conference on Titanium, Kyoto, Japan, 2007.
 87. P. X. Fu, X. H. Kang, Y. C. Ma, K. Liu, Y. Y. Li, “Centrifugal Casting of TiAl Exhaust Valves”, *Intermetallics*, Vol. 16, 2008, pp 130-138.
 88. P. N. Hansen, P. R. Sahm, E. Flender, “How to Select and Use Criterion Functions in Solidification Simulation”, *AFS Transactions*, Vol. 51, 1993, pp 443-446.
 89. L. H. Shang, F. Paray, J. E. Gruzleski, S. Bergeron, C. Mercadante, C. A. Loong, “Prediction of Microporosity in Al-Si Castings in Low Pressure Permanent Mould Casting Using Criteria Functions”, *International Journal of Cast Metals Research*, Vol. 17, 2004, pp193-200.
 90. V. Laurent, C. Rigaut, “Experimental and Numerical Study of Criteria Functions for Predicting Microporosity in cast Al Alloys”, *AFS Transactions*, Vol. 163, 1992, pp 647-655.
 91. G. Yong, Z. Lijing, G. Wenli, Z. Hu, “Prediction and Improvement of Shrinkage Porosity in TiAl based Alloys”, *China Foundry*, Vol. 8, 2011, pp19-24.
 92. Si-Yong Sung, Y. Kim, “Modelling of Titanium Aluminides Turbo-Charger Casting”, *Intermetallics*, Vol. 15, 2007, pp 468-474.
 93. M. Rafique , J. Iqbal, “Modelling and simulation of heat transfer phenomena during investment casting”, *International J. of Heat and Mass Transfer*, Vol. 52, 2009
 94. ProCast 2009, User’s Manual, ESI Group, 2009

95. J. V. Beck, B. Litouhi, C. R. St. Clair Jr, "Efficient Sequential Solution of the Nonlinear Inverse Heat Conduction Problem", *Numerical Heat Transfer*, Vol. 5, 1982, pp 275-286.
96. D. O'Mahoney, D. J. Browne, "Use of Experimental and an Inverse Method to Study Interface Heat Transfer During Solidification in the Investment Casting Process", *Experimental Thermal and Fluid Science*, Vol. 22, 2000, pp 111-122.
97. K. A. Woodbury, Y. Chen, J. K. Parker, T. S. Piwonka, "Measurements of Heat Transfer Coefficients Between Al Castings and Resin-Bonded Moulds", *AFS Transactions*, 1998
98. H. Chi Sun, L. Sun Chao, "Prediction of Interfacial Heat Transfer Coefficients by Using a Modified Lump Capacitance Method for Aluminium Casting in Green Sand Mould", *ISIJ International*, Vol. 47, 2007, pp 1753-1758.
99. H. Jin, J. Li, D. Pan, "Application of Inverse Method to Estimation of Boundary Conditions during Investment Casting Simulation", *Acta Metallurgica Sinica (English Letters)*, Vol. 22, No. 6, 2009, pp 429-434.
100. C. H. Konrad, M. Brunner, K. Kyrgyzbaev, R. Volkl, U. Glatzel, "Determination of Heat Transfer Coefficient and Ceramic Mould Material Parameters for Alloy IN738LC Investment Castings", *Journal of Materials Processing Technology*, Elsevier, 2010.
101. W. Powell, and P. E. Liley, "Thermal Conductivity of the Elements: A Comprehensive Review.", *Journal of Physical and Chemical Reference Data*, volume 3, supplement 1, 1974, pp. I-1 to I-796
102. D.J. Browne, D. O'Mahoney "Interface heat transfer in investment casting of Aluminium alloys", *Met. And Mat. Transactions A*, Vol.32A, Dec.2001
103. D. O'Mahoney: PhD. Thesis, University College Dublin, 2000
104. M. J. Hendricks and D. R. Engelhardt, "Thermal Conductivity and Heat Transfer Measurement for Ceramic Shell Moulds", 8th World Conference on Investment Casting, London, 1993. Paper 11.

105. D. J. Jarvis, D. Voss, "IMPRESS Integrated Project-An overview Paper", *Material Science and Engineering A* 413-414, 2005.
106. I. Egry, R. Brooks, D. Holland-Moritz, R. Novakovic, T. Matsushita, E. Ricci, S. Seetharaman, R. Wunderlich, D. Jarvis, "Thermophysical Properties of γ -Titanium Aluminide: The European IMPRESS Project", *International Journal of Thermophysics*, Volume 28, Number 3, 2007, pp 1026-1036.
107. C. Cagran, B. Wilthan, G. Pottlacher, B. Roebuck, M. Wickins, R.A. Harding, "Thermophysical properties of a Ti-44Al-8Nb-1B alloy in the solid and molten States", *Intermetallics*, Vol. 11, 2003, pp 1327-1334.
108. H. P. Nicolai, Chr. Liesner, "Ti and Ti Alloys: Chapter 9; Investment Casting of Ti Alloys", Betz-druck GMBH, 2005, pp 263-271.
109. C.H. Cáceres, B.I. Selling, "Casting Defects and the Tensile Properties of an Al-Si-Mg Alloy", *Materials Science and Engineering*, A220, 1996.
110. X.J. Xu, J.P. Lin, Y.L. Wang, J.F. Gao, Z. Lin, G.L. Chen, "Microstructure and Tensile Properties of As-Cast Ti-45Al-(8-9)Nb-(W, B, Y) Alloy", *Journal of Alloys and Compounds*, Vol. 414, 2006.
111. J. A. Eady, D. M. Smith, "Effect of Porosity on the Tensile Properties of Al Castings", *Material Forum*, Vol. 9, 1986.
112. Chia-Wei Lin, Chien-Ping Ju, Jiin-Huey Chern Lin, "A Comparison of the Fatigue Behaviour of Cast Ti-7.5Mo with C.P. Titanium, Ti-6Al-4V and Ti-13Nb-13Zr Alloys", *Biomaterials*, Vol. 26, 2005.
113. H.V. ATKINSON, S. DAVIES, "Fundamental Aspects of Hot Isostatic Pressing: An Overview", *METALLURGICAL AND MATERIALS TRANSACTIONS A*, Vol. 31A, 2000, pp 2981

114. D. Hu, X. Wu, M.H. Loretto,” Advances in Optimisation of Mechanical Properties in Cast TiAl Alloys”, *Intermetallics*, Vol. 13, 2005.
115. R. J. Simpkins II, Michael P. Rourke, Thomas R. Bieler, P.A. McQuay, “The Effects of HIP Pore Closure and Age Hardening on Primary Creep and Tensile Property Variations in a TiAl XDTM Alloy with 0.1 wt.% Carbon”, *Materials Science and Engineering*, A 463, 2007, pp. 208–215.
116. F. Appel, J. D. H. Paul, M. Oehring, “Gamma Titanium Aluminide, Science and Technology”, Wiley-VCH, Germany, 2011, pp 502.
117. S. Kalpakjian, S. R. Schmid, “Manufacturing, Engineering & Technology, Fifth Edition”, Chapter 11, ISBN 0-13-148965-8, Pearson Education Inc, 2006.
118. A. N. Diogenes, E. A. Hoff, C. P. Fernandes, “Grain Size Measurement by Image Analysis: An application in the Ceramic and in the metallic industries”, 18th International Congress of Mechanical engineering, Ouro Preto, November 2005.
119. J. C. Russ, ”The Image Processing Handbook”, Second Edition, Library of Congress Cataloguing -in- Publication Data, USA, 1995, pp152,
120. L. J. Jobes, “Noise Reduction in Digital Images”, Carlson Centre for Imaging Science, 1990.
121. Bernd Jähne, “Practical Handbook on Image Processing for Scientific Applications”, Library of Congress Cataloguing -in- Publication Data, USA, 1997.
122. The Manual of Digimizer 2008, MedCalc Software.
123. L. Wojnar, K. J. Kurzydowski, “Practical Guide to Image Analysis; Chapter 7: Analysis and Interpretation”, ASM International, 2000.
124. J. Mi, R. A. Harding, J. Campbell, “The Tilt Casting Process”, *International Journal of Cast Metals Research*, Vol. 14, 2000, pp 325-335.

125. M. E. Brown, "Introduction to Thermal Analysis Techniques and Applications", Dec. 2001, pp 2, 3.
126. Takeo Ozawa, "Thermal Analysis- Review and prospect", *Thermochimica Acta*, vol. 355, 2000.
127. H. Saari, D. Y. Seo, J. Beddoes. "Thermophysical Property Determination of High Temperature Alloys by Thermal Analysis", *Journal of Thermal Analysis and Calorimetry*, Vol. 73, 2003.
128. I. ul-haq, J. Shin, Z. Lee, "Computer-Aided Cooling Curve Analysis of A356 Aluminium Alloy", *Metals and Materials international*, Vol. 10, No. 1, 2004
129. X. Chen, L. Meekisho, G. E. Totten, "Computer Aided Analysis of the Quenching Probe Test", *Proceeding of the 18th Conference "Heat Treating"*, ASM, 1998, pp 545-551.
130. A. Savitzky, M. J. E. Golay, "Smoothing and Differentiation of Data by Simplified Least Squares Procedures", *Analytical Chemistry*, Vol. 36, No. 8, 1964.
131. S. G. Shabestari, S. Ghodrat, "Assessment of modification and formation of intermetallic compounds in aluminium alloy using thermal analysis", *Materials Science and Engineering A* (467), 2007.
132. National Instruments Tutorial, "Temperature Measurements with Thermocouples: How-To Guide", www.ni.com, March 12, 2012.
133. J. Peir'ó, S. Sherwin, *Handbook of Materials Modelling. Volume I: Methods and Models*, Springer. Printed in the Netherlands. S. Yip (ed.), 2005, pp 1-32.
134. A. F. Bower, "Applied Mechanics of Solids", [Solid Mechanics.org/text/Chapter 7_1.htm](http://SolidMechanics.org/text/Chapter_7_1.htm)
135. S. Jones, S. Connolly, P. M. Marquis and D A Ford, "Specific Heat of Investment Casting Shells", *Proceedings Tenth World Conference on Investment Casting*, Monaco 2000, Paper WC 10.8.

136. L. A. Chapman, R. Morrell, P. N. Queded, R. F. Brooks, Li-Hung Chen, D. Ford, "PAMRIC: Properties of alloys and mould materials relevant to investment casting", National Physical Laboratory (NPL) UK, MAT 9, Jan.2008
137. D. J. Browne, K. Sayers, "Simulation of investment casting-The determination of mould thermophysical properties", 8th World Conference Investment Castings, London 1993
138. R. A. Harding, Private Communication, March 2010.
139. W.D. Griffiths, "A model of the Interfacial Heat Transfer Coefficient during Unidirectional Solidification of an Aluminium Alloy", Metallurgical Transactions, 31 B, 2000, pp 285-295.
140. "Thermocouple Specification Criteria", Smart Sensors, 2003.
141. "Report of Calibration", ROLLS-ROYCE, Precision Casting Facility Gate 6, Wilmore Road Sinfon, Derby).
142. T. Z. Kattamis, "Heat and Mass Transfer during Solidification", Proceedings of the International Centre for Heat and Mass Transfer "Heat and Mass Transfer in Metallurgical Systems": edited by: D. Brian Spalding, N. H. Afgan, 1981, pp 375-401.
143. C. A. Santos, J. M. V. Quaresma, A. Garcia, "Determination of transient interfacial heat transfer coefficients in chill mould castings", Journal of Alloys and Compounds 319, 2001, pp 174–186.
144. W. Zhang, G. Xie, D. Zhang, "Application of optimization method and experiment in inverse determination of interfacial heat transfer coefficients in the blade casting process", Exp. Thermal and Fluid Science, 2010, pp 1068-1076.
145. M. C. Flemings, "Solidification Processing", Material Science and Engineering Series, USA, 1974, pp 134-224.

146. B. Bryant, K. D. Carlson, S. Ou, C. Beckermann, "Tilt Pour Trials Analysis", in Proceedings of the 57th SFSA Technical and Operating Conference, paper No. 2.6, steel Founders' Society of America, Chicago, II, 2003.
147. E. Zhao, F. Kong, Y. Chen, "Effect of Different Primary Coating Materials and Mould Temperatures on Fluidity of High-Temperature Titanium Alloy", Proceedings of the Institution of Mechanical Engineers, Part B, DOI: 10.1177/0954405412459007, 2012.
148. J. E. Spinelli, I. L. Ferreira, A. Garcia, "Evaluation of heat transfer coefficients during upward and downward transient directional solidification of Al-Si alloys", 6th World Congresses of Structural and Multidisciplinary Optimization Rio de Janeiro, Brazil, 30 May - 03 June 2005.

APPENDIX A

Publication resulting from research:

Khaled, I.(2013) "Prediction of shrinkage porosity in ti-46al-8nb tilt-casting using the niyama criterion function". International Journal of Metalcasting .Vol. 7 Issue 4, p35-42.